Spatial optical solitons and optical gain in liquid crystal devices

Serena Bolis

Thesis presented in fulfillment of the requirements for the degree of

Doctor of Engineering Sciences from the Université libre de Bruxelles
Doctor of Photonics Engineering from the Ghent University

in a joint PhD program

Supervisors: Pascal Kockaert
Jeroen Beeckman

Université libre de Bruxelles
OPERA-Photonique

Ghent University
ELIS-Department

The private defense of this PhD took place on February 15th 2018 at the Ghent University, and the public defense took place on March 27th 2018 at the Université libre de Bruxelles.

Supervisors: Pascal Kockaert (ULB)
Jeroen Beeckman (UGent)

Members of the Jury

Gaetano Assanto (University of Rome "Roma Tre")
Kristin Bartik (ULB)
Filip De Turck (UGent, Chair at Ugent)
Simon-Pierre Gorza (ULB, Chair at ULB)
Zeger Hens (UGent)
Stephen M. Morris (University of Oxford)
Kristiaan Neyts (UGent)

Fundings that made this work possible:

FRIA grant (Fonds pour la Formation à la Recherche dans l'Industrie et dans l'Agriculture, FNRS)
IAP program (Belgian Science Policy Office, BELSPO, IAP7-35)
Fondation Philippe Wiener - Maurice Anspach
Fonds Van Buuren/Jaumotte-Demoulin
Center for Ultrafast Science and Biomedical Optics (CUSBO) at Politecnico di Milano (Ref. CUSBO 002033)
Research Foundation - Flanders (FWO)

Καίτοι εἰ ῥᾳθυμίᾳ μᾶλλον ἢ πόνων μελέτῃ καὶ μὴ μετὰ νόμων τὸ πλέον ἢ τρόπων ἀνδρείας ἐθέλομεν κινδυνεύειν, περιγίγνεται ἡμῖν τοῖς τε μέλλουσιν ἀλγεινοῖς μὴ προκάμνειν, καὶ ἐς αὐτὰ ἐλθοῦσι μὴ ἀτολμοτέρους τῶν αἰεὶ μοχθούντων φαίνεσθαι.

Eppure, se ci disponiamo a contrastare i pericoli, agili di spensierato abbandono più che gravi di esercizi e fatiche, forti di un ardire sorgivo libero frutto dei nostri principi vitali più che di leggi, ne nasce per noi il vantaggio di non piegarci in anticipo allo sgomento dei sacrifici futuri e, nel fuoco dell'impegno, di non mostrarci meno valorosi di coloro la cui esistenza è un tormentoso susseguirsi di prove.

TUCIDIDE, Storie II 39
Traduzione di E. Savino

Acknowledgments

As probably guessed from the front page, this thesis has been conducted in collaboration between two groups, the Opera Photonics Group at the Université libre de Bruxelles and the Liquid Crystals and Photonics Group at the Ghent University. Although, at least on paper, my thesis was pretty well separated (cell fabrication and numerical simulations in Ghent and optical setup and analysis of the results in Brussels), the real work was much more entangled, with a constant exchange and discussion between the two points of view that constitute my PhD. And these two voices, the nonlinear optics on one side and the liquid crystals on the other one, were very much impersonated by my two supervisors, Pascal and Jeroen. The dialogue with them, separately and together, is the heart of this work. It was challenging, sometimes hard, but also rewarding and (let's say it) fun, and it would have never been possible without their supervision, help and patience in all these years, even before my PhD, during from my Master thesis.

My PhD was not simply a joint PhD between ULB and UGent, it was also enriched by the exchange with other two universities, Politecnico di Milano and University of Oxford. I started in the first one with my Bachelor and my Master, and I spent the last period in the second one, thanks to incredibly opportunity that the Foundation Wiener-Anspach gave me.

At the Politecnico di Milano, I would like to particularly thank Tersilla. She introduced me to the pump-probe spectroscopy during my Master thesis and we had so much fun together that we never split. This is why we continued to collaborate during my whole thesis to achieve the beautiful work that constitutes Ch. 4. Thanks also to Michele, for his magic polarized confocal microscopy and (most importantly) for always knowing where to find the best food, even on the other side of the world.

At the University of Oxford, a warm and heart-felt thanks goes to Steve and Steve. To Steve (the Morris one), for the welcome, the kindness, the always stimulating discussions (I finally could talk about CLC lasing with you! :)), for making me changing my mind about everything, for the support and the understanding he provided in both happy and delicate moments. To Steve (the Elton one), for his excitement about science and the pleasure that was to speak with him about literally everything, going from flexo to the Venice Biennale to all declination of music, for his love for tea, food and good wine, for the wonderful moments and simply for everything.

I also would like to thank Philippe, always willing to just stop by to ask how it goes, Kristiaan, for the stimulating and challenging discussions, even in the most improbable languages, and SimPi, always available for any kind of help, in the lab or for the simulations, for helping me to find a way to handle a PhD or even just to chat about pictures and stars.

Thanks to all the colleagues from the OPERA photonics group. To Laurent, the first person who truly welcomed me in the group, for all the comfort and the support, to Tom, which I had the luck to know mostly after he left the department, for his knowing about almost everything and for the pleasure and the craziest fun that always is to speak with him, to Evdokia, for the wonderful time, for the fears and the joy shared in our office, to Robin, the easiest person to speak with, no matter what, to Charles, for having helped me to grasp and develop the wonderful concept of *vin du mois* and all the nice moments that go with that (and all the science, of course!), to Titi, for solving virtually everything, to Lory, for her always present smile, and to all the other people I had the chance to meet and work with at the department.

Thanks to all the colleagues from the Liquid Crystals and Photonics group. Thanks to Oliver, John, Samira, Inge and Varsenik, for the welcome and help in Ghent, not only in the lab, but also (and mostly) outside.

Thanks to all the colleagues from the Soft Matter and Photonics group. To Chloe, the most wonderful and crazy person I could have ever hoped to meet, for the pleasure to work with her, the way she gets lovely carried away, the easiness to speak with her about all and nothing, and for all the support and the friendship we found in one another. To David, not only for having taught me how to catch a(n American football) ball, but also how

to calm down a little, for the pleasure to talk with him about matlab, speckle, LC mixtures, dogs and cats and for our lovely breakfasts. To Ellis, the craziest person I ever met (I can affirm it quite certainly after Moscow!), always available, kind and full of ideas and new ways to change the world, thanks for all the things he taught me. To Patrick, for his precious help, to John, Taimoor and Konrad, for the lovely and fun moments, within and outside the lab.

A special thanks goes to Guido, my trusted chemist, the only one I believe in when it comes to chemicals and ways to handle them. He is always happy to explain me what they are, what to be afraid of and (most importantly) what to not worry about. I would have probably never survived through my thesis without the special Guido-approved list of do's and dont's. Thanks to Giancarlo, the second trusted chemist in charge, for all the chemistry (/material science!) and the music he taught me.

Thanks to all the people I encountered in these years, with whom I had the pleasure to share thoughts, problems, ideas or even just a cup of coffee or tea. Even if for lack of space it is not possible to thank them all, each one of them help me to develop a part of what I am now, from both a scientific and a human point of view.

The colleagues are not the only ones I need to thank. Of course, hard work is needed to complete a PhD (not really the good place to say the opposite here!), but time off is essential to not go crazy during this (sometimes difficult) period.

Thanks to Daniele, because it goes always better after a (short) phone call, especially if it ends with a *ti voglio bene*, and to Elisa, for all the courage you gave me in so many aspects of life. I do not even have the words to fully express the importance that was for me knowing that our friendship could survive time and space. Thanks for the support, the patience, the fun and the laughs that you both gave me in all these years.

Thanks to Davide and Tobia, because it will always feel like it was yesterday that we were sitting together at lunch, remembering who was mean to whom the first day of university.

Thanks to all the people in the *Orchestre et Harmonie de l'ULB* and in the *Turst Street Orchestra*, for all the moments of fun and relaxation, for all the music we shared together.

Finally, but most importantly, all this would have never been possible without the sustain of my family. My mum and dad, who always believed in me, even if it was difficult and far away. None of this would have ever been possible if they would have not taught me, since I was a little girl, that everything was possible. My big brothers, Amos and Samuel, because nothing really bad can ever happen if they are there. My little sister, Mary-Lin, because no matter what, she will always be there.

The biggest thanks of all is for Anh Dung, for his kindness, congeniality and tranquility, without all his support, faith and love, I would not be here.

List of publications

Some of the results reported in this thesis led to the following publications and presentation at international conferences.

Articles in International Peer-Reviewed Journals

i **S. Bolis**, C.C. Tartan, J. Beeckman, P. Kockaert, S.J. Elston and S.M. Morris, *"Solvent-induced self-assembly of uniform lying helix alignment of the cholesteric liquid crystal phase for the flexoelectro-optic effect"*, Liquid Crystals (2018) (DOI:10.1080/02678292.2018.1425492); cover of the Volume 45, Issue 5 of the same Journal (to be published).

ii E. Parry, **S. Bolis**, S.J. Elston, A. Castrejón-Pita, and S.M. Morris, *"Drop-on-Demand Ink-jet Printing of Thermally Tunable Liquid Crystal Microlenses"*, Advanced Engineering Materials, 1700774 (2017).

iii **S. Bolis**, S.P. Gorza, S.J. Elston, K. Neyts, P. Kockaert,J. Beeckman, *"Spatial fluctuations of optical solitons due to long-range correlated dielectric perturbations in liquid crystals"*, Physical Review A, 96, 031803(R) (2017).

iv **S. Bolis**, T. Virgili, S.K. Rajendran, J. Beeckman, P. Kockaert, *Nematicon-driven injection of amplified spontaneous emission into an optical fiber*, Optics Letters 41, 2245 (2016).

v L. Ghirardini, T. Virgili, **S. Bolis**, J. Beeckman, P. Kockaert, M. Finazzi and M. Celebrano, *The role of segregation in the polarized emission from polyfluorene embedded in a liquid crystal*, Journal of Polymer Science Part B: Polymer Physics 54, 1558 (2016); cover of the Volume 54, Issue 16 of the same Journal.

vi **S. Bolis**, M. Celebrano, L. Ghirardini, M. Finazzi, C. Botta, J. Beeckman, P. Kockaert and T. Virgili, *"Optical gain from polyfluorene keto defects in a liquid crystal mixture"*, Chemical Communications 51, 9686 (2015).

International Peer-Reviewed Conferences

vii E. Parry*, **S. Bolis**, A. Castrejón-Pita, S. J. Elston and S. M. Morris, *"Drop-on-Demand ink-jet printing of tunable liquid crystal microlens arrays"*, accepted as an oral presentation to the Optics of Liquid Crystals Conference, 24-29 September 2017, São Paulo, Brazil. (Oral presentation)

viii **S. Bolis***, S.J. Elston, J. Beeckman, P. Kockaert, *"Spatial instabilities in nematicon propagation generated by correlated noise in liquid crystals"*, Nonlinear Optics Conference, 17-21 July 2017, Waikoloa, USA. (Oral presentation)

ix **S. Bolis***, C.C. Tartan, J. Beeckman, P. Kockaert, S.J. Elston and S.M. Morris, *"Flexoelectro-optic properties of defect-free solvent-induced uniform lying helix"*, European Conference on Liquid Crystals, 25-30 June 2017, Moscow, Russia. (Oral presentation)

x E. Parry*, **S. Bolis**, A. Castrejón-Pita, S. J. Elston and S. M. Morris, *"Drop-on-Demand ink-jet printing of liquid crystals and the fabrication of tuneable microlens arrays"*, European Conference on Liquid Crystals, 25-30 June 2017, Moscow, Russia. (Oral presentation)

xi K. Neyts*, I. Nys, M. Mohammadimasoudi, T. Dadalyan, **S. Bolis** and J. Beeckman, *"Lasing from dye doped liquid crystal devices"*, 6th Workshop on Liquid Crystals for Photonics, 14-16 September 2016, Ljubljana, Slovenia. (Oral presentation)

xii **S. Bolis***, T. Virgili, J. Beeckman and P. Kockaert, *"Strong collection of Amplified Spontaneous Emission with nematicons"*, Nonlinear Photonics Congress (OSA), 5-8 September 2016, Sydney, Australia. (Oral presentation)

xiii **S. Bolis***, O. Debeir, J. Beeckman and P. Kockaert, *"Amplified spontaneous emission injection into an optical fiber with the aid of a nematicon"*, 20th Annual Symposium of the IEEE Photonics Benelux Chapter, 26-27 November 2015, Bruxelles, Belgium (postponed due to security threats in Brussels). (Oral presentation)

xiv **S. Bolis**, M. Celebrano, L. Ghirardini, M. Finazzi, C. Botta, J. Beeckman, P. Kockaert and T. Virgili*, *"Optical Gain from Polyfluorene Keto Defects in a Liquid Crystal Mixture"*, FISMAT 2015, 28 September-2 October 2015, Palermo, Italy. (Oral presentation)

xv **S. Bolis***, M. Celebrano, L. Ghirardini, M. Finazzi, C. Botta, J. Beeckman, P. Kockaert and T. Virgili, *"Anisotropic optical gain from polyfluorene keto defects induced by a liquid crystalline matrix"*, Optics of Liquid Crystals Conference 2015, 13-18 September 2015, Sopot, Poland. (Oral presentation)

xvi **S. Bolis***, J. Beeckman, P. Kockaert and T. Virgili, *"Liquid crystals as a matrix to induce an oriented polyfluorene β-phase"*, *OSA - Advanced Photonics Congress*, 27-31 July 2014, Barcelona, Spain. (Poster)

* Presenting author.

In agreement with the Copyright policy of these journals, we make use in this manuscript of certain sentences, equations and figures published in this reference. As some parts of theses sentences have been rewritten, it would be difficult to quote them all. We have therefore decided to quote none of them, but inform the reader explicitly by means of this note.

Contents

Nomenclature

Physical Constants

μ_0	Vacuum permeability	$4\pi \cdot 10^{-7}$ N/A^2
ε_0	Vacuum permittivity	$8.8541 \cdot 10^{-12}$ F/m
c	Speed of light in a vacuum	$2.9979 \cdot 10^{8}$ m/s
k_B	Boltzman constant	$1.3806 \cdot 10^{-23}$ J/K

Physical Variables

$\bar{\bar{\chi}}$	Susceptibility tensor	
ρ_b	Bound charge density	[C/m^3]
ρ_f	Free charge density	[C/m^3]
$\bar{\bar{\varepsilon}}_r^d$	Relative permittivity in the director frame of reference	
$\bar{\bar{\varepsilon}}_r$	Relative permittivity	
ε_L, ε_{NL}	Linear and nonlinear contribution to the relative permittivity	
$\varepsilon_\perp, \varepsilon_\parallel$	Linear relative permittivities, orthogonal and parallel to the long axis of the molecule, respectively	
α	Propagation losses	[m^{-1}]
$\mathcal{A}$	Slowly varying envelope of the optical electric field	[V/m]
A	Absorbance	
$\bar{B}$	Magnetic field	[T]
$\bar{\bar{C}}$	Correlation matrix	
$\bar{D}$	Displacement field	[C/m^2]
δ	Walk-off angle	[rad or °]
D	Normalized linear PL dichroism	
$\bar{E}$	Electric field	[V/m]
η	Viscosity	[Pa·s]
$\mathcal{E}$	Spatial part of the optical electric field	[V/m]
e_1, e_3	splay and the bend flexoelectric coefficients	[C/m]
$\mathcal{F}$	Free energy	[J]
f	Free energy density	[J/m^3]
ϕ	Tilt angle in the flexoelectro-optic effect	[rad or °]

φ,θ	Angles describing the LC orientation in the laboratory frame of reference	[rad or °]
Γ	Period of the bend-splay deformation	[m]
$\bar{H}$	Magnetizing field	[A/m]
I_0	Peak intensity of a beam	[W/m^2]
I_0^{in},I_0^{out}	Input and output intensity in a sample	[W]
I_p,I_o	Intensity contributions parallel and orthogonal to the LC director	[counts]
$\bar{J}$	Current density	[A/m^2]
k, j, n	Indexes for the discretization along $\hat{x}, \hat{y}, \hat{z}$	
K_1, K_2, K_3	Splay, twist and bend elastic constants	[N]
λ	Wavelength	[m]
l	Thickness of the sample	[m]
l_{eff}	Confinement length due to the planar waveguide in the case of 1D soliton	[m]
$\bar{M}$	Magnetization	[A/m]
M, N	Number of points for the discretization along $\hat{x}$ and $\hat{y}$	
$\bar{\bar{N}}$	Matrix describing the noise orthogonal to the propagation of the soliton	
$\hat{\mathtt{n}}$	Liquid crystal director (unitary vector)	
$\mathscr{N}$	Population density of an energy level	[1/m^3]
$\mathtt{N}$	Soliton order	
n	Refractive index	
n_0	Linear refractive index	
n_2	Nonlinear (Kerr) coefficient	[cm^2/W]
$n_\parallel$,$n_\perp$	Refractive indices parallel and orthogonal to the director, respectively	
$\bar{P}$	Polarization density	[C/m^3]
p,p_0	Pitch and natural pitch of chiral nematic LC	[m]
P_0	Peak power of a beam	[W]
q	Wave vector	[m^{-1}]
$\bar{S}$	Poynting vector	[W/m^2]
S	Singlet state in an energy diagram of a molecule	
σ	Cross section relative to a radiative transition	[cm^2]
T	Triplet state in an energy diagram of a molecule	
τ	Delay between the pump and the probe pulses	[s]
T	Transmission	

T_c	Clearing temperature	[K or °C]
T_m	Melting temperature	[K or °C]
$\hat{x}', \hat{y}', \hat{z}'$	Nematicon frame of reference (unitary vectors)	
$\hat{x}, \hat{y}, \hat{z}$	Laboratory frame of reference (unitary vectors)	
$\hat{x}_d, \hat{y}_d, \hat{z}_d$	Director frame of reference (unitary vectors), $\hat{n}_0 \parallel \hat{z}_d$	
ξ	Coherence length in nematic LC	[m]
ω_0	Angular frequency of the carrier of the optical electric field	[Hz]
w_0	Beam radius at $1/e^2$ of the intensity profile	[m]

Symbols

$\bar{a}$	Vector
$\hat{a}$	Unitary vector
$\mathscr{F}[a]$	Fourier transform of function a
$\nabla \cdot \bar{a}$	Divergence operator on vector $\bar{a}$
$\nabla \times \bar{a}$	Curl operator on vector $\bar{a}$
∇a	Gradient operator on a
$\nabla^2 \bar{a}$	Laplacian operator on vector $\bar{a}$
$\triangle a$	Difference or anisotropy of a

Acronyms

ASE	Amplified spontaneous emission
CLC	Cholesteric or chiral nematic liquid crystal
CR	Contrast ratio
GSB	Ground state photo-bleaching
HA	Helix axis
LC	Liquid crystal
NA	Numerical aperture
NLSE	Nonlinear Schrödinger equation
OA	Optic axis
PIA	Photo-induced absorption
PL	Photoluminescence
SE	Stimulated emission
SHG	Second harmonic generation
SLM	Spatial light modulator

TPP	2-photon photo-polymerization
ULH	Uniform lying helix
USH	Uniform standing helix
WLC	White light continuum generation
wt%	Concentration (percentage) in weight

Summary

In this work, we study the nonlinear propagation of light in liquid crystals (LCs) and the optical gain provided by LCs when they are polymer- or dye-doped.

We will focus on nematic LCs, which are characterized by a mean orientation (also called *director*) of the elongated molecules and by a subsequent birefringence. After a general introduction on LCs, we focus on the nonlinear propagation of light in nematic LCs, and in particular the soliton-like propagation (nematicon). Indeed, if the light injected in the cell is intense enough, it can create a waveguide that counteracts the diffraction of the light. The light then propagates with an almost constant (or periodic) transverse profile.

Our contribution to the subject starts with the numerical modeling of the thermal noise that characterizes the nematic LCs and the study of spatial instabilities of the soliton propagation caused by that noise. In Ch.3 we show that, by explicitly implementing the spatial correlation of the director in the LC thermal noise, it is possible to reproduce some of the features that characterize the LC response, such as the speckle generation or the fluctuating trajectory of the spatial optical soliton in LCs. Indeed, when the nematicon diameter is of the same order of magnitude as or smaller than the refractive index perturbations caused by the thermal noise, the nematicon starts to fluctuate in space. These fluctuations are not present when the noise is not correlated, indicating that the long-range interactions in LCs are crucial to explain the fluctuations. The model also allows us to introduce the propagation losses experienced by the nematicon without the use of an ad-hoc term. The simulations are in agreement with the experimental results. This method could also help the modeling of complex nonlinear phenomena in LCs that rely on noise, such as modulation instabilities or filamentation.

Then, the optical gain is included in the LCs by dissolving photoluminescent polymers or dyes in it. In particular, we show that a particular polymer, the polyfuorene, when dissolved in nematic LCs, creates an intricate supramolecular pattern composed by homogeneous LC-rich regions surrounded by polymer-rich boundaries. The study of these structures through an ultra-fast spectroscopic technique (the pump-probe technique) and confocal microscopy reveals that the boundaries are composed by ordered and isolated chains of polymers. This particular morphology allows the observation of the optical gain from an oxidized unit of the polymeric chain (keto defects). This signal is usually covered by the absorption caused by the chain aggregation in solid state samples, while in LCs it is clearly visible. The optical gain from the keto defects appears also to be polarized orthogonal to the LC director, which is also the orientation of most of the boundaries. When a dye, one of the pyrromethenes, is dissolved in the LCs, the sample appears to be homogeneous. The optical gain from the dye is polarized along the LC director and it shows an important spectral blue-shift (10 nm) passing from a polarization parallel to orthogonal to the LC director. The amplified spontaneous emission (ASE) shows the same shift when changing the direction of the sample excitation.

When the ASE and the nematicon are generated in the same sample, it is possible to study the interaction between the two. In particular, the waveguide induced by the soliton can be used to guide another signal at another wavelength. We show that the nematicon can collect the ASE generated in the same device and guide it to the same fiber used to inject the nematicon in the LC cell. The extraction of the ASE from the device increases almost one order of magnitude when the soliton is present. However, due to the nematicon spatial fluctuations in LCs, an optimal nematicon power has to be found. Indeed, by increasing the soliton power, the light guiding is improved since the refractive index contrast of the nematicon-induced waveguide is increased. However, very high soliton powers have to be avoided, since the power-dependent soliton fluctuations prevent an optimal collection of the light. The nematicon is also found to increase the spectral purity and the polarization degree of the guided signal.

Another LC system is studied, the chiral nematic LCs. In this system, the molecules are disposed following an helicoidal distribution. Due to their optical anisotropy and the periodic distribution, the system presents an optical band-gap. If the LC is also dye-doped, the combination of optical band-gap and gain generates laser emission. We are interested in a fast (sub-ms) reorientation of the helix, with the aim of studying the effect of this reorientation on the laser emission. The first step is the alignment of the LC helix (without the dye) with its axis

parallel to the glass plates that constitute the cell, which is difficult to obtain with a high optical quality. For this reason, an innovative method is developed to align LCs through directional solvent evaporation. The solvent-induced method allows us to obtain particularly homogeneous textures, with a contrast ratio between the bright and the dark states that is a factor of 4 greater than that obtained with traditional methods. The LC samples based on solvent-induced alignment are then stabilized via two-photon photo-polymerization. This technique allows us to polymerize small regions of the device while the rest of the sample can be washed out in a solvent bath. When an achiral material is used to refill the device, it assumes a chiral alignment in the polymerized regions and an achiral nematic distribution in the rest. The first characterization of the laser emission is then presented in the last Chapter, with the aim of achieving sub-ms electrical tuning in future works.

In this work a wide range of aspects have been investigated, leading to the realization of novel techniques for the fabrication of liquid crystal devices, the demonstration of novel phenomena for light amplification in liquid crystals and the experimental verification of new numerical modeling tools for light propagation in liquid crystals. The three key aspects of the work are nonlinear propagation, optical amplification and electrical response of different LC-based mixtures. Although the first few chapters deal with some of the aspects separately, in the last chapter these aspects are combined, revealing interesting new phenomena and pointing out a number of new aspects that could be part of future work. The results in this work have potential applications in fast tunable lasers, optical communication systems and lab-on-chip components.

Résumé

Dans ce travail, nous étudions la propagation nonlinéaire de la lumière dans les cristaux liquides (CLs) et le gain optique produit dans les CLs lorsque ceux-ci sont dopés par des polymères ou des colorants.

Notre travail se focalisera sur les CLs nématiques qui sont caractérisés par une orientation moyenne (appelée *directeur*) des molécules allongées et par la biréfringence qui en découle. Après une introduction génŕale sur les CLs, nous nous concentrerons sur la propagation nonlinéaire de la lumière dans les CLs nématiques et, en particulier, sur la propagation de type soliton (nématicon). En effet, lorsque la lumière injectée dans la cellule est suffisamment intense, elle peut créer un guide d'onde qui contrebalance la diffraction de la lumière. La lumière se propage alors avec un profil transverse presque constant (ou périodique).

Notre contribution sur le sujet commence par une modélisation numérique du bruit thermique qui caractérise les cristaux liquides nématiques et l'étude des instabilités spatiales de la propagation de type soliton causées par ce bruit. Dans le Ch. 3 nous montrons que l'implémentation explicite de la corrélation spatiale du directeur dans le bruit thermique des cristaux liquides permet de reproduire certaines des caractéristiques propres à la réponse des CLs telles que la génération de speckle ou la trajectoire fluctuante du soliton spatial optique dans les cristaux liquides. En effet, quand le diamètre du nématicon est du même ordre de grandeur ou plus petit que les pérturbations de l'indice de réfraction causées par le bruit thermique, le nématicon commence à osciller dans l'espace. Ces fluctuations ne sont pas présentes dans le cas d'un bruit non corrélé, ce qui indique que les corrélations sur longue distance dans les CLs sont cruciales pour expliquer ce phénomène. Le modèle permet aussi de reproduire les pertes de propagation subies par le nématicon sans l'introduction d'un terme *ad hoc* de perted phénoménologiques. Les simulations sont en accord avec les résultats expérimentaux. Ce modèle pourrait aussi aider à la modélisation de phénomènes nonlineaires complexes dans les CLs qui impliquent du bruit, comme l'instabilité de modulation et la filamentation.

Ensuite, le gain optique est inclus dans les CLs en y dissolvant des polymères photoluminescent ou des colorants. En particulier, nous montrons qu'un polymère particulier est dissous dans les cristaux liquides nématiques, le polyfluorène, il crée des structures supramoléculaires intriquées, composée de régions homogènes riches en CL entourées de bords riches en polymère. L'étude des ces structures à l'aide d'une technique de spectroscopie ultra-rapide (la technique pompe-sonde) et de la microscopie confocale révèle que les bords sont composés par des chaînes de polymères ordonnées et isolées. Cette morphologie particulière permet l'observation du gain optique venant d'une unité oxydée de la chaîne polymérique (défaut cétone ou fluorénone). Ce signal est habituellement couvert par l'absorption causée par l'aggrégation des chaînes de polymère dans les échantillons à l'état solide alors que dans les CLs, il est clairement visible. Le gain optique venant du défaut cétone est polarisé orthogonalement au directeur du CL, qui correspond aussi à l'orientation de la majorité des bords. Quand un colorant, un des pyromethenes, est dissous dans les CLs, l'échantillon apparaît comme étant homogène. Le gain optique provenant du colorant est polarisé le long du directeur du cristal liquide et il montre un décalage vers le bleue important (10 nm) passant d'une polarisation parallèle à une polarisation orthogonale au director des cristaux liquides. L'émission spontanée amplifée (Amplified Spontaneous Emission - ASE) montre le même décalage vers le bleue quand la direction de l'excitation de l'échantillon est changée.

Quand l'ASE et le nematicon sont générées dans le même échantillon, il est possible d'étudier l'interaction entre ces deux phénomènes. En particulier, le guide d'onde induit par le soliton peut être utilisé pour guider un autre signal à une autre longueur d'onde. Nous montrons que le nematicon peut collecter cette ASE générée dans la cellule à CL et la guider dans la fibre utilisée pour y injecter le nématicon. L'extraction de l'ASE du dispositif augmente quasiment d'un ordre de grandeur lorsque le soliton est présent. Cependant, à cause des fluctuations spatiales du nématicon dans les CLs, une puissance optimale du nématicon doit être trouvée. En effet, en augmentant la puissance du soliton, le guidage de la lumière est amélioré car le contraste d'indice de réfraction du guide d'onde induit par le nématicon est augmenté. Cependant, des puissances trop importantes de solitons sont à éviter vu que les fluctuations du soliton dépendant de la puissance empêchent une collecte

optimale de la lumière. Le nématicon permet aussi d'augmenter la pureté spectrale et le dégré de polarisation du signal guidé.

Un autre système à CLs est étudié dans ce travail: les CLs nématiques chiraux. Dans ce système, les molécules sont disposées selon une distribution hélicoïdale. Du fait de leur anisotropie optique et de leur distribution périodique, le système présente une bande intérdite optique. Si les cristaux liquides sont également dopés par colorants, la combinaison de la bande intérdite optique avec le gain génère de l'émission laser. Nous nous sommes intéressés à une réorientation rapide (sub-ms) de l'hélice dans le but d'étudier l'effet de cette réorientation sur l'émission laser. La première étape est l'alignement des CLs en hélice (sans le colorant) avec un axe parallèle à la plaque de verre qui constitue la cellule, ce qui est difficile à obtenir avec une bonne qualité optique. Pour cette raison, une méthode innovante a été développée pour aligner les cristaux liquides grâce à l'évaporation directionnelle du solvant. Cette méthode d'alignement induite par le solvant permet d'obtenir des textures particulièrement homogènes avec un rapport de contraste entre les états brillant et noir quatre fois meilleur que ce qui peut être obtenu par les méthodes traditionnelles. Les échantillons de cristaux liquides alignés par cette méthode sont alors stabilisés par la photo-polymérisation à deux photons. Cette technique permet de polymériser de petites régions, alors que le reste de l'échantillon peut être vidé dans un bain de solvant. Quand un matériau achiral est utilisé pour remplir le dispositif, il adopte un alignement chiral dans les régions polymérisées et achiral ailleurs. La première caractérisation de l'émission laser est ensuite présentée dans le dernier chapitre de ce travail, dans l'optique d'arriver dans des travaux futurs à un dispositif accordable en champ électrique et avec une réponse sub-ms.

Dans ce travail différents aspects ont été analysés, ce qui a conduit à la réalisation de nouvelles techniques pour la fabrication des dispositifs à cristaux liquides, la démonstration des nouveaux phénomnès pour l'amplification de lumière dans les cristaux liquides et la vérification expérimentale des nouveaux outils pour la propagation de la lumière dans les cristaux liquides. Les trois aspects clés de ce travail sont la propagation nonlinéaire, l'amplification optique et la réponse électrique pour différents mélanges de CLs. Même si les premiers chapitres traitent certains de ces aspects séparément, dans le dernier chapitre ces aspects sont réunis, en révélant des nouveaux phénomènes et en mettant en avant nombreux nouveaux point qui pourraient être part de travaux futurs. Les résultats de ce travail peuvent avoir des applications potentielles pour des lasers rapidement accordables, des systèmes de communication optique et des composantes lab-on-chip.

Samenvatting

In dit werk wordt de niet-lineaire voortbeweging van licht in vloeibare kristallen (Liquid Crystals, LCs) en de optische versterking door het LC-materiaal bestudeerd in het geval van polymeer- of kleurstof-gedoteerde LCs.

We richten ons vooral op nematische LCs die gekarakteriseerd worden door een gemiddelde oriëntatie van de langwerpige moleculen (ook director genoemd) en als gevolg daarvan door een dubbelbreking. Na een algemene inleiding over LCs kijken we naar de niet-lineaire voortbeweging van licht in nematische LCs en in het bijzonder de soliton-achtige voortbeweging. Deze soliton-achtige voortbeweging wordt ook nematicon genoemd. Immers, als de lichtbundel die geïnjecteerd wordt in de component intens genoeg is, dan wordt een golfgeleider gevormd die de diffractie van het licht tegengaat. Het licht beweegt zich dan voort met een vrijwel constant (of periodiek) transversaal profiel.

Onze bijdrage aan het onderwerp start met de numerieke modellering van de ruis die karakteristiek is voor nematische LCs en de studie van de ruimtelijke instabiliteiten van de solitonvoortbeweging die veroorzaakt wordt door deze ruis. In Hoofdstuk 3 tonen we aan dat het mogelijk is om enkele karakteristieke fenomenen van de voortbeweging van licht in LCs numeriek te reproduceren, zoals de vorming van speckle of het fluctuerende traject van ruimtelijke optische solitonen in LCs. Hiervoor is het nodig om de ruimtelijke correlatie van de director van de thermische ruis in LCs expliciet numeriek te implementeren. Als de diameter van het nematicon van dezelfde grootteorde is of kleiner dan de perturbaties van de brekingsindex, veroorzaakt door de thermische ruis, dan start het nematicon ruimtelijk te fluctueren. Deze fluctuaties zijn er niet wanneer de ruis niet gecorreleerd is, wat aantoont dat interacties in het vloeibaar kristal op lange afstand cruciaal zijn om de fluctuaties te begrijpen. Dit model laat daarnaast ook toe om de voortbewegingsverliezen die het nematicon ondervindt te reproduceren zonder een ad-hoc term in te voeren. De simulatieresultaten zijn namelijk in goede overeenstemming met de experimentele resultaten. Deze methode kan ook helpen bij het modeleren van complexe niet-lineaire fenomenen in vloeibare kristallen die gebaseerd zijn op ruis, zoals modulatie-instabiliteit of filamentatie.

Vervolgens wordt optische versterking in LCs bestudeerd door fotoluminescente polymeren of kleurstoffen in het LC te mengen. In het bijzonder bekijken we een bepaald polymeer, polyfluoreen, dat intrinsieke supramoleculaire patronen vormt wanneer het opgelost wordt in nematisch LC. Deze patronen worden gevormd door homogene regio's rijk aan vloeibaar kristal, omgeven door polymeer-rijke grenzen. De studie van deze structuren via ultra-snelle spectroscopische technieken (de pomp-probe techniek) en confocale microscopie toont aan dat de grenzen bestaan uit geordende en geïsoleerde ketens van polymeer. Deze bijzondere morfologie leidt tot de observatie van optische versterking van geoxideerde eenheden van de polymeerketen (keto defecten). Dit signaal is normaal gezien niet zichtbaar wegens de absorptie die veroorzaakt wordt door de aggregatie van de polymeerketens, terwijl in LCs dit duidelijk kan geobserveerd worden. De optische versterking van de keto defecten blijken gepolariseerd loodrecht op de vloeibaarkristaldirector, min of meer gelijk aan de oriëntatie van de grenzen. Als een kleurstof (bvb. van de klasse van de pyrromethenen) wordt opgelost in het LC, dan blijkt de structuur homogeen te zijn. De optische versterking vanwege de kleurstof is gepolariseerd langs de LC director en vertoont een verschuiving naar het blauw (van ongeveer 10 nm) wanneer de polarisatie verandert van parallel naar loodrecht op de LC director. De versterkte spontane emissie (amplified spontaneous emission of ASE) vertoont dezelfde verschuiving wanneer de richting van de excitatie verandert.

Wanneer de ASE en het nematicon worden gegenereerd in hetzelfde sample is het mogelijk om de interactie tussen de twee te bestuderen. In het bijzonder kan de golfgeleider die gegenereerd wordt door het soliton worden gebruikt om een ander signaal te geleiden bij een andere golflengte. We tonen aan dat het nematicon de gegenereerde ASE kan verzamelen en leiden naar een optische vezel die tegelijkertijd wordt gebruikt om het nematicon te injecteren in de cel. De extractie van het ASE licht verhoogt met bijna 1 grootteorde wanneer het soliton aanwezig is. Door het solitonvermogen te verhogen wordt de lichtgeleiding verbeterd aangezien het brekingsindexcontrast van de nematicongolfgeleider stijgt. Maar te hoge solitonvermogens moeten vermeden worden omdat de solitonfluctuaties bij hogere vermogens een optimale verzameling van het licht teniet doen. Het nematicon verhoogt ook de spectrale zuiverheid en de polarisatiegraad van het signaal.

Tot slot wordt nog een ander type LC materiaal bestudeerd, namelijk chiraal nematisch LC. In dit materiaal ordenen de moleculen zich op een helicoïdale manier. Dankzij de optische anisotropie en de periodieke ordening is er een optische verboden zone. Als het LC ook gedoteerd is met een kleurstof, dan is het mogelijk om via de combinatie van een verboden zone en optische versterking laseremissie te verkrijgen. We zijn geïnteresseerd in een snelle (sub-ms) reoriëntatie van de helix om zo het effect van de reoriëntatie op de laseremissie te kunnen bestuderen. De eerste stap is om een goede aligning van de LC helix te bekomen met de as parallel aan de glasplaten waartussen het LC zit. Het is vooral moeilijk en belangrijk om een zo hoog mogelijke optische kwaliteit te verkrijgen van het LC. Om deze reden werd een innovatieve methode ontwikkeld die het LC aligneert via het directioneel verdampen van solvent. Deze solvent-gebaseerde methode laat toe om zeer homogene texturen te verkrijgen met een contrastverhouding tussen de lichte en de donkere toestand van een factor 4 groter dan mogelijk met traditionele methoden. Het LC met solvent-geïnduceerde alignering is vervolgens gestabiliseerd via twee-foton foto-polymerisatie. Deze techniek is interessant om kleine gebieden te polymeriseren, terwijl de rest van het materiaal kan uitgewassen worden door de component in een solventbad te dompelen. De eerste karakterisatie van laseremissie wordt voorgesteld in het laatste hoofdstuk, maar het sub-ms elektrisch schakelen is helaas het onderwerp van toekomstig werk.

In dit werk werden verschillende fysische aspecten onderzocht en dit heeft geleid tot de realisatie van nieuwe technieken voor de fabricage van vloeibaarkristalcomponenten, de demonstratie van nieuwe fenomenen voor lichtversterking in vloeibare kristallen en de experimentele verificatie van nieuwe numerieke modelering van lichtpropagatie in vloeibare kristallen. De rode draad doorheen dit werk zijn drie aspecten: niet-lineaire optische voortbeweging van licht, optische versterking en elektrische respons van verschillende vloeibaarkristalmengsels. Hoewel de eerste hoofdstukken deze aspecten afzonderlijk behandelen worden meerdere aspecten in het laatste hoofdstuk gecombineerd, waarbij nieuwe fysische fenomenen aan het licht komen en waarbij ook enkele interessante bevindingen worden vermeld die het onderwerp kunnen zijn van verder werk. De resultaten in dit werk kunnen potentieel gebruikt worden voor toepassingen in snelle afstembare lasers, optische communicatiesystemen en lab-on-chip componenten.

Sommario

In questo lavoro studiamo la propagazione nonlineare della luce nei cristalli liquidi (CL) e il guadagno ottico da essi fornito quando dopati con polimeri o coloranti.

Focalizzeremo la nostra attenzione sui CL nematici, caratterizzati da un'orientazione media (nota come direttore) delle molecole di CL allungate e dalla birifrangenza che ne consegue. Dopo un'introduzione generale sui CL, ci concentreremo sulla propagazione nonlineare della luce nei CL nematici e in particolare sulla propagazione di tipo solitone (noto anche come nematicone). Infatti, la luce iniettata, se sufficientemente intensa, può creare una guida d'onda che contrasta la diffrazione della luce, che si propaga quindi con un profilo trasverso quasi costante (o periodico).

Il nostro contributo in quest'area inizia con un modello numerico del rumore termico che caratterizza i CL nematici e con lo studio delle instabilità spaziali da esso causate sulla propagazione del solitone. Nel Cap.3 mostriamo che, costruendo esplicitamente la matrice di correlazione che descrive il rumore termico nei CL, è possibile riprodurre alcuni degli aspetti che caratterizzano il loro comportamento, come la generazione di speckle o le oscillazioni della traiettoria dei solitoni spaziali nei CL. Infatti, quando il diametro del nematicone è dello stesso ordine di grandezza o più piccolo delle perturbazioni dell'indice di rifrazione causate dal rumore termico, il nematicone inizia a oscillare nello spazio. Queste oscillazioni non sono presenti quando il rumore non è correlato, segno del fatto che le interazioni a lunga distanza nei CL sono cruciali per l'esplicazione di tali oscillazioni. Il modello inoltre permette di riprodurre la perdite di propagazione subite dal nematicone senza l'utilizzo di un termine ad hoc per esse. Le simulazioni sono in accordo con i risultati sperimentali. Questo modello potrebbe aiutare la modellizzazione di fenomeni nonlineari complessi nei CL che si basano sul rumore, come l'instabilità di modulazione o la filamentazione.

Successivamente, il guadagno ottico è ottenuto dissolvendo nei CL polimeri o coloranti fotoluminescenti. Mostreremo come un particolare polimero, il polifluorene, quando disperso nei CL, crei dei intricati motivi supramolecolari composti da regioni omogenee ricche di CL, circondate da bordi ricchi in polimero. Lo studio di queste strutture attraverso una tecnica di spettroscopia ultrarapida (tecnica di pump-probe) e la microscopia confocale rivela che i bordi sono composti da catene di polimero ordinate e isolate. Questa morfologia particolare permette l'osservazione del guadagno ottico da parte delle unità ossidate del polimero (difetti chetonici). Questo segnale è in genere coperto dall'assorbimento causato dall'aggregazione –nello stato solido– delle catene di polimero, mentre in CL è chiaramente visibile. Il guadagno ottico da parte di questi difetti è inoltre polarizzato ortogonalmente alla direzione del direttore del CL, direzione che coincide anche con l'orientamento maggior parte dei bordi. Quando un colorante, della famiglia dei *pyrromethenes*, è dissolto in CL, il campione ha un aspetto omogeneo. Il guadagno ottico del colorante è polarizzato lungo la direzione del direttore e presenta uno spostamento dello spettro verso il blu (10 nm) quando la polarizzazione passa da parallela a ortogonale al direttore. L'emissione spontanea amplificata (ESA) mostra lo stesso tipo di spostamento spettrale quando si cambia la direzione di eccitazione del campione.

Quando l'ESA e il nematicone sono generati nello stesso dispositivo, è possibile studiare l'interazione tra i due. In particolare, la guida d'onda indotta dal solitone può essere usata per guidare un altro segnale ad un'altra lunghezza d'onda. Il nematicone può raccogliere l'ESA generata nello stesso dispositivo e guidarla nella stessa fibra utilizzata per iniettare il nematicone nella cella a CL. L'estrazione dell'ESA dal dispositivo aumenta di quasi un ordine di grandezza quando il solitone è presente. Tuttavia, a causa delle fluttuazioni spaziali del nematicone, la potenza ottimale di quest'ultimo deve essere trovata. Infatti, da un lato, grazie ad un aumento del contrasto dell'indice di rifrazione della guida d'onda generata dal nematicone, il guidaggio della luce è migliorato quando la potenza del solitone è aumentata. Dall'altro lato, potenze troppo elevate causano flutuazioni del solitone che impediscono una raccolta ottimale della luce. Infine, osserviamo che che il nematicone migliora la purezza spettrale e il grado di polarizzazione del segnale guidato.

Un altro tipo di CL studiato è il CL nematico chirale. In tale materiale, le molecole sono disposte secondo una distribuzione elicoidale. A causa della loro anisotropia ottica e della loro distribuzione periodica, tale sistema

presenta un band gap ottico. Se il CL è anche dopato con del colorante, la combinazione di band-gap e guadagno ottico genera emissione laser. Siamo interessati in particolare ad una riorientazione rapida (<ms) dell'elica del CL chirale, con l'obiettivo di studiare l'effetto della riorientazione sull'emissione laser. Il primo passo verso tale direzione è l'allineamento dell'asse del CL chirale (non dopato) parallelo ai vetri che costituiscono la cella, allineamento particolarmente difficile ad ottenere con un'elevata qualità ottica. Per tale ragione abbiamo sviluppato un metodo innovativo per allineare i CL attraverso l'evaporazione direzionale di un solvente. Tale metodo permette di ottenere una struttura particolarmente omogenea, con un rapporto tra luminosità del bianco e luminosità del nero quattro volte superiore a quello ottenuto per un allineamento conseguito con metodi tradizionali. Il campione di CL allineato con l'evaporazione di solvente è stabilizzato attraverso la foto-polimerizzazione a due fotoni. Tale tecnica permette di polimerizzare piccole regioni del dispositivo, mentre il resto del materiale può essere eliminato con un bagno di solvente. Quando poi il dispositivo è riempito con un CL non chirale, quest'ultimo assume un allineamento chirale nelle regioni polimerizzate e non chirale nel resto. Una caratterizzazione preliminare dell'emissione laser è infine presentata nell'ultimo capitolo, con l'obiettivo di ottenere in lavori futuri un'emissione che sia accordabile attraverso un controllo elettrico e con tempi di risposta inferiori al millisecondo.

In questa tesi sono stati affrontati diversi temi che hanno portato alla realizzazione di nuove tecniche per la fabbricazione di dispositivi a CL, la dimostrazione di nuovi fenomeni di amplificazione ottica in CL e la verifica sperimentale di nuovi metodi numerici per la modellizzazione della propagazione luminosa nei CL. I tre aspetti chiave di questo lavoro sono la propagazione nonlineare della luce, l'amplificazione ottica e la risposta ai campi elettrici di varie strutture a CL. Sebbene i primi capitoli trattino tali aspetti separatamente, questi sono combinati nell'ultimo capitolo, portando all'analisi di nuovi fenomeni interessanti, utili per eventuali lavori futuri. I risultati di questo lavoro potrebbero avere un umpatto in applicazioni come laser accordabili e a risposta rapida, sistemi per le comunicazione ottiche e dispositivi lab-on-chip.

Chapter 1 Introduction

Liquid crystals (LCs) are a particular phase of matter in between the liquid and solid states. In particular, they possess a long-range order like crystals, while maintaining the possibility to flow like liquids. For this reason, many devices take advantage of the propagation of light in LCs. Thanks to their high birefringence and large response to external stimuli (electrical, mechanical, thermal, ...) they are the perfect candidates for applications such as displays [1–4], smart windows [5, 6], photovoltaic cells [7], lasers [8–11] and spatial light modulators (SLM) [12]. In all these applications the light beam is usually weak enough to not perturb the LC distribution. In this thesis, however, we are interested in the nonlinear behavior that arises when an intense light beam is propagating inside the LC.

When the light is propagating in a linear medium and it is focused into a small area, the beam tends to diffract and its transverse profile tends to change during the propagation. However, if the propagation occurs in a medium with a particular kind of nonlinearity, the beam itself can cause a local increase in the refractive index. In this way, the beam creates its own waveguide during the propagation, counteracting the diffraction and maintaining its (temporal or spatial) profile. This beam is called a (temporal or spatial) soliton.

In LCs, the electric field of the laser beam reorients the LC director causing a local increase of the refractive index due to the birefringence of the LCs. This Kerr-like effect occurs at low powers (some mW) and causes the transverse confinement of the light [13–22]. This soliton-like self-guiding is also called a *nematicon* when it occurs in a particular LC phase called the nematic phase [23]. Since this kind of nonlinearity is non-resonant [16], meaning that the molecular reorientation is not wavelength dependent, a huge variety of sources can been used, ranging from UV [24] to IR laser sources [25], or even incoherent light sources [26, 27]. The description of nematicons, together with the introduction of the LC properties, is the subject of Ch. 2.

Since the interactions in LCs are long-range, the perturbations in these materials extend over a distance much larger than the molecular size (tens of micrometers) [28, Ch.1]. For this reason, the nematicon-induced reorientation spreads over multiple times the size of the optical beam [29, 30]. This means that multiple solitons can interact with each other even if they are much further away than the width of the optical field. In particular they can deviate, intersect or merge their trajectories [31–33]. Since the nematicon-induced waveguide can be used to transmit optical co-polarized signals at other wavelengths [16, 34–37], the interaction among nematicons can be used to implement all-optical logical gates [38] or switching [39]. Also, due to the easy response of LCs to external stimuli, nematicons can be deviated with the action of an electric field or other optical beams, in order to build optical logical gates or re-configurable optical switches [25, 40, 41].

For these all-optical signal handling applications where nonlinear phenomena play a significant role, it is important to keep the intensity of light as constant as possible along the propagation. However, the propagation losses in LCs limit the soliton propagation and interaction distance to a few millimeters. Our work started with the aim of sensibly increasing the propagation length of a nematicon.

The main contribution to the propagation losses in LCs is the scattering in the medium [42]. In particular, the long-range orientational fluctuations of the LC mean distribution gives rise to a scattering that is six orders of magnitude larger than in conventional isotropic fluids [28]. The effect of this long range thermal noise on the nematicon propagation is particularly important since it causes both intensity attenuation and spatial fluctuations of the nematicon intensity profile. Indeed, by increasing the nematicon power, the soliton suffers from thermal instability and/or strong self-focusing [16, 29, 43, 44]. In Ch. 3 we propose a novel modeling scheme for the

physical origin of these fluctuations and its comparison with the experimental results. We show how the nematicon propagation is influenced by the physical quantities that characterize the LC phase, such as the thermal fluctuations of the molecules in LCs, the temperature or the elastic forces among the molecules. We also show that our model can explain the linear propagation of light in LCs, giving rise to the typical speckle formation.

In order to increase the nonlinear propagation length, several attempts have been adopted in the literature in order to overcome the issue of the propagation losses. One solution is to increase the nonlinear response along the propagation in order to compensate for a decrease in the beam intensity [44]. Another option is to compensate the losses via an optical amplification of the soliton. Distributed optical amplification in LCs can easily be achieved by mixing the LC with photoemissive molecules (dyes or polymers) and exciting the system with a pump light beam. However, even if this solution has been predicted theoretically [45], no experimental evidence has been presented until now. The initial aim of our work was to explore this route.

The first step in this direction is an extensive study of the optical gain provided by photoluminescent media dispersed in LCs. In Ch. 4 we analyze how ordered and anisotropic media such as a LC can modify the stimulated emission of emitting dyes and polymers dispersed in it. The first study of the optical gain in LCs with the aid of the pump-probe technique is presented. With the aid of this technique, which allows us to temporally resolve the evolution of the excited states of a molecule or a system, we were able to demonstrate that photoluminescent dyes or polymers dissolved in LCs can provide polarized optical gain. However, despite the different excitation geometries and wavelengths we tried, it was not possible for us to obtain nematicon amplification. We believe that the main reasons are twofold. Firstly, despite the fact that the dye shows a long-living optical gain (Ch. 4), the excitation powers were not sufficient to amplify, even transiently, the continuous-wave beam that is used to generate the nematicon. Secondly, the maximum excitation power was limited by the appearance of amplified spontaneous emission (ASE) or random lasing, depending on the adopted pumping geometry.

The observation of narrow-band and directional emission such as ASE opens up new possibilities for integrated narrow-band intense light sources. Due to its low degree of coherence, ASE is particularly suitable for a range of applications. The low spatial coherence is useful for illumination purposes, due to the low speckle production [46, 47], while the low temporal coherence is suitable for biomedical applications such as optical coherence tomography [48–50]. A requirement for these applications is that the light is efficiently collected and guided within the device. The method we propose is to exploit the nematicon-induced-waveguide for this purpose. The case where the fluorescence is generated by the nematicon itself launched in a dye-doped material was reported in the literature [24, 51]. However, the case where the nematicon was used to collect the light of a laser-like source generated within the same cell had not been previously analyzed. This is the subject of the first half of Ch. 6, where the ASE is generated in a dye-doped LC cell and collected by a nematicon injected in the same device. We show that the nematicon increases the intensity, the spectral purity and the polarization degree of the light extracted from the device. Later, it was shown that a nematicon is able to guide and even tune others types of light sources, such as random lasing [36, 37].

The drawback of ASE is the fact that its wavelength is not tunable. Indeed, since there is no cavity feedback to tune the emission wavelength, the emission peak is fixed at the wavelength with the lowest losses [52–55]. However, some applications need tunable sources, such as selective sample excitation in biology or medicine [56]. This is the reason why we focused our attention to other laser sources, whose emission is chosen to be in the plane of the LC cell in order to eventually maximize the collection of the light from a nematicon propagating in the same plane. There are different ways to obtain in-plane laser emission in LCs, such as the periodic modulation of the gain [57–59] or of the refractive index [60–62] in dye-doped LCs. This last configuration is achieved when a chiral nematic LC, which is characterized by a self-aligning helicoidal distribution of the LC orientation, is aligned with the helix axis in the plane of the cell (uniform lying helix - ULH). Such a periodic distribution generates an optical band-gap in the plane of the cell that can be used as feed-back for lasing emission.

As presented in Ch. 5, the ULH alignment presents a fast (sub-ms) reorientation of the optic axis of the helix when an alternating electric field is applied orthogonal to the periodicity, known as the flexoelectro-optic effect [63–67]. When the light is propagating orthogonal to the ULH axis, the medium acts as a birefringent material whose optic axis can be reoriented with an external electric field. This is of particular interest for technological applications requiring fast switching, such as next generation flat panel displays [68, 69]. In our case, we are interested in the effect of this fast reorientation on the optical band-gap and on the laser emission. Towards

this aim, the first steps are the alignment of a high-quality ULH alignment and the doping of the structure in order to obtain laser emission. In Ch. 5 we apply for the first time the solvent-induced self-alignment method to obtain a high-quality ULH. The characterization of the flexoelectro-optic response in terms of reorientation angle and response time is in agreement with what is found in the literature, indicating that the solvent technique does not alter the ULH properties. The solvent-induced ULH presents an almost defect-free structure, making it a better candidate to obtain laser emission than the ULH obtained with standard techniques. The laser emission from the dye-doped structures is presented in the second half of Ch. 6. The ULH is photo-polymerized in order to improve the stability of the alignment at high electric fields. The polymerization is obtained via two-photon absorption in order to polymerize small areas of the sample. It is then possible to remove the non-polymerized material and refill the cell with nematic LC. The sample obtained in this way presents narrow emission from the polymerized ULH regions, while the surrounding shows a broader ASE at a higher threshold.

The flexoelectro-optic effect is expected to influence the lasing emission. We believe that this would lead to fast-switching in-plane lasing in samples in which also a nematicon could be injected for efficient extraction of the emission.

If not explicitly expressed otherwise, I fabricated the samples, assembled the optical setup for the characterization, wrote the simulation code and analyzed the data.

Liquid crystals and solitons

Chapter 2

In this Chapter, thermotropic liquid crystals, and in particular the nematic phase, will be presented. The basis of the continuum theory will be introduced, as it will be used in Ch. 3 for the numerical model and in Ch. 5 to explain the flexoelectro-optic response. The optical properties of LCs will be analyzed, in particular those of chiral liquid crystals. In the last part of the chapter, after a brief introduction about light propagation in dielectrics, the concept of optical soliton will be introduced. Finally, the nonlinear propagation of light in nematics, in particular the solitonic behavior, will be considered.

2.1 Thermotropic liquid crystals

One of the main reference books for LCs was written by Pierre Gilles de Gennes and Jacques Prost [28]. We will be referring to this book for the general theory of thermotropic liquid crystals. Liquid crystals are a particular phase of matter in between the solid and the liquid phase. In particular, they preserve the possibility to flow, like liquids, while maintaining a long-range order, like crystals. There are different ways to obtain this phase (also called *mesophase*), the two most important ones are changing the relative concentration of the constituents (*lyotropic* LCs) and changing the temperature (*thermotropic* LCs). In this thesis, we will use exclusively thermotropic LCs, that will therefore be referred to simply as LCs.

The molecules that represent the liquid crystalline phase, called *mesogens*, possess a pronounced geometrical anisotropy, such as a disc or rod-shape. This anisotropy is then reflected onto their dielectric, elastic and viscous properties, as seen in more detail in the next chapters. We will focus on rod-shaped molecules characterized by a uniaxial birefringence. The average of the molecular long axis orientation over a significant number of molecules is called the *director* ($\hat{\mathbf{n}}$), and it is a unit vector. The refractive indices in the direction parallel and orthogonal to the director are called, respectively, $n_{\parallel}$ and $n_{\perp}$ (Fig. 2.1a). In Fig. 2.1b it is possible to see some of the phases that can be observed when the temperature of a rod-like mesogen is increased. It goes from the solid (crystalline) to the liquid (isotropic) phase, passing through one or more mesophases. The system passes from the solid to the LC phase at the *melting temperature* (T_m), since at that point the medium acquires viscous

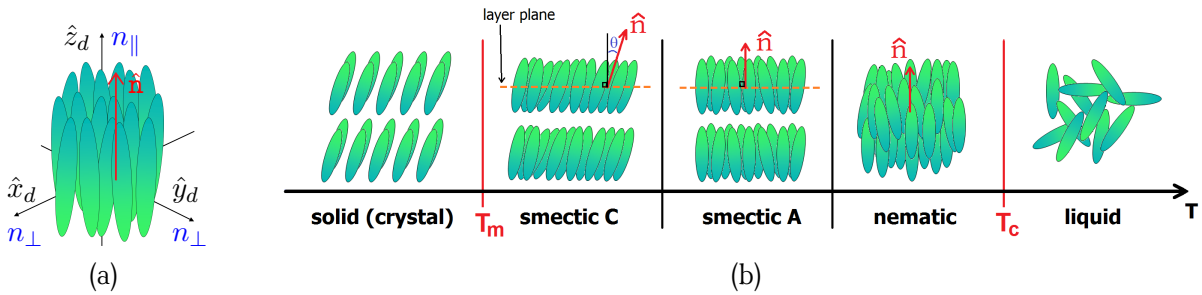

Figure 2.1: (a) The revolution symmetry of an ensemble of molecules around the director $\hat{\mathbf{n}}$ and its uniaxial anisotropy; the frame of reference $\hat{x}_d$,$\hat{y}_d$,$\hat{z}_d$ is defined by the director ($\hat{\mathbf{n}} \parallel \hat{z}_d$). (b) Schematic of the phase transition from the crystalline phase to the liquid phase, passing through some of the LC phases, characterized by a decreasing degree of order when the temperature is increased.

properties. The first phase that is usually encountered is the smectic phase, characterized by an organization into layers. The two most common smectic phases, smectic A and C, are characterized by two translational degrees of freedom (within the layer) and by the director orientation that is orthogonal (smectic A) or at an angle (smectic C) with respect to the layer.

The nematic phase is encountered when further increasing the temperature. Its only degree of order is dictated by the director orientation. The molecules can freely rotate around the director and move along the three directions.

It has to be noted that in all LC phases the long-range interactions tend to order the director orientation. However, without the help of an external stimulus, like the appropriate boundary conditions, the organization would be on a scale that is much larger than the molecular scale but shorter than macroscopic dimensions. This is why when looking at a LC without macroscopic aligning boundary conditions, its appearance is milky. The light is highly scattered by the µm-sized birefringent domains that constitute the bulk. When the system passes to the liquid phase, the long-range interactions are destroyed by thermal agitation and the medium becomes transparent. For this reason, the temperature at which the system passes to the isotropic phase is called the *clearing temperature* (T_c).

The nematic phase, in both its achiral and chiral forms, is the one used in this work.

2.2 Nematics

Nematic LCs are characterized by the fact that the molecules have an average orientation (director) but they can still move freely along the three directions. The average orientation is due to their long-range interaction, whose origin will be discussed in more detail in Ch. 3. The molecules also usually present an electric dipole, even if, macroscopically, no net polarization is present in the medium in the absence of external stimuli. On average, the same number of molecules point in opposite directions. This impossibility to distinguish the head and the tail of the molecule has to be reflected in the way the system is described. Therefore, the physical quantities that describe the system have to be invariant under the transformation $\hat{\mathbf{n}}(\bar{r}) \rightarrow -\hat{\mathbf{n}}(\bar{r})$.

In the following, the optics and the response to an electric field of nematic LCs are described in the bulk, without taking into account the contribution due to the boundary conditions.

2.2.1 Dielectric tensor

Due to their long-range order and molecular anisotropy, nematic LCs can be treated as a birefringent medium.[1] In the coordinate system noted as $\hat{x}_d$,$\hat{y}_d$,$\hat{z}_d$, where the $\hat{z}_d$ axis is defined by the director orientation (Fig. 2.1a), and considering only a linear response, the relative dielectric tensor takes a diagonal form

$$\bar{\bar{\varepsilon}}_r^d = \begin{pmatrix} \varepsilon_\perp & 0 & 0 \\ 0 & \varepsilon_\perp & 0 \\ 0 & 0 & \varepsilon_\parallel \end{pmatrix}, \tag{2.1}$$

where $\varepsilon_\perp$ and $\varepsilon_\parallel$ are the relative permittivities (or dielectric constants) orthogonal and parallel to the director, respectively. At optical frequencies $\varepsilon_\perp = n_\perp^2$ and $\varepsilon_\parallel = n_\parallel^2$.

The relative dielectric tensor can be expressed in a generally oriented frame of reference $\hat{x}$,$\hat{y}$,$\hat{z}$ (Fig. 2.2). The system $\hat{x}$,$\hat{y}$,$\hat{z}$ can be obtained through a double rotation, the first one through an angle φ around the axis $\hat{z}_d$ and the second one through an angle θ around the axis $\hat{y}'_d$ obtained with the first rotation. The rotation matrix associated with this transformation is:

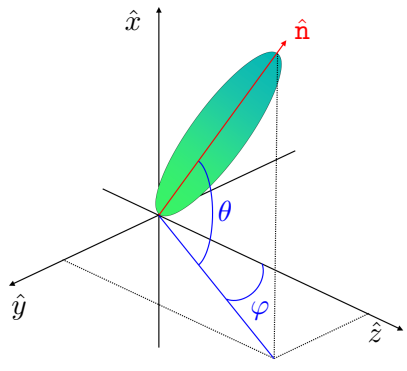

FIGURE 2.2: The generic frame of reference $\hat{x}$,$\hat{y}$,$\hat{z}$, where the director $\hat{\mathbf{n}}$ correspond to the molecular axis for simplicity. The angles φ and θ are positive as represented.

[1] This can always be done, at least locally.

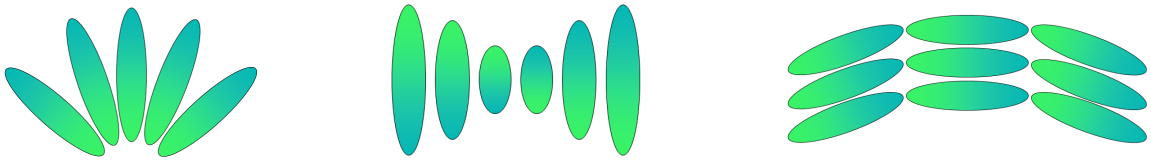

(a) (b) (c)

FIGURE 2.3: Splay (a), twist (b) and bend (c) deformations in nematic LCs.

$$\begin{aligned}\bar{\bar{R}} &= \bar{\bar{R}}(\theta)\bar{\bar{R}}(\varphi) \\ &= \begin{pmatrix} \cos\theta & 0 & -\sin\theta \\ 0 & 1 & 0 \\ \sin\theta & 0 & \cos\theta \end{pmatrix} \begin{pmatrix} 1 & 0 & 0 \\ 0 & \cos\varphi & \sin\varphi \\ 0 & -\sin\varphi & \cos\varphi \end{pmatrix} = \begin{pmatrix} \cos\theta & \sin\theta\sin\varphi & -\sin\theta\cos\varphi \\ 0 & \cos\varphi & \sin\varphi \\ \sin\theta & -\cos\theta\sin\varphi & \cos\theta\cos\varphi \end{pmatrix}. \end{aligned} \tag{2.2}$$

In this frame of reference, the dielectric tensor takes the form:

$$\bar{\bar{\varepsilon}}_r = \bar{\bar{R}}\bar{\bar{\varepsilon}}_r^d\bar{\bar{R}}^T = \begin{pmatrix} \varepsilon_\perp + \triangle\varepsilon\sin^2\theta & \triangle\varepsilon\sin\theta\cos\theta\sin\varphi & \triangle\varepsilon\sin\theta\cos\theta\cos\varphi \\ \triangle\varepsilon\sin\theta\cos\theta\sin\varphi & \varepsilon_\perp + \triangle\varepsilon\cos^2\theta\sin^2\varphi & \triangle\varepsilon\cos^2\theta\sin\varphi\cos\varphi \\ \triangle\varepsilon\sin\theta\cos\theta\cos\varphi & \triangle\varepsilon\cos^2\theta\sin\varphi\cos\varphi & \varepsilon_\perp + \triangle\varepsilon\cos^2\theta\cos^2\varphi \end{pmatrix}, \tag{2.3}$$

where $\triangle\varepsilon = \varepsilon_\parallel - \varepsilon_\perp$ is the dielectric anisotropy of the LC. When $\varphi = 0$, Eq. (2.3) takes the simple form

$$\bar{\bar{\varepsilon}}_r = \begin{pmatrix} \varepsilon_\perp + \triangle\varepsilon\sin^2\theta & 0 & \triangle\varepsilon\sin\theta\cos\theta \\ 0 & \varepsilon_\perp & 0 \\ \triangle\varepsilon\sin\theta\cos\theta & 0 & \varepsilon_\perp + \triangle\varepsilon\cos^2\theta \end{pmatrix}. \tag{2.4}$$

In this case, it is possible to show that, if the light is polarized along $\hat{x}$, the refractive index experienced by the wave can be derived from the index ellipsoid [70, Ch.4]

$$n(\theta) = \sqrt{\varepsilon_r(\theta)} = \sqrt{\frac{\varepsilon_\perp\varepsilon_\parallel}{\varepsilon_\perp\sin^2\theta + \varepsilon_\parallel\cos^2\theta}} = \sqrt{\varepsilon_{xx} - \frac{\varepsilon_{xz}^2}{\varepsilon_{zz}}}. \tag{2.5}$$

2.2.2 Free energy in the continuum theory

When the LC is perturbed at one location, it is deformed over a scale much larger than the molecular size. The LC can therefore be described as a continuum, without referring to discrete details of the molecules. Using the director as a continuous function of the space $\hat{\mathbf{n}}(\bar{r})$, it is possible to define the energy associated with the perturbation of the equilibrium distribution.

For a nematic LC, the state with the lowest energy is the one in which all the molecules are perfectly parallel one to another. Any deviation from the equilibrium is associated with a distortion free energy density [J/m^3] that, in the Oseen-Frank theory [28, Ch.3.1], takes the form

$$f_d = \underbrace{\frac{1}{2}K_1\left(\nabla\cdot\hat{\mathbf{n}}\right)^2}_{\text{splay}} + \underbrace{\frac{1}{2}K_2\left(\hat{\mathbf{n}}\cdot\left(\nabla\times\hat{\mathbf{n}}\right)\right)^2}_{\text{twist}} + \underbrace{\frac{1}{2}K_3\left(\hat{\mathbf{n}}\times\left(\nabla\times\hat{\mathbf{n}}\right)\right)^2}_{\text{bend}}, \tag{2.6}$$

where K_1, K_2 and K_3 are, respectively, the splay, twist and bend elastic constants, expressed in [N]. These deformations are classified according to their geometry (Fig. 2.3). The splay deformation is the one for which the lines traced by the orientation of the molecules are all exiting from one point ($\nabla\cdot\hat{\mathbf{n}} \neq 0$). The twist and the bend define rotations whose curl has a component orthogonal ($\hat{\mathbf{n}}\cdot(\nabla\times\hat{\mathbf{n}}) \neq 0$) and parallel ($\hat{\mathbf{n}}\times(\nabla\times\hat{\mathbf{n}}) \neq 0$) to the director, respectively. All these contributions are squared in order to have a centrosymmetric material and to respect the invariance with the transformation $\hat{\mathbf{n}}(\bar{r}) \to -\hat{\mathbf{n}}(\bar{r})$.

The values of the three constants are close enough to justify, in some cases, the assumption $K_1 = K_2 = K_3 = K$. Then the Eq. (2.6) takes the form

$$f_d = \frac{1}{2}K\left[(\nabla\cdot\hat{\mathbf{n}})^2 + (\nabla\times\hat{\mathbf{n}})^2\right]. \tag{2.7}$$

This equation is much simpler to solve numerically and will be useful in Ch. 3.

2.2.3 Electric field responses

When an electric field $\bar{E}$ is applied to a dielectric material, it induces a polarization density $\bar{P}$ that adds to the electric field within the medium. The sum of these components is the electric displacement $\bar{D}$

$$\bar{D} = \varepsilon_0\bar{E} + \bar{P}, \tag{2.8}$$

where ε_0 is the vacuum permittivity.

The polarization density groups all the different responses that the medium shows in the presence of an electric field. In particular, for a nematic LC, there are usually at least two contributions:

$$\bar{P} = \bar{P}_L + \bar{P}_{flexo} = \varepsilon_0\bar{\bar{\chi}}\bar{E} + \bar{P}_{flexo} \tag{2.9}$$

where $\bar{\bar{\chi}}$ is the first order susceptibility tensor, which is assumed to be real. The first term is due to the dielectric linear response of the medium and the second one is due to the elastic deformation of the medium.

The displacement field [Eq. (2.8) takes then the form

$$\begin{aligned}\bar{D} &= \varepsilon_0\bar{E} + \varepsilon_0\bar{\bar{\chi}}\bar{E} + \bar{P}_{flexo}\\ &= \varepsilon_0\bar{\bar{\varepsilon}}_r\bar{E} + \bar{P}_{flexo},\end{aligned} \tag{2.10}$$

where $\bar{\bar{\varepsilon}}_r = \bar{\bar{1}} + \bar{\bar{\chi}}$ is the relative permittivity of the medium and the electric field $\bar{E}$ is assumed to have one frequency (monochromatic).[2]

The potential free energy density f_{el} associated with the electric field in the presence of the LC is therefore

$$f_{el} = -\frac{1}{2}\bar{E}\cdot\bar{D} \tag{2.11}$$

$$= -\frac{1}{2}\varepsilon_0\bar{E}\bar{\bar{\varepsilon}}_r\bar{E} - \frac{1}{2}\bar{E}\cdot\bar{P}_{flexo} \tag{2.12}$$

$$= f_{diel} + f_{flexo}. \tag{2.13}$$

The first and the second terms are the dielectric and the flexoelectric contributions, respectively. They will be analyzed separately in the following paragraphs.

Dielectric contribution

The dielectric contribution arises from the dielectric anisotropy of the medium. Indeed, the dielectric term can be rewritten as a function of the independent variables $\bar{E}$ and $\hat{\mathbf{n}}$

$$f_{diel} = -\frac{1}{2}\varepsilon_0\bar{E}\bar{\bar{\varepsilon}}_r\bar{E} \tag{2.14}$$

$$= -\frac{1}{2}\varepsilon_0\bar{E}\left(\varepsilon_{\parallel}\left(\bar{E}\cdot\hat{\mathbf{n}}\right)\hat{\mathbf{n}} + \varepsilon_{\perp}\left(\bar{E} - \bar{E}\cdot\hat{\mathbf{n}}\right)\hat{\mathbf{n}}\right), \tag{2.15}$$

where we decompose the electric displacement into its components that are parallel and orthogonal to the director according to Eq. (2.1). Regrouping the terms we obtain

$$f_{diel} = -\frac{1}{2}\varepsilon_0\varepsilon_{\perp}|E|^2 - \frac{1}{2}\varepsilon_0\triangle\varepsilon\left(\bar{E}\cdot\hat{\mathbf{n}}\right)^2. \tag{2.16}$$

[2]For a detailed discussion on the use of the notation for Eq. (2.10), see Appendix A.

Depending on the sign of the anisotropy $\triangle\varepsilon = \varepsilon_{\parallel} - \varepsilon_{\perp}$ of the LC, the molecules will tend to align themselves parallel ($\triangle\varepsilon > 0$, positive anisotropy) or orthogonal ($\triangle\varepsilon < 0$, negative anisotropy) to the electric field, in order to minimize the energy of the system.

In this configuration, where there are slightly more molecules aligned with the field than in the other direction, the symmetry $\hat{\mathbf{n}}(\bar{r}) \rightarrow -\hat{\mathbf{n}}(\bar{r})$ is broken by the field and a net dipole is created. The asymmetry is not large enough, though, to justify the introduction of additional terms in the free energy expression [Eq. (2.6)], since the continuum theory, as already stated, disregards the details of the molecules.

Flexoelectric contribution

The flexoelectric effect is a deformation of the uniform distribution of the director that arises when molecules with a permanent dipole and a non-centrosymmetric geometry are subjected to an electric field. Conversely, if a deformation of the director distribution is generated, a net macroscopic polarization is generated in the material due to the permanent dipole of the molecules. The two molecular shapes that are usually referred to when analysing the flexoelectric effect are the *pear-shaped* molecules (Fig. 2.4a), with a dipole parallel to the axis of the molecules, and the *banana-shaped* molecules (Fig. 2.4b), with a dipole orthogonal to the axis of the molecules.

In the absence of an external field, no net polarization is present in the material. Even for non-centrosymmetric molecules, the $\hat{\mathbf{n}}(\bar{r}) \rightarrow -\hat{\mathbf{n}}(\bar{r})$ symmetry is still present and the net polarization of the medium is zero (Fig. 2.4a,b).

When an electric field is applied, it reorients the molecular dipole parallel to it. Due to the shape of the molecules, a deformation is introduced in the molecular distribution. In the case of pear-shaped molecules, the dipole is usually along the long axis of the molecules and it will be aligned along the electric field. Due to the shape of the molecules, a splay deformation will be formed (Fig. 2.4c). In the case of banana molecules, the

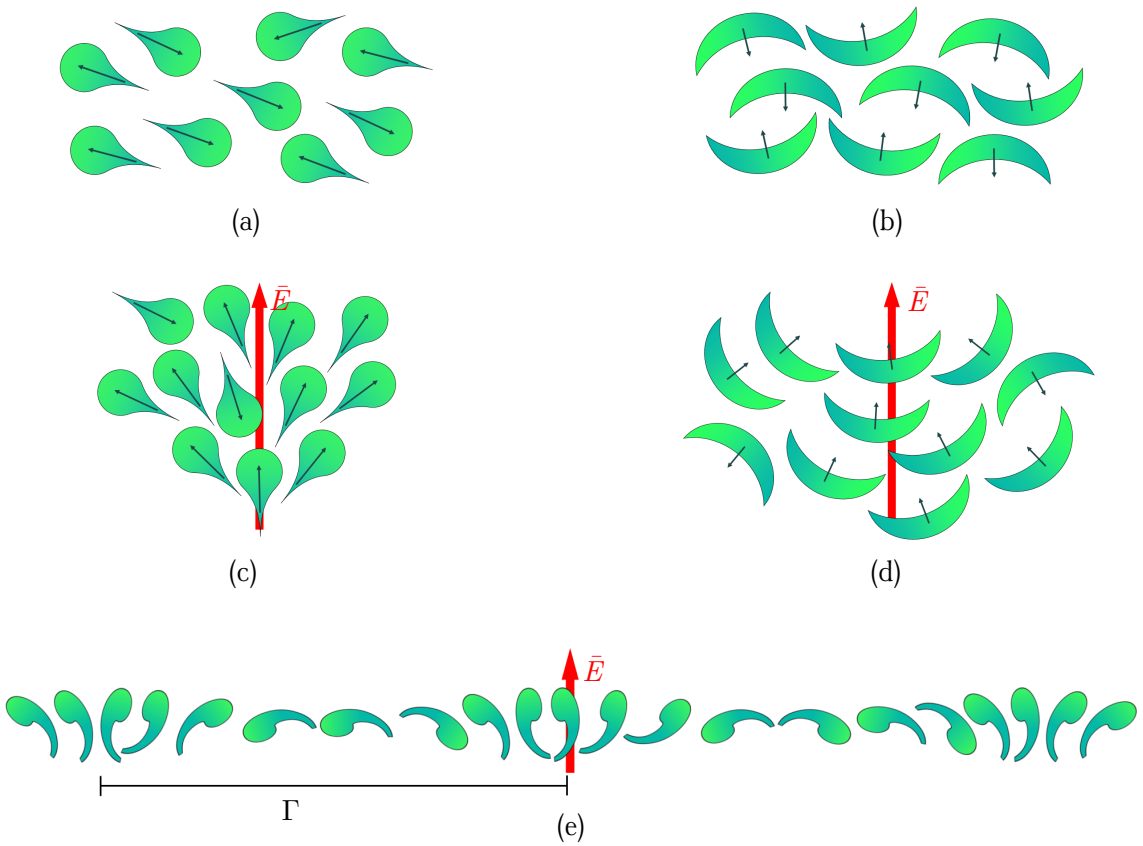

FIGURE 2.4: (a,b) Molecular distribution with no net polarization for the case of the pear-shaped (a) and banana-shaped (b) molecules, in the absence of an applied electric field. The small black arrows are the molecular dipoles. When an electric field $\bar{E}$ is applied, the reorientation of the dipoles induces a splay (c) or a bend (d) deformation in the medium, respectively for the pear and banana-shaped molecules. (e) Splay-bend configuration with a periodicity of Γ.

dipole is usually orthogonal to the long axis. When it tends to align along the field, a bend deformation appears in the material (Fig. 2.4d). In both cases the field breaks one of the symmetries in the system: for the pear-shaped molecules, the $\hat{\mathbf{n}}(\bar{r}) \rightarrow -\hat{\mathbf{n}}(\bar{r})$ symmetry is broken, while the molecules are still free to rotate around the direction defined by the director. For the banana-shaped molecules, the opposite happens: the molecules cannot rotate around the director (orthogonal to the electric field), but the end-to-end symmetry is preserved.

The flexoelectric polarization, as it was introduced by Meyer [71], is defined as

$$\bar{P}_{flexo} = e_1 \left(\nabla \cdot \bar{n}\right) \bar{n} + e_3 \left(\nabla \times \bar{n}\right) \times \bar{n}, \tag{2.17}$$

where e_1 and e_3 [C/m] are the splay and the bend flexoelectric coefficient, respectively. In this sign convention, the net polarization is pointing outwards the center of the deformation for the splay and inwards for the bend deformation (Fig. 2.4).

The free energy for the flexoelectric term can be therefore written as

$$f_{flexo} = -\frac{1}{2}\varepsilon_0 \left[e_1 \left(\nabla \cdot \bar{n}\right) \bar{n} + e_3 \left(\nabla \times \bar{n}\right) \times \bar{n}\right] \cdot \bar{E}. \tag{2.18}$$

The direction of the deformation will depend on the polarity of the electric field, since the free energy f_{flexo} depends linearly on the electric field $\bar{E}$ and it has to be minimized to find the equilibrium configuration.

In a general case, molecules can present both behaviors at the same time. In that case, a splay-bend deformation takes place (Fig. 2.4e). The period Γ that characterizes the alternation of splay and bend deformations is defined as [72]

$$\Gamma = \frac{\pi \left(K_1 + K_3\right)}{\left(e_1 - e_3\right) E}. \tag{2.19}$$

The higher the electric field, the faster is the reorientation of the director in space and shorter is the period.

2.3 Chiral nematic LCs

The chiral nematic phase, also known as *cholesteric* (CLC) phase, is exhibited by chiral molecules. In this phase, the LC molecules tend to arrange themselves at an angle to one another in the direction orthogonal to their long axis, in a configuration of pure twist (Fig. 2.5a). Alternatively, a small quantity of chiral dopant can be added to an achiral LC to obtain the CLC phase. The distance over which the molecule turns over an angle of 2π is the period p_0 of the helicoidal distribution along $\hat{z}$. In the planes orthogonal to $\hat{z}$, the molecules are parallel to one another. We can therefore think of the medium as a series of nematic layers whose director rotates from one layer to another, drawing a helix along $\hat{z}$. The rotation angle θ is defined as $\theta = (2\pi/p_0)z$, as reported in Fig. 2.5b. The angle θ is taken to be positive according to the right hand rule. The rotation angle and therefore the pitch are determined by the rotatory power of the molecule (or by the concentration of the chiral dopant). The helix can be left- or right-handed, depending on the chirality of the molecule.

Due to the geometry of the system, the periodicity of the medium is one-dimensional, along the axis of the helix. Due to the $\hat{\mathbf{n}}(\bar{r}) \rightarrow -\hat{\mathbf{n}}(\bar{r})$ symmetry, the period of the refractive index is half of the pitch p_0.

2.3.1 Optical band-gap

The periodic structure that the molecules assume, due to their birefringence, gives rise to a periodic distribution of the refractive index.

When the light is propagating along the $\hat{z}$ axis, as for Bragg reflectors, the refractive index periodicity causes a light reflection selective in wavelength (optical band-gap). In CLCs, however, the geometry of the system is circular. For this this reason, the most appropriate polarization basis to describe light propagation in CLCs is the circular one. By solving the propagation equation for a birefringent medium whose optic axis is rotating orthogonally to the $\hat{z}$ axis, it is possible to find the explicit form of the wavevectors of the fields propagating in the two opposite directions along $\hat{z}$ [73]. The field with a handedness opposite to the CLC helix has a wavevector that takes real values for all wavelengths and propagates as in an isotropic medium. The field with the same

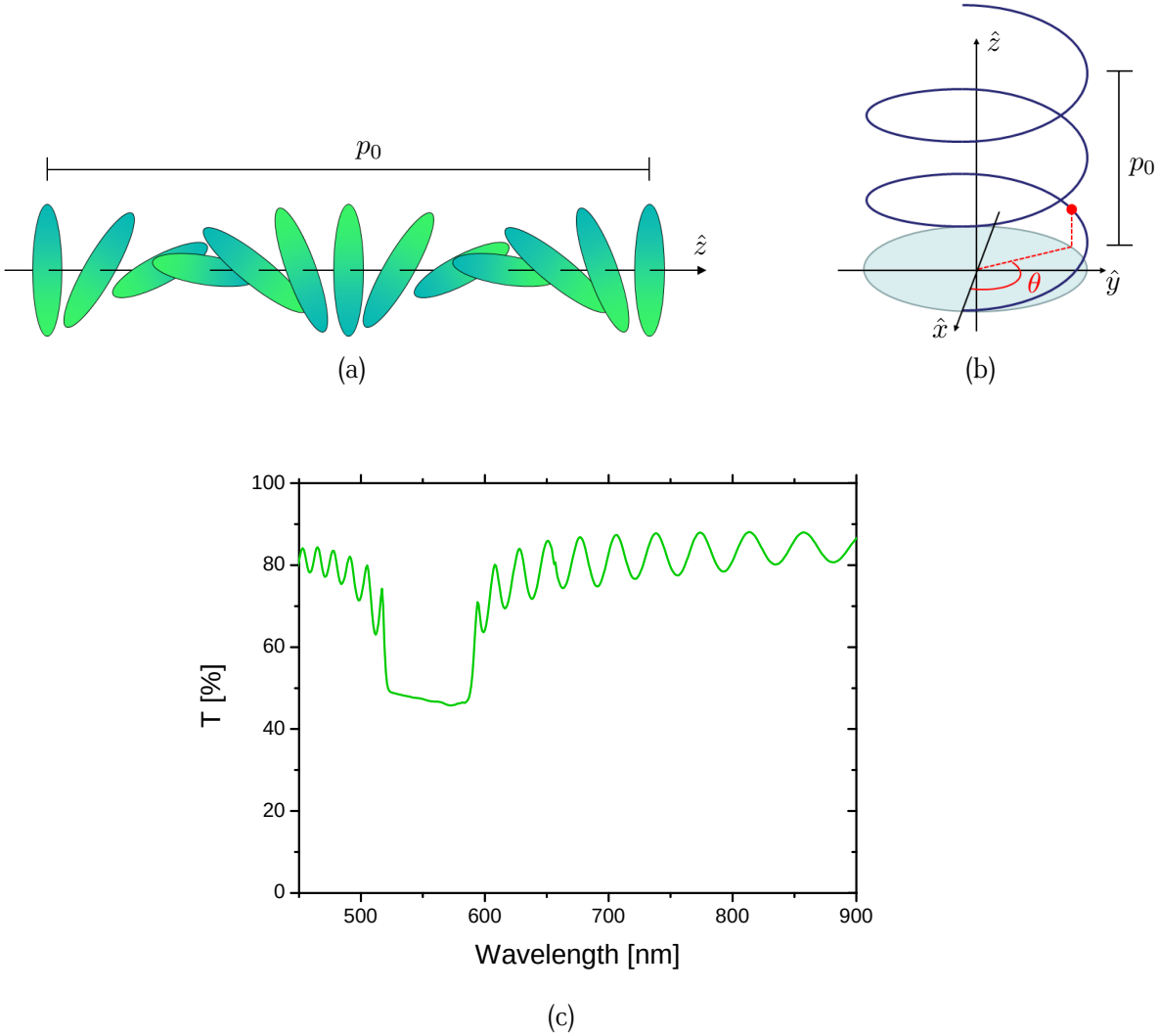

FIGURE 2.5: (a) The molecules of a CLC rotate orthogonal to the $\hat{z}$ axis forming a spiral of pitch p_0. (b) The LC director in each plane draws a spiral whose handedness depend on the chirality (left or right) of the molecule. (d) Example of transmission spectrum of unpolarized light propagating along the CLC axis; the optical band-gap in this case is between 520 and 590 nm.

chirality as the CLC takes complex values for wavelengths around the Bragg wavelength[3] $\lambda_B = p_0(n_\parallel + n_\perp)/2$, which cannot therefore propagate in the medium. The optical band-gap so-formed has a width that is defined by the birefringence of the medium and takes the form [74]

$$n_\perp p_0 < \lambda < n_\parallel p_0 \tag{2.20}$$

in the case of positive anisotropy. The typical transmission spectrum of unpolarized light propagating along the CLC axis is reported in Fig. 2.5c. Outside the bandgap the light progatas unperturbed and the spectrum is modulated only by the Fabry-Perot cavity formed by the two glass substrates that compose the cell. Within the bandgap, half of the light is transmitted because it has a polarization with the opposite handedness as the CLC helix, while the other half is reflected. For this reason, the reflected light is polarized with the same handedness as the CLC helix.

[3]The period of the refractive index is half the helix period p_0 due to the $\hat{\mathbf{n}}(\bar{r}) \to -\hat{\mathbf{n}}(\bar{r})$ symmetry.

2.3.2 Free energy in the continuum theory

In an unperturbed CLC, the director orientation along the helix can be described with the system of equations

$$\begin{pmatrix} n_x \\ n_y \\ n_z \end{pmatrix} = \begin{pmatrix} \cos\theta \\ \sin\theta \\ 0 \end{pmatrix} \tag{2.21}$$

where $\theta = \frac{2\pi}{p_0} z$ is the angle between the director (in each plane orthogonal to $\hat{z}$) and the $\hat{x}$ axis (Fig. 2.5b), and p_0 is the natural pitch of the CLC. In this configuration, the twist term of Eq. (2.6) takes the form

$$\hat{\mathbf{n}} \cdot (\nabla \times \hat{\mathbf{n}}) = -\hat{\mathbf{n}} \cdot (\hat{x}\cos\theta + \hat{y}\sin\theta)\frac{2\pi}{p_0} = -\frac{2\pi}{p_0}. \tag{2.22}$$

Since the twisted configuration is the equilibrium distribution for a chiral system like the CLC, we subtract this term from the free energy equation Eq. (2.6), obtaining

$$f_d = \frac{1}{2}K_1 (\nabla \cdot \hat{\mathbf{n}})^2 + \frac{1}{2}K_2 (\hat{\mathbf{n}} \cdot (\nabla \times \hat{\mathbf{n}}) + q_0)^2 + \frac{1}{2}K_3 (\hat{\mathbf{n}} \times (\nabla \times \hat{\mathbf{n}}))^2 , \tag{2.23}$$

with $q_0 = \frac{2\pi}{p_0}$. This energy contribution is minimum for a chiral configuration such as the CLC case.

2.3.3 Electric field responses

When a CLC is submitted to an electric field applied orthogonal to the helical axis, two kinds of coupling can happen, dielectric and flexoelectric coupling. Only alternating electric fields will be applied in the experiments, with a frequency high enough to to prevent charge transport and electrohydrodynamic instabilities [28, Ch.6].

Dielectric coupling

As we saw for nematics, the dielectric coupling will tend to align the molecules parallel to the electric field (for positive anisotropy), while the restoring elastic forces will try to preserve the helical structure. In a CLC, if the electric field is applied orthogonal to the helical axis, the regions of the helix with the molecules aligned along the electric field will become larger (Fig. 2.6b) [75, 76]. This also causes a change in the birefringence of the medium for the light propagating orthogonal to the helix and polarized orthogonal to the helical axis. Eventually the pitch length starts to increase (Fig. 2.6c) and, for electric fields above the critical field value E_c [77]

$$E_c = \frac{\pi^2}{p_0}\sqrt{\frac{K_2}{\varepsilon_0 \triangle\varepsilon}}, \tag{2.24}$$

the helix is completely unwound. Eq. (2.24) has been obtained by comparing the free energy density associated with the region of twist and the uniform region composed by pure nematic in the presence of an electric field [28]. The first contribution is given by Eq. (2.23), the second one by Eq. (2.6) and the electric field is taken into account through the term in Eq. (2.16).

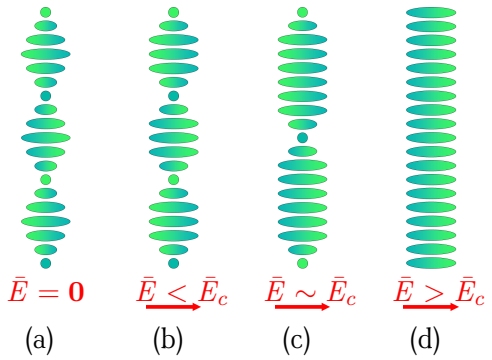

FIGURE 2.6: Evolution of the helix deformation of CLC helix as the electric field intensity is increased.

When also the flexoelectric contribution is taken into account, the expression for the critical field becomes [63, 67, 68, 78]:

$$E_c = \frac{\pi^2}{p_0}\sqrt{\frac{K_2}{\varepsilon_0 \triangle\varepsilon - \frac{\pi^2 (e_1 - e_3)^2}{16(K_1 + K_3)}}}, \tag{2.25}$$

where the flexoelectric distortion effectively decreases the dielectric anisotropy and increases the critical field for the helix unwinding.

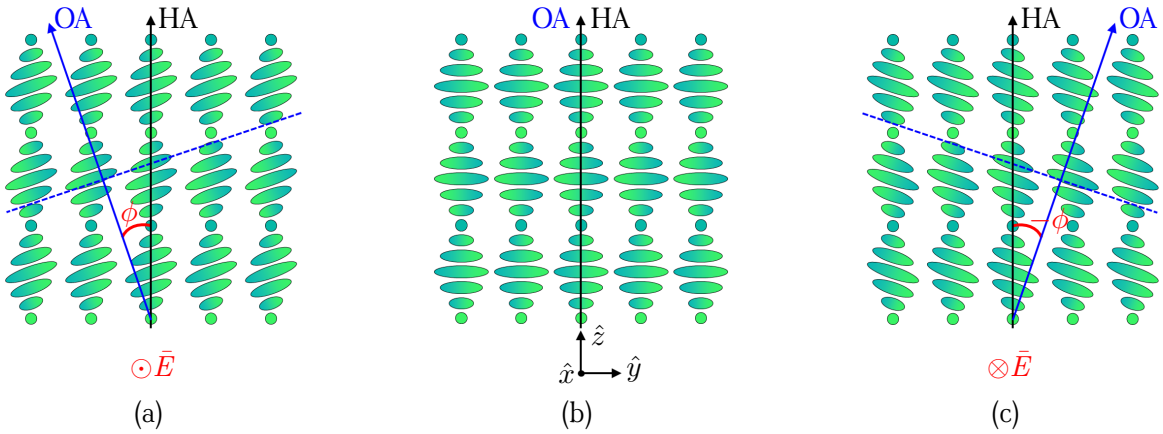

FIGURE 2.7: Helix deformation (a,c) when a field is applied orthogonal to the helical axis. Compared to the unperturbed case (b), the optic axis (OA) is tilted with respect to helix axis (HA) when an electric field is applied. Depending on the polarity of the electric field, the reorientation angle is positive (a) or negative (c).

Flexoelectro-optic response

If non-centrosymmetric molecules in a chiral nematic phase are subjected to an electric field orthogonal to the helical axis, a deformation of the whole helix takes place due to flexoelectric coupling. The optic axis (OA) of the CLC is tilted by an angle ϕ with respect to the helical axis (HA) (Fig. 2.7). The direction and the amplitude of the tilt depend on the polarity and the amplitude of the electric field, due to the linear dependence of the flexoelectricity on the electric field. Patel and Meyer first reported the observation and the theoretical model of this effect, called the *flexoelectro-optic effect* [63, 79]. In the planes orthogonal to the OA, this configuration gives rise to the same bend-splay deformation we presented for nematics (Sect. 2.2.3).

By evaluating the free energy density of the configuration in Fig. 2.7a and finding the equilibrium distribution as a function of ϕ, it is possible to calculate the dependence of the tilt angle as a function of the electric field. In the case of Fig. 2.7a, the CLC director distribution of Eq. (2.21) is modified into

$$\begin{pmatrix} n_{\hat{x}} \\ n_{\hat{y}} \\ n_{\hat{z}} \end{pmatrix} = \begin{pmatrix} \cos\theta \\ \sin\theta\cos\phi \\ \sin\theta\sin\phi \end{pmatrix}, \tag{2.26}$$

where $\theta = q_0 z$ is the same as that defined previously and ϕ is the angle, independent of $\hat{z}$, that we want to optimize to find the equilibrium configuration. Since the director is only a function of $\hat{z}$, its divergence and curl are

$$\nabla \cdot \hat{\mathbf{n}} = \sin\phi\cos\theta\frac{\partial\theta}{\partial z} = \sin\phi\cos\theta\, q_0 \tag{2.27}$$

$$\nabla \times \hat{\mathbf{n}} = \begin{pmatrix} -\cos\phi\cos\theta\frac{\partial\theta}{\partial z} \\ -\sin\theta\frac{\partial\theta}{\partial z} \\ 0 \end{pmatrix} = \begin{pmatrix} -q_0\cos\phi\cos\theta \\ -q_0\sin\theta \\ 0 \end{pmatrix} \tag{2.28}$$

We can then evaluate each term of the elastic deformation contribution [Eq. (2.23)] separately,

$$\text{splay:} \quad f_s = \frac{1}{2}K_1\left(\nabla\cdot\hat{\mathbf{n}}\right)^2 = \frac{1}{2}K_1\left(q_0\sin\phi\cos\theta\right)^2 = \frac{1}{2}K_1 q_0^2\sin^2\phi\cos^2\theta, \tag{2.29}$$

$$\text{twist:} \quad f_t = \frac{1}{2}K_2\left(\hat{\mathbf{n}}\cdot\left(\nabla\times\hat{\mathbf{n}}\right)+q_0\right)^2 = \frac{1}{2}K_2\left(-q_0\cos\phi+q_0\right)^2 = \frac{1}{2}K_2 q_0^2\left(1-\cos\phi\right)^2, \tag{2.30}$$

$$\text{bend:} \quad f_b = \frac{1}{2}K_3\left(\hat{\mathbf{n}}\times\left(\nabla\times\hat{\mathbf{n}}\right)\right)^2 = \frac{1}{2}K_3\left(q_0\sin\theta\sin\phi\right)^2 = \frac{1}{2}K_3 q_0^2\sin^2\theta\sin^2\phi. \tag{2.31}$$

The flexoelectric contribution [Eq. (2.18)], in the case where the electric field is polarized along $\hat{x}$, takes the form

$$f_{flexo} = -\bar{P}\cdot\bar{E} = -E_x\left(e_1\sin\phi\cos^2\theta - e_3\sin\phi\sin^2\theta\right)q_0. \tag{2.32}$$

The total free energy density associated with the elastic distortion and the flexoelectric coupling is then averaged over one period p_0, in order to remove the spatial dependence given by $\theta = \theta(z)$

$$f_{aver} = \frac{1}{p_0}\int_0^{p_0} (f_s + f_t + f_b + f_{flexo})\, dz. \tag{2.33}$$

This equation, with Eq. (2.29) - (2.32), becomes

$$f_{aver} = \frac{K_1}{4} q_0^2 \sin^2\phi + \frac{K_2}{2} q_0^2 (1-\cos\phi)^2 + \frac{K_3}{4} q_0^2 \sin^2\phi - E_x (e_1 - e_3)\frac{q_0}{2}\sin\phi. \tag{2.34}$$

This is the equation that has to be minimized in order to find the equilibrium distribution. If we assume the pitch p_0 is constant [64, 78], we can differentiate Eq. (2.34) with respect to ϕ and set it to zero to find the angle ϕ that minimizes the energy

$$\frac{K_1 + K_3}{2} q_0^2 \sin\phi\cos\phi + \frac{K_2}{2} q_0^2 (-2\cos\phi\sin\phi + 2\sin\phi) - \frac{E_x}{2}(e_1 - e_3) q_0 \cos\phi = 0. \tag{2.35}$$

Therefore, reorganizing the terms

$$\tan\phi = \frac{p_0}{2\pi}\frac{(e_1 - e_3)}{2K_2} E_x - \frac{K_1 - 2K_2 + K_3}{2K_2}\sin\phi, \tag{2.36}$$

where we substituted $q_0 = 2\pi/p_0$. From this equation it is possible to see that the tilt angle ϕ is linearly dependent on the applied electric field, at small angles.

The system is also subjected, in general, to dielectric coupling. Since, for small tilt angles, the dielectric coupling depends quadratically on the electric field, the flexoelectro-optic effect will be predominant at small electric field amplitudes. Increasing the electric field, the dielectric coupling will take place, saturating the switching angle and unwinding the helix.

2.4 Liquid crystal cells

As introduced above, LCs need macroscopic boundary conditions in order to present a macroscopic order. The simplest geometry is represented by two large glass plates, assembled with a glue mixed with spacers that provide the desired thickness (Fig. 2.8a). The glass plates have to be cleaned and then coated with a layer that forces a definite orientation of the LC director at the interface. In the homeotropic alignment, the director is aligned orthogonal to the glass plate, while in the planar case they are parallel to it (Fig. 2.8b). In this thesis both uniform homeotropic and planar alignments are used.

2.4.1 Fréedericksz threshold

The glass plates do not only fix the orientation at the interfaces. Due to the elastic forces among the molecules, they also modify the response to an electric field. Indeed, if an electric field is applied to the cell, the molecular electrical reorientation is counteracted by the restoring elastic forces and the fixed orientation at the interfaces.

This introduces a threshold that depends on different factors, such as the cell thickness (the thinner the cell, the smaller the reorientation freedom for the molecules) and the elastic constants of the LC [28, Ch.3]. Also, varying the orientation of the electric field with respect to the initial LC director, the electric torque on the molecular dipole can be modified and different elastic deformations (involving different elastic constants) can be excited.

These considerations will dictate the choice of the cell geometry, notably for the nonlinear propagation, as we will see in the next paragraphs.

2.4.2 Cell fabrication

The glasses used in this thesis are either 1.1 mm thick glass covered with a ∼100 nm layer of indium-tin-oxide (ITO, a transparent conductor) or a 100 µm thick glass substrate.

The homeotropic alignment layer is obtained with a commercial polyimide layer (SE-4811, Nissan Chemical). The solution is spin-coated (2500 rpm, 15 seconds) on the substrate. Due to the viscosity of the solution and the poor wettability of the substrate, the glass is immediately transferred to a pre-heated hot-plate (100°C) for a few minutes, in order to have a fast solvent evaporation and avoid the breaking-down of the film [80, 81]. The film is then processed in the oven for 1h at 180°C.

To obtain planar alignment, a solution of 1 wt% Nylon 6,6 in 2,2,2 trichloroethanol is spin coated on to the glass (3500 rpm, 45 seconds) and cured in the oven at 180°C for 4 hours. The surface is then rubbed with a rotating cylinder covered with a velvet wipe. The direction of the rubbing determines the direction of the LC director on the surface. Due to the rubbing process, the molecules have a small tilt (a few degrees) at the surface [82]. The two glasses are assembled with the rubbing direction in an antiparallel configuration, in order to avoid a splay distortion across the thickness of the cell (Fig. 2.8b). For both kinds of alignment, the thickness of the layer is of the order of some hundreds of nanometers.

The two glasses are assembled with UV-curable glue mixed with spherical spacers of a defined diameter. The spacers define the thickness of the cell. The cell is then heated on a hot plate to some degrees Celcius above the clearing temperature of the LC. A small quantity of LC is put at the entrance of the cell and the LC fills the gap by capillary action.

In some of the samples, a non-commercial optical fiber is slid between the two glasses. The fiber has a cladding diameter of 64.4 µm, a core diameter of 2.9 µm and a cut-off wavelength of 550 nm. This refractive index profile supports a mode with a radius (at $1/e^2$) of 3.7 µm at 1064 nm. The fiber has to be adequately prepared before the insertion. The polymeric coating is soften for 20 minutes in a dichloromethane bath and then removed mechanically. Due to the nonstandard diameter of the fiber and its particularly fragile glass, it has to be cleaved with an ultrasonic cleaver (Precision Fiber Optic Cleavers, Photon Kinetics). The quality of the fiber facet is checked in an optical fiber splicer and only then the fiber is carefully inserted in the LC cell. In this thesis we will use only one LC, the commercially available E7 (Merck). The chemical structure of the components that constitute the E7 mixture are shown in Fig. 2.9 and the E7 properties are reported in Tab. 2.1.

Unless stated otherwise, we fabricated the cells used in this thesis in the clean room facilities at Ghent University.

2.5 Optical solitons

The concept of soliton goes back to the year 1848 when John Scott Russel described a water wave propagating in a canal [87]: "I was observing the motion of a boat which was rapidly drawn along a narrow channel by a pair of horses, when the boat suddenly stopped - not so the mass of water in the channel which it had put in motion; it accumulated round the prow of the vessel in a state of violent agitation, then suddenly leaving it behind, rolled forward with great velocity, assuming the form of a large solitary elevation, a rounded, smooth and well-defined

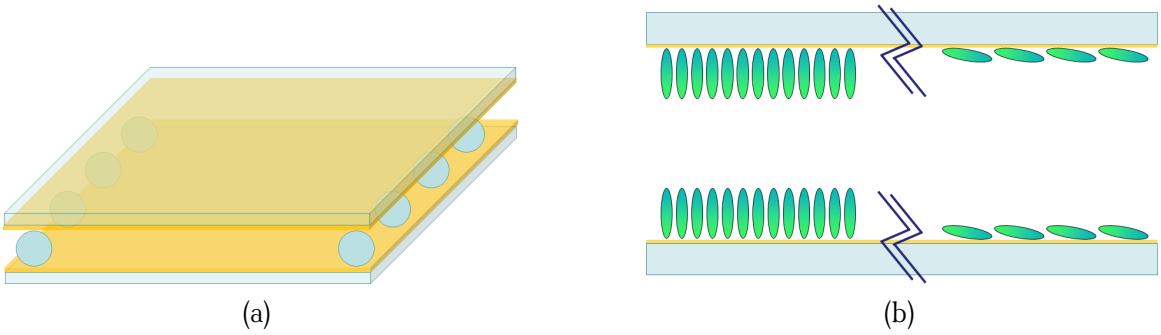

Figure 2.8: (a) Structure of a LC cell where it is possible to notice the alignment layer on the glass substrates and the spherical spacers; (b) Homeotropic (left) and planar (right) alignment in a LC cell.

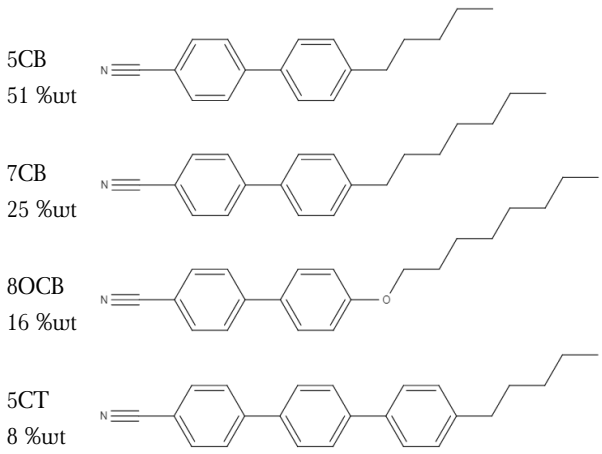

FIGURE 2.9: Chemical structures of the components of the E7 liquid crystal mixture.

Elastic Constants [83]	K_1	10.7 pN
	K_2	6.5 pN
	K_3	16.0 pN
Viscosity [84]	η	0.08 Pa·s
Optical properties at 1064 nm [85]	$\varepsilon_{\parallel}$	2.9204
	$\varepsilon_{\perp}$	2.2681
	$\triangle n$	0.2029
Electrical properties [83]	$\triangle\varepsilon$	13.7
Transition temperatures [86]	T_m	-9 °C
	T_c	60 °C

TABLE 2.1: Characteristics of the E7 LC.

heap of water, which continued its course along the channel apparently without change of form or diminution of speed." In this first description, Russel already describes the main characteristics of a soliton. He speaks about a wave arising alone - solitary, that propagates without changing its shape and speed. Water wave solitons are not the only ones observed in nature. In particular, soon after the invention of the laser (1960), the first optical soliton was observed [88, 89]. They are described as self-trapped optical beams that maintain an invariant (temporal or spatial) profile during their propagation.

In this section, after a brief introduction on light propagation, we will explain the concept of spatial soliton in media that exhibit Kerr nonlinearity.

2.5.1 Light propagation in dielectric media

We start from the macroscopic formulation of Maxwell's equations

$$\nabla \cdot \bar{D} = \rho_f, \tag{2.37}$$

$$\nabla \times \bar{E} = -\frac{\partial \bar{B}}{\partial t}, \tag{2.38}$$

$$\nabla \cdot \bar{B} = 0, \tag{2.39}$$

$$\nabla \times \bar{H} = \bar{J}_f + \frac{\partial \bar{D}}{\partial t}, \tag{2.40}$$

where ρ_f and $\bar{J}_f$ are the free charge and current densities, $\bar{E}$ and $\bar{B}$ are the electric and the magnetic field. The electric displacement field $\bar{D}$ and the magnetizing field $\bar{H}$ are defined as

$$\bar{D} = \varepsilon_0 \bar{E} + \bar{P}, \tag{2.41}$$

$$\bar{H} = \frac{\bar{B}}{\mu_0} - \bar{M}, \tag{2.42}$$

where μ_0 is the vacuum permeability, $\bar{P}$ is the polarization density and $\bar{M}$ is the magnetization of the medium. In our case, we will work in media with no magnetization ($\bar{M} = 0$) and no free charge or current densities ($\rho_f = 0$ and $\bar{J}_f = 0$).

Taking the curl of Eq. (2.38) and combining it with Eq. (2.40) and Eq. (2.42), we obtain

$$\nabla \times \nabla \times \bar{E} = -\mu_0 \frac{\partial^2 \bar{D}}{\partial t^2} \tag{2.43}$$

Using Eq. (2.37) and Eq. (2.41), and assuming that the average density of bound charges ρ_b is zero (so that $\nabla \cdot \bar{P} = -\rho_b = 0$) or that $\bar{P}$ is slowly varying in space, we obtain

$$\nabla^2 \bar{E} - \frac{1}{c^2} \frac{\partial^2 \bar{E}}{\partial t^2} = \mu_0 \frac{\partial^2 \bar{P}}{\partial t^2}. \tag{2.44}$$

This is the propagation equation for the electric field of an electromagnetic wave.

The electric susceptibility tensor $\bar{\bar{\chi}}$ can be decomposed in to a linear and a non linear contributions.

$$\bar{\bar{\chi}} = \bar{\bar{\chi}}^{(1)} + \bar{\bar{\chi}}^{(2)}\bar{E} + \bar{\bar{\chi}}^{(3)}\bar{E}\bar{E} \tag{2.45}$$

where $\bar{\bar{\chi}}^{(j)}$ are the susceptibiliy tensors of the j^{th}-order and the electric field $\bar{E}$ is assumed to be monochromatic.

In particular, we will focus on media with a Kerr (or cubic) nonlinearity, where the second-order term is not present since the medium is supposed to be centrosymmetric [90, ch.1]. For a medium with a local and instantaneous response, the polarization takes the form

$$\bar{P} = \varepsilon_0\bar{\bar{\chi}}\bar{E} = \varepsilon_0\bar{\bar{\chi}}^{(1)}\bar{E} + \varepsilon_0\bar{\bar{\chi}}^{(3)}\bar{E}\bar{E}\bar{E} = \bar{P}_{\text{L}} + \bar{P}_{\text{NL}}, \tag{2.46}$$

where $\bar{P}_{\text{L}}$ and $\bar{P}_{\text{NL}}$ are the linear and nonlinear contributions to the polarization. Eq. (2.41) becomes then

$$\bar{D} = \varepsilon_0\left(\bar{\bar{1}} + \bar{\bar{\chi}}^{(1)} + \bar{\bar{\chi}}^{(3)}\bar{E}\bar{E}\right)\bar{E} \tag{2.47}$$

$$= \varepsilon_0\bar{\bar{\varepsilon}}_r\bar{E} \tag{2.48}$$

where $\bar{\bar{1}}$ is the identity matrix and $\bar{\bar{\varepsilon}}_r(\bar{E})$ is the relative permittivity.

With this relation, Eq. (2.44) becomes

$$\nabla^2\bar{E} - \mu_0\varepsilon_0\bar{\bar{\varepsilon}}_r\frac{\partial^2\bar{E}}{\partial t^2} = 0, \tag{2.49}$$

which is the well-known wave equation.

Associated with the electromagnetic wave is the so-called Poynting vector $\bar{S}$, defined as [70, Ch.1]

$$\bar{S} = \bar{E} \times \bar{H}. \tag{2.50}$$

It gives the power density [W/m^2] of the beam. The integral of this vector over a surface gives the optical power flowing through that area.

2.5.2 Linear propagation

We start from the case of light propagation in a linear medium. This means that $\bar{\bar{\chi}}^{(3)} = 0$ and the tensor $\bar{\bar{\varepsilon}}_r$ does not depend on the electric field. In that case, one solution to the wave equation is the plane wave [70]

$$\bar{E}(\bar{r}, t) = \bar{\mathcal{E}}_0 e^{i\omega_0 t - i\bar{k}\cdot\bar{r}}, \tag{2.51}$$

where $\bar{\mathcal{E}}_0$ is the amplitude of the plane wave, ω_0 is the angular frequency, and $\bar{k}$ is the wave vector. These last two quantities follow the relation $|\bar{k}| = (\omega_0/c)n^{\bar{k}} = (\omega_0/c)\sqrt{\varepsilon_r^{\bar{k}}}$, where $n^{\bar{k}}$ and $\varepsilon_r^{\bar{k}}$ are the refractive index and the relative permittivity seen by the wave of Eq. (2.51).

The plane wave, when injected into Maxwell's equations Eq. (2.38) and Eq. (2.40), gives the orthogonality relations

$$\bar{k} \times \bar{E} = -\omega_0\bar{B} \Rightarrow \begin{cases} \bar{k} \perp \bar{B} \\ \bar{E} \perp \bar{B} \end{cases} \tag{2.52}$$

$$\bar{k} \times \bar{H} = \omega_0\bar{D} \Rightarrow \begin{cases} \bar{k} \perp \bar{D} \\ \bar{H} \perp \bar{D} \end{cases} \tag{2.53}$$

The fields $\bar{E}$ and $\bar{B}$ are always orthogonal, and so are the fields $\bar{D}$ and $\bar{H}$. The displacement field $\bar{D}$ is orthogonal to the wavevector $\bar{k}$, but the electric field $\bar{E}$ not necessarily, due to the permittivity tensor [Eq. (2.48)]. Indeed, when light propagates in a birefringent medium (and it is not polarized along one of the principal optic axes), the displacement field $\bar{D}$ and the electric field $\bar{E}$ are no longer parallel [Eq. (2.48)]. The angle between them is called the walk-off angle δ and it can be calculated as

$$\tan\delta = \frac{\|\bar{D} \times \bar{E}\|}{\bar{D} \cdot \bar{E}}, \tag{2.54}$$

where $\|\cdot\|$ indicates the norm of a vector.

Due to the relations of orthogonality derived above, δ is also the angle between the wavevector $\bar{k}$ and the Poynting vector $\bar{S}$.

2.5.3 Optical Kerr soliton

In this section, we will follow Kivshar and Agrawal's dissertation [91] on Kerr solitons, reporting only the principal results and assumptions.

In our case, the medium is considered isotropic and the electric field is considered polarized along $\hat{x}$. The electric field can be written as

$$\bar{E}(\bar{r},t) = \frac{1}{2}\hat{x}\left[\mathcal{E}(\bar{r})e^{i\omega_0 t} + \text{c.c.}\right], \tag{2.55}$$

where $\bar{r} = (\hat{x},\hat{y},\hat{z})$ is the frame of reference of the laboratory (Fig. 2.2) and $\mathcal{E}(\bar{r})$ is the spatial part of the optical electric field. With these assumptions, the polarization and the displacement field take the form

$$\bar{P}(\bar{r},t) = \frac{1}{2}\hat{x}\left[\mathcal{P}(\bar{r})e^{i\omega_0 t} + \text{c.c.}\right], \tag{2.56}$$

$$\bar{D}(\bar{r},t) = \frac{1}{2}\hat{x}\left[\mathcal{D}(\bar{r})e^{i\omega_0 t} + \text{c.c.}\right]. \tag{2.57}$$

The spatial component of the linear polarization can therefore be written as

$$\mathcal{P}_{\text{L}}(\bar{r}) = \varepsilon_0\bar{\bar{\chi}}^{(1)}\mathcal{E}(\bar{r}) \tag{2.58}$$

while, by inserting Eq. (2.55) in Eq. (2.46) and neglecting the terms with the highest frequency ($\propto e^{i3\omega_0 t}$), we obtain the following expression for the nonlinear polarization

$$\mathcal{P}_{\text{NL}}(\bar{r}) \approx \varepsilon_0\frac{3}{4}\chi^{(3)}|\mathcal{E}(\bar{r})|^2\mathcal{E}(\bar{r}). \tag{2.59}$$

The electric displacement [Eq. (2.48)] can therefore be written as

$$\mathcal{D}(\bar{r}) \approx \varepsilon_0\left(1+\chi^{(1)}+\frac{3}{4}\chi^{(3)}|\mathcal{E}(\bar{r})|^2\right)\mathcal{E}(\bar{r}). \tag{2.60}$$

The term between parenthesis is the total relative permittivity $\varepsilon_r = \varepsilon_{\text{L}} + \varepsilon_{\text{NL}}$, which includes the linear and the nonlinear contributions

$$\varepsilon_{\text{L}} = 1+\chi^{(1)}, \tag{2.61}$$

$$\varepsilon_{\text{NL}}(\bar{r}) = \frac{3}{4}\chi^{(3)}|\mathcal{E}(\bar{r})|^2. \tag{2.62}$$

Since the refractive index n of a medium is defined as the square root of the relative permittivity and the nonlinear contribution is supposed to be a perturbation of the linear response, we can write

$$n(\bar{r}) = \sqrt{1+\chi^{(1)}+\frac{3}{4}\chi^{(3)}|\mathcal{E}(\bar{r})|^2} \tag{2.63}$$

$$\approx 1+\chi^{(1)}+\frac{3}{8n_0}\chi^{(3)}|\mathcal{E}(\bar{r})|^2 \tag{2.64}$$

$$= n_0 + n_2|\mathcal{E}(\bar{r})|^2, \tag{2.65}$$

where $n_0 = 1+\chi^{(1)}$ is the linear refractive index and $n_2 = \frac{3}{8n_0}\chi^{(3)}$ is the cubic nonlinear, or Kerr, coefficient. Both of them are assumed to be independent of $\bar{r}$, and n_2 is assumed to be very small so that we can limit the development to the first order in n_2.

With all these relations, it is possible to obtain the time-independent equation from Eq. (2.44)

$$\nabla^2\mathcal{E}(\bar{r}) + \frac{\omega_0^2}{c^2}\mathcal{E}(\bar{r}) = -\frac{\omega_0^2}{c^2}\left(\chi^{(1)}+\frac{3}{4}\chi^{(3)}|\mathcal{E}(\bar{r})|^2\right)\mathcal{E}(\bar{r}), \tag{2.66}$$

Using Eq. (2.61) and (2.62) we obtain

$$\nabla^2\mathcal{E}(\bar{r}) + k_0^2\varepsilon_r(\bar{r})\,\mathcal{E}(\bar{r}) = 0 \tag{2.67}$$

where $k_0 = \omega_0/c$. This equation is also known as the *Helmholtz equation* for the envelope of the electric field of an electromagnetic wave.

The Equation 2.66, by introducing the Kerr coefficient of Eq. (2.65), becomes

$$\nabla^2 \mathcal{E}(\bar{r}) + k_0^2 \left(n_0 + 2n_0 n_2 |\mathcal{E}(\bar{r})|^2\right)^2 \mathcal{E}(\bar{r}) = 0. \tag{2.68}$$

Supposing a wave that is propagating along $\hat{z}$ so that the wavevector has only one component (paraxial approximation [92]), we can decompose the spatial part of the electric field [Eq. (2.55)] in to an envelope and a carrier

$$\mathcal{E}(\bar{r}) = \mathcal{A}(\bar{r})\, e^{-ik_0 n_0 z}, \tag{2.69}$$

where $\mathcal{A}(\bar{r})$ is the slowly varying envelope, $k_0 = 2\pi/\lambda$ is the wavevector in vacuum and $\lambda = 2\pi c/\omega_0$ is the wavelength. The refractive index n_0 used in the planar wave is the same uniform linear refractive index of Eq. (2.65). Inserting Eq. (2.69) into Eq. (2.68), we obtain

$$2ik_0 n_0 \frac{\partial \mathcal{A}(\bar{r})}{\partial z} = \nabla_\perp^2 \mathcal{A}(\bar{r}) + \frac{\partial^2 \mathcal{A}(\bar{r})}{\partial z^2} + 2k_0^2 n_0 n_2 |\mathcal{A}(\bar{r})|^2 \mathcal{A}(\bar{r}), \tag{2.70}$$

where $\nabla_\perp^2 = \partial^2/\partial x^2 + \partial^2/\partial y^2$ is the transverse part of the Laplacian operator. Since the envelope is slowly varying, the variations of the envelope derivative are slow along $\hat{z}$ (therefore $|\partial^2 \mathcal{A}/\partial z^2| \ll |2k_0 n_0\, \partial \mathcal{A}/\partial z|$, slowly varying envelope approximation [93]) and can be neglected. Eq. (2.70) becomes

$$2ik_0 n_0 \frac{\partial \mathcal{A}(\bar{r})}{\partial z} = \nabla_\perp^2 \mathcal{A}(\bar{r}) + 2k_0^2 n_0 n_2 |\mathcal{A}(\bar{r})|^2 \mathcal{A}(\bar{r}). \tag{2.71}$$

This equation is also know as cubic Nonlinear Schrödinger Equation (NLSE).

The solutions of this equation can be classified as a function of the dimensions of the problem. In the case where the nonlinearity takes place only along one direction (x) and the confinement along the other direction is provided, for example, by a planar waveguide, we can separate the variables in the envelope $\mathcal{A}(\bar{r}) = \sqrt{I_0} u(x,z) v(y)$, where u and v are the normalized amplitudes and I_0 is the peak intensity of the beam. In this way, Eq. (2.71) takes the form [94]

$$i \frac{\partial u(x,z)}{\partial z} = \frac{1}{2k_0 n_0} \frac{\partial^2 u(x,z)}{\partial x^2} + k_0 n_2 \frac{P_0}{l_{\text{eff}}} |u(x,z)|^2 u(x,z), \tag{2.72}$$

where P_0 is the peak power of the beam and l_{eff} is the confinement length due to the planar waveguide along the $\hat{y}$. In order to better understand the properties of the solution of this equation, the diffraction and nonlinear lengths are introduced

$$L_{\text{D}} = k_0 n_0 w_0^2, \qquad L_{\text{NL}} = \left(k_0 n_2 \frac{P_0}{l_{\text{eff}}}\right)^{-1}, \tag{2.73}$$

where w_0 is the beam width. Introducing the dimensionless variables

$$Z = z/L_{\text{D}} \qquad X = x/w_0, \tag{2.74}$$

Eq. (2.72) can be written as

$$i \frac{\partial u(X,Z)}{\partial Z} = \frac{1}{2} \frac{\partial^2 u(X,Z)}{\partial X^2} + \frac{L_{\text{D}}}{L_{\text{NL}}} |u(X,Z)|^2 u(X,Z). \tag{2.75}$$

The ratio $L_{\text{D}}/L_{\text{NL}} = \mathtt{N}$ defines the parameter $\mathtt{N}$, which is the order of the soliton. In the case $L_{\text{D}} = L_{\text{NL}}$, the solution is the fundamental soliton ($\mathtt{N} = 1$) [91]

$$u(X,Z) = \sqrt{P_0}\, \text{sech}\,(X)\, e^{\frac{iZ}{2}}, \tag{2.76}$$

or, in physical units

$$u(x,z) = \sqrt{P_0}\, \text{sech}\left(\frac{x}{w_0}\right) e^{\frac{iz}{2L_{\text{D}}}}. \tag{2.77}$$

This electric field profile preserves its shape along the propagation and after the interaction with another soliton. This solution has been found with the hypothesis that the characteristic length of diffraction L_{D} corresponds to the characteristic length of the nonlinear effect L_{NL}. This means that the inclination of the beam to diffract is exactly compensated by the self-focusing nonlinear effect. From this condition it is possible to extract the critical beam power P_c necessary to excite a soliton of a definite size w_0

$$L_{\mathrm{D}} = L_{\mathrm{NL}}, \tag{2.78}$$

$$k_0 n_0 w_0^2 = (k_0 n_2 \frac{P_c}{l_{eff}})^{-1}, \tag{2.79}$$

$$P_c = (k_0^2 n_0 n_2 \frac{w_0^2}{l_{eff}})^{-1} = (k_0 n_2 \frac{L_{\mathrm{D}}}{l_{\mathrm{eff}}})^{-1}. \tag{2.80}$$

For higher-order solitons ($\mathtt{N} > 1$), the beam intensity is larger than this critical value. It is possible to show [95, Ch.5] that in that case the profile of the beam is no longer constant, but its width and peak intensity follow an oscillatory behavior along $\hat{z}$. If the initial profile is not a soliton, the system spontaneously evolves towards the closest integer $\mathtt{N}$.

It is possible to show that, for a medium that is instantaneous and local, the solution of the cubic (Kerr) NLSE is stable only for the 1-D case [96]. In the 2- and 3-D cases, the nonlinear effect acts on more than one dimension. This induces an over-focusing of the field causing the so-called *catastrophic collapse*, or the medium is damaged. The collapse can be prevented including a mechanism for which the energy cannot concentrate too tightly or the electric field cannot grow too much. In the 2-D case it has been demonstrated that the solution is stable for a nonlocal medium [97, 98], for a saturable nonlinearity [99] or considering the non-paraxial term in the propagation equation [100, 101].

2.6 Nematicons

The nonlinearities that we have analyzed until now have an electronic origin. In the case of nematic LCs, the nonlinear response of the medium can have different causes.

In the case of intense laser illumination or in the presence of a dye absorbing the laser frequency, the LC is heated by the incident light. This can cause a change in the temperature or in the density of the LC [102, Ch.7], inducing in both cases a change in the refractive index. Another way to modify the refractive index is through the reorientation of the birefringent LC. Indeed, when a laser beam is sent onto a LC sample, the optical electric field can reorient the LC due to the dielectric interaction and locally increase the refractive index. These intensity-induced refractive index modifications in LCs are called *Kerr-like nonlinearities*. In the following, we will be focusing onto the light-induced LC reorientation to induce a change in the refractive index.

Due to the viscosity of the medium, the LC reorientation is slow ($\sim$ms) [103] compared to the response time of the electronic nonlinear responses ($\sim$as) [90, Ch.4]. Moreover, due to the elastic interaction among the molecules, a perturbation of the LC distribution in a point causes a molecular reorientation at long distances (tens of micrometers). Finally, the increase of the refractive index is limited by the birefringence of the LC. This saturable and non-local Kerr-like nonlinearity is responsible for the stable 2-D solitons observable in LCs [104].

However, the nonlocality of the LC response would add a spatial convolution between $\bar{\bar{\chi}}$ and $\bar{E}$ in Eq. (2.46) that would notably increase the difficulty of the study of the NLSE.[4] For this reason, the nonlocality and the saturation are taken into account with a second equation that describes the molecular distribution and interaction with the optical electric field.

In the following, we will derive the propagation equation in the case of a non-homogeneous birefringent material, while a second equation describes the LC distribution, its saturable and nonlocal response and interaction with the optical electric field. The solution of the coupled equations describes the propagation of light in LCs. In particular, in the case where the nonlinearity compensates for the diffraction, we have the formation of a solitary wave that, as it occurs in nematic LCs, is called *nematicon*.

[4]The non-instantaneous response is simplified due to the monochromatic approximation [Eq. (A.8)], since we are interested only in the equilibrium regime and the transient evolution is not analyzed.

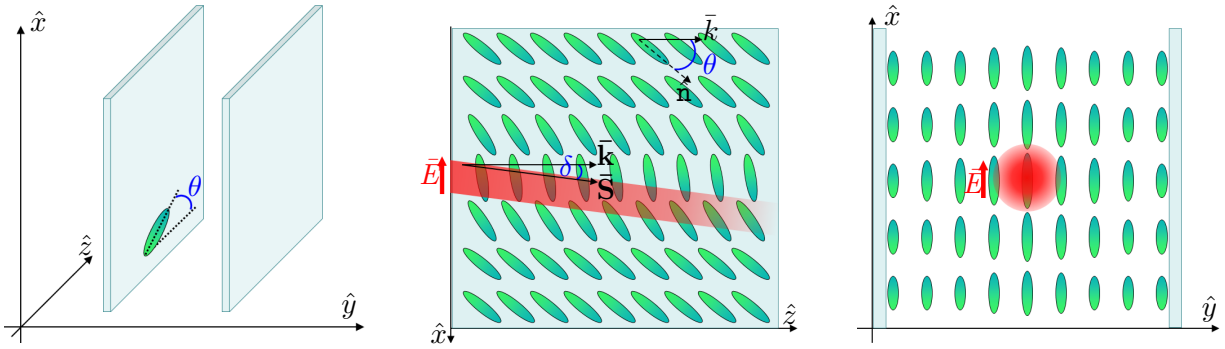

FIGURE 2.10: (a) Geometry of the LC cell and the LC orientation in the laboratory frame of reference. (b) Soliton propagation in the $\hat{x}\hat{z}$ plane; θ is the angle between the propagation vector $\bar{k}$ and the director $\hat{\mathbf{n}}$, δ is the walk-off, which is the angle between the Poynting vector $\bar{S}$ and the vector $\bar{k}$. (c) Soliton profile in the plane $\hat{x}\hat{y}$. The director reorientation due to the optical electric field takes place in the plane $\hat{x}\hat{z}$.

2.6.1 Constitutive equations

The cell geometry adopted in this work is reported in Fig. 2.10a. The liquid crystal molecules lie in the plane $\hat{x}\hat{z}$, where the reorientation takes place. Their orientation can be described with only the angle θ.[5] The LC director has an initial orientation θ_0 due to the rubbing direction. In this way, the torque induced by the electric field is increased (compared to the case where the molecules lie along $\hat{z}$) and the Fréedericksz threshold for the reorientation, presented in Sect. 2.4.1, is minimized [19, 22, 25].

We start from the Helmoltz equation [Eq. (2.67)] and, as before, we consider the case of light propagating along $\hat{z}$ and polarized along $\hat{x}$. At the interface with the LC, the electric field is tilted towards the vector $\bar{k}$ by the walk-off angle δ, and the orthogonality between $\bar{E}$ and $\bar{S}$ is maintained [Eq. (2.50)]. However, as a first approximation in case of a small walk-off, the electric field can be considered parallel to the $\hat{x}$ axis within the LC. The scalar approximation developed in the previous paragraphs can therefore be maintained.

In contrast to the case explained in the previous section, LCs present a *Kerr-like nonlinearity*. This means that, even if the Kerr coefficient n_2 is negligible, they present an intensity-dependent refractive index modification, which has however a non-electronic origin. In the case of LCs, the local increase of the refractive index is due to the molecular reorientation induced by the optical electric field of the beam propagating in the medium. For this reason, the relative permittivity can be written as a function of θ and $\bar{r}$

$$\varepsilon_r(\bar{r},\theta) = n^2(\bar{r},\theta), \tag{2.81}$$

where the nonlinearity is hidden in the dependence of θ on the electric field. Due to the long-range interaction, we can assume that the spatial variations of the permittivity are slow enough to allow the approximation used for Eq. (2.44). The Equation 2.67 can therefore be written as

$$\nabla^2\mathcal{E}(\bar{r}) + k_0^2\varepsilon_r\left(\bar{r},\theta\right)\mathcal{E}(\bar{r}) = 0. \tag{2.82}$$

We assume an electric field profile like the one expressed in Eq. (2.69), where n_0 is the unperturbed refractive index seen by the incoming wave. Since the electric field is polarized along $\hat{x}$, the unperturbed refractive index is $n_0 = \sqrt{\varepsilon_\perp + \triangle\varepsilon\sin^2(\theta_0)}$ (from Eq. (2.4)), where θ_0 is the angle between the initial orientation of the director and the wavevector k_0. In the following, n_0 will indicate the linear unperturbed contribution to the refractive index, while $\varepsilon(\bar{r},\theta)$ (or $n(\bar{r},\theta)$) will take into account the electric field-induced reorientation.

With the same assumption made before (paraxial approximation and slowly varying envelope $\mathcal{A}(\bar{r})$), we obtain

$$2ik_0n_0\frac{\partial\mathcal{A}(\bar{r})}{\partial z} = \nabla_\perp^2\mathcal{A}(\bar{r}) + k_0^2\left(\varepsilon_r(\bar{r},\theta) - n_0^2\right)\mathcal{A}(\bar{r}). \tag{2.83}$$

In an homogeneous medium, it is possible to choose $n_0^2 = \varepsilon_r = \varepsilon_r(\bar{r},\theta)$ for the carrier wave, making the last term disappear.

[5] Referring to Fig. 2.2, we consider the case where the angle φ is negligible.

Since the LC is a birefringent medium, the light experiences a walk-off when the vector $\bar{k}$ is not parallel to one of the principal optical axes of the LC. Due to the relation of Eq. (2.48) and Eq. (2.4), the walk-off angle of Eq. (2.54) takes the form

$$\tan\delta(\theta) = \frac{\triangle\varepsilon \sin\theta\cos\theta}{\varepsilon_\perp + \triangle\varepsilon\cos^2\theta} = \frac{\varepsilon_{xz}(\theta)}{\varepsilon_{zz}(\theta)}. \tag{2.84}$$

Since we are treating a birefringent medium with a scalar approximation, we need to add a phenomenological term in the propagation equation Eq. (2.83) that takes into account the walk-off effect during the propagation [91]

$$2ik_0n_0\frac{\partial\mathcal{A}(\bar{r})}{\partial z} = \nabla_\perp^2\mathcal{A}(\bar{r}) + \left[k_0^2\left(\varepsilon(\bar{r},\theta) - n_0^2\right)\right]\mathcal{A}(\bar{r}) + 2ik_0n_0\tan\delta(\theta)\frac{\partial\mathcal{A}(\bar{r})}{\partial x}, \tag{2.85}$$

as also reported in [19, 22, 105]. The last term in Eq. (2.85) takes into account the fact that the light, with a wavevector $\bar{k}$ at an angle θ with respect to the director, experiences a walk-off $\delta(\theta)$ during its propagation (Fig. 2.10b).

Until now the orientation of the LC has been taken into account only through the angle θ. We need now to introduce the LC elastic forces among the molecules and the response to electric field. In order to do that, we can write the total free energy for our configuration

$$\mathcal{F} = \iiint f_{tot}(\theta)\,dx\,dy\,dy = \iiint (f_d(\theta) + f_{diel}(\theta))dx\,dy\,dy, \tag{2.86}$$

and minimize it to find the equilibrium position, with the angle θ as free parameter. The spatial distribution of θ that gives the lowest energy is the one that the LC spontaneously adopts. The director distribution is described by

$$\hat{\mathrm{n}} = \sin\theta\,\hat{x} + \cos\theta\,\hat{z}, \tag{2.87}$$

where the reorientation only takes place in the plane $\hat{x}\hat{z}$. We also consider that the director distribution is slowly varying along $\hat{z}$, therefore $\theta = \theta(x, y)$.

The elastic contribution to the free energy density in the one-constant approximation [Eq. (2.7)] becomes

$$f_d = \frac{1}{2}K\left[(\nabla\cdot\bar{\mathrm{n}})^2 + (\nabla\times\bar{\mathrm{n}})^2\right] \tag{2.88}$$

$$= \frac{1}{2}K\left[\left(\cos\theta\frac{\partial\theta}{\partial x}\right)^2 + \left(-\sin\theta\frac{\partial\theta}{\partial y}\hat{x} + \sin\theta\frac{\partial\theta}{\partial x}\hat{y} + \cos\theta\frac{\partial\theta}{\partial y}\hat{z}\right)^2\right] \tag{2.89}$$

$$= \frac{1}{2}K\left[\left(\frac{\partial\theta}{\partial x}\right)^2 + \left(\frac{\partial\theta}{\partial y}\right)^2\right]. \tag{2.90}$$

The dielectric contribution is derived from Eq. (2.16), from which only the term dependent on θ is considered[6]

$$f_{diel} = -\frac{1}{2}\varepsilon_0\triangle\varepsilon\left(\bar{E}\cdot\hat{\mathrm{n}}\right)^2 \tag{2.91}$$

$$= -\frac{1}{2}\varepsilon_0\triangle\varepsilon|E|^2\sin^2\theta \tag{2.92}$$

$$= -\frac{1}{2}\varepsilon_0\triangle\varepsilon\mathcal{A}^2\sin^2\theta. \tag{2.93}$$

The total energy $\mathcal{F}$ is a function of the variable θ and its derivatives, that are noted as

$$\theta_i = \frac{\partial\theta}{\partial\xi_i}, \tag{2.94}$$

where ξ_i are the spatial coordinates ($i = 1, 2, 3$ for x, y and z, respectively).

[6]Note that in our frame of reference the angle between $\bar{E}$ (which is parallel to $\hat{x}$) and $\hat{\mathrm{n}}$ is $\pi - \theta$.

Finding the minimum of the integral $\mathcal{F}$ for the total energy involves solving the Euler-Lagrange equation for the integrand f_{tot} [106, Ch.3]

$$\sum_{i=1}^{3} \frac{\partial}{\partial \xi_i} \left(\frac{\partial f_{tot}}{\partial \theta_i} \right) - \frac{\partial f_{tot}}{\partial \theta} = 0. \tag{2.95}$$

In our case, this last equation takes the form

$$K \left[\frac{\partial^2 \theta}{\partial x^2} + \frac{\partial^2 \theta}{\partial y^2} \right] + \frac{1}{2} \varepsilon_0 \triangle \varepsilon \mathcal{A}^2 \sin 2\theta = 0. \tag{2.96}$$

In our simple geometry, the surface interaction that induces the alignment at the interface is evaluated via the boundary conditions used to solve the equation.

Indeed, due to the walk-off, the electric field $\bar{E}$ is tilted towards the vector $\bar{k}$ and the torque is therefore decreased. For this reason, in order to take into account the walk-off contribution, the angle $\delta(\theta)$ is subtracted from the angle θ [19, 107]

$$K \left[\frac{\partial^2 \theta}{\partial x^2} + \frac{\partial^2 \theta}{\partial y^2} \right] + \frac{1}{2} \varepsilon_0 \triangle \varepsilon \mathcal{A}^2 \sin 2(\theta - \delta(\theta)) = 0. \tag{2.97}$$

The walk-off angle can be subtracted directly in the last equation only because the molecular reorientation takes place over a scale much larger than the beam size (as shown in Ch. 3). For this reason, $\delta(\theta)$ is almost constant across the field section and the derivative $\partial\delta/\partial\theta$ is negligible. As an alternative, the angle $\delta(\theta)$ can be considered as a constant during the propagation and it can be calculated at the beam peak [20, 108] or for the initial orientation (rubbing direction) of the director [22].

The Equations (2.85) and (2.97) form a system of coupled equations that will be solved numerically in the next Chapter. The numerical solution for the profile of the electric field is not an eigensolution of the propagation equation. Indeed, the beam profile is not constant along the propagation, but it is continuously focusing and defocusing with a periodicity that depends on the nematicon power, similar to the breathing behavior of high order solitons [44, 109]. For this reason, nematicons are often referred to as *soliton-like* phenomena. However, for simplicity, we will continue to use the word *soliton* and *nematicon* as synonyms.

Chapter 3 Spatial fluctuations of solitons in LCs

The aim of this chapter is the modeling of the thermal noise in nematic liquid crystals and the spatial fluctuations of the soliton propagation. The results reported in this Chapter have been published in *Physical Review A* [110].

Since the thermal noise induces local variations of the director orientation, LCs are characterized only by an average order. These fluctuations, which cannot be too abrupt in space due to elastic restoring forces between the molecules, are well described by the de Gennes' theory [28, 111]. Starting from the Oseen-Frank continuum theory for LCs, de Gennes' theory predicts the value of the spatial correlation of the director fluctuations. These long-range fluctuations are responsible for optical scattering in liquid crystal materials. This scattering is six orders of magnitude larger than in conventional isotropic fluids which are dominated by the Rayleigh scattering [28]. It is also the main contribution to optical propagation losses in liquid crystals [42].

From the de Gennes' theory, it is possible to extract the variance of the molecular fluctuations, which can be used to predict nuclear spin fluctuations [112], asymmetry in electron resonance spectra [113] and to define the order parameter that characterizes nematic LCs [28]. The off-diagonal elements of the covariance matrix described by de Gennes take into account the long-range interactions of the molecules and the spatial correlation of the director within the LC cell. These correlations are often neglected when considering director fluctuations in liquid crystals.

The accurate modeling of the director fluctuations is of particular importance for the understanding of phenomena that depend on noise, such as modulation instability [114, 115], filamentation [116], or speckle formation [117, 118]. Also, the thermally-induced refractive index fluctuations are responsible for soliton spatial fluctuations. Indeed, when the power is high enough to induce the nematicon diameter to be of the same order of magnitude as or smaller than the refractive index grains, nematicon spatial fluctuations are observed [29, 43]. Different ways to quench the fluctuations have been proposed, ranging from applying an external electric field [119] to the polymerization of the medium [120]. However, until now, no model has been proposed to explain the physical origin of this behavior. This is the aim of this Chapter.

In the first part of this Chapter, the discussion of the numerical implementation of the solution of the coupled equations described in Sect. 2.6 is presented. Then the theory of the director correlation in LCs and its numerical implementation is introduced. Starting from the elastic constants of the LCs and the thermal energy of the system, the correlation matrix is explicitly written in our simulations to generate a model of long-range correlated noise. First, the linear propagation regime is considered in order to explain the origin of speckle formation. Then the nonlinear propagation and the soliton formation are analyzed and our model is experimentally verified. The results demonstrate that the consideration of the correlation is crucial to explain the origin of the nematicon fluctuations.

3.1 Soliton propagation in LCs without noise

This section reports the description of the method used to numerically solve the propagation equation [Eq. (2.85)] and the reorientation equation [Eq. (2.97)]. The geometry of the sample is the one described in Sect. 2.6 (Fig. 3.1). The director lies in planes parallel to the glass plates, where the electric field-induced reorientation also takes place. Its initial orientation is $\theta_0 = 45°$, defined by the rubbing direction, and the optical beam is polarized along

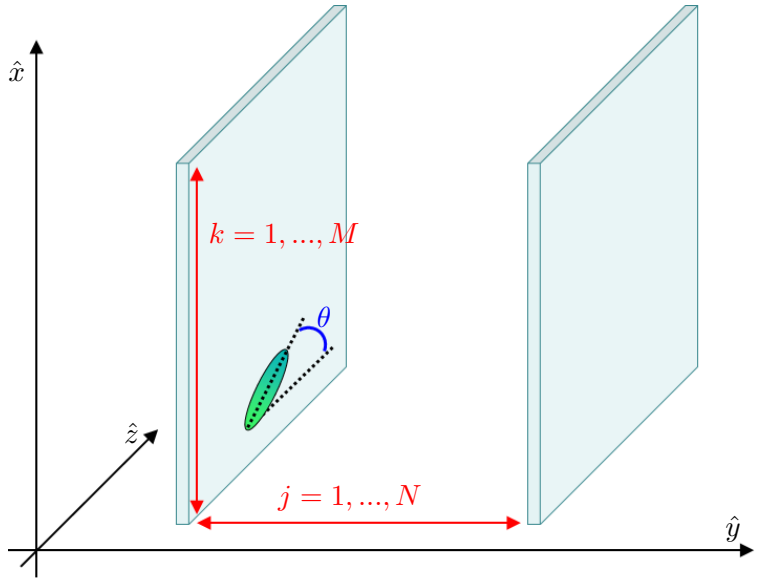

FIGURE 3.1: Scheme of the discretization variables, the orientation of the glass plates and the liquid crystal.

$\hat{x}$. The first equation is integrated with the beam propagation method (BPM) along $\hat{z}$, while the second one is solved with the Newton-Raphson method [121]. Both Equations are discretized with a Crank-Nicholson method, in order to conserve the energy of the propagating beam [121, Ch.19].

3.1.1 Propagation equation

In the case where the director is at 45°with the respect to the $\hat{x}$ axis, a beam polarized along $\hat{x}$ experiences a walk-off $\delta \simeq 7.2°$, defined according to Eq. (2.84). It can be demonstrated that for such an angle the paraxial approximation introduces a relative error of just a few percent [122]. However, in order to minimize the numerical error, a coordinate transformation is used which effectively tilts the frame of reference by an angle $\delta(\theta_0)$ with respect to $\hat{z}$, in the same way that is usually done for the group velocity in the wave propagation equation [91, pp.11-12]

$$\begin{cases} x' &= x + \tan\delta\left(\theta_0\right) z \\ y' &= y \\ z' &= z\,. \end{cases} \tag{3.1}$$

The propagation equation Eq. (2.85) then becomes

$$2ik_0 n_0 \frac{\partial \mathcal{A}\left(\bar{r}'\right)}{\partial z'} = \nabla_\perp^2 \mathcal{A}\left(\bar{r}'\right) + \left[k_0^2\left(\varepsilon\left(\bar{r}', \theta\right) - n_0^2\right)\right] \mathcal{A}\left(\bar{r}'\right) \tag{3.2}$$

$$+ 2ik_0 n_0 \left[\tan\delta(\theta) - \tan\delta(\theta_0)\right] \frac{\partial \mathcal{A}\left(\bar{r}'\right)}{\partial x'}, \tag{3.3}$$

where the change of coordinates does not affect the transverse Laplacian $\nabla_\perp^2$ or the orientation of the electric field polarization.

Introducing the parameters

$$\eta = 2ik_0 n_0, \tag{3.4}$$

$$\gamma(\theta) = k_0^2\left(\varepsilon(\bar{r}', \theta) - n_0^2\right), \tag{3.5}$$

$$\zeta(\theta) = 2ik_0 n_0 \left[\tan\delta(\theta) - \tan\delta(\theta_0)\right], \tag{3.6}$$

we obtain

$$\eta \frac{\partial \mathcal{A}(\bar{r}')}{\partial z'} = \nabla_\perp^2 \mathcal{A}(\bar{r}') + \gamma(\theta)\mathcal{A}(\bar{r}') + \zeta(\theta)\frac{\partial \mathcal{A}(\bar{r}')}{\partial x'}. \tag{3.7}$$

This is the equation that has to be solved numerically. The equation is discretized using the Crank-Nicholson method [121, pp. 847-851]

$$\mathcal{A} = \frac{\mathcal{A}^{n+1}_{k,j} + \mathcal{A}^{n}_{k,j}}{2}, \tag{3.8}$$

$$\frac{\partial \mathcal{A}}{\partial z'} = \frac{\mathcal{A}^{n+1}_{k,j} - \mathcal{A}^{n}_{k,j}}{\triangle z}, \tag{3.9}$$

$$\frac{\partial \mathcal{A}}{\partial x'} = \frac{1}{2\triangle x}\left(\frac{\mathcal{A}^{n+1}_{k+1,j} + \mathcal{A}^{n}_{k+1,j}}{2} - \frac{\mathcal{A}^{n+1}_{k-1,j} + \mathcal{A}^{n}_{k-1,j}}{2}\right), \tag{3.10}$$

$$\frac{\partial^2 \mathcal{A}}{\partial y'^2} = \frac{1}{\triangle y^2}\left(\frac{\left(\mathcal{A}^{n+1}_{k,j+1} - 2\mathcal{A}^{n+1}_{k,j} + \mathcal{A}^{n+1}_{k,j-1}\right) + \left(\mathcal{A}^{n}_{k,j+1} - 2\mathcal{A}^{n}_{k,j} + \mathcal{A}^{n}_{k,j-1}\right)}{2}\right), \tag{3.11}$$

where the superscript n indicates the step number in the $\hat{z}'$ direction (with increment $\triangle z$), and the superscript k, j are the indices along $\hat{x}'$ and $\hat{y}'$, respectively (with a discretization grid $\triangle x$ and $\triangle y$) (Fig. 3.1). In the plane orthogonal to the propagation direction, M intervals are taken in the $\hat{x}'$ direction and N in the $\hat{y}'$ one.

The Crank-Nicholson scheme is shown to be unconditionally stable and second-order accurate in $\hat{z}'$ [121, pp. 847-851]. This method is also unitary, meaning that the integral of the square modulus of the function $\mathcal{A}$ (*i.e.* the energy of the beam) is conserved during the propagation [121, pp. 851-853]. There is therefore no need to normalize the energy of the beam at every step along $\hat{z}'$. This will be particularly important to evaluate the propagation losses in Sect. 3.4.2.

The Equation (3.7) becomes for the point (k, j)

$$\begin{aligned}\eta\frac{\mathcal{A}^{n+1}_{k,j} - \mathcal{A}^{n}_{k,j}}{\triangle z} =& \frac{1}{2\triangle x^2}\left(\mathcal{A}^{n+1}_{k+1,j} - 2\mathcal{A}^{n+1}_{k,j} + \mathcal{A}^{n+1}_{k-1,j} + \mathcal{A}^{n}_{k+1,j} - 2\mathcal{A}^{n}_{k,j} + \mathcal{A}^{n}_{k-1,j}\right)\\ &+ \frac{1}{2\triangle y^2}\left(\mathcal{A}^{n+1}_{k,j+1} - 2\mathcal{A}^{n+1}_{k,j} + \mathcal{A}^{n+1}_{k,j-1} + \mathcal{A}^{n}_{k,j+1} - 2\mathcal{A}^{n}_{k,j} + \mathcal{A}^{n}_{k,j-1}\right)\\ &+ \gamma(\theta)\frac{\mathcal{A}^{n+1}_{k,j} + \mathcal{A}^{n}_{k,j}}{2} + \zeta(\theta)\frac{1}{4\triangle x}\left(\mathcal{A}^{n+1}_{k+1,j} + \mathcal{A}^{n}_{k+1,j} - \mathcal{A}^{n+1}_{k-1,j} - \mathcal{A}^{n}_{k-1,j}\right).\end{aligned} \tag{3.12}$$

Grouping the coefficients

$$\begin{aligned}&\underbrace{\left(\frac{\eta}{\triangle z} - \frac{\gamma(\theta)}{2} + \frac{1}{\triangle x^2} + \frac{1}{\triangle y^2}\right)}_{a}\mathcal{A}^{n+1}_{k,j} + \underbrace{\left(-\frac{\zeta(\theta)}{4\triangle x} - \frac{1}{2\triangle x^2}\right)}_{-b}\mathcal{A}^{n+1}_{k+1,j} + \underbrace{\left(\frac{\zeta(\theta)}{4\triangle x} - \frac{1}{2\triangle x^2}\right)}_{-c}\mathcal{A}^{n+1}_{k-1,j}\\ &\qquad + \underbrace{\left(-\frac{1}{2\triangle y^2}\right)}_{-d}\mathcal{A}^{n+1}_{k,j+1} + \underbrace{\left(-\frac{1}{2\triangle y^2}\right)}_{-d}\mathcal{A}^{n+1}_{k,j-1}\\ &= \underbrace{\left(\frac{\eta}{\triangle z} + \frac{\gamma(\theta)}{2} - \frac{1}{\triangle x^2} - \frac{1}{\triangle y^2}\right)}_{f}\mathcal{A}^{n}_{k,j} + \underbrace{\left(\frac{\zeta(\theta)}{4\triangle x} + \frac{1}{2\triangle x^2}\right)}_{b}\mathcal{A}^{n}_{k+1,j} + \underbrace{\left(-\frac{\zeta(\theta)}{4\triangle x} + \frac{1}{2\triangle x^2}\right)}_{c}\mathcal{A}^{n}_{k-1,j}\\ &\qquad + \underbrace{\left(\frac{1}{2\triangle y^2}\right)}_{d}\mathcal{A}^{n}_{k,j+1} + \underbrace{\left(\frac{1}{2\triangle y^2}\right)}_{d}\mathcal{A}^{n}_{k,j-1}.\end{aligned} \tag{3.13}$$

In order to be able to write the equation in the form $\bar{y} = \bar{\bar{A}}\bar{x}$, we need to re-number the elements of Eq. (3.13) in a such a way that $\mathcal{A}$ can be written as a vector. The two indices k and j can be grouped in to new index ind

$$ind = j + N(k-1) \tag{3.14}$$

where

$$\begin{array}{rcll} \hbar & = & 1, \ldots, M & \text{along } \hat{x} \\ j & = & 1, \ldots, N & \text{along } \hat{y} \end{array} \tag{3.15}$$

In this way the elements of the matrix are numbered line by line and Eq. (3.13) becomes

$$a\mathcal{A}^{n+1}_{in\ell} - b\mathcal{A}^{n+1}_{in\ell+1} - c\mathcal{A}^{n+1}_{in\ell-1} - d\mathcal{A}^{n+1}_{in\ell+N} - d\mathcal{A}^{n+1}_{in\ell-N} \tag{3.16}$$

$$= f\mathcal{A}^{n}_{in\ell} + b\mathcal{A}^{n}_{in\ell+1} + c\mathcal{A}^{n}_{in\ell-1} + d\mathcal{A}^{n}_{in\ell+N} + d\mathcal{A}^{n}_{ind-N} \tag{3.17}$$

This is the equation for the generic point $(\hbar, j)$. Writing this relation for all the points we can introduce the matrices

$$\bar{\bar{A}} = \begin{vmatrix} a & -b & \cdots & -d & & \\ -c & a & -b & \cdots & -d & \\ \vdots & -c & a & -b & \cdots & -d \\ -d & \vdots & -c & a & \ddots & \\ & -d & \vdots & \ddots & \ddots & \\ & & -d & & & \end{vmatrix} \quad \text{and} \quad \bar{\bar{B}} = \begin{vmatrix} f & b & \cdots & d & & \\ c & f & b & \cdots & d & \\ \vdots & c & f & b & \cdots & d \\ d & \vdots & c & f & \ddots & \\ & d & \vdots & \ddots & \ddots & \\ & & d & & & \end{vmatrix} \tag{3.18}$$

$$\bar{u}^{n+1} = \begin{vmatrix} \vdots \\ \mathcal{A}^{n+1}_{in\ell-1} \\ \mathcal{A}^{n+1}_{in\ell} \\ \mathcal{A}^{n+1}_{in\ell+1} \\ \vdots \end{vmatrix}. \tag{3.19}$$

We obtain

$$\bar{\bar{A}}\bar{u}^{n+1} = \bar{\bar{B}}\bar{u}^{n} \tag{3.20}$$

and then

$$\bar{u}^{n+1} = \bar{\bar{A}}^{-1}\bar{\bar{B}}\,\bar{u}^{n}. \tag{3.21}$$

The graphical representation of the structure of the matrices $\bar{\bar{A}}$ and $\bar{\bar{B}}$ is reported in Fig.3.2a. The sparse nature of these matrices is exploited in the numerical code to increase the efficiency of the program (Alg. B.1, Sect. B.5).

Cyclic boundary conditions

As already mentioned, light propagating in liquid crystals experiences losses due to the scattering induced by the director fluctuations. The reorientation of the director ($i.e.$ the variation of θ), and therefore the walk-off, depends on the intensity of the electric field of the beam. Since the walk-off angle $\delta(\theta)$ [Eq.(2.54)] is intensity dependent, the soliton trajectory is expected to deviate from the initial walk-off $\delta(\theta_0)$. This means that the soliton will not stay centered in the frame of reference that is shifting according to Eq. (3.1). Also, as it will be presented in Sect. 3.4.2, the director fluctuations cause deviations in the nematicon propagation path. If we want a soliton propagation over long distances, the walk-off drifting and the soliton oscillations imply that we should adopt a large window in $\hat{x}$, sensibly increasing the calculation time. Another solution is to implement *cyclic boundary conditions* along $\hat{x}$,[1] which is the option adopted in the following.

From Eq. (3.10) and Eq. (3.11) we obtain

$$\hbar = 1 \quad \Rightarrow \quad \frac{\partial^2\mathcal{A}}{\partial x'^2} = \frac{1}{\triangle x^2}\left(\mathcal{A}_{2,j} - 2\mathcal{A}_{1,j} + \mathcal{A}_{M,j}\right), \qquad \frac{\partial\mathcal{A}}{\partial x'} = \frac{1}{2\triangle x}\left(\mathcal{A}_{2,j} - \mathcal{A}_{M,j}\right) \tag{3.22}$$

$$\hbar = M \quad \Rightarrow \quad \frac{\partial^2\mathcal{A}}{\partial x'^2} = \frac{1}{\triangle x^2}\left(\mathcal{A}_{1,j} - 2\mathcal{A}_{M,j} + \mathcal{A}_{M-1,j}\right), \qquad \frac{\partial\mathcal{A}}{\partial x'} = \frac{1}{2\triangle x}\left(\mathcal{A}_{1,j} - \mathcal{A}_{M-1,j}\right) \tag{3.23}$$

[1] This also implies that, if the beam is diffracting, there could be interferences between the beam going out from one side and the beam that is entering. We will pay attention to avoid this situation, such as by limiting the propagation distance to 2.7 mm and by analyzing the beam propagation for powers higher than the nematicon threshold, for which the beam is not diffracting.

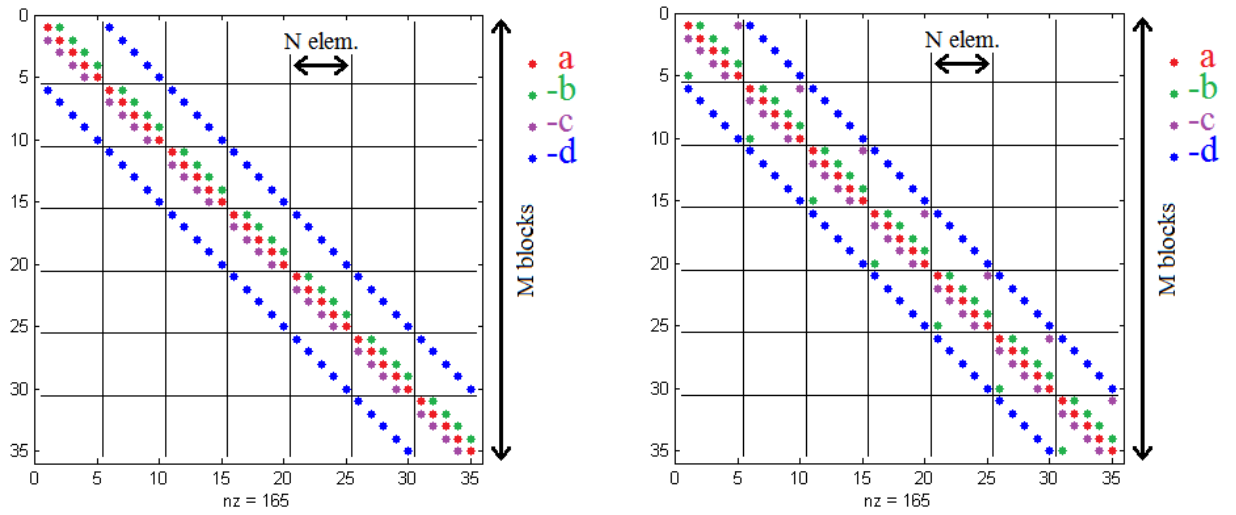

FIGURE 3.2: Structure of the matrix $\bar{\bar{A}}$, for a discretization $(M, N) = (6, 4)$, in the case of open (a) and cyclic (b) boundary conditions. The matrix $\bar{\bar{B}}$ has the same form as the matrix $\bar{\bar{A}}$, but the terms $a, -b, -c, -d$ are replaced with f, b, c, d [Eq. (3.18)].

We do not need to implement these conditions along $\hat{y}$ since all of the cell thickness is considered in the simulations. The structure of the matrix is reported in Fig. 3.2b.

In the Appendix B we report the matlab code issued from our modeling. The function *nematicon.m* (Sect. B.1) is where all the parameters and the variables are defined, while *Propagation_Crank_Nich.m* (Sect. B.2) describes the soliton propagation. The function that writes the matrices $\bar{\bar{A}}$ and $\bar{\bar{B}}$ is reported in Sect. B.5, Alg. B.1.

When reporting the nematicon propagation, we will transform the frame of reference back to $\hat{x}\hat{y}\hat{z}$ with Eq. (3.1) and we will unfold the soliton path in order to avoid discontinuities.

3.1.2 Reorientation equation

Now we have to take into account the fact that the LC is reoriented by the light propagating inside the medium. At equilibrium, the electric field of the incoming light counterbalances the restoring elastic forces of LCs. In the one-constant approximation and for the optical field in the $\hat{x}$ direction, the equation that describes the equilibrium state is Eq. (2.97), which is reproduced here for clarity

$$K\left[\frac{\partial^2\theta}{\partial x^2}+\frac{\partial^2\theta}{\partial y^2}\right]+\frac{1}{2}\varepsilon_0\sin 2\left(\theta-\delta(\theta)\right)\triangle\varepsilon\left|\mathcal{E}\right|^2=0, \tag{3.24}$$

where $\theta = \theta(\bar{r})$. Since the transverse Laplacian is not affected by the change of coordinates, it is possible to keep the coordinate system $\hat{x}\hat{y}\hat{z}$. The equation, dicretized with Eq. (3.8) and Eq. (3.11), becomes

$$\underbrace{\frac{K}{\triangle x^2}\left(\theta_{\hbar+1,j}-2\theta_{\hbar,j}+\theta_{\hbar-1,j}\right)+\frac{K}{\triangle y^2}\left(\theta_{\hbar,j+1}-2\theta_{\hbar,j}+\theta_{\hbar,j-1}\right)}_{\text{linear term}}$$
$$+\underbrace{\frac{1}{2}\varepsilon_0\triangle\varepsilon\left|\mathcal{E}_{\hbar,j}\right|^2\sin 2\left(\theta_{\hbar,j}-\delta_{\hbar,j}(\theta_{\hbar,j})\right)}_{\text{nonlinear term}}=0. \tag{3.25}$$

Using the same change of index of Eq. (3.14), we can write the equation in matrix notation

$$\bar{\bar{F}}_{\mathrm{L}}\bar{\theta}+\bar{F}_{\mathrm{NL}}\left(\bar{\theta}\right)=0, \tag{3.26}$$

where $\bar{\bar{F}}_{\mathrm{L}}\bar{\theta}$ is the linear contribution and $\bar{F}_{\mathrm{NL}}\left(\bar{\theta}\right)$ is the nonlinear one.

To solve this equation, the term on the left has to be minimized. The standard way to do that is the Newton-Raphson optimization method. The complete theory of the method is reported in [121, Ch. 9.4], here only the most important parts are reported. A general function $\bar{F}(\bar{g})$ of type

$$F_q\left(g_1 \dots g_\ell \dots g_L\right) = 0, \qquad q = 1, \dots Q \tag{3.27}$$

can be written as a Taylor's series

$$F_q(\bar{g} + \triangle\bar{g}) = F_q(\bar{g}) + \sum_{\ell=1}^{L} \underbrace{\left(\frac{\partial F_q}{\partial g_\ell}\right)}_{J_{q\ell}} \triangle g_\ell + \mathcal{O}\left(\triangle\bar{g}^2\right), \tag{3.28}$$

where $J_{q\ell}$ is the element (q, ℓ) of the Jacobian matrix $\bar{\bar{J}}$. In matrix notation it becomes

$$\bar{F}\left(\bar{g} + \triangle\bar{g}\right) = \bar{F}\left(\bar{g}\right) + \bar{\bar{J}}\,\triangle\bar{g} + \mathcal{O}\left(\triangle\bar{g}^2\right). \tag{3.29}$$

Starting from a generic point $\bar{g}$, we want to find the variation $\triangle\bar{g}$ so that [121, Ch. 9.4]

$$\bar{F}\left(\bar{g} + \triangle\bar{g}\right) = 0. \tag{3.30}$$

From Eq. (3.29) and Eq. (3.30)

$$\bar{\bar{J}}\,\triangle\bar{g} = -\bar{F}\left(\bar{g}\right) \tag{3.31}$$

and

$$\triangle\bar{g} = -\bar{\bar{J}}^{-1}\,\bar{F}\left(\bar{g}\right). \tag{3.32}$$

Starting from an initial guess $\bar{g}_{old}$ of the parameters, this last equation gives the correction $\triangle\bar{g}$ to add to the parameter $\bar{g}$ in order to satisfy Eq. (3.30)

$$\bar{g}_{new} = \bar{g}_{old} + \triangle\bar{g}. \tag{3.33}$$

In our case

$$\bar{F}(\bar{\theta}) = \bar{\bar{F}}_{\mathrm{L}}\bar{\theta} + \bar{F}_{\mathrm{NL}}(\bar{\theta}) \tag{3.34}$$

and the Jacobian is

$$\bar{\bar{J}} = \frac{\partial\bar{F}}{\partial\bar{\theta}} = \frac{\partial\left(\bar{\bar{F}}_{\mathrm{L}}\bar{\theta} + \bar{F}_{\mathrm{NL}}(\bar{\theta})\right)}{\partial\bar{\theta}} = \bar{\bar{F}}_{\mathrm{L}} + \mathrm{diag}\left(\varepsilon_0\triangle\varepsilon\left|\mathcal{E}\right|^2\cos 2\left(\bar{\theta} - \bar{\delta}(\bar{\theta})\right)\left(2 - 2\frac{\partial\bar{\delta}(\bar{\theta})}{\partial\bar{\theta}}\right)\right), \tag{3.35}$$

where the operator $\mathrm{diag}(\bar{g})$ produces a square diagonal matrix where the elements of the vector $\bar{g}$ are on the diagonal. The elements that compose the derivative of $\bar{\delta}(\bar{\theta})$ are

$$\frac{\partial\delta(\theta)_{in\ell}}{\partial\theta_{in\ell}} = \frac{\partial}{\partial\theta_{in\ell}}\left(\mathrm{atan}\left(\frac{\varepsilon_{xz}(\theta_{in\ell})}{\varepsilon_{zz}(\theta_{in\ell})}\right)\right) = \frac{1}{1 + \left(\frac{\varepsilon_{xz}(\theta_{in\ell})}{\varepsilon_{zz}(\theta_{in\ell})}\right)^2}\frac{\left(\partial\varepsilon_{xz}(\theta_{in\ell})/\varepsilon_{zz}(\theta_{in\ell})\right)}{\partial\theta_{in\ell}} = \tag{3.36}$$

$$= \frac{1}{1 + \left(\frac{\varepsilon_{xz}(\theta_{in\ell})}{\varepsilon_{zz}(\theta_{in\ell})}\right)^2}\left(\frac{\triangle\varepsilon\left(\cos^2\theta_{in\ell} - \sin^2\theta_{in\ell}\right)}{\left(\varepsilon_\perp + \triangle\varepsilon\cos^2\theta_{in\ell}\right)^2} + \frac{\left(\triangle\varepsilon\sin\theta_{in\ell}\cos\theta_{in\ell}\right)^2}{\left(\varepsilon_\perp + \triangle\varepsilon\cos^2\theta_{in\ell}\right)^2}\right) \tag{3.37}$$

$$= \frac{\triangle\varepsilon\left(\left(\triangle\varepsilon + 2\varepsilon_\perp\right)\cos\left(2\theta_{in\ell}\right) + \triangle\varepsilon\right)}{\triangle\varepsilon^2 + \triangle\varepsilon\left(\triangle\varepsilon + 2\varepsilon_\perp\right)\cos\left(2\theta_{in\ell}\right) + 2\varepsilon_\perp\triangle\varepsilon + 2\varepsilon_\perp^2}, \tag{3.38}$$

where Eq. (2.84) has been used for the definition of $\delta(\theta)$. The variation of $\bar{\theta}$ is

$$\triangle\bar{\theta} = -\bar{\bar{J}}^{-1}\left(\bar{\bar{F}}_{\mathrm{L}}\bar{\theta} + \bar{F}_{\mathrm{NL}}(\bar{\theta})\right). \tag{3.39}$$

This correction is added to the angle $\bar{\theta}$ and a new $\triangle\bar{\theta}$ is calculated in the next iteration. This iterative process is followed until the correction is smaller than a certain value ($0.5 \cdot 10^{-13}$ in our case), chosen in such a way that a larger accuracy would not change significantly the solution.

Boundary conditions

The boundary condition for the angle θ can be separated into two regions, along the glass plates of the LC cell and along the thickness of the cell.

Along the thickness of the cell ($\hbar = 1$ and $\hbar = M$)), cyclic boundary conditions are adopted. Indeed, since cyclic boundary conditions are implemented along the axis $\hat{x}$ for the propagation equation, a continuum behavior is needed along that direction also for the angle θ. The equations for the discretization of the linear part of Eq. (3.25) are

$$\hbar = 1 \qquad \Rightarrow \qquad \frac{K}{\triangle x^2}\left(\theta_{2,j} - 2\theta_{1,j} + \theta_{M,j}\right) + \frac{K}{\triangle y^2}\ldots = 0, \tag{3.40}$$

$$\hbar = M \qquad \Rightarrow \qquad \frac{K}{\triangle x^2}\left(\theta_{1,j} - 2\theta_{M,j} + \theta_{M-1,j}\right) + \frac{K}{\triangle y^2}\ldots = 0. \tag{3.41}$$

Along the glass plates ($j = 1$ and $j = N$), the orientation of the molecules is assumed to be fixed by the rubbing direction ($\theta_{\hbar,j} = \theta_0$). To model this behavior, the condition $\triangle\bar{\theta} = 0$ is imposed for these points (Alg. B.6).

In the simulation program, the optimization of $\bar{\theta}$ is done through the matlab function *theta_opt.m* (Alg. B.3), where the linear and nonlinear part are discretized separately (respectively Alg. B.5 and Alg. B.6).

3.2 Numerical results

In this section the numerical results, obtained with the model explained until this point, are reported.

The system is a standard LC cell (75 µm thickness, planar alignment, rubbing at $\theta_0 = 45°$ with respect to the entrance window), filled with E7. The elastic constant K in the one-constant approximation is taken as 12 pN. The laser beam is injected with the optical fiber described in Sect. 2.4.2 and the electric field profile is assumed to be gaussian

$$\mathcal{A}\left(\bar{r}\right) = \hat{\mathcal{A}}\exp\left(-\frac{x^2}{w_{0x}^2} - \frac{y^2}{w_{0y}^2}\right), \tag{3.42}$$

where the radius w_0 ($= w_{0x} = w_{0y}$) is 3.7 µm at the wavelength 1064 nm. The phase front is assumed to be planar at the exit of the fiber.

For the simulations, we adopt a window of 55 µm×75 µm in the $\hat{x}\hat{y}$ plane. The discretization is M=155 points along $\hat{x}$ and N=211 points along $\hat{y}$, with $\triangle x$=$\triangle y$=355 nm.

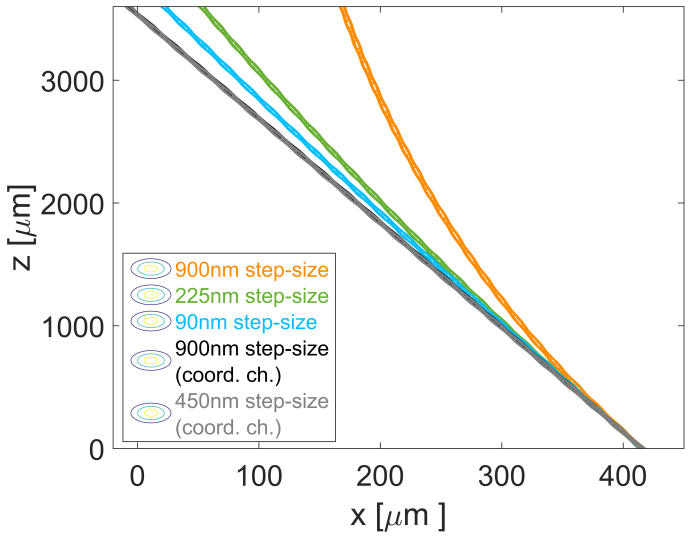

FIGURE 3.3: Nematicon trajectories for different step-sizes, before (orange, green and blue) and after (black and grey) the change of coordinate. The soliton power is 3.7 mW.

3.2.1 Importance of the frame of reference

We start by reporting on the importance of the moving frame of reference of Eq. (3.1).

The profile in the $\hat{x}\hat{z}$ plane (obtained by integrating the intensity of the beam along the $\hat{y}$ axis) is reported in Fig. 3.3 for different step-sizes, and for the cases before (orange, green and blue curves) and after (black and gray curves) the change of variables of Eq. (3.1). The power of the beam is high enough to observe a soliton behavior, with light confinement along the propagation. However, it is possible to see that, before the change of variables, the large numerical error causes a curved propagation path for the nematicon. Passing from $\triangle z$ =900 nm to $\triangle z$ =90 nm the bending is decreased, but the computation time is increased from 1 hour to 8 hours (for a propagation length of 3.6 mm).

When adopting a system of frame shifting with the walk-off [Eq. (3.1)], the propagation path is straight and corresponds to the theoretical walk-off. This is the expected behavior for a soliton propagation in a medium without losses, as was assumed here above. The intensity of the beam is constant along the propagation. The LC reorientation and therefore the walk-off are constant too.

Using a step-size of the same order of magnitude as the wavelength (900 nm) or half of it (450 nm) gives a difference for the output position that is less than a µm after 3.6 mm of propagation. The computation time is, however, doubled. For these reasons, in the following, we use a step-size of 900 nm in the $\hat{z}$ direction.

3.2.2 LC reorientation, beam profile and walk-off

In Fig. 3.4 we report the spatial distribution for the angle θ in a plane orthogonal to the light propagation (plane $\hat{x}\hat{y}$). The LC is reoriented by the electric field of the optical beam, increasing the value of θ in the center of the section. The reorientation extends over a distance much larger than the beam size (Fig. 3.5), due to the nonlocality of the LCs. The reorientation peak has no radial symmetry because along $\hat{y}$ there are the boundary conditions given by the glass plates (the director is pinned at θ_0=45°), while along $\hat{x}$ there are no constraints.

In Fig. 3.3 it is possible to see that the beam profile is not constant along the propagation, but it is continuously focusing and defocusing with a periodicity that depends on the nematicon power, similar to the breathing behavior of high order solitons [44, 109].

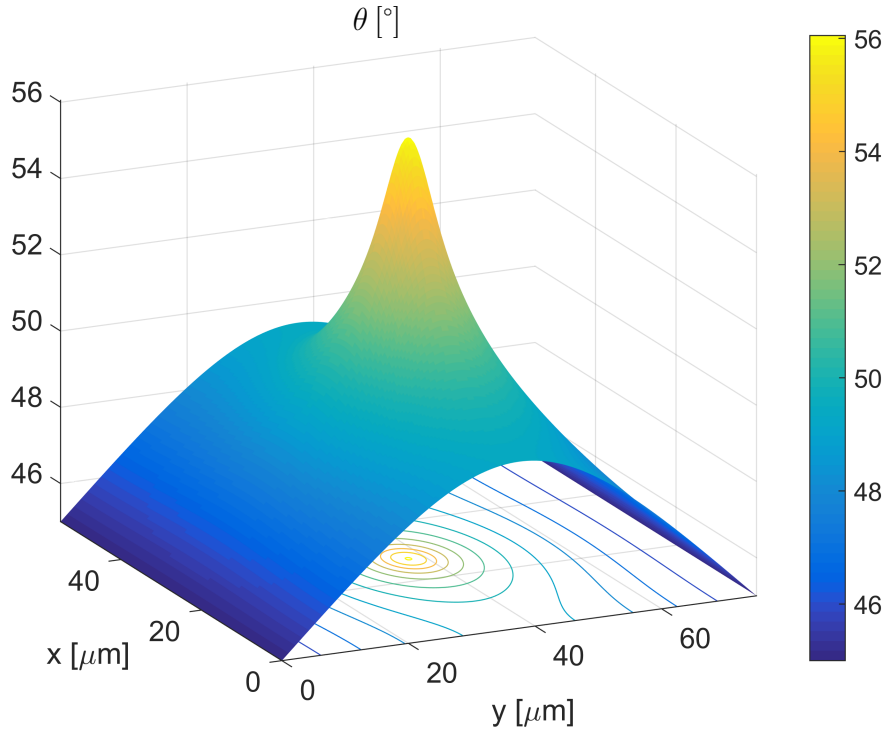

FIGURE 3.4: Spatial distribution of the angle θ on the plane $\hat{x}\hat{y}$ (at $\hat{z}$=0).

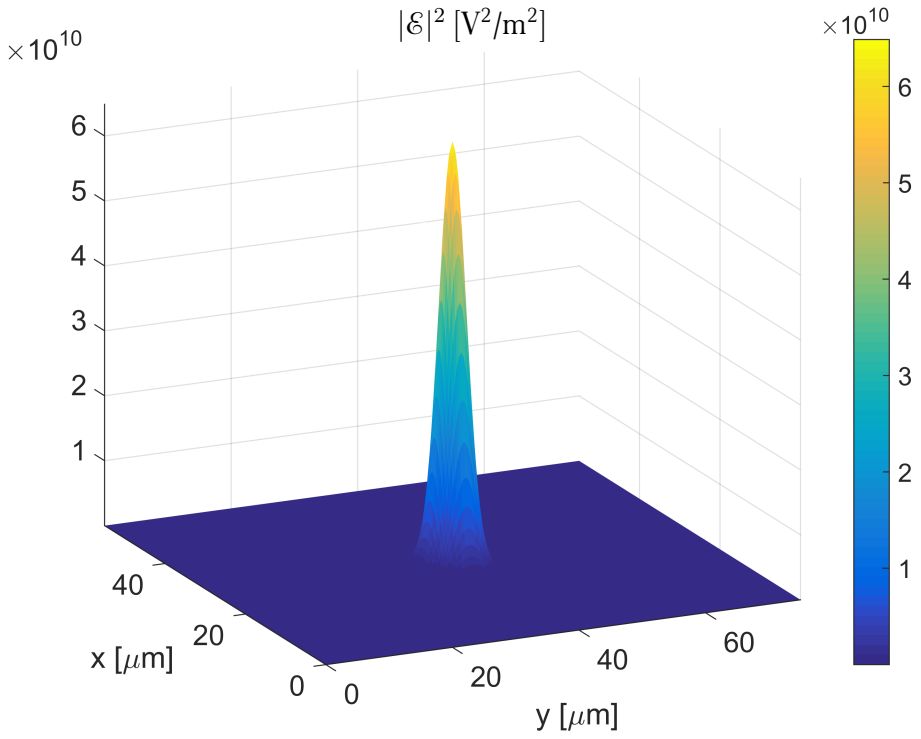

FIGURE 3.5: Intensity profile of the laser beam on the plane $\hat{x}\hat{y}$ (at $\hat{z}$=0).

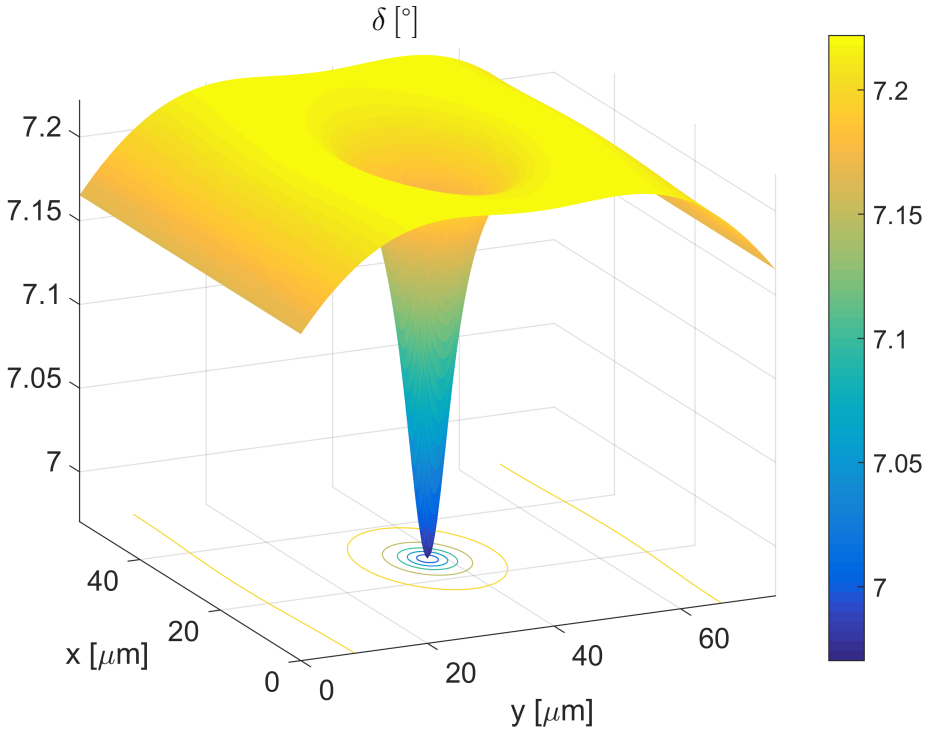

FIGURE 3.6: Spatial evolution of the walk-off angle δ in a plane $\hat{x}\hat{y}$ (at $\hat{z}$=0).

From the angle θ it is possible to calculate the spatial evolution of the walk-off through Eq. (2.54). The result is reported in Fig. 3.6. Since the beam size is much smaller than the region where the LC is reoriented, the beam is expected to have a walk-off close to the minimum value reached at the center of the beam.

3.3 Correlated thermal noise in LCs

As it was introduced in the first Chapter, nematic LCs are characterized by a mean orientation of the LC molecules, called the *director* and represented by the unitary vector $\hat{\mathtt{n}}$. The director is a statistical concept: it takes into account volumes that are much larger than the molecular size and that includes a significant number of molecules. If the molecules were not interacting (and in the absence of structured external stimuli), this local average would be constant all over the sample and it would be enough to characterize the system macroscopically.

However, LC molecules interact with one another due to the elastic forces that connect them. This means that a perturbation in one point will cause a perturbation at a distance much larger than the size of the molecule. The average over a volume much larger than a molecule but smaller than the macroscopic sample, as it is the case for the vector $\hat{\mathtt{n}}$, can therefore vary in space due to these long range fluctuations.

It is convenient to define the director as composed of two contributions[2]

$$\hat{\mathtt{n}}(\bar{r}_d) = \hat{\mathtt{n}}_0 + \triangle\bar{\mathtt{n}}(\bar{r}_d), \tag{3.43}$$

where $\hat{\mathtt{n}}_0$ is the macroscopic average of the director, $\triangle\bar{\mathtt{n}}(\bar{r}_d) = \mathtt{n}_{\hat{x}_d}(\bar{r}_d)\hat{x}_d + \mathtt{n}_{\hat{y}_d}(\bar{r}_d)\hat{y}_d$ defines the director fluctuations and $\bar{r}_d = (\hat{x}_d, \hat{y}_d\hat{z}_d)$ designates the frame of reference of the director, where $\hat{z}_d$ is parallel to $\hat{\mathtt{n}}_0$. The macroscopic average of these fluctuations is zero.

3.3.1 Director correlation

As presented by de Gennes in [28, Ch3.4] and [111], the director fluctuations can be evaluated in terms of correlation between two points at a distance $\bar{R}$. Here, we report the main points of de Gennes' theory before introducing our contribution to the model in Sect. 3.3.2.

The free energy of the system is composed of

$$\mathcal{F} = \mathcal{F}_0 + \mathcal{F}_d + \mathcal{F}_{diel}, \tag{3.44}$$

where $\mathcal{F}_0$ is a constant contribution independent of $(\mathtt{n}_{\hat{x}_d}(\bar{r}_d), \mathtt{n}_{\hat{y}_d}(\bar{r}_d))$, $\mathcal{F}_d$ is the distortion energy and $\mathcal{F}_{diel}$ is the contribution due to the dielectric coupling with an external electric field $\bar{E}_{ext}$. These last two terms can be evaluated to the second order in terms of the variation of the director. The elastic contribution $\mathcal{F}_d$ takes the form

$$\mathcal{F}_d = \frac{1}{2}\int \left\{ K_1 \left(\frac{\partial \mathtt{n}_{\hat{x}_d}}{\partial \hat{x}_d} + \frac{\partial \mathtt{n}_{\hat{y}_d}}{\partial \hat{y}_d} \right)^2 + K_2 \left(\frac{\partial \mathtt{n}_{\hat{x}_d}}{\partial \hat{y}_d} - \frac{\partial \mathtt{n}_{\hat{y}_d}}{\partial \hat{x}_d} \right)^2 + K_3 \left[\left(\frac{\partial \mathtt{n}_{\hat{x}_d}}{\partial \hat{z}_d} \right)^2 + \left(\frac{\partial \mathtt{n}_{\hat{y}_d}}{\partial \hat{z}_d} \right)^2 \right] \right\} d\bar{r}_d \tag{3.45}$$

and $\mathcal{F}_{diel}$

$$\mathcal{F}_{diel} = \frac{1}{2}\varepsilon_0 \int \triangle\varepsilon \left|E_{ext}\right|^2 \left(\mathtt{n}_{\hat{x}_d}^2 + \mathtt{n}_{\hat{y}_d}^2\right). \tag{3.46}$$

The Fourier coefficients are defined as

$$\tilde{\mathtt{n}}_{\hat{x}_d}(\bar{q}) = \int \mathtt{n}_{\hat{x}_d}(\bar{r}_d) e^{i\bar{q}\cdot\bar{r}_d} d\bar{r}_d, \tag{3.47}$$

where the components of $\bar{q}$ are $q_\beta = 2\pi/\beta$ with $\beta = x_d, y_d, z_d$. The Fourier transforms of the fluctuations are

$$\begin{aligned} \mathcal{F} = \mathcal{F}_0 + \frac{1}{2\Omega}\sum_q \Big\{ & K_1 \left|\tilde{\mathtt{n}}_{\hat{x}_d}(\bar{q}) q_{\hat{x}_d} + \tilde{\mathtt{n}}_{\hat{y}_d}(\bar{q}) q_{\hat{y}_d}\right|^2 + K_2 \left|\tilde{\mathtt{n}}_{\hat{x}_d}(\bar{q}) q_{\hat{y}} - \tilde{\mathtt{n}}_{\hat{y}}(\bar{q}) q_{\hat{x}_d}\right|^2 \\ & + \left(K_3 q_{\hat{z}_d}^2 + \varepsilon_0 \triangle\varepsilon \left|E_{ext}\right|^2\right) \left[\left|\tilde{\mathtt{n}}_{\hat{x}_d}(\bar{q})\right|^2 + \left|\tilde{\mathtt{n}}_{\hat{y}_d}(\bar{q})\right|^2 \right] \Big\}, \end{aligned} \tag{3.48}$$

where Ω is the sample volume. It is possible to find a new coordinate system $(\tilde{\mathtt{n}}_1(\bar{q}), \tilde{\mathtt{n}}_2(\bar{q}))$ where Eq. (3.48) is diagonalized in the form [28, (pp.141-150)]

$$\mathcal{F} = \mathcal{F}_0 + \frac{1}{2\Omega}\sum_q \sum_{\iota=1,2} \left|\tilde{\mathtt{n}}_\iota(\bar{q})\right|^2 \left(K_3 q_\parallel^2 + K_\iota q_\perp^2 + \varepsilon_0 \triangle\varepsilon \left|E_{ext}\right|^2\right), \tag{3.49}$$

[2] Note that in this work we analyze only the spatial behavior of the director, and not its temporal dynamics.

where $q_{\parallel} = q_z$ and $q_{\perp} \perp q_{\parallel}$. Since the formulation is now diagonalized, the equipartition theorem can be applied to each degree of freedom

$$\left\langle \frac{1}{2\Omega} \left|\tilde{\mathtt{n}}_{\iota}\left(\bar{q}\right)\right|^2 \left(K_3 q_{\parallel}^2 + K_{\iota} q_{\perp}^2 + \varepsilon_0 \triangle\varepsilon \left|E_{ext}\right|^2\right)\right\rangle = \frac{1}{2} k_B T \qquad \iota = 1,2 \tag{3.50}$$

and, in the one-constant approximation for LC, we have

$$\left\langle \left|\tilde{\mathtt{n}}_{\iota}(\bar{q})\right|^2 \right\rangle = \frac{\Omega k_B T}{K\left(q^2 + \xi^{-2}\right)} \qquad \iota = 1,2 \tag{3.51}$$

where $\xi = K/\left(\varepsilon_0 \triangle\varepsilon \left|E_{ext}\right|^2\right)$.

Since the average of the fluctuations in the coordinate system $\hat{x}_d\hat{y}_d\hat{z}_d$ is zero, the correlation of $\mathtt{n}_{\hat{x}}$ between two different points is $\langle \mathtt{n}_{\hat{x}_d}(\bar{r}_{d,1})\mathtt{n}_{\hat{x}_d}(\bar{r}_{d,2})\rangle$. Developing in series the components

$$\mathtt{n}_{\hat{x}_d}(\bar{r}_d) = \Omega^{-1} \sum_{q} \tilde{\mathtt{n}}_{\hat{x}_d}\left(\bar{q}\right) e^{-i\bar{q}\cdot\bar{r}_d}, \tag{3.52}$$

it is possible to write

$$\begin{aligned}\langle \mathtt{n}_{\hat{x}_d}(\bar{r}_{d,1})\mathtt{n}_{\hat{x}_d}(\bar{r}_{d,2})\rangle &= \frac{1}{\Omega^2}\left\langle \left(\sum_{q} \tilde{\mathtt{n}}_{\hat{x}_d}(\bar{q})\, e^{-i\bar{q}\cdot\bar{r}_{d,1}}\right)\left(\sum_{q'} \tilde{\mathtt{n}}_{\hat{x}_d}(\bar{q}')\, e^{-i\bar{q}'\cdot\bar{r}_{d,2}}\right)^*\right\rangle \\ &= \frac{1}{\Omega^2}\sum_{qq'}\left\langle \tilde{\mathtt{n}}_{\hat{x}_d}(\bar{q})\tilde{\mathtt{n}}^*_{\hat{x}_d}(\bar{q}')\right\rangle\, e^{i(\bar{q}'\cdot\bar{r}_{d,2} - \bar{q}\cdot\bar{r}_{d,1})}.\end{aligned} \tag{3.53}$$

Since the Fourier coefficient $\tilde{\mathtt{n}}_{\hat{x}_d}(\bar{q})$ and $\tilde{\mathtt{n}}_{\hat{x}_d}(\bar{q}')$ are orthogonal if $q \neq q'$, the last equation takes the form

$$\langle \mathtt{n}_{\hat{x}_d}\left(\bar{r}_{d,1}\right)\mathtt{n}_{\hat{x}_d}\left(\bar{r}_{d,2}\right)\rangle = \frac{1}{\Omega^2}\sum_{q}\left\langle \left|\tilde{\mathtt{n}}_{\hat{x}_d}(\bar{q})\right|^2\right\rangle\, e^{(i\bar{q}\cdot\bar{R})}, \tag{3.54}$$

where $\bar{R} = \bar{r}_{d,2} - \bar{r}_{d,1}$ is the distance between the two points. Since the norm of the fluctuation vector is conserved in the change of variables, *i.e.* $\left|\tilde{\mathtt{n}}_{\hat{x}_d}(\bar{q})\right|^2 + \left|\tilde{\mathtt{n}}_{\hat{y}_d}(\bar{q})\right|^2 = \left|\tilde{\mathtt{n}}_1(\bar{q})\right|^2 + \left|\tilde{\mathtt{n}}_2(\bar{q})\right|^2$, and the average fluctuations on the two axis are the same, *i.e.* $\left\langle \left|\tilde{\mathtt{n}}_{\hat{x}_d}(\bar{q})\right|^2\right\rangle = \left\langle \left|\tilde{\mathtt{n}}_{\hat{y}_d}(\bar{q})\right|^2\right\rangle$, it is possible to write

$$\langle \mathtt{n}_{\hat{x}_d}(\bar{r}_{d,1})\mathtt{n}_{\hat{x}_d}(\bar{r}_{d,2})\rangle = \frac{1}{2\Omega^2}\sum_{q}\left\langle \left|\tilde{\mathtt{n}}_1(\bar{q})\right|^2 + \left|\tilde{\mathtt{n}}_2(\bar{q})\right|^2\right\rangle\, e^{i\bar{q}\cdot\bar{R}} \tag{3.55}$$

and then, with Eq. (3.51)

$$\langle \mathtt{n}_{\hat{x}_d}(\bar{r}_{d,1})\mathtt{n}_{\hat{x}_d}(\bar{r}_{d,2})\rangle = \frac{1}{\Omega}\sum_{q}\frac{k_B T}{K\left(q^2 + \xi^{-2}\right)}\, e^{i\bar{q}\cdot\bar{R}}. \tag{3.56}$$

Going from the sum to the integral ($\sum_q \to \int \frac{\Omega}{(2\pi)^2} d\bar{q}$) we have finally

$$\langle \mathtt{n}_{\hat{x}_d}(\bar{r}_{d,1})\mathtt{n}_{\hat{x}_d}(\bar{r}_{d,2})\rangle = \frac{k_B T}{K}\frac{1}{(2\pi)^3}\int \frac{1}{q^2 + \xi^{-2}}\, e^{i\bar{q}\cdot\bar{R}} d\bar{q}. \tag{3.57}$$

The lower and the upper bounds of the integral are respectively zero and a certain $q_{max} = 2\pi/a$, where a is the smallest size below which the continuum theory is no longer valid.

Equation (3.57) describes the covariance matrix that characterizes the nematic director fluctuations. The off-diagonal elements of the matrix are obtained from Eq. (3.57) in the limit $R \gg a$

$$\langle \mathtt{n}_{\hat{x}_d}(\bar{r}_{d,1})\mathtt{n}_{\hat{x}}(\bar{r}_{d,2})\rangle = \frac{k_B T}{4\pi K R}\, e^{-R/\xi}. \tag{3.58}$$

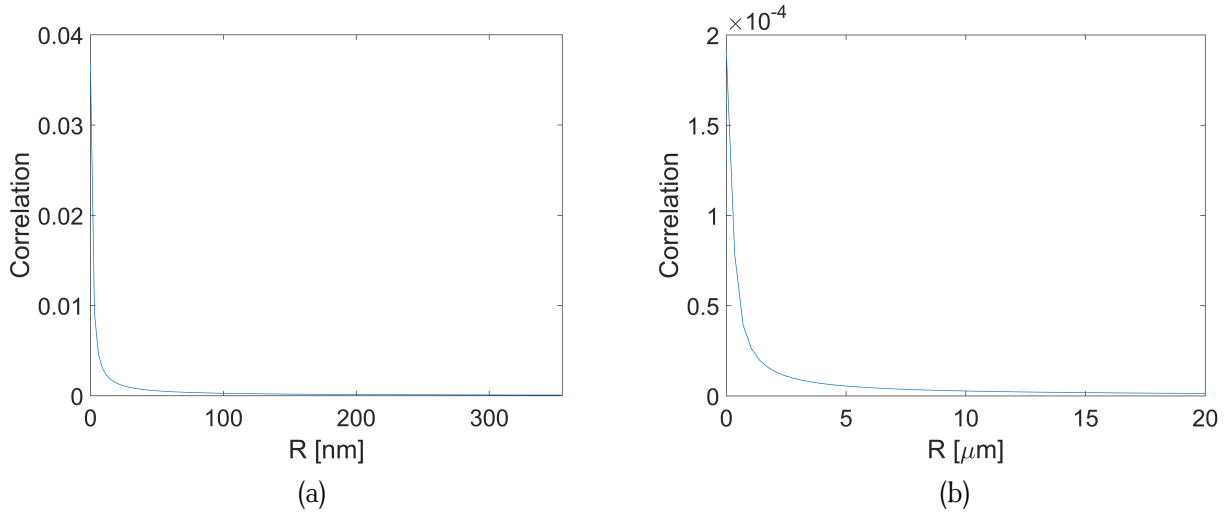

FIGURE 3.7: (a) Evolution of the correlation over a grid size, according to Eq. (3.58) and Eq. (3.59); (b) evolution of the correlation over a scale much larger than the grid size and in the case where the diagonal is defined according to Eq. (3.63).

The correlation expressed by Eq. (3.58) depends, through the coefficient ξ, on the applied electric field and the distance R between the two considered points. In the absence of the electric field, the correlation is considered as long range since it is slowly decreasing ($\propto 1/R$). Indeed, in that case, it is not possible to define a characteristic distance above which the fluctuations decrease fast enough to be considered negligible [28, Ch.3]. The effect of an electric field is to exponentially dump the fluctuations, which then take place over the coherence length ξ.

The diagonal of the correlation matrix (the variance) cannot be calculated with Eq. (3.58), since the coefficient diverges for $R \to 0$. A method to estimate the variance is to truncate the integral at q_{max}, obtaining [28, p.148]

$$\left\langle \mathtt{n}^2_{\hat{x}_d} \right\rangle \simeq \frac{k_B T}{2\pi^2 K} \left(q_{max} - \frac{\pi}{2\xi} \right) \tag{3.59}$$

As $q_{max} = 2\pi/a$, the proper choice of a is crucial in order to evaluate the amplitude of the fluctuations and it is usually taken to be of the order of magnitude of the intermolecular [28, 113] or intermicellar [112] distance (a few nm), values below which the continuum theory of LCs is no longer valid.

3.3.2 Director correlation on the discretization grid

In our case the correlation function is not a continuous function, but the values of R in Eq. (3.57) are limited to the points on the discretization grid. Since this grid ($\triangle x = \triangle y = 355$ nm, $\triangle z = 900$ nm) is much larger than the intermolecular distance (a few nm) due to computing memory limitations, the correlation is greatly decreased over the grid length scales $\triangle x$, $\triangle y$ and $\triangle z$. In Fig. 3.7a it is possible to see that the correlation passes from a value of $\sim 4 \cdot 10^{-2}$ to $\sim 7 \cdot 10^{-5}$ over $\triangle x$ =355 nm.

As explained above, we should take the maximum value, given by Eq. (3.59), as the diagonal element and therefore the representative value over the grid length scale. Such an almost-diagonal matrix would then describe a largely uncorrelated system, and we would lose the benefit of our approach, as will be shown later.

This approximation overestimates the value of the diagonal, for this reason we take as diagonal elements the average E of the correlation function [Eq. (3.57)] over one grid unit size, *i.e.* along $\hat{x}$:

$$\mathrm{E}\left[\langle \mathtt{n}_{\hat{x}_d}(\bar{r}_{d,1}) \mathtt{n}_{\hat{x}_d}(\bar{r}_{d,2}) \rangle\right] = \frac{k_B T}{K\,(2\pi)^3} \frac{1}{\triangle x} \int_0^{\triangle x} \int_0^{q_{max}} \frac{1}{(q^2 + \xi^{-2})} e^{i\bar{q}\cdot\bar{R}} d\bar{q}\, dR, \tag{3.60}$$

where $\bar{r}_{d,2} - \bar{r}_{d,1} = R < \triangle x$. Since in our case the limit of the continuum theory is given by the grid size, it is

possible to take $q_{max} = 2\pi/\triangle x$

$$\begin{aligned}\mathrm{E}\left[\langle \mathtt{n}_{\hat{x}_d}(\bar{r}_{d,1})\,\mathtt{n}_{\hat{x}_d}(\bar{r}_{d,2})\rangle\right] &= \frac{k_B T}{2K\pi^2}\frac{1}{\triangle x}\int_0^{\triangle x}\int_0^{2\pi/\triangle x}\frac{q^2}{(q^2+\xi^{-2})}\frac{\sin(qR)}{qR}dq\,dR \\ &= \frac{k_B T}{2K\pi^2}\frac{1}{\triangle x}\int_0^{2\pi/\triangle x}\frac{q^2}{(q^2+\xi^{-2})}\int_0^{\triangle x}\frac{\sin(qR)}{qR}dR\,dq. \end{aligned} \tag{3.61}$$

Introducing the definition of the sine integral

$$\mathrm{Si}(x) = \int_0^x \frac{\sin t}{t}dt, \tag{3.62}$$

Eq. (3.61) takes the form

$$\mathrm{E}\left[\langle \mathtt{n}_{\hat{x}_d}(\bar{r}_{d,1})\mathtt{n}_{\hat{x}_d}(\bar{r}_{d,2})\rangle\right] = \frac{k_B T}{2K\pi^2}\frac{1}{\triangle x}\int_0^{2\pi/\triangle x}\frac{q}{(q^2+\xi^{-2})}\mathrm{Si}(q\triangle x)\;dq, \tag{3.63}$$

which constitutes the value on the diagonal elements (the variance) of the covariance matrix

$$\mathrm{E}\left[\langle \mathtt{n}_{\hat{x}_d}(\bar{r}_{d,1})\mathtt{n}_{\hat{x}_d}(\bar{r}_2)\rangle\right] = \left\langle \mathtt{n}^2{}_{\hat{x}_d}(\bar{r}_d)\right\rangle. \tag{3.64}$$

The evolution of the correlation, defined by Eq. (3.58) and Eq. (3.63), is reported in Fig. 3.7b. It is possible to see that now the values of the correlation at the peak and at several micrometers from it are only one order of magnitude different, which is different from the case of Fig. 3.7a. The function *average.m* (Alg. B.8) calculates this integral, while the function *correlation_plane_xy.m* (Alg. B.8) writes the correlation matrix.

3.3.3 Generate a correlated noise

Using Eq. (3.63) and Eq. (3.58) respectively for the diagonal and off-diagonal elements, it is possible to generate the correlation matrix $\bar{\bar{C}}$. An uncorrelated random variable $\bar{\bar{N}}$ normally distributed is generated and the correlation is forced through the relation [123]

$$\bar{\bar{N}}_{corr} = \bar{\bar{U}}\bar{\bar{N}} \tag{3.65}$$

where $\bar{\bar{N}}_{corr}$ is the correlated noise and $\bar{\bar{U}}$ is the upper triangular form of the Cholesky decomposition of the correlation matrix ($\bar{\bar{C}} = \bar{\bar{U}}\bar{\bar{U}}^{\dagger}$, with $\bar{\bar{U}}^{\dagger}$ the conjugated transpose).

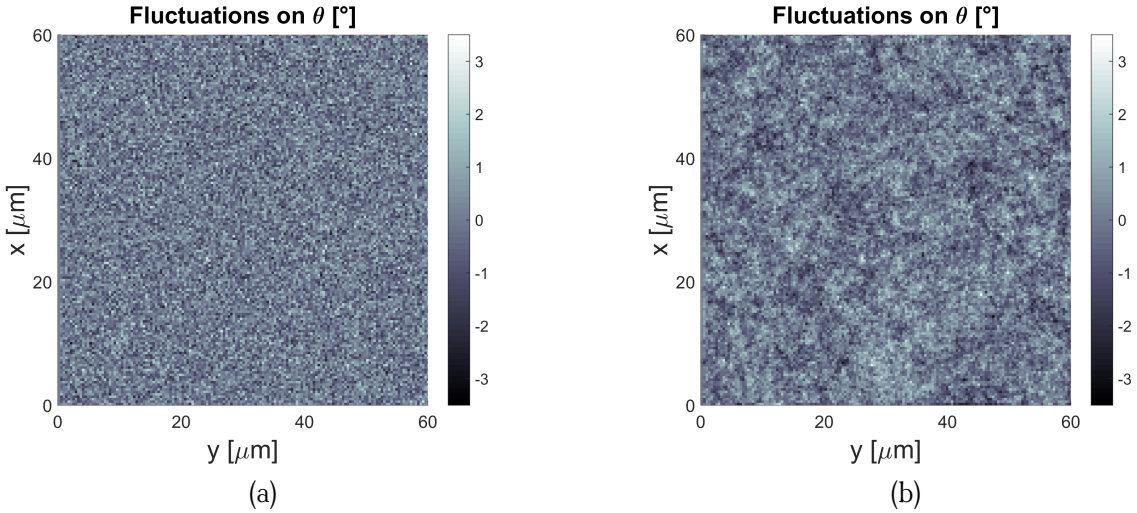

FIGURE 3.8: (a) Uncorrelated normally distributed random noise on θ; (b) Correlated noise on θ obtained by forcing the correlation $\bar{\bar{C}}$ on the noise reported in (a) with Eq. (3.65).

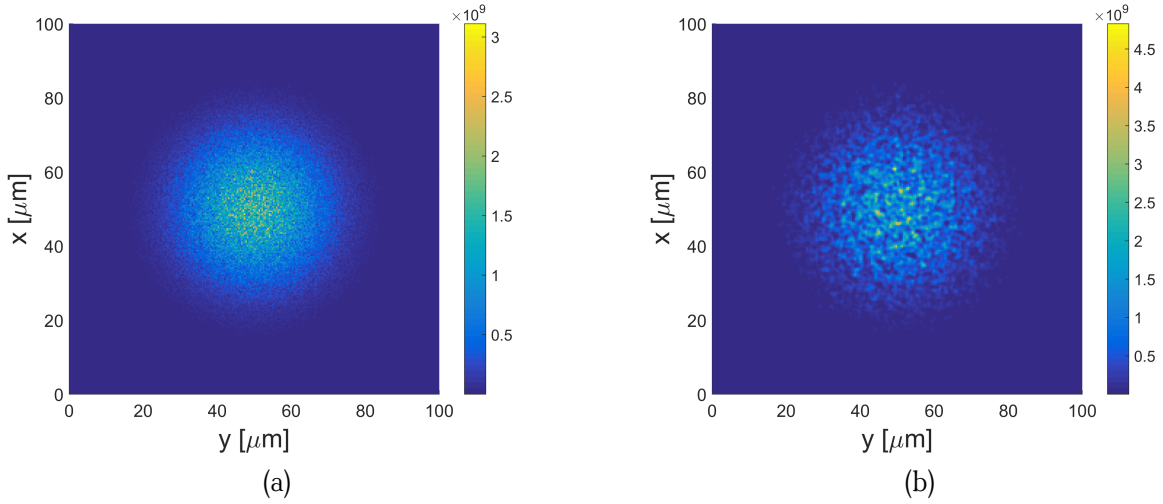

FIGURE 3.9: Profile of $|\mathcal{E}|^2$ of the transmitted visible light (532 nm) through a 50 μm thick cell for the case of uncorrelated (a) and correlated (b) thermal noise. The beam power is 3.7 mW and its radius is w_0=25μm.

The matrix $\bar{\bar{N}}_{corr}$ therefore describes the spatial distribution of $\mathtt{n}_{\hat{x}_d}$, characterized by a correlation $\bar{\bar{C}}$. Since the variable that describes the LC is θ, we choose one of the two fluctuation components, $\mathtt{n}_{\hat{x}_d}$, to lie in the plane $\hat{x}\hat{z}$. In this way, the angular variation $d\theta$ can easily be calculated with

$$d\theta = \arctan(\mathtt{n}_{\hat{x}_d}). \tag{3.66}$$

In order to show the effect of the correlation on the fluctuation distribution, in Fig. 3.8 we report the uncorrelated (a) and the correlated (b) noise generated in the $\hat{x}\hat{y}$ plane. The uncorrelated noise $\bar{\bar{N}}$ is generated with the formula

$$\bar{\bar{N}}_{uncorr} = \sqrt{\langle \mathtt{n}^2_{\hat{x}_d}(\bar{r}_d)\rangle}\,\bar{\bar{N}}, \tag{3.67}$$

where only the variance is forced on the noise. This is done in order to have the same amplitude oscillations for both $\bar{\bar{N}}_{corr}$ and $\bar{\bar{N}}_{uncorr}$ and to be able to evaluate the effect on light propagation due only to the grain size of the director fluctuation.

The uncorrelated noise presents a uniform random distribution, while in the correlated case the slowly varying oscillations of the angle θ occurring over tens of μm can clearly be seen. This result is in agreement with the experimental observation of the director fluctuations reported in the literature [118].

Due to the large volume covered by the soliton propagation and the finite availability of computational memory, it is not possible to write the complete 3-dimensional correlation matrix, as it scales with the square of the number of points. Given the geometry of the system (BPM and one-constant approximation), we generate the correlated noise in planes $\hat{x}\hat{y}$ orthogonal to the soliton propagation.

The $\hat{x}\hat{y}$-correlated noise is not generated at every step, since it would mean a completely uncorrelated noise along $\hat{z}$, but every 10 μm, which is the same order of magnitude as the grains in the correlated noise pattern. The noise is then linearly interpolated along $\hat{z}$, in order to have a noise profile slowly varying along $\hat{z}$, with an appropriate level of correlation in this direction. Finally, since we do not apply a homogeneous electric field to the cell and since the peak of the optical electric field is too small to induce a significant quenching of the director fluctuations [124], in the simulations we consider E_{ext} null and hence ξ infinite.

The so-generated noise $d\theta$ is added to the angle θ at every propagation step after the optimization of Eq. (3.25).

3.4 Light propagation in LCs

In this section the results of the simulations are presented, for both linear and nonlinear regimes. The comparison between experimental and numerical results is presented for the case of the nematicon propagation.

3.4.1 Linear propagation and speckle formation

The first step is to analyze the light propagation for powers low enough to avoid any nonlinear effects. We thus expect to reproduce by numerical simulations the observed speckle pattern produced when a laser-beam propagates through a liquid crystal device. In order to compare the results with the literature [117, 118], we simulate the propagation of visible light (532 nm) through a planar aligned 50 µm cell filled with E7.

The effect of the spatial correlations is highlighted in Fig. 3.9 by comparing the propagation through LC with uncorrelated and correlated noise. For the uncorrelated case, the noise is randomly generated at every step along the propagation. The resulting output is an almost unperturbed beam profile (Fig. 3.9a). Since the noise grain size equals the simulation grid, which is smaller than the wavelength, the light cannot be locally focused. It therefore follows a homogeneous output profile without any speckle pattern. Also, the noise induced diffraction is averaged along $\hat{z}$: since the director fluctuation is generated at every simulation step, this effectively removes any correlated-like pattern along the propagation.

For the case of noise which is correlated (Fig. 3.9b), the smooth variation of the director distribution (and therefore of the refractive index) causes a local (random) focusing and defocusing of the light as it propagates. The characteristic speckle pattern is therefore generated.

The spatial correlation of the LC director is therefore essential to account for the characteristic speckle generation in LCs.

3.4.2 Nematicon propagation, numerical and experimental

In this section, the experimental measurements and the numerical results will be presented for the nonlinear propagation regime. We will compare the nematicon fluctuations and the propagation losses obtained in the two cases.

Experimental measurement

The sample geometry is the one used for the numerical simulations described in Sect. 3.2. A standard LC cell is employed (thickness defined by 75 µm spacers, planar alignment, rubbing at $\theta_0 = 45°$ with respect to the entrance side of the cell). It is filled with a solution of 1 wt.% of pyrromethene 597 dye (PM597, Sigma-Aldrich) in E7, since this same cell will be used in Ch. 6 for amplified spontaneous emission together with soliton generation.

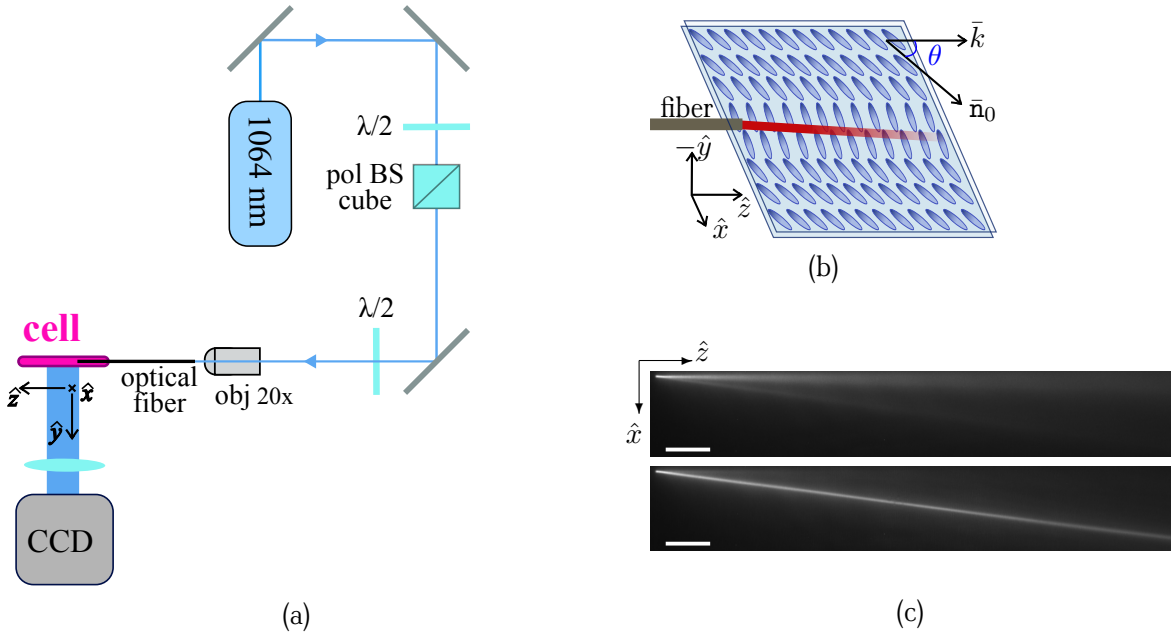

FIGURE 3.10: (a) Scheme of the setup for the nematicon injection and (b) schematic of the nematicon injection into the LC cell through an optical fiber; (c) propagation of the IR beam (1.7 mW) for a polarization parallel to the $\hat{y}$ axis (above) or to the $\hat{x}$ axis (below), for the same exposure time; the scale bar is 500 µm.

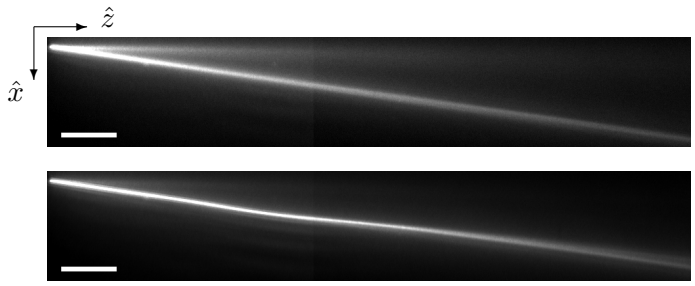

(a)

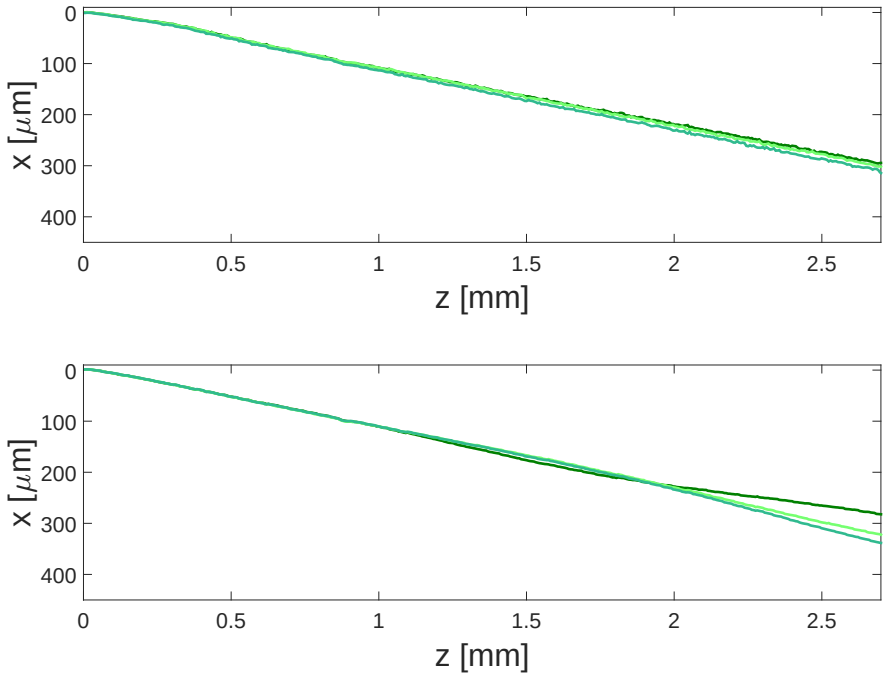

(b)

FIGURE 3.11: Experimental measurement of the nematicon profile. (a) Example of two nematicon profiles observed for a beam of 1.1 mW (above) and 3.7 mW (below) at 23 °C; the scale bar is 500 µm; (b) three frames of the experimental soliton trajectory for an input power of 1.1 mW (top) and 3.7 mW (bottom).

Note that for this study the presence of the dye is not relevant since, as it will be shown in the next Chapter, the dye does not absorb the CW 1064 nm infrared light of the laser used to excite the nematicons. Through a microscope objective (f=8.0 mm, numerical aperture 0.5), the IR beam is injected into an optical fiber slid between the two glasses (Fig. 3.10b). The fiber, whose characteristics are reported in Sect. 2.4.2, supports a mode with a radius (at $1/e^2$) of 3.7 µm at 1064 nm.

If the beam polarization is along $\hat{y}$, the torque of the optical electric field on the LC director is minimum. The director does not reorient, and the beam diffracts. If the input beam is polarized along $\hat{x}$, the optical torque is maximized, and the nematicon is created [19, 22, 25]. This behaviour is reported in Fig. 3.10c.

In Fig. 3.11a two intensity profiles acquired for two different powers are shown. At low power, the trajectory of the soliton is stable and straight. A weak ordinary beam is visible, probably due to the perturbation of the LC due to the optical fiber and the consequent depolarization of the light [125]. The soliton propagates over a few millimeters with almost no diffraction. However, by increasing the power, the nematicon starts to deviate from the straight path and starts to oscillate in space.

In order to quantify these oscillations, the trajectories at different times are compared. The soliton trajectory

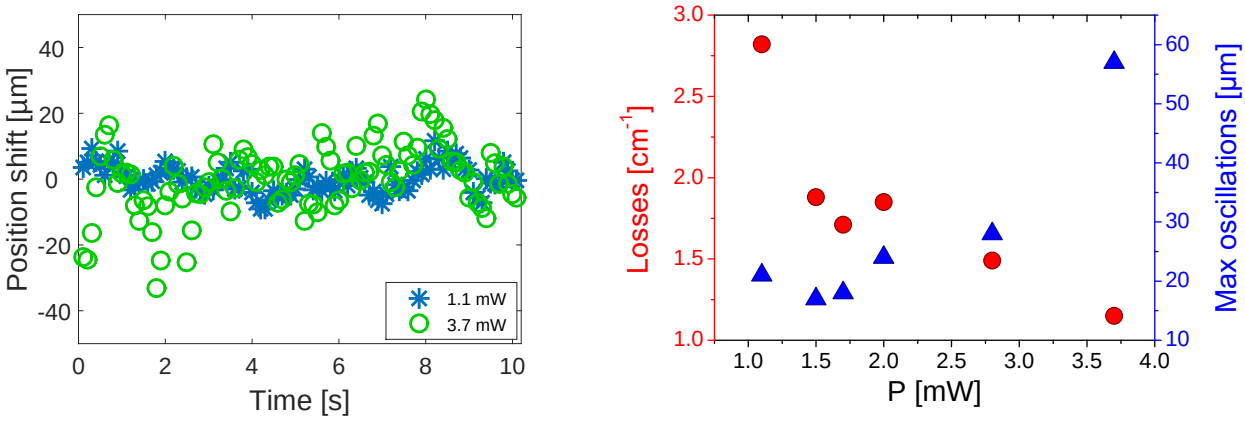

(a) (b)

FIGURE 3.12: (a) Position of the beam after 2.7 mm of propagation as a function of time for a soliton of 1.1 mW (stars) and of 3.7 mW (empty circles); (b) oscillation amplitudes (blue triangles, right axis) and losses (red circles, left axis) as a function of the power.

along the propagation distance is estimated by interpolating, at a different $\hat{z}$ position, the measured intensity profile along $\hat{x}$ with a Gaussian function. Three frames of the soliton propagation paths for two powers are shown in Fig. 3.11b. It is possible to see that the oscillation amplitude increases with the soliton power.

Since the LC molecules fluctuate due to thermal noise, the refractive index profile and therefore the soliton path vary in time. Plotting the soliton position as a function of time after 2.7 mm of propagation for 2 different powers (Fig. 3.12a) shows that the soliton oscillates around a mean value and that the largest oscillations appear at the highest power. In Fig. 3.12b we plot the amplitude of the oscillations as a function of the power. The oscillations increase almost by a factor 3 from 1.1 mW to 3.7 mW. It has been demonstrated that the intrinsic breathing behavior of nematicons, where the beam becomes overfocused periodically, has an oscillation period that decreases by increasing the nematicon power [30, 126]. Indeed, when the soliton diameter becomes smaller than the director fluctuation grain size, the nematicon, instead of being diffracted and destroyed, is rather refracted [127] and hence its propagation path deviates.

From the gaussian fit to the measured intensity profile along $\hat{x}$ it is also possible to compute the integral of the intensity profile, in order to obtain the evolution of the energy as a function of $\hat{z}$. The exponential decay is fitted with a function $\propto \exp(-\alpha z)$, where α represents the loss coefficient. The evolution of α as a function of the power is also shown in Fig. 3.12b. Increasing the power, and therefore the focusing of the soliton, we observe a decrease of the loss coefficient as the photons are less scattered. This is consistent with the fact that the soliton is refracted (leading to propagation path deviation), rather than scattered, by the refractive index perturbations.

Numerical results

We performed 50 simulations of the propagation of solitons for input powers ranging from 1.1 mW to 3.7 mW. The number of simulations is high enough to obtain a reliable statistics, without requiring a too large computational time (every simulation takes around one hour). For every simulation, a different correlated director noise pattern is generated every 10 μm, as described in Sect. 3.3. In Fig. 3.13a examples of soliton trajectories at the two different powers are reported. Even if abrupt changes in the path direction are not present, the spatial oscillations obtained in the numerical simulations are in good agreement with the experimental results.

In order to evaluate this behavior, the nematicon position after 2.7 mm of propagation is shown in Fig. 3.13b for 1.1 mW and 3.7 mW. Since our model does not describe the temporal behavior of the system, every simulation is independent of previous ones. For this reason, when the oscillation amplitudes at different times (referred to as frames here) are presented, we do not observe a continuous evolution as in the experiments. However, comparing the maximum deviation of the soliton from the straight path, it is possible to observe larger oscillations for increasing powers, which is consistent with the experimental observations.

Importantly, comparing models of the soliton oscillations at high power for cases where the modeled noise

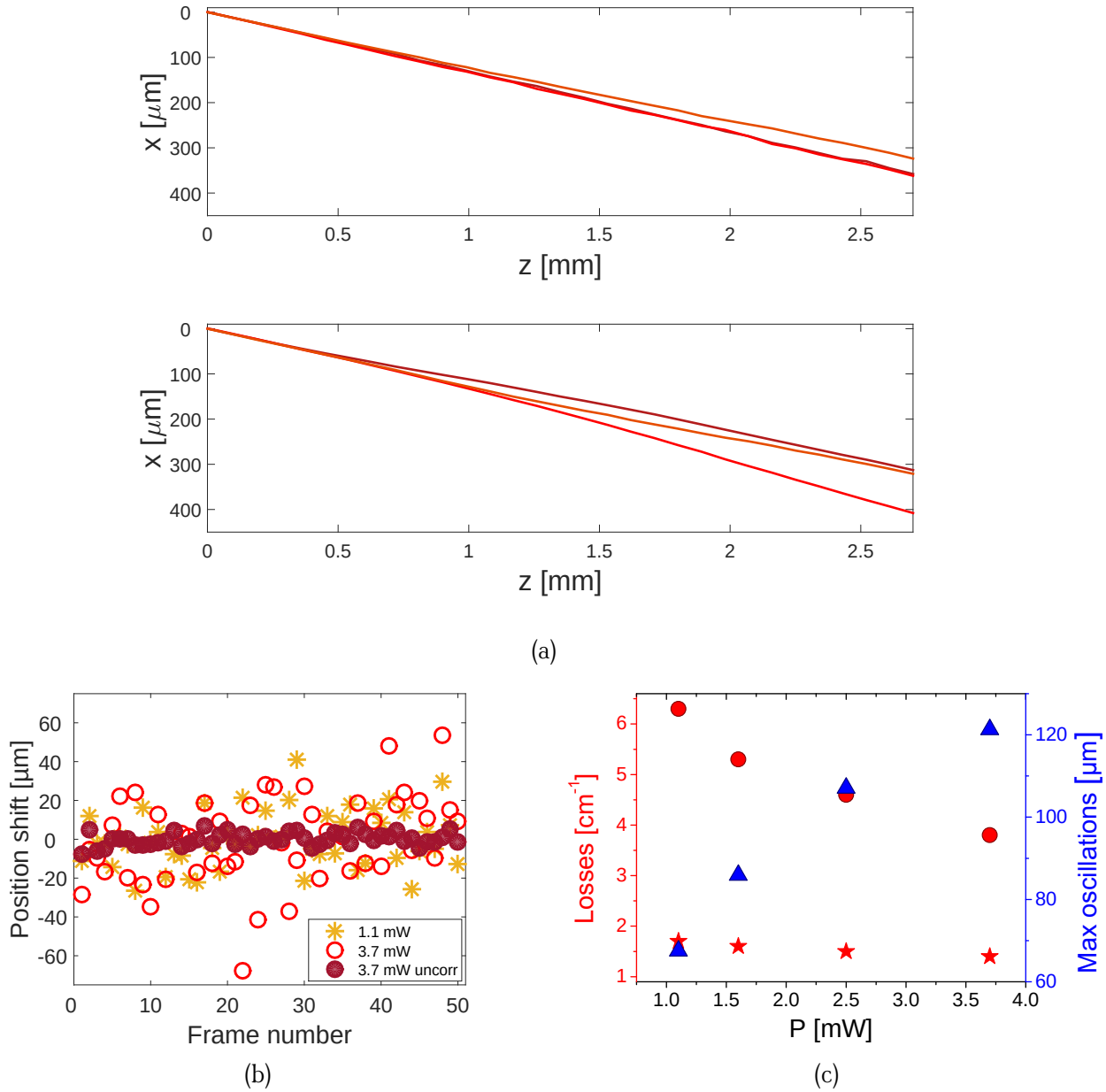

FIGURE 3.13: Numerical simulations of the nematicon profile. (a) Three of the numerical simulations of the soliton trajectory with a soliton power of 1.1 mW (top) and 3.7 mW (bottom); (b) position of the beam after 2.7 mm of propagation for 50 generations of the noise for a soliton of 1.1 mW (stars), 3.7 mW (empty circles) and 3.7 mW for the case of uncorrelated noise (full circles); (c) oscillation amplitudes (blue triangles, right axis) and losses (red circles, right axis) as a function of the power. The losses are plotted for the case of correlated (circles) and uncorrelated (stars) noise.

is correlated and uncorrelated (Fig. 3.13b), we observe a drop in the nematicon oscillation amplitudes from ∼120 µm to ∼15 µm in the latter case. Without the spatial correlation of the director fluctuations, the length-scale of the refractive index variations is much smaller than the soliton diameter. In practice, the length-scale of these variations is then defined by the discretization grid used for the simulations. In that limit, the soliton only slightly deviates during propagation even at high powers. The spatial correlation of the director fluctuations is therefore an important phenomenon to take into consideration for the proper modeling of the spatial instabilities of soliton propagation in LCs.

The correlated noise in the numerical modeling causes a power-dependent behavior of the oscillation amplitudes (Fig. 3.13c, blue triangles) that is in good agreement with the experimentally observed behavior. The difference between the experimental results and the simulations with correlated noise can be explained by the fact that in practice, when the fiber is slid into the LC cell, it causes a perturbation in the LC director profile that

is not taken into account in our model. This perturbation extends over a distance that is a multiple times the thickness of the cell [125] and therefore causes a delay in the formation of the soliton equilibrium profile. For this reason, in the experiment, the nematicon does not oscillate from the beginning of its propagation (Fig. 3.11b). The oscillation amplitudes are therefore measured at a distance that is effectively shorter than 2.7 mm. The amplitudes experimentally measured are therefore smaller than the ones obtained from the simulations, where the soliton starts to oscillate close to the injection. Also, in our one-constant approximation, the correlation is assumed to be isotropic. However, along the $\hat{z}$ axis, a dominant bend-splay deformation takes place, which may be associated with a larger elastic constant (K_3). Since the correlation is inversely proportional to the elastic constant K, we are overestimating the correlation and therefore the scattering as the nematicon propagates.

In Fig. 3.13c (red circles), the loss coefficient α is showed as a function of the input power for the case of correlated noise. The values and the power-dependent behavior of α, ranging from 6.3 cm^{-1} to 3.8 cm^{-1} over our range of powers, are in good agreement with the experiments. The factor of 2 difference may be due to the overestimation of the scattering in the one-constant approximation. The same order of magnitude for the loss coefficient can be found in the literature [20, 109], even if no dependence on the nematicon power is reported.

On the same graph, as a comparison, the losses obtained for the case of uncorrelated noise are also shown, for which almost no dependence on the nematicon power is observed. The losses are substantially less ($\sim$1.5 cm^{-1}) when the director fluctuation noise is uncorrelated, compared to the case of correlated noise. Indeed, when the noise is uncorrelated, the size of the noise grains is defined by the discretization grid, which is much smaller than the nematicon diameter at all powers. The nematicon is therefore not scattered or deviated by the director fluctuations, since the soliton does not experience the effects of speckle formation (as observed in Fig. 3.9). There is consequently no loss of energy in the central part of the beam, independently on the soliton power and its focusing. This is not what happens in the case of correlated noise, where the nematicon diameter at high powers becomes comparable or smaller than the noise grain size. The soliton is refracted and therefore deviated, rather than scattered by the refractive index perturbations. This shows once again how taking into account the correlation in director fluctuations improves the description of soliton propagation in liquid crystalline systems.

3.5 Conclusions

In this Chapter, we have demonstrated a new method to properly include the thermal fluctuations of the director in LCs when modelling nematicon propagation, starting from the common parameters of LCs and without the need for an *ad hoc* loss term in the propagation equation. In such systems, the long range interaction among the molecules must be taken into account when generating the thermal noise, through the spatial correlation of the director fluctuations. The computed correlated noise allows us to explain the experimentally observed spatial fluctuations of nematicons at high powers and the propagation losses experienced by the nematicons. Further improvements could be added to our model, for example through the introduction of full modeling of the correlation along the $\hat{z}$ direction, the temporal evolution of the director orientation, the power dependence of the loss coefficient or the introduction of the three elastic constants. However, the oscillation amplitudes obtained with our model are in good agreement with the values experimentally measured. We believe that this method could also help the modeling of both linear phenomena involving speckle generation and more complex nonlinear behavior in LCs, such as modulation instabilities or filamentation. In Ch. 6, the power dependent soliton fluctuations, will be particularly important to understand the optimization of the soliton collection of light generated within the same dye-doped LC cell.

Optical gain in liquid crystals

Chapter 4

In this Chapter, we will focus on the optical gain that dye-doped and polymer-doped LCs can provide. This gain will be used in the next Chapters for amplification and lasing or for the interaction with the soliton propagation.

Part of this work, the one related to the polymer-doped LC, was performed as a continuation of my Master thesis at the Politecnico di Milano [128], conducted in collaboration with the Université libre de Bruxelles and the Ghent University. Some of the figures and the descriptions used for the theoretical introduction have been published in that Master thesis [128], but all the results reported here are original. The results presented in this Chapter have been published in *Chemical Communications* [129], *Journal of Polymer Science Part B* [130] and *Optics Letters* [131].

There are different ways to obtain optical gain from LC-based devices. It is possible, for example, to synthesize photoluminescent molecules that also present a mesophase [132–135]. Another way is to dope a standard non-emitting LC with materials that provide optical gain. These materials can have different origins, ranging from dyes [57, 136–139] to quantum dots [140, 141]. Different geometries can be adopted, for example the gain medium can be uniformly dispersed [10, 142–144] or separated in to layers [145–147] within the device.

In this work, we will focus on the case where the photoemitting molecules (dyes or polymers) are dispersed in the LC. One of the advantages of this configuration is that, in most cases, it is quite easy to dissolve small quantities of organic molecules in the LC. The cell can then be filled by capillarity with the doped mixture in the same way as presented in Ch. 2. Elongated molecules, like dyes or polymers, that are dispersed in nematic LCs show the tendency to align themselves along the director [148, 149]. When such a mixture is introduced in a cell, the dye/polymer assumes a well defined macroscopic orientation together withe the LC. The transition dipole of the fluorescent molecules is also well aligned in the samples, which therefore exhibits polarized absorption and photoluminescence (PL) spectra [136, 150]. Also, since the LC can be reoriented by an external electric field and the guest organic molecules are reoriented with it, it is possible to switch the polarization of the emitted light [151, 152]. These remarkable features are particularly interesting for applications such as displays [3] or to increase the laser pump efficiency [153]. Usually, such well-aligned samples are obtained in solid state samples through mechanical, thermal or solvent treatment [154–156]. On the other hand, in the case of LC-dispersed organic molecules, the alignment of the dye or the polymer is spontaneously obtained thanks to the LC self-alignment.

What we are interested in is not only the photoluminescence, but the optical gain provided by these molecules. The optical gain is the capacity of the medium to amplify the light that is traversing it. This is the result of a positive balance between the amplification, provided by the polymer or the dye, and the propagation losses mainly due to scattering and absorption. The main technique employed to study the temporal evolution of the optical gain is the pump-probe spectroscopy. This technique spectrally and temporally characterizes the optically-induced excited states of the system. It is possible to study the formation and evolution of the excited states, and how they provide gain or losses for the light traversing the material. The pump-probe technique is therefore used for the photophysical characterization of the medium.

The first two Sections of this Chapter will be devoted to the introduction of both the physics of organic molecules and the pump-probe spectroscopy. This technique will then be used in the second part of the Chapter to characterize two different systems, the dye- and the polymer-doped LC.

In Sect. 4.3, the properties of a dye-dispersed LC will be analyzed. The dye is easily dissolved in the LC matrix. Also, the slightly elongated dye molecules are aligned by the nematic liquid crystals, giving rise

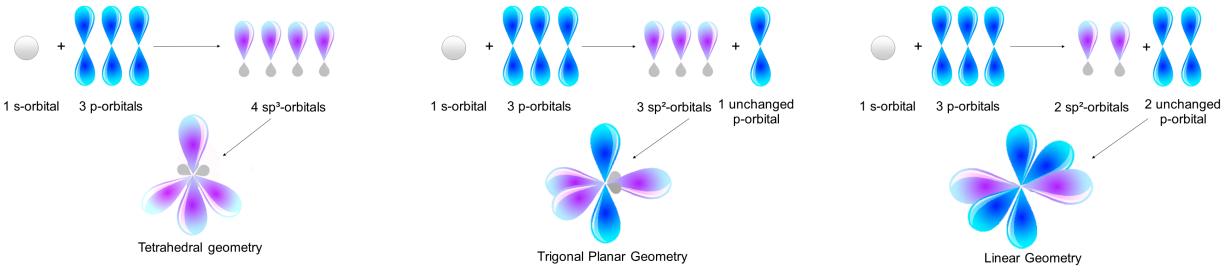

(a) sp^3 (b) $\mathrm{sp}^2 + \mathrm{p}_z$ (c) $\mathrm{sp} + \mathrm{p}_z + \mathrm{p}_y$

FIGURE 4.1: Possible hybridizations of the Carbon atom.

to polarized emission [136, 157]. Indeed, the spectral properties of an organic molecule can be modified by the solvent that is used to disperse it [158, Ch.7]. In particular, the anisotropy and the alignment provided by the LC induces the polarization of the dye spectrum [136]. The optical gain provided for such a system has been exploited for different purposes, such as pulse amplification [159, 160], lasing [8, 10, 11, 58] or amplified spontaneous emission [161, 162]. Surprisingly, no pump-probe spectroscopy had been conducted on this kind of system before our work. In Sect. 4.3 we will present the polarized pump-probe spectra of a particular dye, the PM597, mixed with the E7 LC. The dye molecules are not randomly oriented as in a liquid solution, but they are well aligned by the LC matrix. It is therefore possible to separate the contribution of the gain parallel and orthogonal to the long axis of the dye. A particular kind of emission, the amplified spontaneous emission, will then be studied in dye-doped LC.

In Sect. 4.4 the photophysical properties of a polymer, the polyfluorene, dispersed in a LC matrix will be discussed. Indeed, longer molecules are better aligned by LCs than shorter ones [148] and they present the advantage to increase the order of a LC molecular distribution [153]. We will also study the complex morphology induced by the polymer in the LC with the aid of a particular kind of confocal microscopy. The combined study of the morphology and the photophysics of the sample provides a useful insight in to the optical properties of the sample.

4.1 Organic semiconductors

In this Section we give a general introduction about semiconducting organic materials. For a detailed dissertation on the subject we refer to the literature [163, 164].

Organic molecules are carbon-based structures. The electronic configuration of the ground state of the Carbon atom is $1s^2 2s^2 2p^2$. The four electrons in the external shell contribute to chemical bonds, while the two electrons in the $1s$ shell have an ionization potential that is too high to interact with other atoms. We will then focus on the outer shell, responsible for the chemical interactions and the optical excitation.

It is possible to represent the three different hybridizations sp^3, sp^2 and sp as a combination of the s and p orbitals (Fig. 4.1) [165, Ch.10.2].

If three p orbitals and one s orbital combine, they form four identical orbitals sp^3 in which the electron cloud points at the vertexes of a tetrahedron (4.1a), where the nearest atoms are located. The overlap of the orbitals responsible for the chemical bonding is localized between the two atoms and it has an even symmetry with respect to the plane of the molecule (σ bond). In this case, the carbon atom forms four single covalent bonds with four different atoms, as for example ethane ($\mathrm{CH}_3 - \mathrm{CH}_3$).

If two p and one s orbitals combine, they give rise to three sp^2 lying in the plane of the molecules. The remaining p orbital (for convention the p_z) stays orthogonal to that plane. The sp^2 orbitals give rise to σ bonds. The p_z orbitals, when overlapping, generate chemical bonds with an odd symmetry with respect to the plane and a node in that plane (π bonds). In order to have the maximum overlap, the molecule has to be planar and the p_z orbitals have to point in the same direction.

In the case of sp hybridization, the p and the s orbitals combine in two sp with σ symmetry. Together with the remaining p orbitals, they form a triple bond between the two atoms.

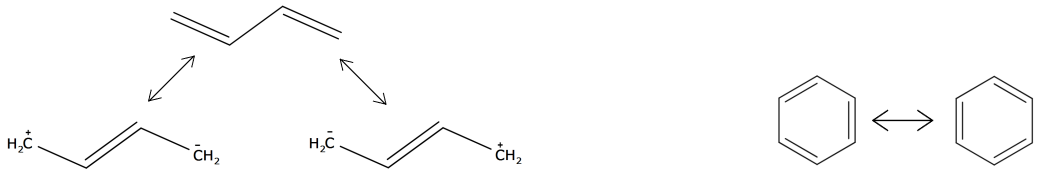

(a) (b)

FIGURE 4.2: Resonance structures in the case of 1,3-butadiene (a) and benzene (b).

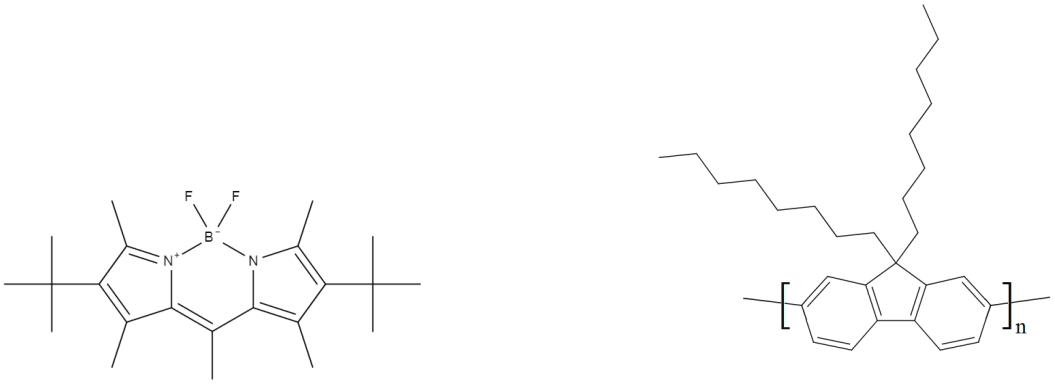

(a) (b)

FIGURE 4.3: Chemical structures of the PM597 dye (a) and PFO (b).

We consider a sequence of sp^2 hybridized carbon atoms. This is the case for example of the 1,3-butadiene ($H_2C = CH - CH = CH_2$). The electrons forming a σ bond need higher energy than the π electrons to be excited, since σ electrons are well localized between two atoms. They will not be considered in the excitation process hereafter.

The π bonds have the electronic density that is not localized between the two atoms, but pointing orthogonal to direction of the bond. When the molecules is planar, adjacent π bonds overlap and the electrons are delocalized over all the atoms sharing a π electron. This delocalization, called π *conjugation*, allows the electrons to move freely along the conjugation, making the molecule behave as a semiconductor. When the conjugation takes place in an cyclic molecule, it is called aromaticity.[1] The sharing of π electrons is represented as an alternation of single and double bonds, while in reality all the bonds are equivalent and the p_z orbitals are not simply localized at the position of the double bond. For this reason, it is possible to draw different resonance structures for the same molecule (Fig. 4.2), while the actual structure is in-between all of them.

The rigorous way to study the energy levels is to build the molecular orbitals starting from the atomic orbitals that we just described [167, Ch.1]. Indeed, it is possible to show that that their combination forms energy bands, in the same way as the atomic orbitals combine to form the conduction and the valence band of a crystal [168, Ch.8]. However, the rigorous discussion of the process goes beyond the scope of this work.

A simplified but extremely useful way to understand the behavior of π energy levels is to think of the π electrons that compose the conjugation as particles in a quantum well of finite height [169, Ch.9]. The larger the well (*i.e.* the longer the conjugation), the less confined are the particles and the more the energy levels become closer together [170, Ch.2]. This means that, by increasing the conjugation of a molecule, the energy required to excite an electron is decreased and the absorption and the photoluminescence are shifted towards red wavelengths.

This means that their fundamental state is when the lowest energetic levels are filled and there is an energy gap between the highest occupied molecular orbital (HOMO) and the lowest unoccupied molecular orbital

[1] An aromatic molecule, in addition to exhibit conjugated π electrons, be planar and cyclic, also has to have a number of π electrons that is even, but not multiple of 4. The analysis of these features, and the way they confer enhanced chemical stability to aromatic molecules [166, Ch.4], lies outside the aim of the dissertation.

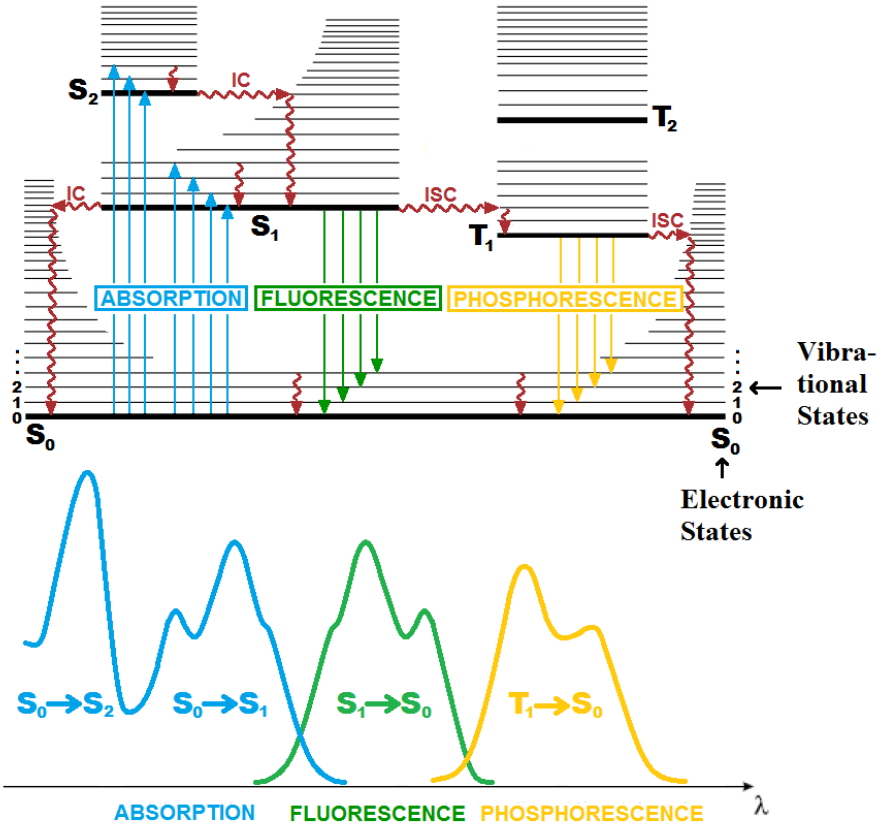

FIGURE 4.4: Perrin-Jablonski representation of the states of the system and the possible phenomena that can occur: radiative recombinations (straight arrows) and non radiative recombinations (undulating arrows), such as intersystem crossing (ISC) and internal conversion (IC). Figure from [158, Ch.3].

(LUMO). If the conjugation is extended enough, the energy gap falls in the range of wavelengths in the visible and the molecule is considered an organic semiconductor.[2]

The chemical structures of the pyrromethene 597 dye (PM597) and Poly(9,9-dioctylfluorene) (PFO) are reported in Fig. 4.3, both are aromatic structures. These are the molecules employed in this work.

The Perrin-Jablonski diagram (Fig. 4.4) is an instructive and clear way to look at the different processes that can occur during the excitation of a molecule. The diagram reports the electronic states of the molecules. Since, as we said, they usually have an even number of electrons, the total spin $\mathbf{S}$ is $\mathbf{S} = 0$ and the spin multiplicity is $2\mathbf{S}+1 = 1$. This state is called the *singlet state* and the fundamental state is denoted by $\mathbf{S}_0$. For each electronic level there is a set of vibrational and rotational levels, that are populated according to the Boltzmann law.

The Perrin-Jablonski diagram reports these electronic and vibro-rotational levels. If an electron is excited through a radiative transition, the spin is conserved and the system stays in the singlet state. In the Perrin-Jablonski diagram the radiative transitions (excitations or disexcitation) are represented by straight arrows; the non-radiative transitions are represented with undulating arrows.

What we observe if we send a white light beam through the sample is the absorption of a part of the light. The absorption is represented by the blue part of the Fig. 4.4. We cannot resolve the rotational levels but we can distinguish the vibrational levels if they are sufficiently separated (as for the polyfluorene, as it will be analyzed in Sect. 4.4).

The system can follow different paths for the disexcitation, depending also on which state the system reaches after the excitation. If the system is in the $\mathbf{S}_1$ state, it quickly thermalizes (vibronical relaxation, vertical undulating arrows) towards the least energetic vibronical state and then it decays in a radiative way towards the ground

[2]Note that the energy gap is larger than in inorganic semiconductors (1-2 eV). Indeed, in order to be semiconductors, the molecules have to be doped with the injection of charges [163]. However, we are only interested in the fact that the optical band-gap falls in the visible region, therefore we will not investigate the electric properties of organic molecules.

state. These emitted photons are called *fluorescence emission*. The fluorescence is also usually specular to the absorption due to the similarity of the vibrational levels for the ground and for the excited state. Since part of the energy is dissipated into non-radiative processes, the emitted photon has a lower energy than the absorbed photon. The distance between the maximum of the absorption and the emission bands is called the *Stokes shift*. The presence of a solvent can also influence the relaxation of the molecule and change the amplitude of the Stokes shift. The larger the Stokes shift, the smaller the self-absorption (i.e. the superposition between the absorption and the emission spectra).

If the system is excited into $\mathbf{S}_2$, it thermalizes towards the lowest vibronical state, and can then follow two paths. The first one is to decay radiatively (usually this process has a low probability of occurring, so it is not reported in Fig. 4.4). The second way is to undergo internal conversion (IC): it is a mechanism in which the system passes to a state with the same energy and spin multiplicity of the initial state, but that is at a higher vibro-rotational level of the lower excited electronic system $\mathbf{S}_1$. It is a non-radiative mechanism. After that, it thermalizes and then contributes to fluorescence. This same internal conversion can also happen between the $\mathbf{S}_1$ and the $\mathbf{S}_0$, but in that case we have a full non-radiative path from the excited to the ground state, and so the fluorescence will be decreased.

Mechanism	Timescale [s]
Absorption	$\lesssim 10^{-15}$
Vibronical relaxation	$10^{-14} - 10^{-11}$
Fluorescence	$10^{-12} - 10^{-6}$
IC	$10^{-14} - 10^{-11}$
ISC	$10^{-12} - 10^{-4}$
Phosphorescence	$10^{-6} - 1$

TABLE 4.1: Timescales of the different phenomena that can take place in an organic system [164].

Another non-radiative process is the intersystem crossing (ISC), in which the spin is flipped for one of the electrons and the system changes the multiplicity. This transition occurs between two levels of the same energy, and then the system undergoes thermalization. The system can decay radiatively from the lowest energetic triplet level $\mathbf{T}_1$, but since this transition is not electric-dipole allowed, its decay time is much longer than that of fluorescence. This last radiative decay is known as *phosphorescence*.

All these mechanisms act on different timescales, reported in Tab. 4.1. As it will be explained later, the pump-probe technique allows for the study of the temporal evolution of the system through these levels.

4.1.1 Excited species in organics

In this Section, we analyze in further detail how the excitations in organic materials look like. When an electron is excited to the LUMO level, a hole is created in the HOMO level. The Coulomb attraction keeps the electron and the hole together and they form a neutral species called an *exciton*. The distance between the hole and the electron distinguishes between excitons, polarons and free charges [164, Part I, Ch. D].

In organic materials the dielectric constant is usually lower than for inorganic crystals and the interaction between the electron and the hole tends to be stronger. Due to their linear structure, the system is also susceptible to structural distortions that tends to stabilize the excited state [163, Ch. 2] (what we previously called "vibronical relaxations"). This is the Frenkel exciton, which is localized to the local distortion of the organic material and usually has a radius of the same order as the intermolecular distance.

If the distance between the electron and the hole increases, the coulombic interaction between the two decreases and becomes comparable to the thermal energy [164, Part II, Ch. B]. If they still feel each other, we speak about *polaron pairs*. The polarons are usually accompanied by a local deformation of the molecule. If the thermal fluctuations are high enough, the two charges become free single charge carriers. All these excitations can move along the conjugation and, eventually, from one molecule to another, if the molecules are close enough.

All these species present their own absorption spectra, which can overlap with the emission spectrum and decrease the optical gain. This will be of particular importance for the study of the polyfluorene pump-probe spectra in Sect. 4.4.

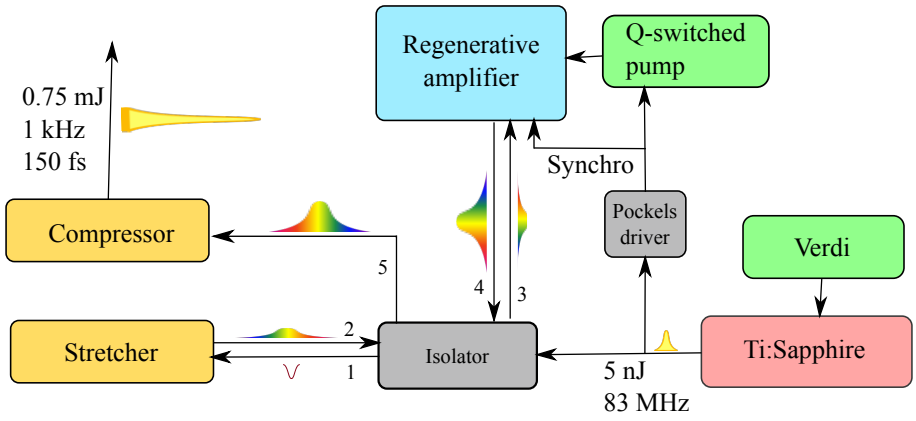

FIGURE 4.5: Scheme of the setup for the femtosecond pulse generation. Figure from [128].

4.2 Pump-probe technique

In this Section we introduce one of the main methods employed to resolve the temporal dynamics of an excited system: the pump-probe technique. The setup used in this work is located in the optical laboratories of the Physics Department at the Politecnico di Milano, in the Center for Ultrafast Science and Biomedical Optics (CUSBO).

I familiarized myself with the setup and the technique during my Master thesis [128]. During my PhD, I spent two weeks as a visiting researcher at Politecnico di Milano (Milano, Italy) with a Laserlab Europe grant (Ref. CUSBO 002033) in order to refine the polarized pump-probe technique and to take the measurements on the PFO samples. I was hosted by Dr. Tersilla Virgili, who later took the measurements on the PM597 sample together with Dr. Sai Kiran Rajendran.

In the pump-probe technique two pulses are sent to the sample, the first one excites the molecules while the second one probes the levels of the system for different wavelengths and at different time delays from the pump. In this Section, after a brief introduction on the setup for the generation of the pulses, we will focus on the analysis of the signals that the technique can provide.

4.2.1 The experimental setup

Fig. 4.5 shows the setup used to obtain suitable pulses for the pump-probe measurements. The Nd:YVO4 (Verdi) laser, doubled in frequency, pumps a Ti:sapphire rod that is placed in a cavity for a classical Kerr-lens mode locking laser [169]. The cavity emits pulses of around 100 fs at 83 MHz repetition rate centered at 780 nm. The energy of these pulses is however quite low (∼5 nJ/pulse) and they need to be amplified. To avoid damaging the amplifying medium, the pulses are first dispersed with a gratings pair (the stretcher), in order to lower their peak power. The isolator at the output of the Ti:Sa cavity prevents back-reflections from destroying the mode-locking regime. The regenerative amplifier then amplifies the pulses in the following way. First, a Pockels cell lets one pulse enter the amplifier cavity. The pulse is sent onto a Ti:sapphire rod pumped by a Q-switched Nd:YAG laser at 1 kHz repetition rate. The pulse circulates inside the cavity until the rod is able to provide gain. Then the Pockels cell lets the pulse exit the cavity. The Q-switched laser and the Pockels cell are synchronized by a driver triggered on the pulses that have to be amplified. At the output of the amplifier, the pulses are of around 750 µJ at 1 kHz repetition rate. A grating compressor compresses them to their Fourier transform limit (around 150 fs).

The pulse is then split in two pulses, the pump and the probe (Fig. 4.6). The probe is focused on a sapphire plate for the white light continuum (WLC) generation. The white light has the same polarization as the incident monochromatic light. With a broadband probe pulse, all the wavelengths are probed at the same time. The pump wavelength has to be in the spectral range of the sample absorption, in order to induce the excitation of the molecules. If the sample absorbs in the UV region, the pump is focused on a beta-barium borate (BBO) crystal for the second harmonic generation (390 nm). This will be the case of PFO. If the sample absorbs in the

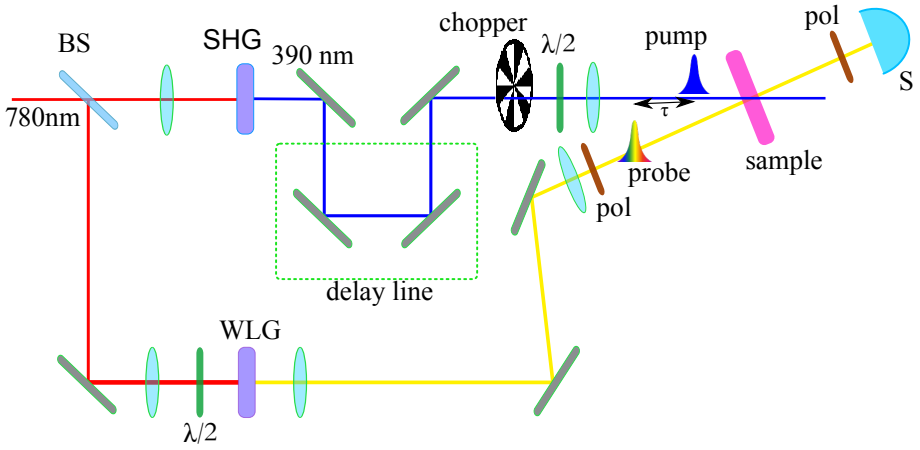

FIGURE 4.6: Scheme for the pump-probe measurement. BS: beam splitter; SHG: second harmonic generation; WLG: white light generation; S: spectrometer. Figure from [128].

visible, the pump pulse is sent onto an optical parametric amplifier (OPA) in order to obtain pulses centered at a tunable wavelength [171, Ch.5]. This will be the case for PM597, for which the excitation wavelength is 550 nm.

The pump and the probe beams are focused on the sample on a circular spot (radius ≈75 µm). The two pulses have to be spatially overlapped on the sample in order to observe a signal, while the temporal delay τ between the two pulses can be varied with the delay line. The temporal resolution of the system is given by the convolution between the pump and the probe pulse, and in our case is of around 250 fs.

In order to study the optical anisotropy induced by the LC matrix, the polarization of the probe is set either parallel or orthogonal to the LC director. This is obtained by rotating the polarization of the IR beam before the WLC generation, which has the same polarization as the incoming pulse. A polarizer is also placed before the sample, to get rid of eventual depolarizations of the probe. Another polarizer, always parallel to the probe polarization, is placed after the sample, to filter out the depolarization due to the LC scattering.

Finally, the chopper stops one pump pulse over two, in order to measure the transmission of the probe through both the excited (T^{ex}) and the ground state (T^{gr}) of the sample.

4.2.2 The pump-probe signal

The collected signal is the differential transmission spectra $\triangle T/T(\lambda, \tau)$ of the probe through the sample

$$|\frac{\triangle T}{T}(\tau, \lambda)| = \frac{T^{\text{pump}} - T^{\text{no pump}}}{T^{\text{no pump}}}(\tau, \lambda), \tag{4.1}$$

where T^{pump} and $T^{\text{no pump}}$ are the transmissions of the probe through the sample that has been excited and which is in its ground state, respectively. The modulus is due to the fact that the cross section is defined as a positive quantity, but the signal $\Delta T/T$ can be positive or negative since the transmission of the probe can be increased or decreased compared to the unexcited sample case. It is a function of the delay τ between the pump and the probe and of the wavelength λ of the probe. This definition allows us to get rid of the constant contributions from the unexcited sample and to look only at the excited system. It is possible to demonstrate [171, Ch.9] that

$$\frac{\triangle T}{T}(\tau, \lambda) = \mathcal{N}(\tau)\sigma(\lambda)l, \tag{4.2}$$

where $\mathcal{N}(\tau)$ is the population density of the excited state, $\sigma(\lambda)$ is the cross section of the transition and l is the thickness of the sample. For a fixed wavelength, we can extract the temporal dynamics of the population of the excited state $\mathcal{N}(\tau)$.

Here we present some examples of dynamics that it is possible to observe. Imagine a molecule whose states are those seen in the previous section (Fig. 4.7a). Since the thermalization is much faster than the pulse duration, we suppose that the system immediately thermalizes to the bottom of the $\mathbf{S}_1$ band after the absorption of the pump photon (with frequency ω_0).

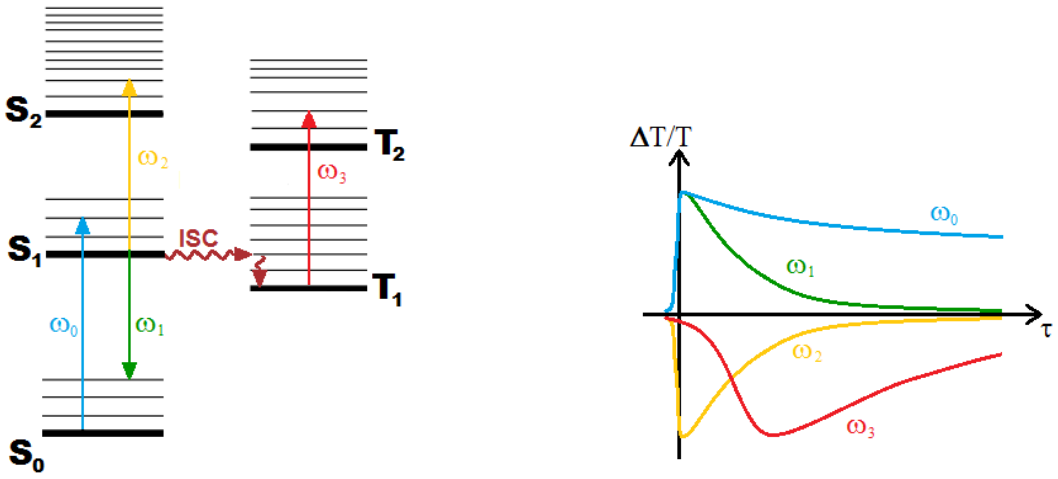

FIGURE 4.7: (a) Perrin-Jablonski diagram of the states of the system; (b) dynamics of the $\Delta T/T$ signal for the frequency ω_0 (GSB), ω_1 (SE), ω_2 (PIA) and ω_3 (PIA). Figure from [128].

If we send a photon of energy $\hbar\omega_1$ on to the sample at a delay τ after the pump, the incoming photon induces stimulated emission (SE) and a second photon of the same energy is emitted. The signal is therefore increased and the $\triangle T$ is positive. If we increase the delay, this contribution decreases with a time constant given by the lifetime of the excited level (Fig. 4.7b).

If a photon of frequency ω_0 arrives on the sample, it has a lower probability to be absorbed since there are fewer molecules in the ground state that can be excited. The signal is therefore increased with respect to a probe passing through an unexcited sample, and this contribution is known as ground state photo-bleaching (GSB). The lifetime of this contribution is equal or higher than SE, since it will be present until there are molecules in some excited levels (ω_0 dynamic in Fig. 4.7b). Both SE and GSB cause an increase of the $\triangle T$, but only the SE is a true amplification of the signal, while the GSB is only a decrease in the absorption. The distinction between these two contributions is done with the help of the absorption-PL spectra. Indeed, the SE takes place in the spectral region of the fluorescence, while the GSB is localized in the region of the absorption. By comparing the absorption-PL spectra with the pump-probe traces, it is possible to identify the spectral region where the optical gain is located.

If the excited sample is illuminated with a photon of energy $\hbar\omega_2$, this will be absorbed in the transition $\mathbf{S}_1 \rightarrow \mathbf{S}_2$ and the $\triangle T$ is negative. This contribution is called photo-induced absorption (PIA) and has the lifetime of the $\mathbf{S}_1$ level (as the SE signal), since it will go to zero when the S_1 level is completely depopulated.

If the system has also triplet states, the molecules can pass from $\mathbf{S}_1$ to $\mathbf{T}_1$ level through the ISC process and then they can absorb a photon of frequency ω_3 to reach the $\mathbf{T}_2$ state. This is still a PIA term but its growing time is given by the rate of ISC, while its decay constant is the lifetime of the $\mathbf{T}_1$ state. These dynamics are reported in Fig. 4.7b.

4.3 Dyes in LCs

We start applying this technique to a small molecule, the PM597 dye (Sigma-Aldrich, Fig. 4.3a), mixed in nematic LC E7 (Merck). Short molecules are less aligned by LCs [148] , but they are often easier to dissolve in the LC matrix.

The solution of 1 wt.% of PM597 in E7 is prepared mixing it with a stirring magnet on a hot plate above the clearing temperature of E7 (∼70 °C) until homogeneity is reached (several minutes).

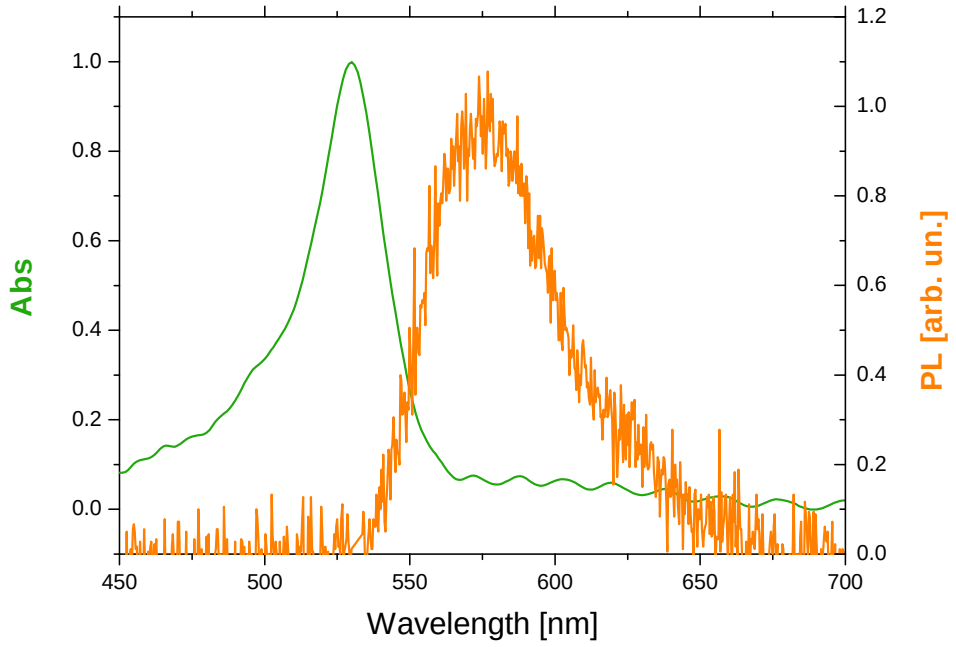

FIGURE 4.8: Normalized absorbance polarized orthogonal to the LC director (left axis) and unpolarized PL spectra (right axis) for the PM597 dissolved in nematic E7 (after the subtraction of the constant background).

4.3.1 Photophysical characterization

A commercial cell (Instec), with a thickness of 6.8 µm, and a planar antiparallel alignment is filled with the solution of PM597 and E7. We use thinner samples than those used for the nematicon generation in order to limit the depolarization of the beams during the propagation in such a scattering medium such as LCs. Also, the absorption of the pump and the probe through the sample is minimized.

In order to interpret the pump-probe signal, we need to know the spectrum of the absorption and the photoluminescence of the dye dispersed in the LC. Indeed, this is essential to distinguish between SE and GSB, as they both give rise to a positive pump-probe signal only in different spectral regions. Depending on the solvent, the maximum of the absorption of the PM597 is between 520 nm and 530 nm, while the maximum of the PL emission is centered between 560 nm and 570 nm [172]. We need therefore to characterize the absorption and the emission of the dye in the LC matrix.

The normalized absorbance of PM597 in E7 is measured with a UV-Vis spectrometer (Perkin-Elmer) and reported in Fig. 4.8. The absorbance $\mathtt{A}$ is defined as

$$\mathtt{A}(\lambda) = \log_{10} \frac{I_0^{in}(\lambda)}{I_0^{out}(\lambda)}, \tag{4.3}$$

where I_0^{in}, I_0^{out} are the input and output peak intensities of the optical beam traversing the medium, respectively. Only the contribution orthogonal to the LC director is reported, since the one parallel to the director was saturated even if the sample was thin. In the same Figure, the normalized unpolarized PL spectrum is reported. It is obtained exciting the sample with a Q-switched frequency doubled Nd:YAG laser (532 nm, 400-ps pulses at 100 Hz). A fiber spectrometer (Ocean Optics USB2000), synchronized with the pump laser, is placed close to the excited spot to collect the emitted light.

In Fig. 4.9 we report the pump-probe spectra for the polarizations of the probe beam parallel (a) and orthogonal (b) to the LC director. For all the measurements, the pump is at 550 nm and it is polarized parallel to the LC director, with an energy of 10 nJ/pulse. The spectra are taken at different time delays from the excitation pulse, in order to show the temporal evolution of the excited states.

The contribution polarized parallel to the rubbing is twice as large as the orthogonal one. This indicates that the dye molecules are mainly aligned along the LC director. Both signals are instantaneous within the time resolution of the setup. The parallel signal is monotonously decreasing in time, while the orthogonal one increases at large delays. This is due to the fact that there is a depolarization of the excited molecules in time. Indeed, at the beginning, the molecules with an electric dipole parallel to the pump polarization are excited more than the others. With time, the excitons migrate from molecule to molecule, eventually reaching molecules with the dipole oriented in a different direction. This is why, at larger delays, the orthogonal contribution grows while the parallel decreases.

The pump-probe spectrum for the PM597 presents one positive band from 500 nm to 700 nm. It is composed of two positive bands. The first one is in the same spectral range as the absorption (530 nm) and it is therefore due to the GSB. The second contribution is at around 575 nm, where the PL is centered, and it is due to the SE. The two bands merge and they are not really distinguishable. The slight periodic modulation of the spectrum is due to a Fabry-Perot cavity effect generated by the two glasses composing the LC cell. There is no formation

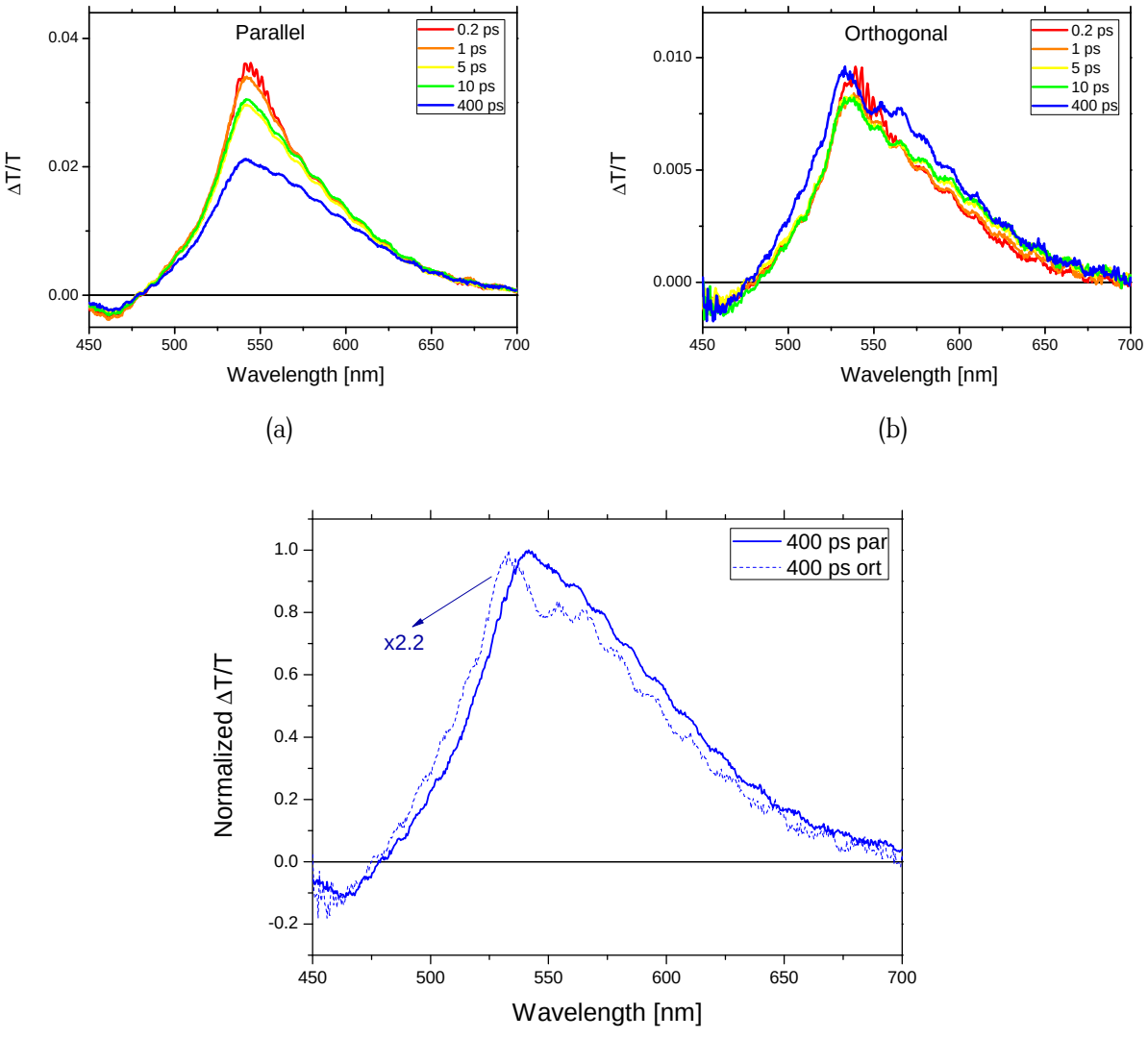

FIGURE 4.9: Pump-probe spectra for the PM597 in E7 in the case where the probe is parallel (a) or orthogonal (b) to the director and for a pump of 10 nJ/pulse. (c) Comparison of the spectra for the two polarizations taken at 400 ps delay. The parallel spectrum (solid) is around two times higher than the orthogonal one (dashed).

of PIA over the visible, allowing for a long-living (>400 ps) optical gain in the red part of the spectrum where the SE is present.

Since we aim to use the optical gain of the system for the soliton (CW) or with long pulses excitation (400 ps), we compare the spectra at large delays. In Fig. 4.9c the spectra parallel and orthogonal to the director are reported for a delay of 400 ps. The parallel contribution of both GSB (below 550 nm) and SE (above 550 nm) is shifted towards the longer wavelengths by around 10 nm compared to the orthogonal contribution. This could be due to the anisotropy of the LC host. Indeed, the spectral position of the absorption and the emission of a molecule depends on the physical properties of the solvent used to disperse it. The effect is also known as *solvatochromism* [173]. In the case of an anisotropic solvent such as the LC, the transition dipole experiences a different environment depending on its orientation with the respect to the director orientation, which could lead to a spectral anisotropy between the two polarizations [174]. The complex details of this phenomenon are, even though interesting, beyond the aim of this work. Finally, we believe that the anistropy of the scattering [125, 175] plays a minor role, since it would not explain a spectral shift of the GSB.

A way to further characterize the optical gain of the molecules is to measure the amplified spontaneous emission of the sample, since it occurs at the wavelength with the highest optical gain.

4.3.2 Amplified spontaneous emission

Amplified spontaneous emission (ASE) arises in gain media that are excited over a long and thin volume, as in fiber amplifiers or bulk amplifying materials. Photons that are emitted spontaneously along the long axis of the excited volume are amplified more than those emitted in other directions. The ASE is therefore directional and narrow-band, since during the propagation the wavelength with the highest optical gain emerges from the photoluminescence broadband spectrum [52–55]. The absence of feedback simplifies the architecture of the device with respect to lasers and is also responsible for a low spatial coherence. ASE is therefore a better candidate for illumination purposes than broadband and narrow-band lasers, which are impaired by speckle [46, 47].

ASE has been widely studied in solid state films [176–180], microfluidic devices [181, 182] and only recently in dye-doped nematic liquid crystals (LCs) [161, 162]. In our case we analyze how the anisotropy of the gain measured in the pump-probe spectra affects the ASE characteristics.

A non-commercial 75 µm-thick cell, with planar antiparallel alignment (see Sect. 2.4.2), is filled with the same mixture used above. Such a thick cell is employed because we want to observe optical amplification in the same sample that we use for the nematicon generation, in order to study the interaction of the two at the

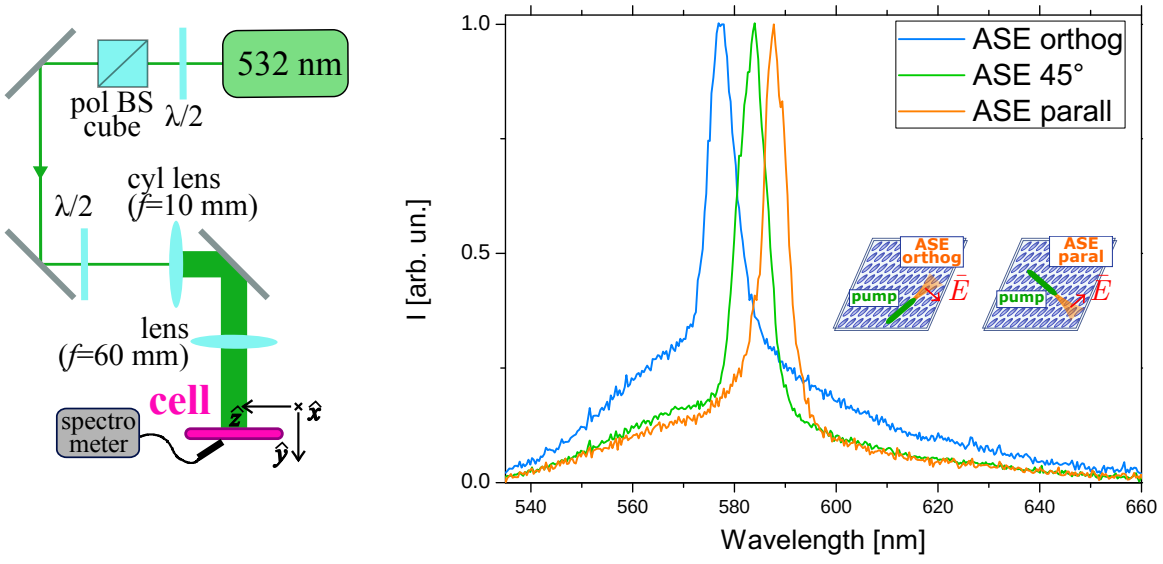

(a) (b)

FIGURE 4.10: (a) Scheme of the ASE generation in the dye-doped nematic LC cell; (b) normalized ASE spectra taken for a pump intensity of 7.6 µJ/pulse (100 Hz) for the cases where the electric field $\bar{E}$ of the emission is parallel, orthogonal or at 45° to the rubbing direction. Inset: scheme of the ASE measurement in two of the configurations.

same time. The optical setup used for the ASE generation is reported in Fig. 4.10a. A Q-switched frequency doubled Nd:YAG laser (532 nm, 400-ps pulses, 100 Hz) is used to pump the dye. On the laser path, the ensemble of the half-wave plate and the polarizing beam splitter allows to control the beam power, while the second half-wave plate turns the polarization angle with respect to the LC director. The polarization is set parallel to the LC director and then slightly turned (few degrees) in order to compensate small misalignment of the rubbing directions and maximize the fluorescence. The beam is focused with a spherical achromatic lens (f=60 mm) and a cylindrical lens (f=60 mm) in order to obtain an elliptical spot of around 20 µm × 7 mm on the cell. The ASE threshold is as low as 0.4 µJ/pulse, and all the measurements presented here are taken well above the threshold.

The pump stripe is oriented into three different directions in the cell, parallel, orthogonal or at 45° to the LC director. Indeed, since the ASE emission is mainly polarized in the plane of the cell due to the LC-induced dye orientation and to the geometry of the sample [183], the orientation of the stripe within the cell determines the orientation of the ASE polarization with respect to the LC director. In particular, when the pumping stripe is parallel (orthogonal) to the rubbing, the ASE is polarized mainly orthogonal (parallel) to the director (inset of Fig. 4.10b).

In Fig. 4.10b the ASE spectra are reported for the different orientations of the pump stripe with respect to the rubbing direction. The scattered light is collected at the edge of the stripe through the glass plate. Changing the emission polarization from orthogonal to parallel with respect to the director, the ASE peak shifts from 577 nm to 588 nm. The tunability of the ASE wavelength has been demonstrated changing the thickness of the amplifying film [177, 179, 183, 184]. This happens when the thickness of the gain medium is close to the cut-off thickness for the ASE propagation (∼100 nm), which is not our case. Since the ASE red-shift is of the same order of magnitude as the shift observed in the pump-probe spectra, we believe that the large red-shift of the ASE is mostly due to the optical gain anisotropy of PM597 dissolved in LC.

4.4 Polymers in LCs: PFO

In this Section, we are going to exploit Onsager's old prediction [148, 185] that long molecules are better aligned in a nematic environment than short molecules. Therefore, instead of using a dye, we are going to use a photoluminescent polymer. Previous works show that the liquid crystalline solvent can unwind the polymer bundle into a rod-like configuration with the axis aligned with the director of the nematic [149, 185]. Increasing the polymer weight, the anisotropy of absorption and emission of the photoluminescent polymer increases [186, 187]. Since the macroscopic alignment of LC is given by the boundary conditions of the cell, the LC solvent can provide an aligned polymer over a large scale. This method is easier compared to the techniques used to obtain oriented solid-state films, which usually require thermal cycling or mechanical treatments [156, 188].

Photoluminescent polymers present, however, two main drawbacks that limit their use as photonic devices: creation of free charges or polaron pairs after pump excitation [189] and easy degradation in air [190].

In polymeric samples, the photo-induced charges, due mainly to inter-chain interactions, produce self-absorption in the material since their absorption band partially overlaps with the emission and gain spectral region of the excitons [191]. Different approaches have been explored to quench photoinduced charges in organic materials, such as tailored synthesis of molecules [180, 192] or dispersion of the polymer in an inert matrix [193]. In particular, it has been shown that the dispersion of PFO, the most studied polyfluorene derivative, in an inert matrix allows us to isolate the PFO chains, preventing the formation of inter-chain photoinduced charges and therefore allowing the formation of a large SE band up to 600 nm [191, 194]. Indeed it has been demonstrated that, by isolating the molecules, it is still possible to observe intrachain charge formation, while the interchain charges are inhibited [191, 195]. However, the poor miscibility of the PFO and the host used in these works is responsible for the large sample inhomogeneity [193].

The second issue is that PFO easily reacts with oxygen creating a defect along its polymeric chain, the so-called keto defect (also known as *fluorenone*) [196–198], which degrades the color purity of the emission band and decreases the device efficiency and stability [199]. Photoluminescence and electroluminescence (EL) studies indicate that Förster energy transfer to, and charge carrier trapping on, fluorenone defects (with subsequent fluorenone emission) are responsible for color degradation [200, 201], *i.e.* the characteristic blue emission is replaced by a green-whitish one [202]. This process is so efficient that it becomes significant at a very low

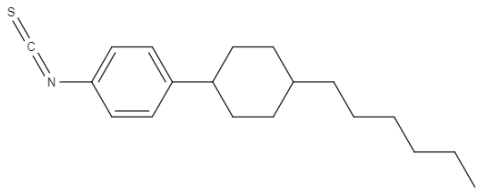

FIGURE 4.11: Chemical structure of the 6CHBT liquid crystal.

Optical properties [207]	$n_{\parallel}$	1.68
	$n_{\perp}$	1.52
	$\triangle n$	0.16
Transition temperatures [207]	T_m	12.5 °C
	T_c	43.0 °C

TABLE 4.2: Characteristic of the 6CHBT LC.

fluorenone fraction [203]. Whether the green emission from this defect is due to a single-chain defect [202, 203] or to an aggregation effect [204–206] has been the subject of a long debate. In any case, the presence of high transient charge concentrations in degraded polyfluorene makes it difficult to obtain optical gain (stimulated emission), hindering applications of this material in photonic devices such as optical amplifiers or lasers.

We discovered that a large polarized SE band from isolated polyfluorene keto defects is obtained in a mixture of polyfluorene with a nematic low molecular weight LC, shedding new light on the single-chain nature of the keto defect. In this blend a peculiar phase separation generates an ordered network of LC-rich micro-domains with most of the polyfluorene chains isolated on the boundaries of the micro-domains.

In this Section we present both the morphological and the photophysical study of the PFO in LC. Indeed, the pump-probe spectra can be fully understood only through the study of the morphology of the sample, while this last one was guided by the features observed in the pump-probe, such as the linear polarization and the spectral position of the bands. The study of the morphology is done by means of polarized confocal photoluminescence microscopy, which was performed by Dr. Michele Celebrano and Lavinia Ghirardini in the laboratories of Politecnico di Milano. The data presented in this chapter are the result of the strong interaction between the two groups and the combination of the two techniques. For this reason, even if I did not perform myself the confocal measurements, the technique will be briefly introduced and the confocal maps of the sample presented, in order to provide a complete analysis of the samples.

4.4.1 Preparation of the sample

The polymer used in this work is the PFO (American Dye Society, ADS129BE, molecular weight: 40 000 – 120 000). It is mixed in 6CHBT (4-(trans-40-n-hexylcyclohexyl)-isothiocyanatobenzene; Military University of Technology, Warsaw, molecular weight: 301, synthesis details in [207]), since it presents a better miscibility than in the E7 LC. The 6CHBT chemical structure is shown in Fig. 4.11 and its characteristics are reported in Tab. 4.2.

The polymer-LC mixture is obtained by first dissolving PFO in toluene (10 mg·ml^{-1}) and then adding the LC. The solvent is evaporated by heating the solution at about 110 °C for some hours and then commercial cells (Instec), with a thickness of 9 µm and a planar antiparallel alignment, are filled at the constant temperature of 70 °C. Two samples with different PFO concentrations are investigated: Low Concentration Sample (LCS, 0.26 wt% of PFO) and High Concentration Sample (HCS, 0.61 wt% of PFO).

4.4.2 Morphology, absorption and photoluminescence of the samples

The morphology of the sample is strictly correlated to the concentration of the PFO that is dissolved in the LC host. For low concentrations (0.26 wt% of PFO), the polymer is dispersed uniformly. However, larger concentrations of polymers are needed in order to have an optical gain large enough to observe amplification or lasing, typically of the order of 1 wt% or higher [142, 153, 208]

When increasing the concentration of the PFO, a complex pattern appears in the LC cell. In this section we will present the study of this pattern through the polarized optical microscopy and the polarized confocal microscopy techniques.

Polarized optical microscopy

Figure 4.12 shows the bright-field polarized optical microscopy (POM) images for the LCS (a) and HCS (b) samples. The first cell (LCS) shows a homogeneous texture indicating a good dispersion of the polymer in the LC matrix. Differently, the HCS shows a much more complex structure extending all over the cell. In Fig. 4.13 are reported the bright (a) and the dark (b) states for the HCS, obtained with the rubbing at 45° and parallel to one of microscope polarizers. Long filaments (structures of tens of micrometers) define small domains that present a homogeneous alignment of the LC. From these images, however, it is not possible to define the nature of these boundaries, if they are due to a misalignment of the LC or to a polymer aggregate. The confocal photoluminescence microscopy will clarify the origin of these filaments.

Absorption and photoluminescence

The polarized absorption and emission spectra for the two samples are reported in Fig. 4.14. The photoluminescence is obtained by exciting the sample with pulses at 400 nm (60 fs, 1 kHz) polarized along the LC director. The LC matrix is transparent at this wavelength [209], therefore we do not expect to observe a contribution from the LC.

The LCS (Fig. 4.14a) shows an absorption characterized by a broad peak for wavelengths shorter than 400 nm, while the PL spectrum is characterized by a series of vibronic peaks (440 nm, 467 nm and 502 nm). A pronounced anisotropy is present in both the absorption and PL spectra.

The small peak at around 430 nm in the absorption spectrum indicates the presence of a particular conformation of the PFO chain. Indeed, the PFO can assume different phases, mainly the α and the β phase. The PFO in the α phase takes an helicoidal conformation and it presents one broad absorption peak at 390 nm. In the β phase, the fluorine units lie almost in the same plane: in addition to increase the packing of the molecules, the conjugation length of the molecules is increased and a lower energy level is created [132, 210]. This gives rise to two additional absorption peaks at 400 nm and 430 nm (Fig. 4.14a), that are respectively the 0-0 and the 0-1 vibrational peaks of the β phase of the PFO [211, 212]. The photoluminescence of the β phase is also characteristic, showing more resolved vibronical peaks [211, 213], while the peak at 420 nm is decreased due to the self-absorption with the new absorbing peak.

The LC matrix can indeed flatten the PFO, inducing some of the chains to take the β phase. However, the distinction between α and β or other conformations is not always simple, often requiring other analysis such as X-rays diffraction or PL at extremely low temperatures [211, 214–216]. In this case, we are not interested in the conformation of the PFO as much as we are in the presence of oxidized units in the chain, the so-called keto defects. Our aim is to show that the keto defects, often associated with a degradation of the optical properties

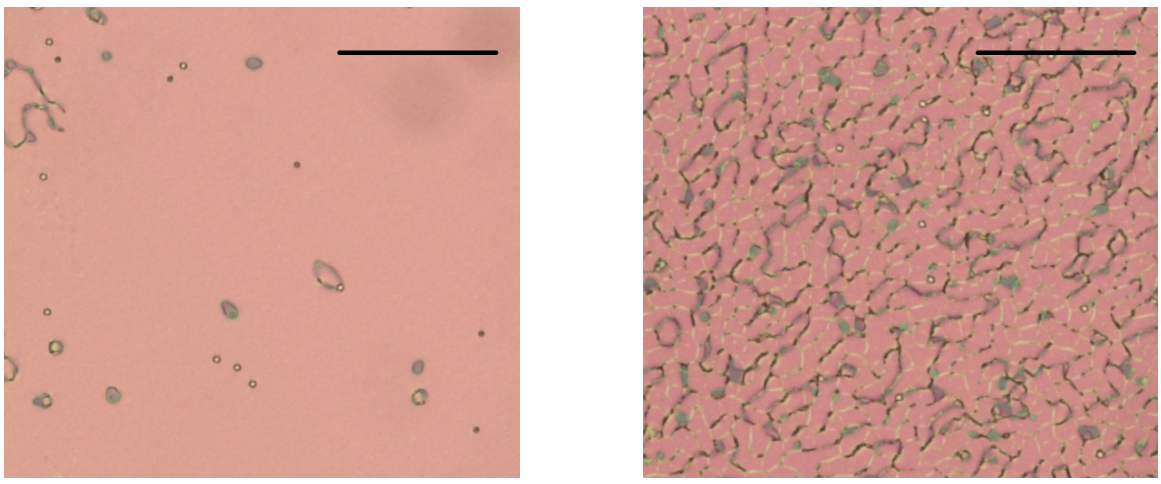

(a) (b)

Figure 4.12: POM images of the LCS (a) and the HCS (b), obtained for uncrossed polarizers. The scalebar is 200 µm.

(a) (b)

FIGURE 4.13: Bright (a) and dark (b) POM images of the HCS under a cross-polarized light microscope. The red arrow indicates the rubbing direction, the scalebar is 50 µm.

of the polymer, can provide optical gain when the polymer chains are isolated.

The presence of even a small fraction of keto defect causes the emission of an intense and broad band centered at 550 nm [196, 217]. This band, slightly visible for the LCS (Fig. 4.14a), becomes more intense for the HCS (Fig. 4.14b). It is important to note that the concentration of keto defects in polyfluorene chains is still very low, as the blue emission from the polyfluorene backbone is quite intense and not completely depleted by the efficient energy transfer to the keto defect. Also, the HCS displays a less pronounced anisotropy in both the absorption and in the PL spectra with respect to the LCS, as expected from the POM images.

Polarized photoluminescence confocal microscopy

To better understand the complex microscopic organization in the HCS, we recorded diffraction-limited confocal PL maps (shared objective numerical aperture NA = 0.8). This is achieved by exciting the sample with a circularly-polarized 405 nm diode laser and recording the total PL intensity-maps, with linear polarizations both parallel (I_p) and orthogonal (I_o) to the LC director. The details of the technique are presented in [130].

Fig. 4.15 shows four confocal PL maps (80 µm×80 µm). The first one (Fig. 4.15a) displays the total emission intensity collected from the sample and shows that most of the PL intensity comes from the boundaries of the micro-domains, while elsewhere just a few emitting spots are detected. The other three maps instead show

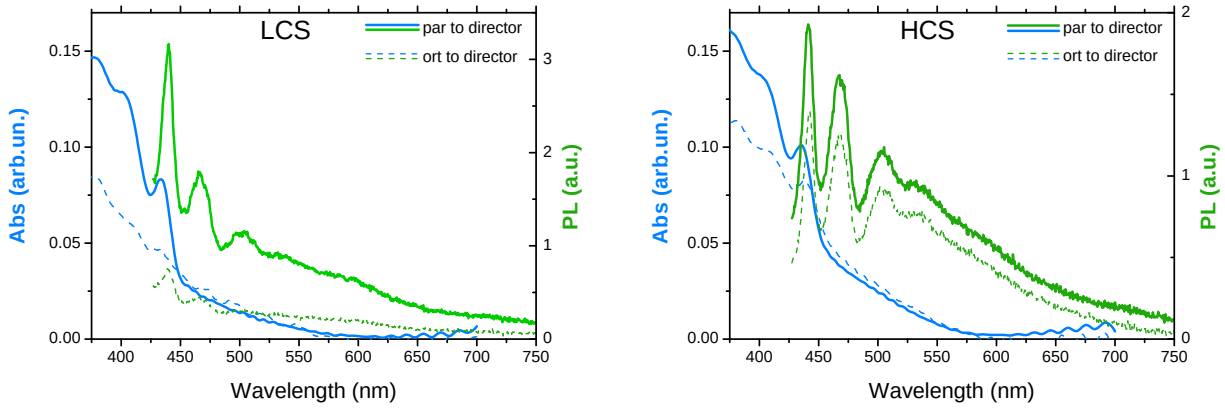

(a) (b)

FIGURE 4.14: The absorption and the emission parallel and orthogonal to the LC director (after Savitzky-Golay filtering and the subtraction of the constant background) for the LCS (a) and the HCS (b).

the normalized linear PL dichroism. The linear PL dichroism D is defined as the difference between the two polarization maps: $D = (I_p - I_o)$. Fig. 4.15b represents the map of parameter D obtained by taking into account the overall fluorescence emission from the sample, while Fig. 4.15c and Fig. 4.15d show the isolated contributions from the defect-free PFO and from the keto defect, respectively. These last two are collected with 10 nm pass filters centered at 440 nm and 560 nm, respectively.

In these PL maps, the red color represents the emission polarized parallel to the LC director (the rubbing direction is horizontal in the images), while the blue color is associated with the one polarized mainly orthogonal to it (see arrows in Fig. 4.15). All four maps show a similar supramolecular structure, as already seen via a bright field microscope (Fig. 4.12b), composed of a matrix of domains separated by rather thick boundaries. Fig. 4.15c and Fig. 4.15d demonstrate that there are polyfluorene chains with keto defects all over the sample, in particular on the cell boundaries. Moreover, the measured polarized emission reveals that the low energy emission (generated by the keto defects) is polarized along the same axis as the high-energy blue emission, showing that the transition dipole moment of the green emission band lies basically parallel to the chain direction, as previously reported [218].

The orientation of the boundaries defines the polarization of their emission: boundaries orthogonal (parallel) to the LC director display an emission orthogonal (parallel) to the director. In our case the majority of the boundaries are orthogonal to the LC director. Inside the domains a few polymeric chains, also containing keto defects and all aligned parallel to the LC director, are responsible for the weak photoluminescence visible in Fig. 4.15a. The organization of the phase-separated sample closely resembles the network lattice formation observed in mixtures with high-molecular-weight (HMW) polymer LC and low-molecular-weight (LMW) LC [219, 220]. In these systems, phase separation results in a well-ordered honeycomb network structure wherein the LMW-rich phase is accommodated in micro-domains surrounded by walls constituted by the HMW polymer-rich phase. In our case, during the filling procedure of the cell (where the temperature is kept constant at $\sim$70 °C) the PFO can be considered as a HMW LC, as its glass-transition temperature is around 80 °C, [154] so phase separation appears. The anchoring effect from the boundary becomes so significant that the polymeric chains are forced to align parallel to its surface [219] despite the LC director orientation, as observed in our case. Since the presence of this structure depends on the composition of the mixture, we assume that in the LCS the PFO concentration is too low to induce it.

4.4.3 Photophysical characterization

For the photophysical characterization, we have set the pump (λ=390 nm) polarization orthogonal (excitation density 2.6 mJ/cm^2, equivalent to 150 nJ/pulse) to the LC director, to increase the signal from the PFO chains placed on the boundaries of the micro-domains.

In Fig. 4.16a and Fig. 4.16c the polarized pump-probe spectra of the LCS are reported. The transient signal appears strongly polarized along the direction parallel to the LC director. The $\triangle T/T(\lambda)$ spectra coincide with those of aggregated PFO, showing a SE band extending up to 500 nm and a PIA_c band centered at around 560 nm attributed to the absorption of the inter-chain photo-induced charges [191, 221]. It is also known from the literature that there is another PIA_1 band centered around 700 nm that is due to the absorption from the first singlet state $\mathbf{S}_1$ [193, 222].

In the LCS case, the spectra reveal that the polyfluorene chains are mainly aligned along the LC director, The anisotropy between the contribution parallel and orthogonal to the director is larger than that found for the PM597, in agreement with Onsager's prediction. This results in the pinning of the polarization of the SE and of the charge-induced PIA band. Comparing the spectra parallel and orthogonal to the LC director (Fig. 4.16e), it is possible to observe a red-shift ($\sim$5 nm) that is smaller than the case of PM597 ($\sim$10 nm), even if the emission anisotropy is two times higher. This is probably due to the fact that the conjugation length of a long chain (such as the PFO) is less affected by environmental changes than a small molecule (such as the PM597).

The anisotropy factor is defined as

$$r(\tau) = \frac{I_p(\tau) - I_o(\tau)}{I_p(\tau) + 2I_o(\tau)}, \tag{4.4}$$

where $I_p(\tau), I_o(\tau)$ are the temporal dynamics $\triangle T/T(\tau)$, for the same wavelength, for a polarization parallel or orthogonal to the LC director, respectively. It is a measure of the anisotropy of the spectra as a function of the

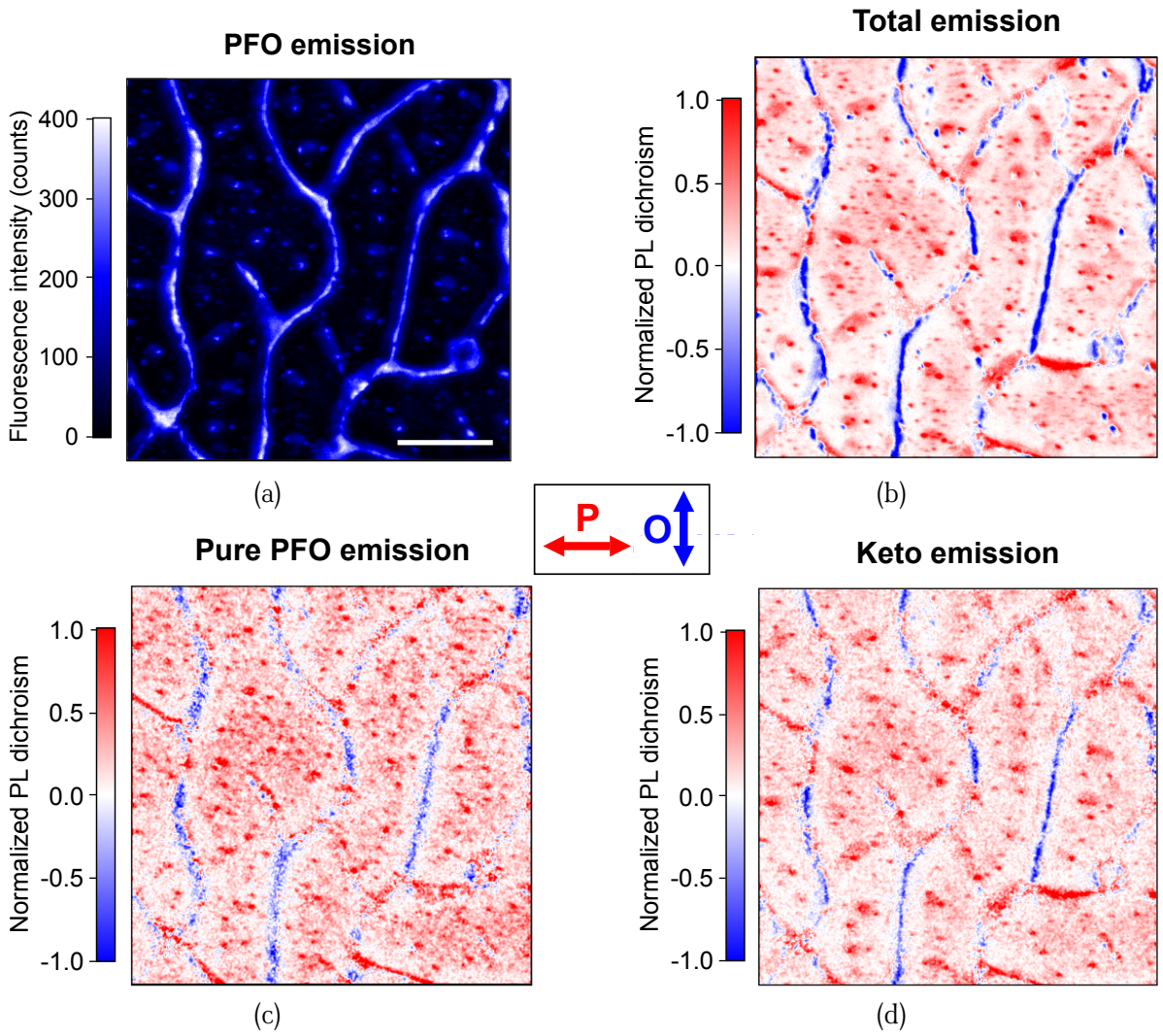

FIGURE 4.15: Confocal fluorescence maps. (a) Total PFO fluorescence emission; (b) normalized linear dichroism (D) of the total PL from PFO. Both are collected using a long pass color filter cutting wavelengths below 455 nm. Normalized D from the defect-free PFO collected using a 10-nm band pass filter centered at 440 nm (c) and from the keto defect collected using a 10-nm band pass filter centered at 560 nm (d). The red and blue colors indicate an emission polarized parallel and orthogonal to the LC director, respectively. The scalebar is 20 µm.

time. For the LCS the absolute value of the anisotropy factor remains constant over more than 10 ps (Fig. 4.16f), meaning that the excitons and charges do not experience migration along differently oriented polymeric chains on that time scale [191].

Moreover, since the absorption band associated with inter-chain photoexcited charges is typically characterized by a long lifetime [189], similar to the one we measured for the LCS (PIA_c), our data also demonstrate that the polyfluorene chains are not isolated but packed or aggregated, despite the low concentration.

Figure 4.16b and Fig. 4.16d show the transient transmission spectra of the HCS with probe polarization either parallel or orthogonal to the LC director, respectively. When the probe is polarized along the LC director, the pump-probe spectra for the HCS and the LCS are very similar. On the other hand, when the probe polarization is rotated by 90°, a completely new feature appears: in the spectral region of the keto defect fluorescence, an intense SE band (SE_k), which has never been seen before and is not present in the spectra of the LCS.

Our pump spot area is almost three times larger than the whole area shown in the confocal images (spot radius ∼75 mm), so our transient $\triangle T/T$ signal is an average of signals coming from many micro-domains comprising homogeneous areas and boundaries. However, thanks to the confocal fluorescence maps, it is possible to distinguish the origin of the two contributions. Indeed, the main contributions to the PL parallel to the director comes from the homogeneous regions. For this reason, we assume that the pump-probe signal shown

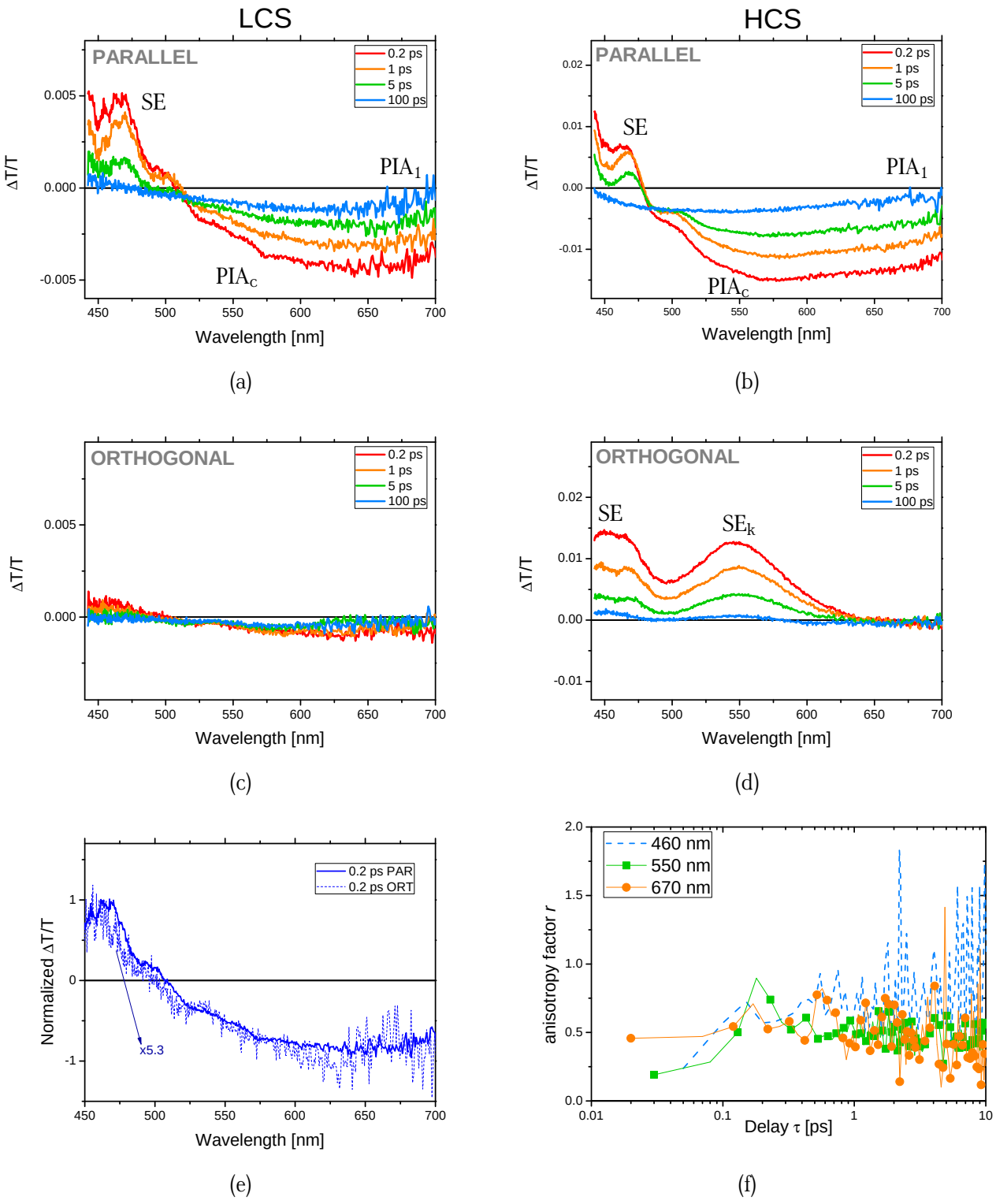

FIGURE 4.16: Transient absorption spectra of the LCS (a, c) and the HCS (b, d). For each sample we distinguish between a probe linear polarization parallel (a, b) or orthogonal (c, d) to the LC director. In (e) the comparison between the spectra at 0.2 ps for the LCS case are reported. The normalization is obtained as follows: the spectrum polarized parallel to the LC director is divided by the maximum; the other spectrum is divided by the same value as the other one and then it is multiplied by the factor 5.3. In (f) we report the temporal dynamics,for the LCS, of the anisotropy factor r at different wavelengths.

in Fig. 4.16b, similar to the one of the LCS Fig. 4.16a, is due to a few aggregated polymeric chains placed inside the micro-domains and aligned parallel to the LC director. Instead, the micro-domain boundaries, composed mainly

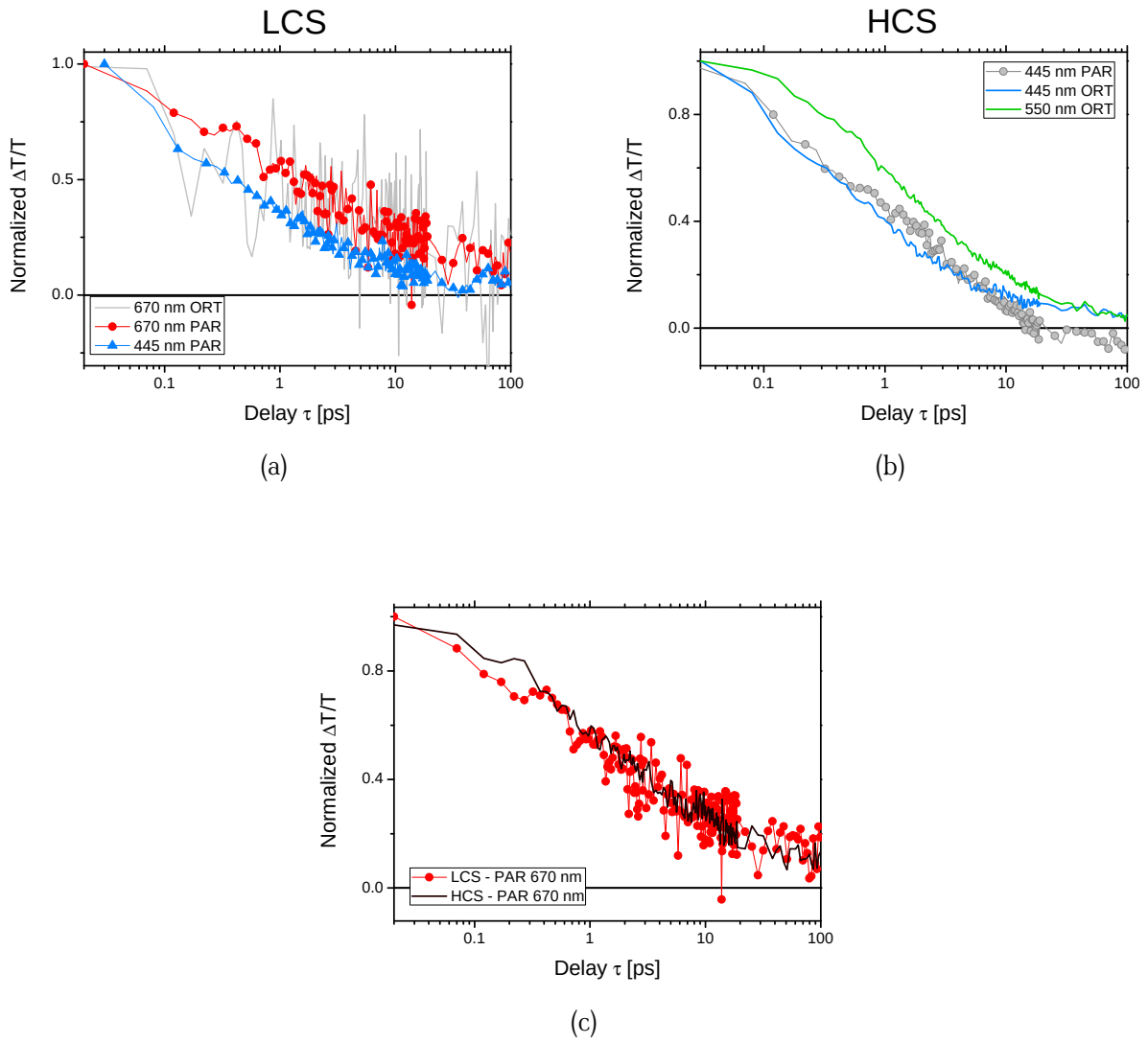

FIGURE 4.17: Comparison of the dynamics for the two polarizations of the probe (parallel and orthogonal to the LC director) and for different wavelengths in the case of LCS (a) and HCS (b); (c) comparison of the dynamics at 670 nm parallel to the LC director in the two samples.

of polymeric chains orthogonally aligned with respect to the LC director, are responsible for the signal shown in Fig. 4.16d. Interestingly, this $\triangle T/T(\lambda)$ signal does not present a PIA_c band due to inter-chain photoinduced charges, indicating that the polyfluorene chains (with and without keto defects) on the boundaries are mainly isolated. The fact that the PFO chains at the domain boundaries are mainly isolated is not surprising since their concentration in the LC matrix is very low.

A further analysis of the species present in the samples can be achieved through the temporal dynamics $\triangle T/T(\tau)$ of the different spectral regions (Fig. 4.17). Figure 4.17a reports the normalized $\triangle T/T(\tau)$ dynamics for the LCS case. The dynamics at 670 nm are the same for the probe set parallel or orthogonal to the director. The other wavelengths of the spectrum present the same behavior (not reported). This means that the same species are visible in the two signals, but that they are polarized mainly along the LC director (and therefore along the polymer chain for the LCS) [223]. In the same figure the dynamic at 445 nm is reported. The temporal decay is different from the 670 nm case, probably since the charge-induced PIA_c is overlapping the signal at a shorter wavelength.

Figure 4.17b shows the dynamics for the HCS. The two temporal dynamics (parallel and orthogonal to the director) at 445 nm (SE) and at 550 nm (SE_k, signal orthogonal to the director) have an instantaneous rise time. No competition with an underlying PIA negative signal is visible, at least within our time resolution, as typically

observed for isolated chains [194]. For the signal orthogonal to the director, the fact that the two wavelengths are characterized by a different temporal evolution confirms that the two bands are originating from different transition dipole moments: one from the defect-free polyfluorene and one from the fluorenone. The comparison with the dynamics at 445 nm parallel to the LC director underlines the effect of the charge-induced PIA at long delays. The gain is no longer present at 10 ps and the signal becomes negative. For light polarized orthogonal to the director, the optical gain is still present after 100 ps.

The dynamics at 670 nm for the two samples are characterized by the same decay time (Fig. 4.17c), indicating that the same species is present in the two cases. Indeed, the confocal maps of Fig. 4.15 show that, for the HCS, the main contribution to the signal parallel to the LC director is coming from the homogeneous small regions of the sample. These regions are very similar to the LCS. Also, the fact that the two samples show the same PIA_1 despite the larger PIA_c contribution for the HCS (due to the higher concentration of PFO) means that mainly the contribution from the exciton is present at this wavelength.

To our knowledge this is the first time that optical gain from fluorenone and its temporal decay are reported. So far, the appearance of the keto defect along the polyfluorene chain has been considered always detrimental for any photonic application, due to the fact that its presence in aggregated films induces a higher concentration of inter-chain photoinduced charges. Conversely, in our system we were able to isolate it and, by reducing inter-chain interactions, we were able to detect its transient optical gain. Our results demonstrate that the fluorenone emission originates from a single-chain defect, since sizable polymer aggregation at the boundaries of the microdomains can be excluded by the absence of the photo-induced absorption band typically associated with inter-chain photoinduced charges in aggregated samples.

4.5 Conclusion

In this Chapter we showed that it is possible to obtain optical gain from two different organic species mixed in a LC, a dye and a polymer. In both cases, when the photoluminescent molecule is homogeneously mixed in the LC host, the optical gain is polarized along the LC director.

In the case of the dye, the sample presents a homogeneous texture and a broad long-living optical gain polarized along the LC director. The dye-doped sample also supports ASE when excited with an elongated beam. Both the optical gain and the ASE peak present a red-shift of around 10 nm when their polarization changes from orthogonal to parallel to the LC director.

In the case of the polymer, by increasing the concentration in order to reach a larger gain, the sample becomes non homogeneous. Thanks to the LC nature of polyfluorene and by mixing it with a low molecular weight nematic LC matrix, we obtain a supramolecular structure where polyfluorene chains with keto defects are isolated and aligned. The peculiar phase separation between the LC and polyfluorene produces well-defined phase boundaries, with an anchoring effect so strong that the polymeric chains are forced to align parallel to these boundaries regardless of the direction of the nematic LC director induced by the rubbing layers. The optical gain studied in this Chapter is for light propagating across the thickness of the cell. When the ASE configuration was tested, no results were obtained both for the low concentration and the high concentration samples. Probably, in the first case the gain was too low, while in the second case the scattering due to the boundaries was too high to obtain ASE.

Since in this work we are interested in the optical gain in the plane of the cell, where the soliton is propagating, the PFO as amplifying medium will not be considered any further in the next chapters. Only the dye will be used in the rest of the work: it can be uniformly mixed in the LC host, it provides large and long-living optical gain, supports ASE and, as we will see in Ch. 6, in-plane lasing.

Chiral nematic liquid crystals for tuning and feedback

Chapter 5

This Chapter is dedicated to the study of the electrical response of chiral nematic liquid crystals (CLCs), and in particular to the flexoelectro-optic effect presented in Sect. 2.3.3. A new technique for aligning LCs will also be presented, the solvent-induced self-alignment. The particular alignment obtained in this way, together with the optical gain from the dye studied in the previous Chapter, will be used in Ch. 6 to obtain in-plane lasing from the cell.

This study has been carried out under the supervision of Prof. Stephen M. Morris and Prof. Steve J. Elston from the Soft Matter Photonics group, University of Oxford, where I was able to spend six months as a visiting student thanks to a Research grant from the Philippe Wiener - Maurice Anspach Foundation. The results reported here have been published in *Liquid Crystals* [224].

5.1 Uniform lying helix

As explained in Sect. 2.3.3, flexoelectro-optic switching is a fast in-plane rotation of the optic axis of CLCs and it can be observed when an electric field is applied perpendicular to the helix axis [63, 67, 79, 225].

Two different geometries can be adopted (Fig. 5.1). In the first one (Fig. 5.1a), the CLC helix is orthogonal to the cell glasses and the electric field is in the plane of the cell. Such a CLC distribution can be easily achieved with a planar alignment on the glass plates, which promotes a uniform standing helix (USH) configuration. The in-plane electric field orthogonal to the helix has to be generated with interdigitated electrodes. The advantage of this configuration is that it is quite easy to obtain a uniform alignment, since the boundary conditions match well the helix distribution. The drawback is the use of interdigitated electrodes, which can result in highly non-uniform electric fields [68, 226–228].

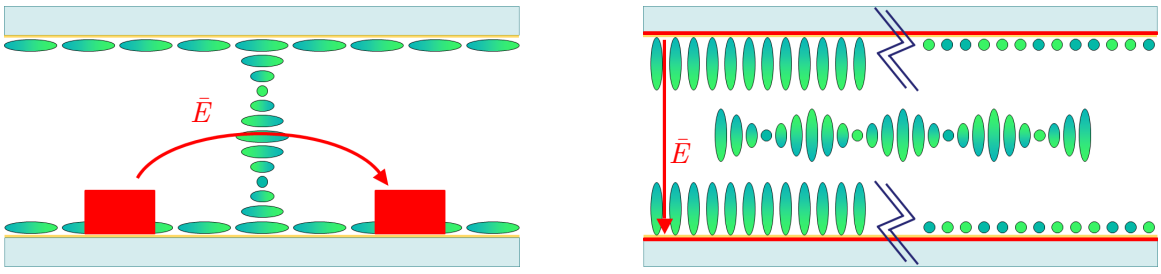

(a) (b)

Figure 5.1: (a) Uniform standing helix (USH) configuration. The planar alignment on the glasses induces a Grandjean texture of the CLC helix, while the planar electrodes generate an electric field orthogonal to the helix that is not perfectly uniform over the cell. (b) Uniform lying helix (ULH) configuration. The electric field generated by the planar electrodes is uniform over all the cell, however both the planar (right side) and the homeotropic (left side) alignments do not match the helical distribution of the CLC in some points.

In the second geometry (Fig. 5.1b), the electric field is homogeneously applied throughout the cell with planar electrodes. In this configuration, the CLC has to have its axis lying in the plane of the cell in the uniform lying helix (ULH) alignment. However, both planar and homeotropic alignments do not match the helical distribution at some points. This causes defect formation [229, 230] and difficulty in the alignment. Therefore, despite the obvious benefits in the cell fabrication for a ULH configuration, achieving a high quality alignment still remains a challenge [66, 83, 229, 231]. To date, a number of techniques have been considered to induce a ULH alignment: for example, shear flow through the application of mechanical stress to the glass substrates [231], the application of an electric field with [83] or without [232] thermal cycling, bespoke surface anchoring conditions [233, 234], periodic structured templating [235, 236] and, recently, polymer network structuring by two-photon photopolymerization [237]. Even though many of these reports have shown promising results, such techniques either require complex fabrication procedures to form the lying helix alignment or they result in a relatively low optical contrast between the bright and dark states.

In this Chapter, we present an easy to implement technique that allows for the formation of a high quality ULH configuration, the solvent evaporation technique. Solvent evaporation methods have been widely studied as an effective way of self-aligning patterns of nanoparticles: the solvent screens the weak forces among the nanoparticles that slowly start to interact as the solvent evaporation process begins [238–246]. In these systems, the interaction force among the particles is stronger than the thermal fluctuations, but, at the same time, weak enough to allow the system to reach the lowest energy equilibrium configuration [241, 245]. The weak interactions among the nanoparticles drive the self-assembly and they can be of different origins, ranging from van der Waals attraction to electrostatic interactions and hydrogen bonding [242].

The self-assembled structures can be of one-, two- and three-dimensions [239, 245, 247]. The packing, and therefore the type of lattice, can be determined by the shape of the nanoparticles [239], the interactions among the nanoparticles [239, 248] and by the boundary conditions that are used in the growth process [249]. The evaporation rate determines the regularity of the structure [250, 251], while the choice of the solvent can change the interaction among the nanoparticles, inducing aggregates or uniform layers [252, 253]. Finally, by carefully choosing the geometry of the sample, it is possible to control the direction of evaporation and therefore the direction of the growth of the lattice [249, 254].

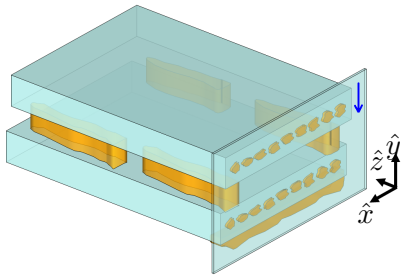

FIGURE 5.2: Scheme of the LC cell, composed by two thick glass plates coated with homeotropic alignment and a thin side window coated with planar alignment (the blue arrow is the rubbing direction). The standard glue is distributed along the edges and the highly viscous glue is used at the bottom side of the side window.

In this work we apply this technique to LCs, in particular to obtain a highly defect-free ULH alignment. In LCs, the interactions among the nanoparticles are replaced by the weak elastic forces among the LC molecules. The freedom of movement provided by the solvent allows the molecules to reach the lowest energy configuration, which is dictated by the boundary conditions. In our case, the homeotropic alignment on the glass plates and at the interface with the solvent gives rise to a ULH alignment. This is the case for the different kinds of CLC, either composed by E7 and chiral dopant (as it will be the case for this Chapter) or for mixtures with a high (∼30%wt) concentration of reactive polymer monomer (Ch. 6), indicating that this technique has a high potential for effortless defect-free LC self-alignment.

In the first part of the Chapter, the solvent evaporation technique is described in detail, together with the shear-flow one. The two ULH alignments are then characterized in terms of optical properties and electric response, the results are then compared.

5.2 Sample preparation

The cells are fabricated as described in Sect. 2.4.2, by assembling two glass plates that are spin-coated with the homeotropic alignment layer SE4811 (Nissan). The LC layer thickness is defined by 10 µm spacers. A thin (∼100 µm) glass plate coated with a planar alignment layer (rubbed Nylon 6,6) is then glued onto one edge of

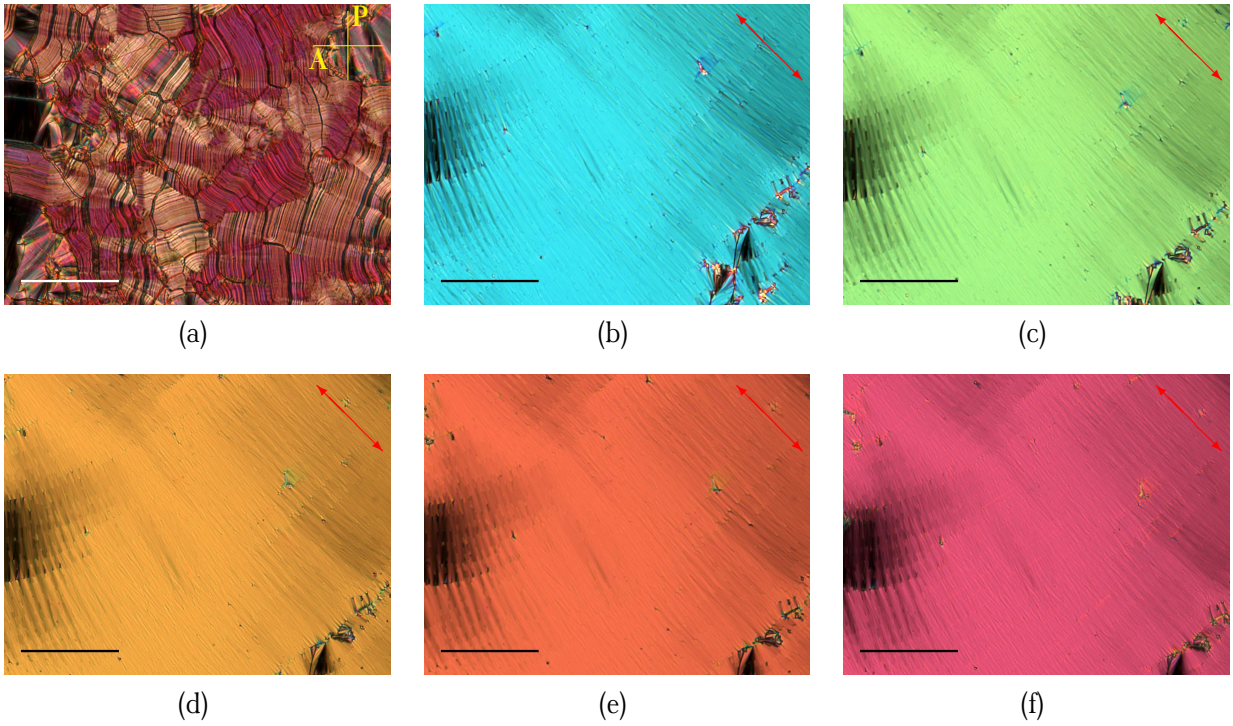

FIGURE 5.3: Polarized optical microscopy (POM) images (transmission mode) of the as-filled cell at room temperature (a) and shear-flow-induced ULH at 55 °C (b), 54 °C (c), 49 °C (d), 45 °C (e) and 36 °C (f). The red arrow indicates the helix axis orientation (scale bar: 100 µm).

the cell. The geometry of the cell is reported in Fig. 5.2. The glue is mixed with 3 µm spacer beads, in order to prevent a complete filling of the cell gap when gluing the side glass. The glue distribution on the side glass window is arranged so that it is not continuous, but instead consists of gaps to allow for a relatively slow and directional evaporation of the solvent. Finally, to add mechanical stability to the side glass wall, a highly viscous glue (Norland Optical Adhesive 68T) is used to fix the side window.

One of Chloe C. Tartan's mixtures was used to fill the cells, consisting of 3.86%wt BDH1281 chiral dopant (Merck KGaA) in E7 (Merck). The mixture exhibits a reflection band in the range 530 nm - 605 nm and, consequently, a pitch of ∼350 nm. Two kinds of ULH alignments are grown in the same glass cell, first the shear-flow in one side of the cell and then the solvent-induced one in the other side. This is done in order to have a direct comparison between the well-known shear-flow technique with the solvent-induced method proposed here, when all the other parameters are the same (mixture and cell parameters).

5.2.1 Shear-flow technique

Fig. 5.3 reports the steps of the ULH formation with the shear-flow technique. The pristine state of the cell presents a focal conic texture (Fig. 5.3a), due to the fact that the cell is filled with the CLC above the clearing temperature and then cooled without any particular precaution. The helix axis is therefore randomly oriented in the cell, due to the mismatch of the boundary conditions on the glass substrates.

The sample is heated above the clearing temperature (62 °C). The cell is then slowly cooled in the presence of a voltage of ±5 V at 1kHz while mechanically shearing the cell to induce an oscillatory flow. The electric field promotes the ULH over the Grandjean texture, while the shear flow establishes the orthogonality of the helix axis relative to the direction of the flow [66, 231, 255]. The shear-flow action is particularly important during the transition between the isotropic and the nematic phase, when the molecular mobility is still quite high and one direction for the helix axis has to emerge among all the others in the plane of the cell. Once the ULH is established, the sample is slowly cooled. Fig. 5.3 reports the evolution of the ULH texture decreasing the temperature. The change in color is due to the temperature-induced change in the birefringence and in the pitch of the CLC [256].

5.2.2 Solvent evaporation technique

The solvent-induced ULH is then grown at room temperature by depositing a small quantity (few µl) of acetone onto the entrance/opening of the cell which was pre-filled with the CLC mixture. The small amounts of acetone that enters the cell by capillary action is not enough to displace the LC from the cell but instead it diffuses into the LC, in a sufficient quantity to cause a transition from the liquid crystalline to the isotropic state. In Fig. 5.4, it is possible to observe the as-filled CLC texture that is not directly influenced by the solvent (top right of Fig. 5.4), together with the interface between the isotropic state (larger concentration of acetone, black region) and the LC phase (low concentration of acetone, colored region). The color sequence adjacent to the black isotropic region towards the center of the cell is indicative of an increase in the birefringence. This arises due to a gradient in the diffusion of the acetone inside the cell and a consequent gradient of the LC concentration in the direction of the diffusion. Due to the confinement provided by the two glass plates forming the cell, the acetone gradually evaporates from the edge of the cell. Depending on the region we are looking at, the solvent can evaporate from the side window or from the open entrance of the cell. The evaporation process leads to a progression in the acetone concentration gradient and is therefore visualized by the progress of the colors over time.

Only a very small flow of the LC is associated with this process. In fact, flow alignment, and similarly diffusion, both tend to align CLCs with their helical axis perpendicular to the flow direction because flow/diffusion

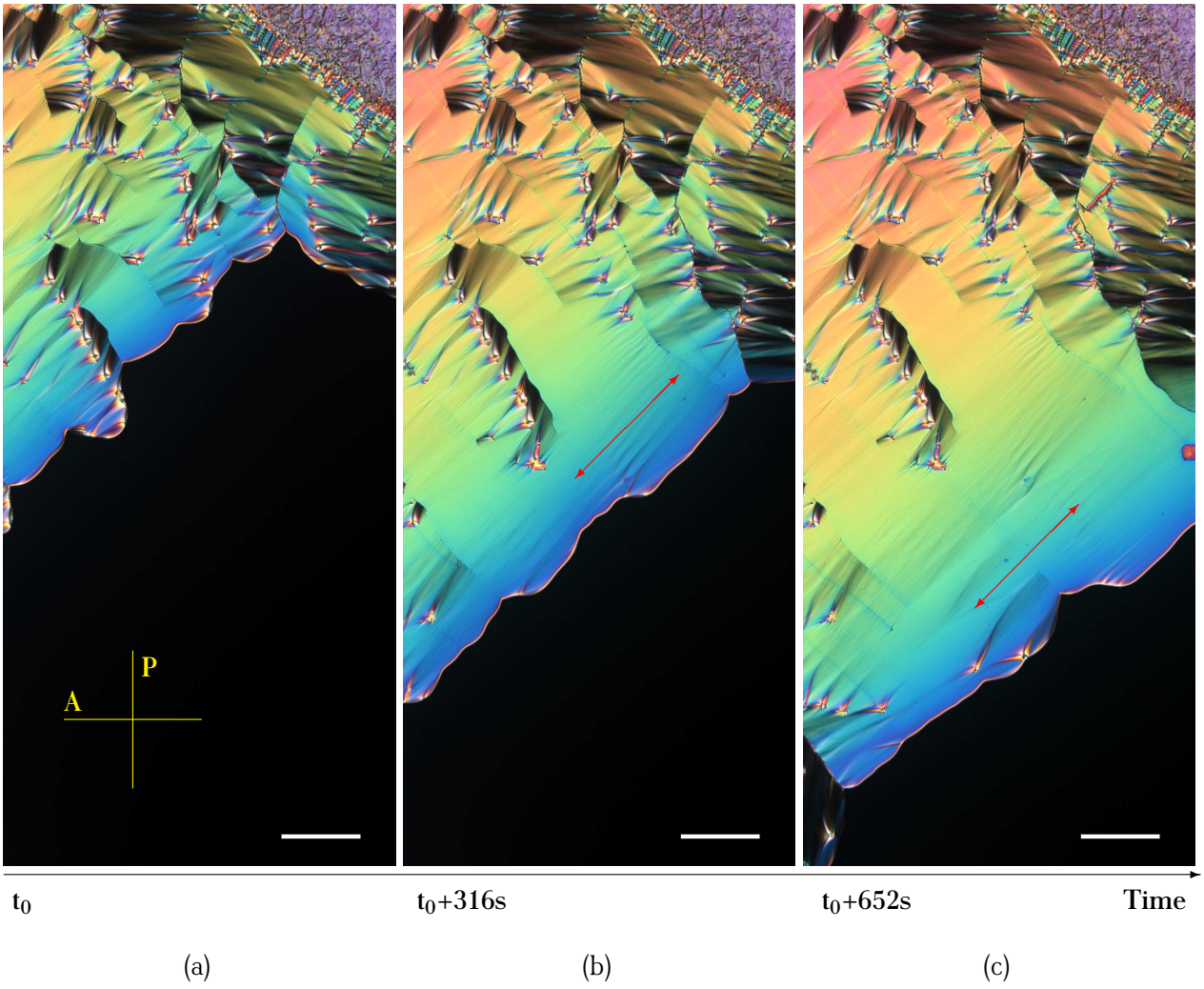

FIGURE 5.4: POM images (transmission mode) of the formation of the ULH alignment over time. The black areas are the isotropic regions induced by the acetone, while the rainbow colors in the ULH are due to a birefringence gradient dictated by an increasing concentration of acetone towards the black region. The red arrow indicates the helix axis orientation (scale bar: 100 µm).

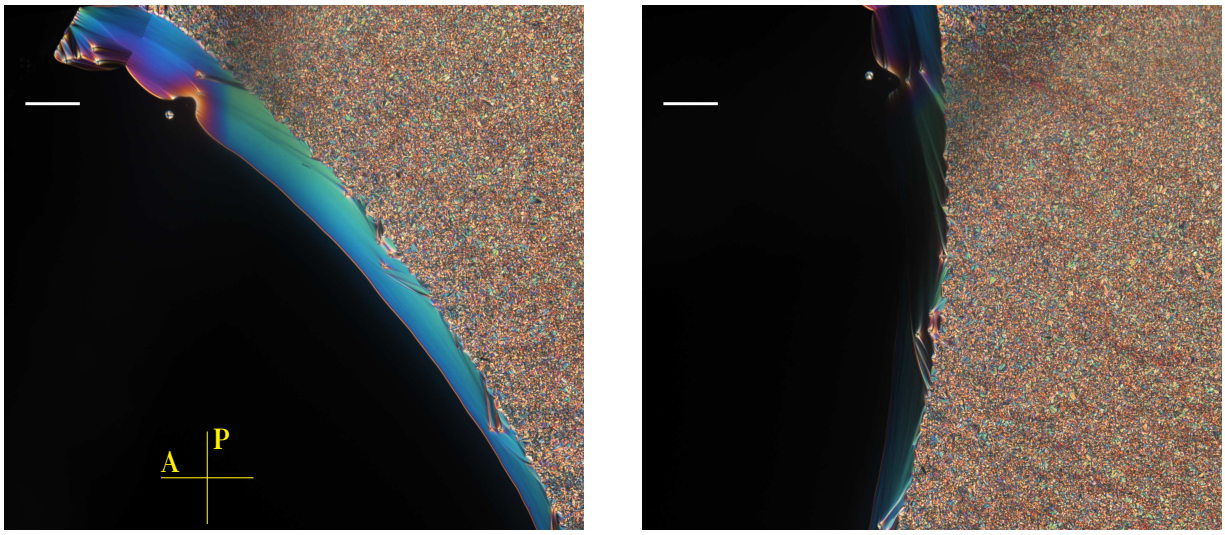

(a) (b)

FIGURE 5.5: POM images (transmission mode) of the bright (a) and dark (b) states of the solvent-induced ULH growth in the case where the diffusion/evaporation is not unidirectional. The helix axis is parallel to the curved front between the isotropic and LC phases (scale bar: 100 µm).

along the helical axis is hindered [231].

A way to evaluate the importance of the flow-induced alignment is the Ericksen number [257]

$$Er = \frac{\eta v L}{K} \tag{5.1}$$

where v is the flow velocity ($v \simeq 0.6 \times 10^{-6}$ µm/s, extracted from the image sequence shown in Fig. 5.4), L is the characteristic length scale of the system ($L = 10$ µm, the thickness of the cell), η=0.08 Pa·s is the viscosity of the LC and $K = K_3 = 16$ pN is the highest of the three elastic constants of the LC (see Tab. 2.1 for the E7 coefficients). With these values, we obtain $Er \simeq 0.03 \ll 1$, indicating that the effect of flow is probably insignificant for the alignment of the LC in our case [257]. Also note that v is evaluated with the velocity of the phase transition front, which is only the upper bound for the actual LC velocity, so the flow effect is likely to be rather small. Indeed, the few defects which are present in regions where the ULH has formed do not change position while the birefringence colors change as the acetone diffuses from the cell, indicating that the acetone concentration is low and it slowly decreases without significant flow of the LC. However, if the flow does contribute to the alignment, it is such that the helix axis would form parallel to the evaporation front and orthogonal to the shear flow. From Fig. 5.4 it is possible to see that the ULH texture is formed over the course of several minutes. However, the slow color progression indicates that an amount of solvent may remain in the sample. For this reason we left the solvent to completely evaporate (and the cell to acquire a uniform color) over a period of two days before the device characterization was carried out.

Due to the slow evaporation rate of the acetone coupled with the high mobility of the LC molecules in the solvent-induced isotropic state, the LC molecules at the isotropic/nematic interface are able to rearrange themselves in a lower energy configuration, which is dictated by the chirality of the mixture, the spin-coated homeotropic surface on the two glasses and the homeotropic alignment at the interface with the acetone (a polar solvent) [258]. For these reasons, the helix is lying in the plane of the cell at the interface, with its axis parallel to the evaporation boundary. The orientation of the helix axis has been verified with a Berek compensator.

In Fig. 5.5 we show that, when the evaporation/diffusion process takes place far from the side window, the isotropic-nematic interface front can be curved and the helix axis orientation follows the shape of the phase-transition front. It is also possible to see that the ULH alignment is reached independently of the initial conditions of the LC alignment (focal conic texture in our case, as can be seen in the left part of the Fig. 5.5). Indeed, the LC self-assembly, starting from an isotropic-like phase where the LC molecules are randomly oriented in the

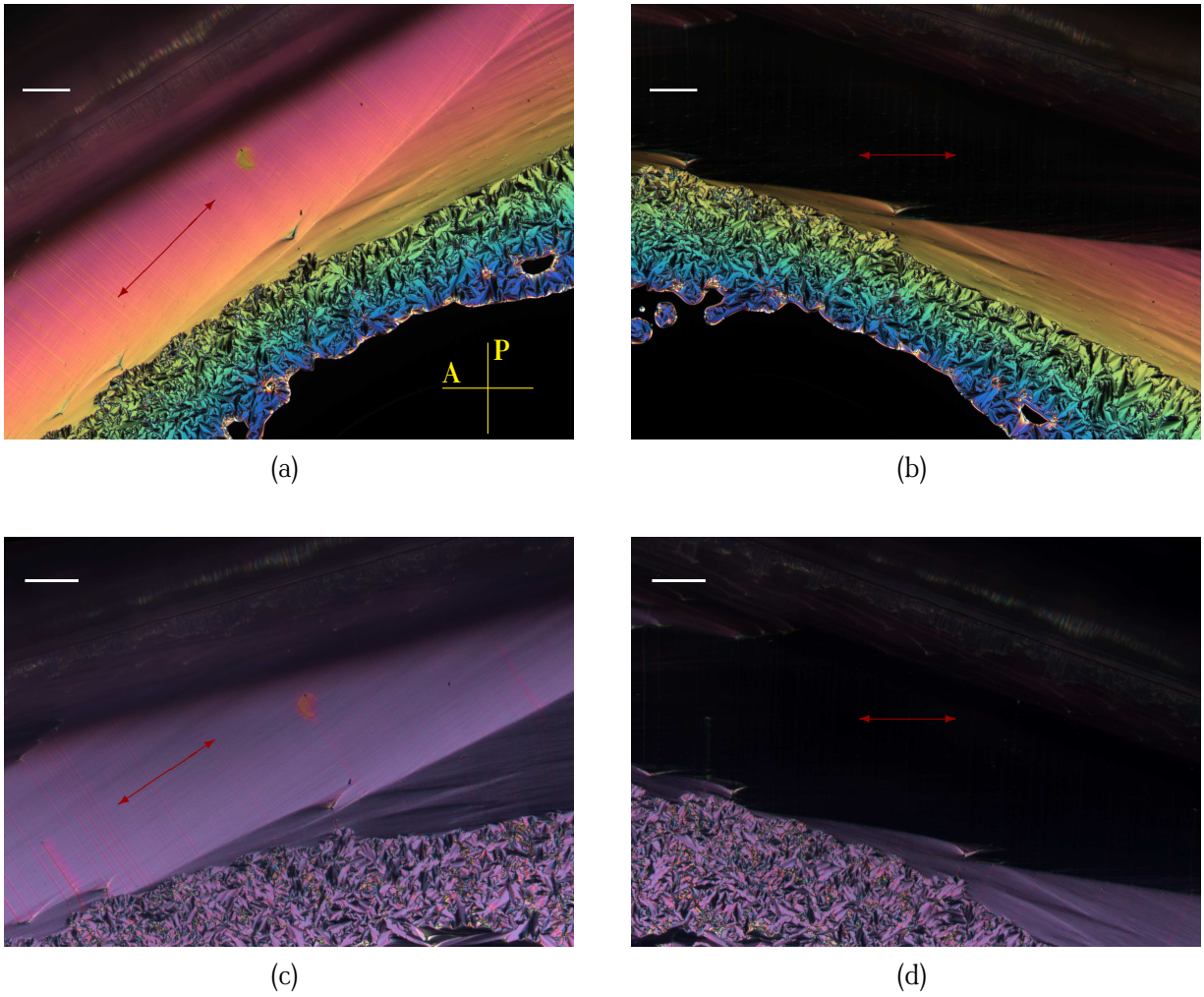

FIGURE 5.6: POM images (transmission mode) of the bright (a,c) and dark (b,d) states of the solvent-induced ULH growth in the case where the diffusion and evaporation is controlled by the side window. The color sequence, indicating a gradient of the birefringence, is present during the solvent diffusion and evaporation (a,b), while a uniform sample is obtained when no acetone is left in the sample (c,d). The ghost image in the upper part of the figures is due to the reflection from the side glass window, while the glue used to fix the glass also leads to a blurry dark shadow close to the edge. The red arrow indicates the helix axis orientation (scale bar: 100 µm).

solvent, is only dictated by the interaction among the molecules, the boundary conditions and the direction of the solvent diffusion. It is for this reason that the side glass mentioned above was added to the cell, in order to control the solvent evaporation and hence diffusion direction within the cell.

In Fig. 5.6 we show the result of the self-assembly close to the side window, during (a-b) and after (c-d) the complete evaporation of the solvent. In this region the highly homogeneous ULH alignment extends over several hundreds of micrometers. Its extent is only limited by the fact that, after initial evaporation of the solvent close to the edge, the acetone tends to be trapped in the central region of the cell, where it tends to diffuse in all directions at the same time, generating the rather scrambled alignment texture visible in the lower region of the images. Close to the edge of the device, the evaporation/diffusion is almost unidirectional and the ULH grows into much larger homogeneous regions (Fig. 5.6). Indeed, the diffusion direction is orthogonal (or close to orthogonal) with respect to the side window. The almost flat front of the phase transition then causes the helix axis orientation to be homogeneous over large regions.

5.3 Contrast ratio

In this Section, we analyze the optical quality of the ULH alignments obtained with the two methods. In both cases, the images are taken with no voltage applied and at room temperature (∼23 °C).

Fig. 5.7 reports the bright (a,b) and dark (c,d) states for the respective shear flow and solvent-induced ULH alignments (in the region toward the side window). The ULH sample acts as a uniaxial material for wavelengths larger than the CLC pitch, as it is in this case. The ordinary refractive index experienced by the light linearly polarized along the helix axis is $n_{\perp}$, while the light polarized orthogonal to it experiences an effective refractive index given by the average of $n_{\parallel}$ and $n_{\perp}$.

The bright state of the shear flow induced ULH exhibits some striping in the direction of the helix axis, which is comparatively non-existent in the solvent-induced alignment. Enhancing the acquisition time of the camera (Fig. 5.7e,f), it is possible to visualize the defects in the dark state images, where the elongated domains from the shear-flow case are much more evident, and the homogeneous texture for the solvent case is highlighted. Some

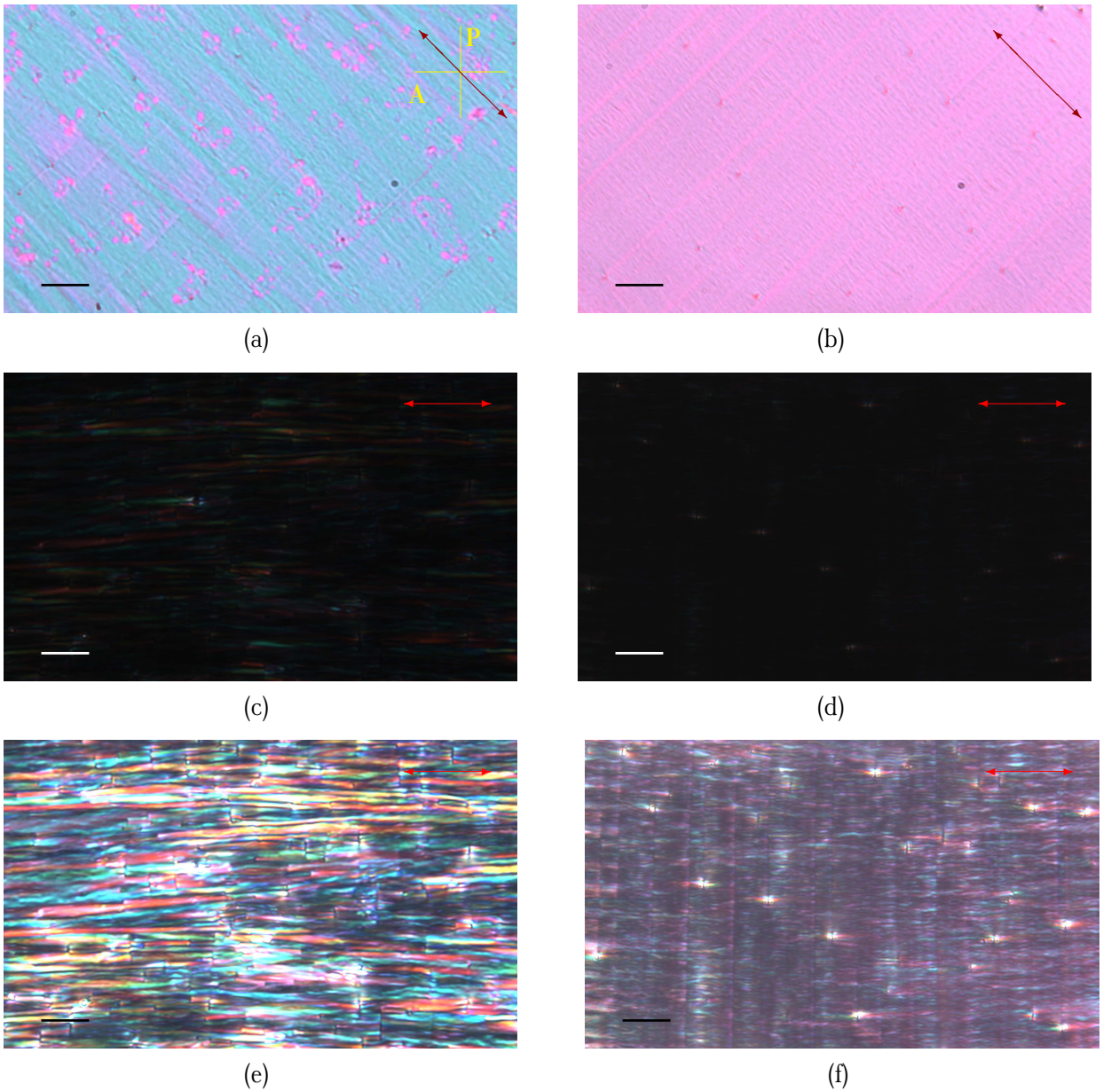

FIGURE 5.7: POM images (transmission mode) of the bright and dark states for the shear-flow (a,c,e) and solvent (b,d,f) induced ULH alignment; (e,f) enhanced brightness images of the dark states. The red arrow indicates the helix axis orientation (scale bar: 20 µm).

defect points of a few μm in diameter are still visible in the solvent-induced ULH, but the improvement in the alignment is evident.

In order to quantify the quality of the ULH texture, we measured the contrast ratio (CR), defined as the ratio of the intensity of the bright state to the intensity of the dark state. The images of the bright and the dark states for the same ULH are taken with the same integration time, in order to be able to compare the transmission for the two states. The intensity is averaged over an area of around 100 μm^2 and, for both the dark and the bright state, the dark level for the camera is subtracted. The CR is measured with a broad-spectrum white light source focused on the sample with the condenser of the microscope set to a numerical aperture (NA) of 0.8, and collected with a 50x objective (Nikon, NA=0.7). For the shear flow case, a large amount of micro-domains can be seen in Fig. 5.7e. The difference in the orientation of the optic axis between each sub-domain leads to optical scattering that degrades the overall quality of the dark state, resulting in a CR of ~ 30. However, for the solvent-induced ULH alignment case we obtain a CR of ~ 120, on account of the largely defect-free structure that results from the latter technique. For this reason, the CR increases by a factor of four for the solvent-induced case, demonstrating the higher quality of the ULH alignment. For comparison, using the same measurement technique, the CR for a planar nematic E7 device of 5 μm thickness was found to be ~ 160. Therefore, the contrast ratio of the solvent-induced ULH aligned device is approaching that of a planar aligned nematic device with a similar optical retardation. This underlines the highly uniform ULH alignment that is possible to obtain with this technique.

5.4 Flexoelectro-optic effect

In this Section, after a brief introduction on the method used to measure the reorientation angle of the CLC optic axis, the flexoelectro-optic responses for the two ULH alignments are compared.

5.4.1 Measurement of the tilt angle

A square-wave electric field is applied to the LC cell to characterize the flexoelectro-optic response. As presented in Ch. 2, for small angles, the tilt of the CLC optic axis induced by the flexoelectro-optic response is a near-linear function of the amplitude of the electric field. In the case of a helix with a pitch fixed at the natural pitch p_0, the tilt angle follows the relation given by Eq. (2.36), rewritten here for clarity

$$\tan\phi = \frac{p_0}{2\pi}\frac{(e_1 - e_3)}{2K_2}E - \frac{K_1 - 2K_2 + K_3}{2K_2}\sin\phi, \tag{5.2}$$

where, as a reminder, ϕ is the tilt angle of the optic axis with respect to the helix axis, E is the magnitude of the applied electric field, K_1, K_2 and K_3 are the splay, twist and bend elastic coefficients, respectively, and e_1 and e_3 are the splay and bend flexoelectric coefficients, respectively.

The reorientation angle due to the flexoelectro-optic response is measured using the following standard technique [233, 237]. The cell is placed on the microscope with the collected transmitted light passing to a photo-diode connected to an amplifier to measure the intensity of the light transmitted by the cell (measured in [V]). No electric field is applied at this stage. Since the pitch of the ULH is shorter than the wavelength of visible light, the ULH layer acts as an optically uniaxial material. The transmission is therefore described by $T = T_{max}\sin^2(2\eta)$, where η is the angle between the ULH field-dependent optic axis and the transmission axis of one of the polarizers, and T_{max} is the difference in transmission between the bright and the dark states. T_{max} is measured in the sample. Then, the ULH is placed with the helix axis at 22.5° from the polarizer axis, in the linear regime of the transmission response. In that case, the amplitude $\triangle\eta$ of small fluctuations in the optic axis orientation angle is related to the amplitude $\triangle T$ of the modulated transmission through the relation

$$\triangle\eta = \triangle T/(2T_{max}). \tag{5.3}$$

A square wave of amplitude E is then applied to the cell. After an equilibrium is reached, the transmitted intensity for the reorientation of the ULH is recorded as a function of time (Fig. 5.8a). From the measurement of the amplitude of the modulation it is possible to obtain the reorientation angle $\triangle\eta$ [Eq. (5.3)], which is the electric field dependent tilt angle ϕ in Eq. (5.2).

5.4.2 Flexoelectro-optic characterization

Both the shear-flow-induced and solvent-induced ULH alignments exhibit a flexoelectro-optic response when an a.c. electric field is applied. The temporal dynamics of the transmitted intensity for both ULH states is shown in Fig. 5.8a. In the Figure, the offset of every curve has been subtracted to simplify the comparison. For low voltages, both textures tend to show the same dynamic behavior, while, for higher voltages, we observe a drop in the response for the solvent-induced alignment. The response time, defined as the time required for the transmission to increase from 10% to 90%, decreased from 70 µs to 50 µs when the electric field increased from 1.5 V/µm to 5 V/µm for both textures. From the amplitudes of the data shown in Fig. 5.8a we can extract the tilt angle ϕ as a function of the electric field as explained above. Fitting Eq. (5.2) to the experimental data, it is possible to find the value for the flexoelectric difference $e_1 - e_3$ that provides the best-fit, as shown in Fig. 5.8. Using the values for the elastic constants reported in Tab. 2.1 and p_0 =350 nm, we obtain $e_1 - e_3 = 12.1 \pm 1.0$ pC/m for both the shear-flow-induced and solvent-induced alignment, indicating that no solvent or impurities are left in the sample, as this would tend to influence the flexoelectro-optic response. Also, the value for $e_1 - e_3$ is in good agreement with the values reported in the literature [83, 233].

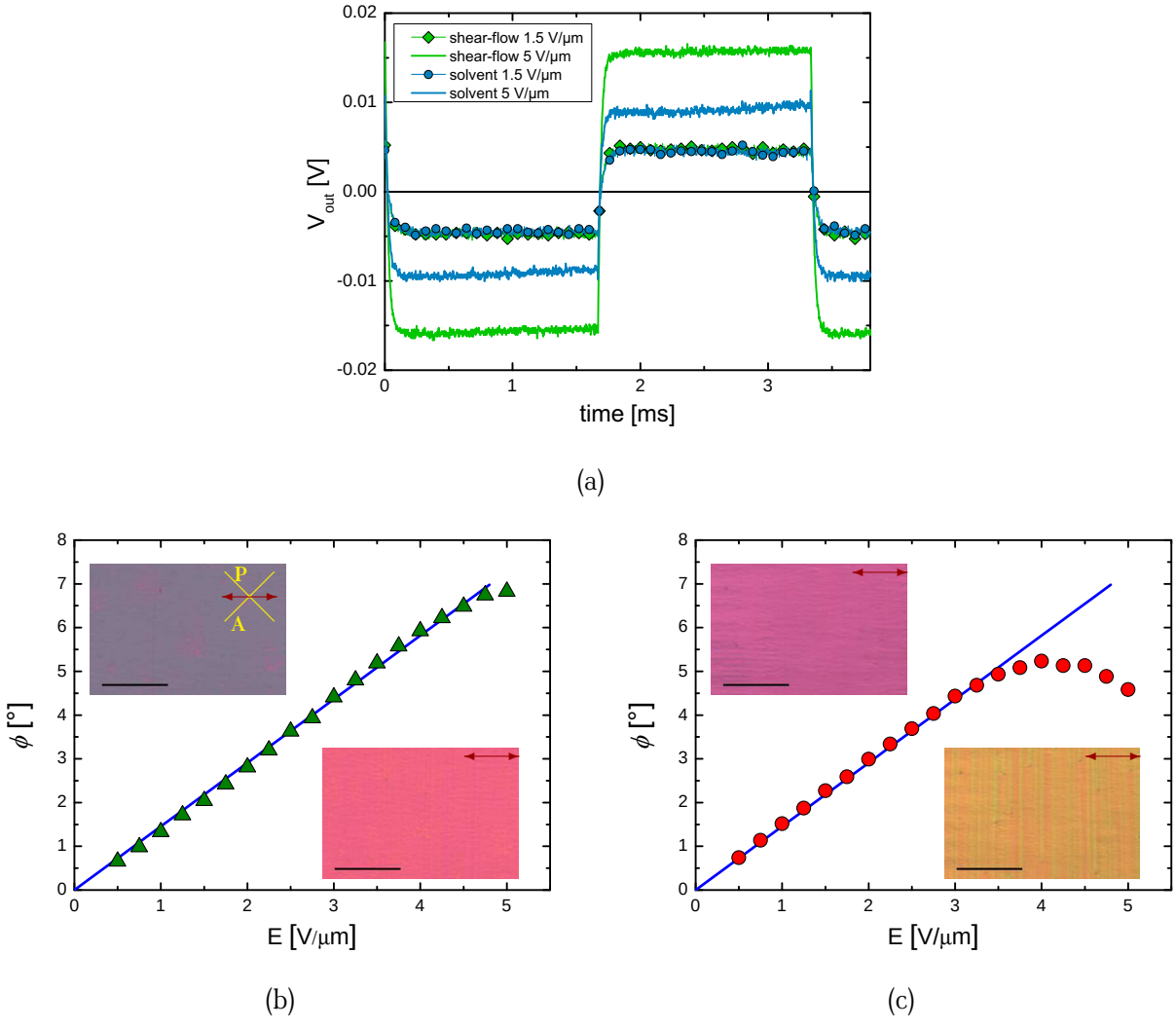

FIGURE 5.8: (a) Temporal dynamics of the transmitted light through the ULH CLC between two crossed polarisers, for both types of alignment at two different voltages; the offset of every dynamic plot has been subtracted. (b-c) Experimental values (symbols) and fit based on Eq. (5.2) (line) of the tilt angle of the optic axis as a function of electric field for the shear-flow (b) and the solvent (c) induced ULH. The frequency of the square-wave electric field was 300 Hz. Insets: POM images (transmission mode) of the alignment at E =2.5 V/µm (top left) and E =5.0 V/µm (bottom right) for the shear flow (b) and the solvent (c) induced ULH. The red arrow indicates the helix axis orientation (scale bar: 50 µm).

Increasing the field amplitude, the tilt angle of the shear-flow-induced ULH remains approximately linear over the entire electric field regime considered here, with a small deviation at 5 V/µm. The shear-flow-induced ULH texture also appears to remain homogeneous for all field strengths (insets Fig. 5.8b).

On the other hand, the tilt angle for the solvent-induced ULH deviates substantially from linear behavior for electric fields greater than around 4 V/µm. Interestingly, above this field strength, defect lines are observed propagating orthogonal to the helix axis (insets Fig. 5.8c). Of course, some distortion in the helix may be expected for applied fields approaching the critical field E_c [259]. However, importantly, here it seems that unwinding is taking place through the propagation of the defect lines for fields greater than around 4 V/µm. The critical field for the unwinding of the helix, including the flexoelectric contribution, is given by Eq. (2.25), which is rewritten here for simplicity of reading:

$$E_c = \frac{\pi^2}{p_0}\sqrt{\frac{K_2}{\varepsilon_0 \triangle\varepsilon - \frac{\pi^2(e_1-e_3)^2}{16(K_1+K_3)}}}. \tag{5.4}$$

For the values of the physical constants for E7 reported in Tab. 2.1 and for the value of $e_1 - e_3$ obtained above, the critical electric field is $E_c = 6.9$ V/µm.

When the applied electric field approaches this value, the constrained pitch of the helix is somewhat different from its equilibrium value. There is therefore a tendency for the helix pitch to change through an unwinding process. In principle, two unwinding mechanisms are possible, one where the pitch changes continuously, and one where the pitch changes discontinuously (through defect formation/growth). In general, we do not expect the first of these to take place in ULH devices due to surface and bulk helix pinning interactions. However, helix unwinding through defect formation/growth is possible. Interestingly, we observe this to be much more prevalent in the high quality solvent-induced ULH alignment (inset of Fig.5.8c) than in the lower quality shear-flow induced alignment. It therefore appears that the high concentration of domain edges in the latter case tends to block the growth of the unwinding lines (i.e. growth of defects and dislocations are pinned). In the unwound portions of the helix, the dielectric interaction tends to suppress the flexoelectro-optic tilt angle and therefore we observe a drop in the electro-optic response at higher fields for the solvent-induced ULH alignment where significant helix unwinding takes place (Fig. 5.8c). This indicates that in practice structural stabilization, using for example a polymer network, is very important to ensure electric field-stability of the solvent-induced ULH structure [237]. This is crucial in the case where the ULH is used to provide the feedback for lasing, since in that case a disruption of the periodicity would deteriorate the laser emission. The polymer-stabilized ULH will be the subject of Sect. 6.2.

5.5 Spatial instabilities

Finally, the high degree of homogeneity in the solvent-induced ULH allows for the observation of an apparent periodic buckling instability in some regions of the device. Even if the details of the instability and its origin are not clear and even if further investigation is not possible for lack of time, we decided to report here the experimental observations for sake of completeness.

The wave-vector of the instability occurs in planes containing the nematic director, which are perpendicular to the helix axis of the ULH alignment (Fig. 5.9). The period, Γ, of this instability is independent of the frequency of the applied electric field in the range of 40 Hz to 100 kHz and it decreases by increasing the amplitude of the electric field.

The period of the observed instability appears to follow the behavior normally expected for flexoelectric instabilities in achiral nematics described by Eq. (2.19), reported here for simplicity of reading

$$\Gamma = \frac{\pi\,(K_1 + K_3)}{(e_1 - e_3)\,E}, \tag{5.5}$$

where the electric field E is applied along the director of the nematic and the bend-splay periodic deformation takes place orthogonal to it (see Fig. 2.4e). In Fig. 5.10 we report the experimental evolution of the period and the fit given by Eq. (5.5), where $e_1 - e_3 = 12.1$ pC/m as found in the previous section.

Experimentally, the period appears to reach a plateau at low electric fields, which is not taken into account in the theory. Indeed, it seems that the maximum period length is limited to one or two times the thickness

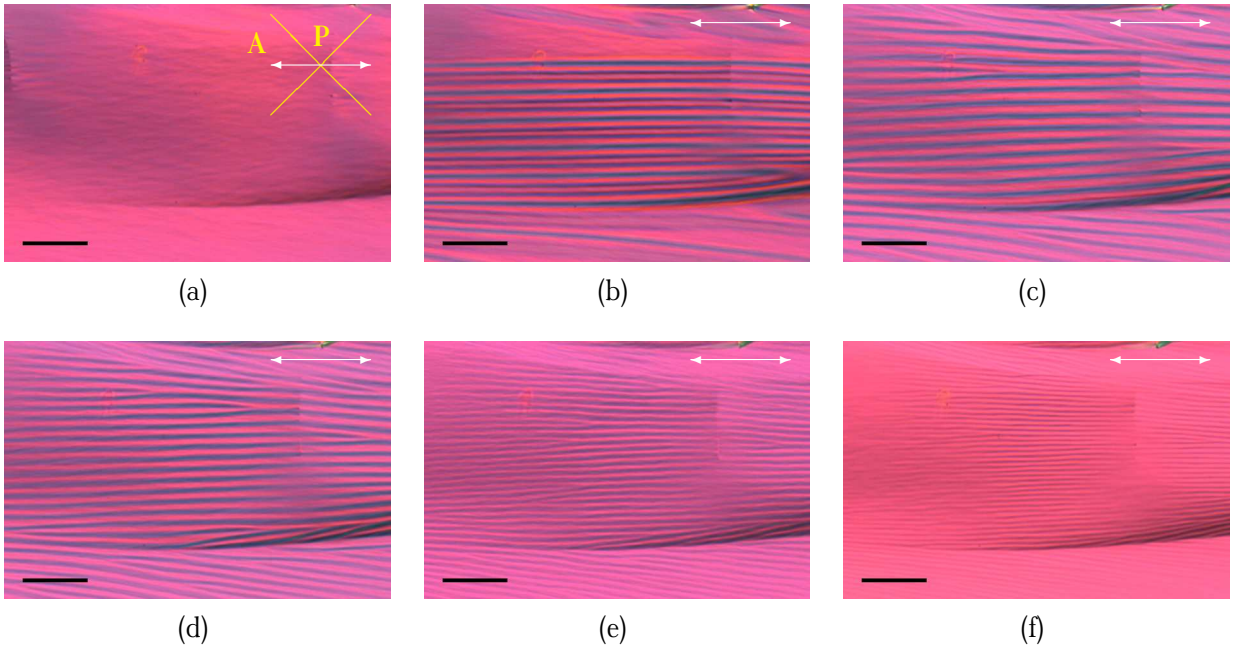

FIGURE 5.9: POM images (transmission mode) of the equilibrium states of the instabilities in the ULH for electric fields of 0 V/µm, 0.15 V/µm, 0.75 V/µm, 1 V/µm, 1.75 V/µm, 3 V/µm, (a)-(f). The white arrow indicates the helix axis orientation (scale bar is 50 µm).

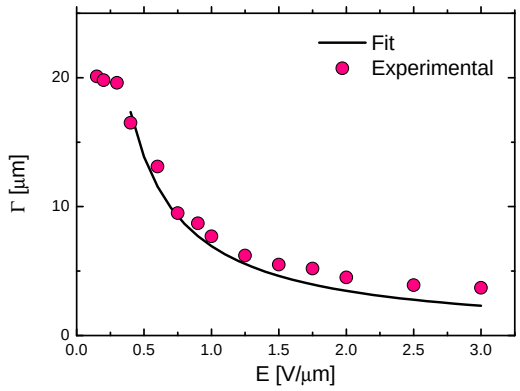

FIGURE 5.10: Experimental and theoretical evolution of the period Γ as a function of the applied electric field.

of the cell. Of course, a systematic study of the instability for different cell thicknesses should be performed to support this theory.

The basis of Eq. (5.5) is a d.c. field induced bend-splay instability in a nematic, whereas the signal applied to our device is a.c. (square wave) - it is therefore not entirely clear why it might be applicable here. Normally, the flexoelectrically induced tilt angle given by Eq. (5.2) is associated with bend-splay structures in planes containing the reoriented nematic director, but instabilities of the form observed here are not generally seen in chiral nematics in a ULH state. Indeed, further investigation is required to fully understand the origin of this behavior.

5.6 In-plane characterization

Until now, the side window was exploited to induce a slow and directional evaporation of the solvent. Originally, this same side window should have allowed the observation of the ULH optical band-gap in the plane of the cell. However, it was not possible to completely fill the cell, as a thin air bubble was always present between

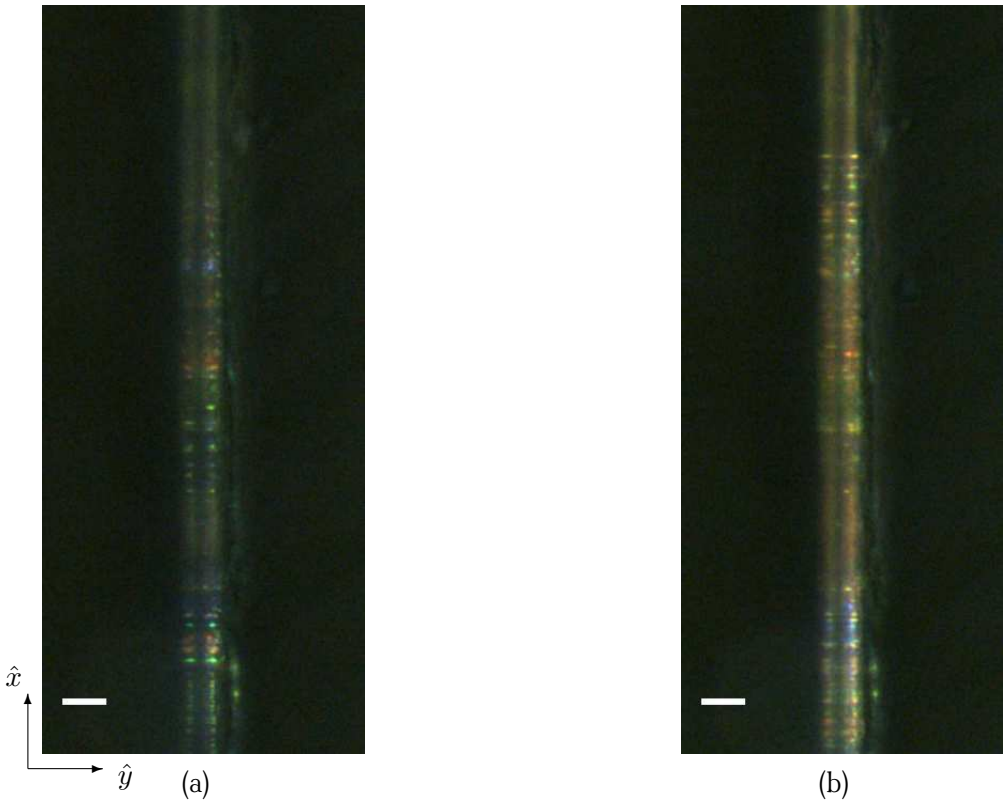

FIGURE 5.11: POM images (reflection mode) of the cell filled close to the side window in the case where (a) no field and (b) an electric field of 2.5 V/µm (1 kHz) is applied (scale bar: 20 µm).

the LC and the side glass. We believe that this was due to the fact the E7 LC tends to form large contact angles at the interface with the Nissan SE4811 alignment layer compared to other alignment layers [260]. Close to the side window, the formation of a meniscus at the LC interface is also promoted by the very small gap due to the spacers (∼3 µm), the roughness of the side facets of the large glass plates and the small thickness of the cell (10 µm). This air gap is very difficult to avoid, even with repeated thermal cycles or by filling the cell in vacuum. Since the cells were fabricates in the UGent facilities, it was not possible to change the alignment layer to improve the filling during my six-month stay in Oxford.

Even if the interface towards the side window always presented defects, it is possible to observe some light reflection from the side window. Fig. 5.11 reports the light reflected from the side window for no field and an electric field of 2.5 V/µm. The images are taken with the optical microscope in reflection mode, since we are looking at the reflection due to the optical band-gap of the CLC. If a uniform ULH was present, with the HA along the $\hat{z}$ axis, we should be able to see a uniform reflective region corresponding to the reflection of the ULH. However, in our case, the distribution is not homogeneous enough to measure the reflection spectrum, however, it is possible to observe a change in the color when an electric field is applied.

5.7 Conclusion

In this Chapter we have demonstrated how a solvent-induced self-assembly technique can be applied to LC alignments. The slow and directional diffusion/evaporation of the solvent allows the system to reach the minimal energy configuration, which corresponds to the ULH state in our case. The ULH obtained with this technique exhibits an extremely homogeneous alignment that translates into a high optical quality and a larger contrast ratio than is typically observed using conventional alignment procedures, with the advantage that no external stimulus is needed to obtain the alignment. The flexoelectro-optic response shows that the technique does not alter the electric response (at low fields), while increasing the optical quality of the alignment. We believe that this technique could provide new opportunities for defect-free self-assembly of LC textures and phases, with

particular interest for templated and structured devices, where LC defects are difficult to avoid.

Even though these regions are only a few hundreds of micrometers across, they can be of interest for applications such as thin film lasers [261] and spatial light modulator technology [69], where small high-quality areas of alignment are required. Indeed, in the next Chapter, this technique will be applied to other mixtures with photo-polymerizable polymer dissolved in it and we will demonstrate lasing from polymer-stabilized dye-doped solvent-induced ULH.

Interplay between gain, nonlinearities and feedback

Chapter 6

The aim of this Chapter is to combine the different concepts and phenomena presented in this thesis. In the first part of the Chapter, the nonlinear propagation in LCs (Ch. 3) will be combined with the ASE observed in dye-doped LC samples (Ch. 4). We will show how the waveguide induced by the soliton can be used to collect and extract the ASE generated in the same sample. These results have been published in *Optics Letters* [131].

In the second part of the Chapter, the optical gain provided by the dye will be combined with the feedback provided by the CLC to induce laser emission. In particular, the ULH alignment configuration will be exploited in order to observe in-plane laser emission. The aim of that Section is to use the flexoelectro-optic effect in order to have sub-ms tuning or switching of the lasing emission. Even if this last aspect is only outlined in this Chapter, we decided to report here the results since they are the preliminary interesting steps towards a fast-switching in-plane laser.

6.1 ASE and nematicon

In Ch. 4 we presented some of the advantages of dispersing photoluminescent materials in LCs, such as polarized emission or suppression of charge formation. The main drawback of LC as a host for photoluminescent materials is their need to be integrated onto macroscopic aligning substrates, in order to have a macroscopic order of the LC. In the case where the emission is orthogonal to the substrates, there is no particular issue with the extraction of the light. However, when the emission is in the plane of the cell, such as for ASE or (as it will be seen in the next Section) for in-plane lasing, the collection and the extraction of the light can be more difficult. The edges of the cell are either sealed with glue or left open; in both cases a depolarization and a de-focusing of the beam take place. Also, in the case of ASE, the divergence of the source is quite high. This implies that the excitation stripe has to be close to the edge of the cell in order to be able to efficiently collect the light at the output of the device. This configuration would also cause the scattering of the pump beam due to the cell edges, deteriorating the beam output profile and making necessary a color filtering at the output of the device.

In this Section a new way to efficiently collect and extract the ASE from a LC cell is proposed, through the combined action of a nematicon and an optical fiber slid into the cell. The nematicon waveguide induced at the fiber end collects the ASE and guides it back into the fiber, and then outside of the device where it can be used for applications, such as incoherent lighting or optical coherent tomography [47–49]. The ASE guided by the nematicon does not diffract along the propagation direction, in this way it is better injected into the fiber than a diffracted beam. We demonstrate that the presence of the soliton increases the intensity of the ASE collected by the fiber by one order of magnitude. Finally, also referring the ultra-fast spectroscopy technique presented in Ch. 4, we show that the ASE wavelength tunability, obtained as a function of the soliton power, depends mainly on the interaction with the nematicon rather than on the gain anisotropy of the dye molecules.

6.1.1 The optical setup

The 75-µm-thick LC cell is the same as that used for the nematicon observation in Ch. 3. The cell glass substrates are coated with nylon and then rubbed in order to induce a preferential orientation of the LC director on these two surfaces. The rubbing direction is at 45° with respect to the cell edges. Once assembled, the cell is infiltrated

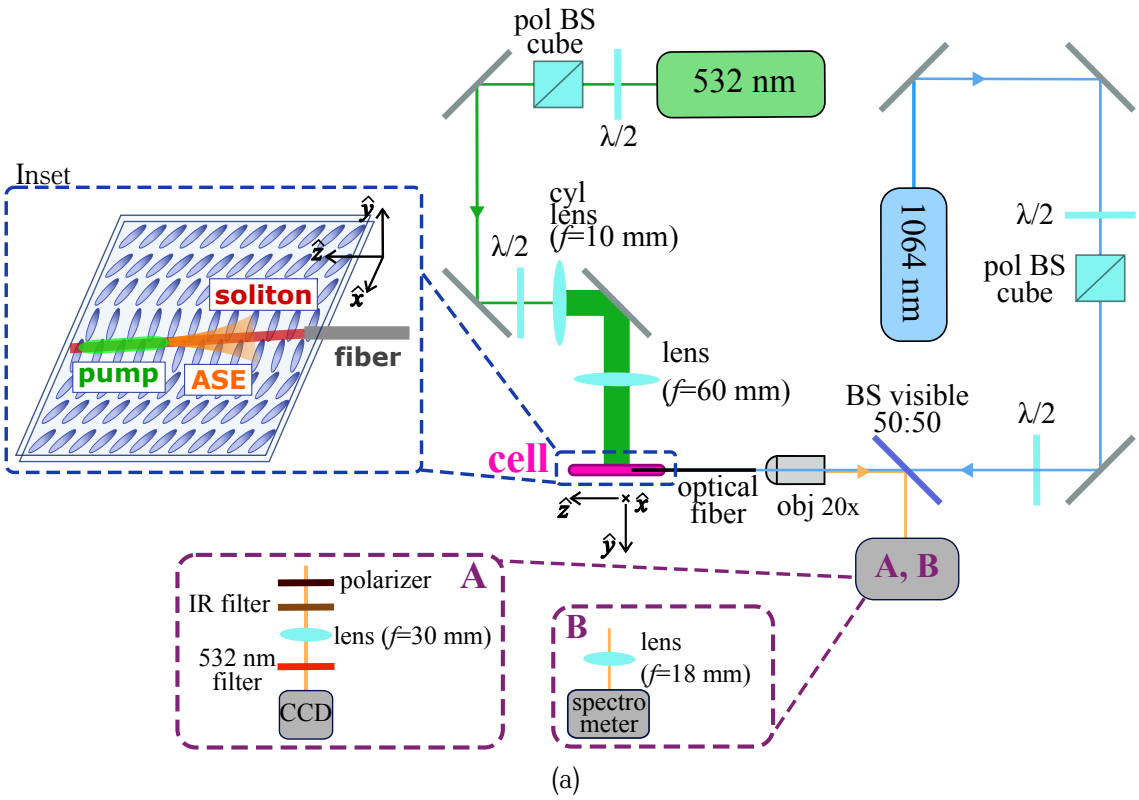

FIGURE 6.1: (a) Scheme of the nematicon injection and the ASE generation in the dye-doped nematic LC cell. The light extracted from the cell is sent either to a CCD camera or a spectrometer. Inset: Scheme of the cell with the fiber slid inside it and the stripe-shaped pump coming orthogonal to the cell surface. (b) Picture of the dye-doped LC cell, with the optical fiber slid from the right and the green laser beam focused on a stripe.

by capillarity with a solution of 1 wt.% of pyrromethene 597 dye (PM597, Sigma-Aldrich) in E7 LC (Merck). A non-standard optical fiber (see Sect. 2.4.2 for details) is slid inside the cell along the $\hat{z}$ direction (Inset of Fig. 6.1a).

The optical setup and a picture of the LC cell are reported in Fig. 6.1. The two optical sources used to create the nematicon and to excite the dye are, respectively, a continuous wave Nd:YAG laser (1064 nm) and a Q-switched frequency doubled Nd:YAG laser (532 nm, 400-ps pulses at 10 or 100 Hz). On both arms, the first half-wave plate and the polarizing beam splitter allow us to control the beam power while the second half-wave plate defines the input polarization angle with respect to the LC director. We set the polarization of the green beam (pump) to maximize the fluorescence and we align the polarization of the IR beam (soliton) along $\hat{x}$.

With the aid of a microscope objective (f=8.0 mm, NA=0.5), the IR beam is injected into the optical fiber slid into the cell. As seen in Ch. 3, the nematicon propagates with a walk-off with respect to the $\hat{z}$ axis due to the rubbing direction at 45° with respect to the fiber and to the optical anisotropy of the LC. The stripe-shaped green beam is therefore also tilted to maximize the overlap with the nematicon (Inset of Fig. 6.1a). This beam is focused with a spherical achromatic and a cylindrical lens in order to obtain an elliptical spot of around 20 μm × 7 mm on the cell. The pump stripe is aligned to form a gap of around 2 mm between the pumping area and the end of

the fiber. The ASE threshold, measured ad the power at which the ASE peak arises from the broad fluorescence spectrum, is as low as 0.4 µJ/pulse, and all the measurements presented here are taken for a pump power above this value.

The ASE beam is emitted at both ends of the stripe, due to the symmetry of the system. Some of the ASE enters the fiber and is guided outside the cell. The beam is then collimated with the same microscope objective used to inject the IR into the fiber, then reflected on to a beam splitter for the visible light. This light is then characterized spatially, with the ensemble of 532 nm notch/IR filters and a monochromatic CCD camera (JAI AM-800 GE-C, case A in Fig. 6.1a), and spectrally, using a spectrometer (Ocean Optics USB2000, case B in Fig. 6.1a).

In the following Section, we will show how the waveguide generated by the soliton collects and guides the ASE towards the fiber, increasing the fraction of light coupled outside the device trough the fiber.

6.1.2 Results and discussion

The ASE collected by the nematicon and exported from the sample is analyzed in terms of spatial profile, collected power, and spectral properties.

Collected ASE intensity

Using the configuration reported in Fig. 6.1a (case A), the far field intensity profiles of the ASE light collected by the nematicon and coming out of the fiber are shown in Fig. 6.2. In these measurements we separate the emission polarized along $\hat{x}$ (parallel to the substrate surface, Inset of Fig. 6.1a) from that one polarized along $\hat{y}$ (orthogonal to the substrate surface). Due to its high directionality, a small amount of the ASE is coupled into the fiber even if the soliton is not present (Fig. 6.2a). The power ratio between the two linear polarization components is $\sim$5.1. A similar ratio ($\sim$4.4) is obtained if the end of the pump stripe is placed close to the fiber and the ASE does not travel inside the unexcited LC. The ASE is therefore mainly polarized in the plane of the substrate. This is due to the geometry of the waveguide where the ASE is generated, as also reported for solid state films [183], and to the anisotropy of the dye emission, mainly polarized along the axis of the molecule and therefore the LC director.

When an IR beam of 2.0 mW is injected into the cell through the fiber, it creates a nematicon that captures the ASE light and efficiently couples it into the fiber. The intensity profiles of the collected ASE at the exit of the fiber are modified as reported in Fig. 6.2b-d for different nematicon powers. Initially, increasing the soliton power, the intensity of the collected ASE increases too. The peak of the collected light polarized along $\hat{x}$ for the case of 2.0-mW soliton power is one order of magnitude ($\sim$9.0) higher than the case without nematicon. This factor is almost double than what was obtained by Henninot and co-workers with a thermal soliton in LC collecting non-directional fluorescence [262]. The power ratio between the two polarizations is also significantly increased ($\sim$7.0), due to the fact that the waveguide profile is created only for the light polarized in the plane $\hat{x}\hat{z}$ [16]. By further increasing the soliton power, however, we observe a drop in the collected ASE.

In order to evaluate the variation of the collection efficiency of the ASE as a function of the soliton power, the intensity profile at the end of the fiber is integrated as a measure of the collected ASE power. The results are reported in Fig. 6.3. At powers below 0.7 mW, the nematicon is not formed. The ASE beam is therefore not guided along a preferential direction resulting in a small amount of ASE coupled into the fiber. Above this threshold, the nematicon is created. The ASE is guided by this self-induced waveguide up to the fiber, allowing an efficient coupling and causing an important increase of the intensity of the collected ASE. As the refractive index contrast of the waveguide increases with the soliton power, due to a stronger LC reorientation, the guiding efficiency increases also. Therefore, the intensity of the collected ASE increases with the nematicon power and reaches a maximum at around 2 mW. Above this value, the soliton spatial fluctuations studied in Ch. 3 start to play an important role. By increasing the power of the IR beam, the soliton starts to overfocus: the beam waist becomes of the same order of magnitude as the thermal fluctuations of the refractive index and the nematicon is deviated from its path [29, 43]. The spatial oscillations induce a rapid decrease in the efficiency of the ASE collection and waveguiding. The optimum ASE collection is therefore obtained as a trade-off between a higher waveguiding due to a stronger director reorientation and the minimization of the nematicon fluctuations.

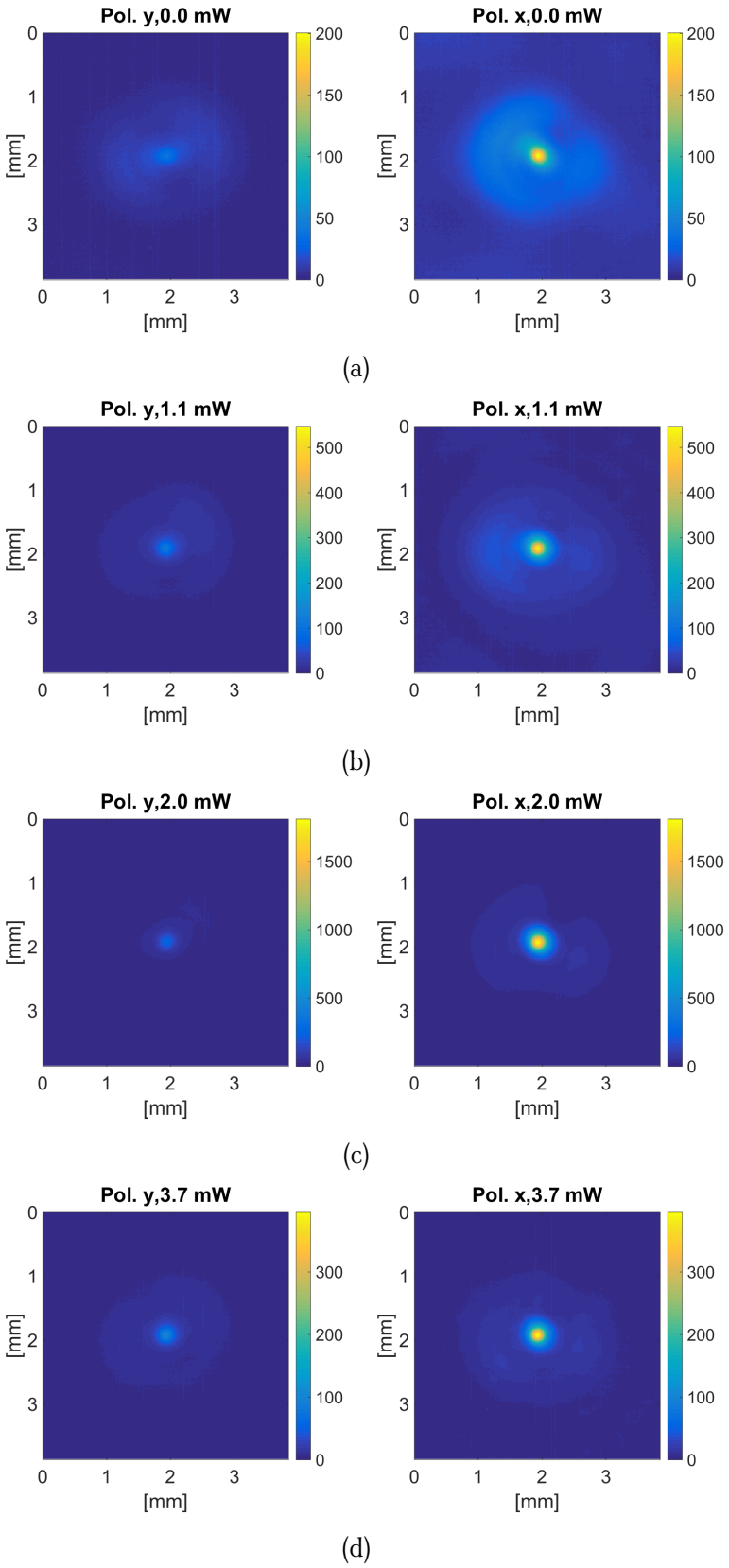

Figure 6.2: Intensity profiles of the collected ASE at the output of the fiber for the case without nematicon (a), and for a nematicon of 1.1 mW (b), 2.0 mW (c) and 3.7 mW (d). The spatial scale indicates the real size of the image on the CCD camera. The two polarizations, orthogonal (left column) or parallel (rigth column) to the substrate surface, are shown. The images are taken at 35 cm from the microscope objective and the pump delivers pulses of 2.0 μJ/pulse at 10 Hz; each profile is an average of 100 images, and all the images are taken with the same integration time. The presence of the nematicon increases both the polarization ratio and the intensity of the collected ASE.

Spectral properties

Using the configuration reported in Fig. 6.1a (case B), we analyze the spectrum of the light collected by the nematicon and guided into the optical fiber (Fig. 6.4). The normalized spectra are acquired for the same pump intensity (2.0 µJ/pulse) and for different nematicon intensities. Quite interestingly, we observe a blue-shift of the ASE peak (∼3 nm) at high soliton powers for which the collected power is also decreasing due to the nematicon fluctuations.

This blue-shift cannot be due to the combination of the director reorientation and the anisotropy of the optical gain of the dye. Indeed, as we presented in Sect. 4.3, the optical gain polarized parallel to the LC director is red-shifted with respect to the other polarization, as reported in Fig. 4.9 and Fig. 4.10b. Since the electric field of the nematicon tends to align the LC (and therefore the dye) molecules parallel to its direction, we should observe a red-shift instead of the blue-shift reported in Fig. 6.4.

If the reason of the spectral shift is not the gain anisotropy of the dye, then its origin can be considered in terms of the change in the environment. Indeed, at high nematicon powers, the soliton beam starts to oscillate in space due to thermal fluctuations, inducing wavelength-dependent bend losses [263]. The observed blue-shift could therefore be due to the change in the waveguiding properties of the soliton as a function of the power. The oscillations of the nematicon at high powers can be seen as a bending of the waveguide. Since the bend losses are higher for the longer wavelengths [263], the soliton oscillations could act as a spectral filter, inducing a blue-shift in the collected ASE.

Other contributions should be taken into account for a complete model of the system. Indeed, the scattering coefficient parallel to the director is higher than the one orthogonal to it, increasing therefore the losses experienced by the light polarized along the LC director [125, 157, 175, 264]. Their wavelength dependence is expected to be different, since the spectral evolution of the ordinary and extraordinary refractive indices is not the same [85], which would cause a change in the balance between the gain provided by the dye and the losses due to the scattering and therefore a change in the ASE wavelength.

It is, however, difficult to decouple experimentally these two contributions in our device. Indeed, even if the pump stripe is placed right next to the entrance of the fiber, the ASE is not generated only at the edge of the stripe but along most of the length of the stripe [265]. Therefore, the nematicon-induced waveguide could therefore influence the spectrum of the collected ASE both through the waveguide properties (post-ASE generation) and through the change in the medium losses (during the ASE generation).

Finally, it is important to notice that both the nematicon waveguiding and the injection into the optical fiber act as filters for the non-directional and non-polarized light, eliminating the broad-band photo-luminescence spectrum present in Fig. 4.10b and leaving only the ASE peak (Fig. 6.4).

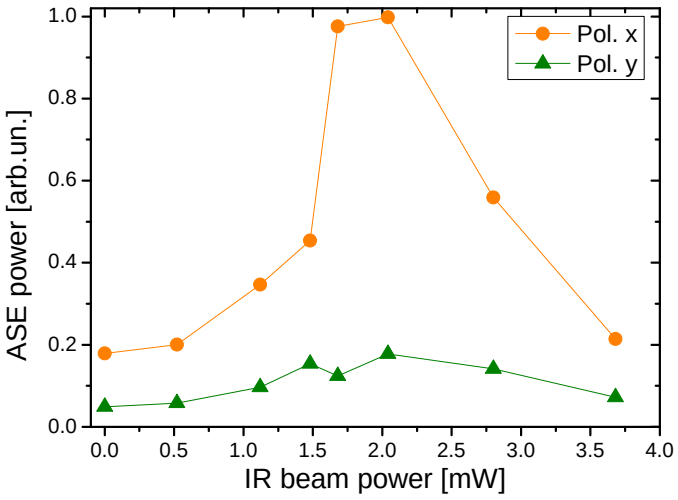

Figure 6.3: ASE collected power as a function of the IR beam power. The ASE power is obtained integrating the intensity profiles like those reported in Fig. 6.2. The pump delivers pulses of 2.0 µJ/pulse at 10 Hz.

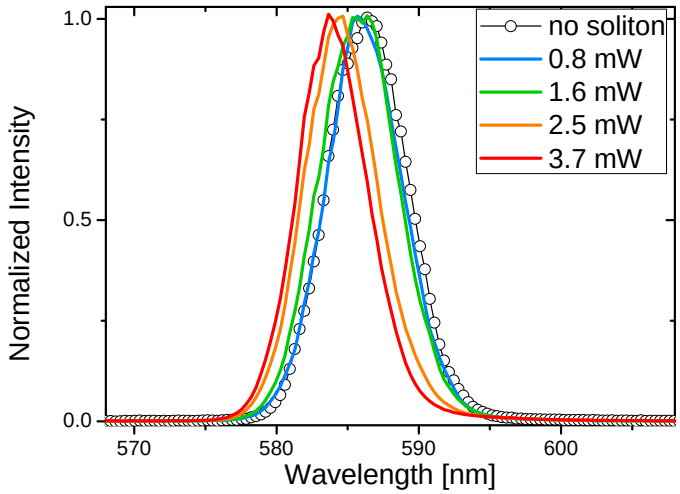

FIGURE 6.4: Normalized spectra collected at the output of the fiber at different IR beam powers; each spectrum is an average of 200 scans. The pump delivers pulses of 6.6 µJ/pulse at 100 Hz.

6.2 Investigation of lasing from dye-doped solvent-induced polymerized ULH

As it was explained in Sect. 2.3, chiral nematic LCs present an optical band-gap. The feedback provided by this selective reflection gives rise to laser emission when coupled to the optical gain provided by a dye dissolved in it [8–11, 137, 139], in the same way it is observed in distributed feedback lasers.

The periodic structure affects the way the molecules spontaneously decay and does not simply spectrally filter the emission [266]. Indeed, if the emission curve of the dye overlaps the band-gap of the CLC, the spontaneous emission of the molecule is suppressed inside the band-gap, since these wavelengths cannot propagate inside the medium, and enhanced at the edges where the density of photon states is higher [267]. The two edges of the band-gap are not equivalent: if the dye dipole moment is parallel (or orthogonal) to the LC director, the density of states is higher at the longer- (or shorter-) wavelength edge of the band-gap [267]. The laser threshold is minimum if the band-gap edge with the highest density of states is centered under the peak of the PL curve of the dye [10]. CLC lasers are interesting for their simple fabrication and the possibility to tune the emission wavelength by shifting the CLC band-gap under the emission curve of the LC. Due to the large response of LC to external stimuli, a tuning of some tens of nanometere can be achieved via mechanical [268], thermal [153, 256, 269], electrical [256, 270] or photochemical [271–273] stimuli.

In the previous Chapter we introduced the ULH alignment, where the helix axis lies parallel to the glass plate. If a dye is added in to the system, the laser emission takes place in the plane of the cell when the dye is excited [60–62, 261]. This configuration presents a lower threshold compared to the case of Grandjean alignment [60, 61]. Indeed, the cavity length (and therefore the feedback from the CLC) is increased from some tens to some hundreds of micrometers, while the pumping is kept uniform over the cavity length since the laser is focused orthogonal to the glass plates. The drawback of this configuration is the difficulty to obtain a homogeneous defect-free ULH. In Ch. 5, we presented the solvent-induced method to achieve highly homogeneous ULH alignment. The solvent-induced ULH, however, presented discrete helix unwinding when high electric fields were applied (see Ch. 5). For this reason, in this Section, the ULH alignment is stabilized via 2-photon photo-polymerization.

The 2-photon photo-polymerisation (TPP) technique allows us to write three-dimensional polymer structures with a high spatial resolution due to the nonlinear 2-photon absorption from the photo-initiator mixed with the reactive monomer in the LC [274]. Indeed, adding a photo-initiator and a reactive mesogen to the LC, it is possible to photo-induce a polymer network that freezes the LC molecular orientation. Using the TPP technique instead of the traditional UV polymerisation, it is possible to pin µm-sized structures or defects in the LC host, while the surrounding preserves the mobility and the responsiveness to electric fields typical of LCs [237, 275, 276].

When the sample is then left in an acetone bath for several hours, the non-reacted monomers and the LC

molecules are washed out of the cell, while the polymer network stays in the sample. The cell can then be refilled with other materials. In particular, it has been demonstrated that, when the polymerization is induced by UV light and the cell is refilled with achiral nematic LC, the chiral polymer network forces the nematic LC to follow the chiral distribution assumed by the CLC before the polymerization [277, 278]. As it will be shown later, this is also the case for the 2-photon-polymerized network.

When the cell is filled with achiral nematic LC, only the polymerized regions assume a chiral distribution. When a dye-doped LC is introduced in the cell, in order to have the optical gain needed for the laser emission, the optical feedback is localized in polymerized regions while the rest of the cell exhibits a uniform homeotropic distribution. This could be particularly interesting for the study of the interaction between the lasing emission generated from the polymerized structures and a nematicon injected in the achiral nematic regions of the same cell.

Finally, the flexoelectro-optic response of the medium is less hindered when the medium is photo-polymerized via TPP than with UV absorption [237]. Since the final aim is the electrical control of these structures, the TPP technique is preferred. These structures are therefore the perfect candidates for the study of the influence of the flexoelectro-optic sub-ms switching on lasing emission. In this Chapter, we report the first characterization of the lasing emission from these structures, leaving the study of the electric switching for further works.

6.2.1 Sample preparation via two-photon photopolymerization

The mixture used for these samples is the one prepared by Chloe C. Tartan for [237] and it consists of 68.5 wt% E7, 4.1 wt% of the chiral dopant BDH1281 (Merck), 26.8 wt% RM257 reactive mesogen (Merck), and 0.6 wt% IRG819 photoinitiator (Merck). The mixture has a pitch $p_0 \sim 400$ nm and an optical band-gap between 600 nm and 680 nm. We decided to center the left edge of the band-gap under the PL curve, even if it is the less efficient one, in order to be able to eventually distinguish between a LC director tilting and a change in the periodicity of the ULH. Indeed, if the pitch is fixed but the molecules are reoriented by the electric field via dielectric coupling, we observe a decrease of the effective extraordinary refractive index of the helix, which defines the long-wavelength edge of the band-gap [Eq. (2.20)]. On the other hand, if the periodicity changes due to a tilt of the optic axis of the ULH, both edges should shift accordingly. This mixture is introduced by capillarity in a 10-µm cell composed by glass substrates coated with homeotropic alignment SE4811 (Nissan) (see Sect. 2.4.2).

The two-photon polymerization is performed in the homogeneous regions of the ULH. The photo-polymerization of the structures presented in this Section have been performed by Dr. Patrick S. Salter within the facilities at the University of Oxford. The setup used for the polymerization is reported in Fig. 6.5a. The details of the setup are described in the literature [237, 279], while here only the main features are reported. The laser used for the polymerization is a mode-locked Ti:Sapphire laser (790 nm wavelength, 100 fs pulse width and 80 MHz repetition rate) with a maximum power of 300 mW. A spatial light modulator (SLM) pre-compensates the aberrations introduced by the sample surface, before focusing the laser onto the sample (10× Zeiss objective, NA=0.3). In particular, the SLM corrects the aberrations caused by the thick glass plates that constitute the cell and allows us to write 3-dimensional structures within the thickness of the cell with a resolution of some microns [237, 276]. The sample is translated with respect to the laser beam with the aid of a precision translation stage.

The solvent-induced ULH is grown in the cell as described in Ch. 5 (Fig. 6.5b). The photoinitiator and the reactive mesogen, when illuminated with intense laser light, generate a polymer network that locally pins the LC distribution (Fig. 6.5c). It is possible to monitor the polymerization during the writing thanks to a light emitting diode, a CCD and a lens system mounted on the same setup [237, 279]. The intensity of the beam is set empirically on the sample and it is typically some tens of milliwatts [237]. It has to be high enough to see a stable shade forming in the LC due to the polymerization (as it will be shown later), but low enough not to burn the sample. The sample is then continuously moved with respect to the laser beam, in order to write lines. Alternatively, the sample is fixed and the laser is switched on and off to write pillars. The writing speed in the first case and the exposure time in the second one are the key parameters for the fabrication. However, this being only a preliminary demonstration of lasing from such structures, the optimization of these parameters is not the subject of this work.

The cell can then be washed out in acetone and refilled with achiral nematic LC. This is particularly important

since the laser wavelength (790 nm) corresponds to the 2-photon absorption of both the photoinitiator and the PM597 dye, since both of them present a quite strong absorption in the UV range. The structures are therefore polymerized without the dye, in order to minimize the losses of the laser along the thickness of the cell. The cell is then washed out for 4 days in acetone at room temperature and refilled with a solution of 1.0 wt.% PM597 in E7. The dye-doped ULH alignment is present only in the polymerized regions, while the rest of the cell shows a homeotropic alignment (Fig. 6.5d).

Figure 6.6 reports microscope images of the fabrication steps for different structures. When the laser lines are almost superposed, a filled polymerized square is formed (F_1,F_2 and F_3). Alternatively, the lines written by the laser can be spaced and periodic walls are generated (W_1,W_2 and W_3). Finally, if the cell is kept fixed instead of continuously in movement with respect to the laser, it is possible to form pillars that can be disposed in regular arrays (P_1 and P_2).

The as-generated structures are reported in the first column of Fig. 6.6. As it is possible to see comparing the polymerized regions with the surroundings, the TPP process and the high power of the laser beam perturb the LC and introduce defects in the ULH alignment. A faster writing speed seems to generate less perturbed

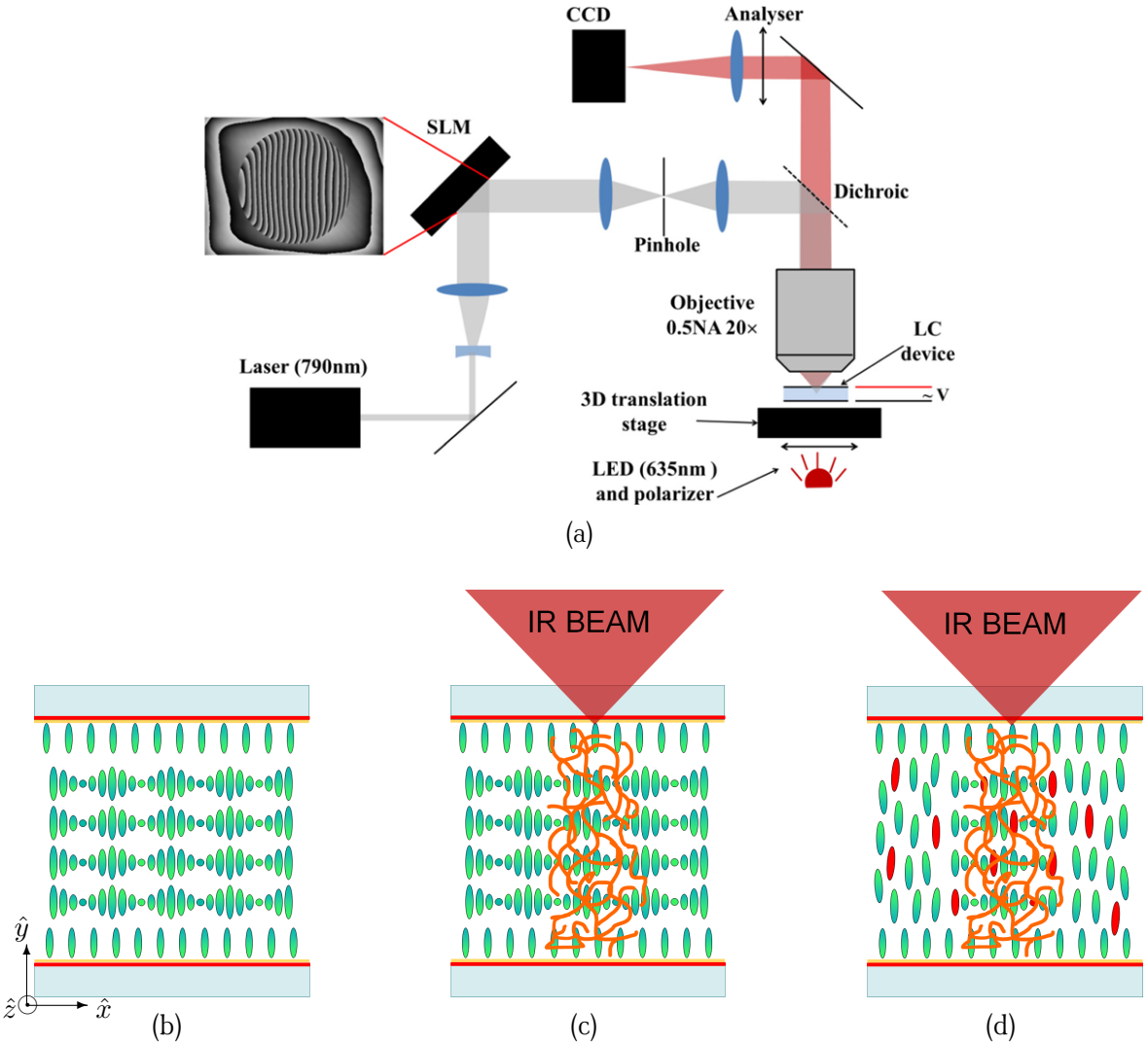

FIGURE 6.5: (a) Setup used for the TPP process (image from [237]). (b)-(d) Fabrication of the structures via TPP (not to scale). (b) A solvent-induced ULH alignment is obtained in a homeotropic cell filled with a mixture of LC and photo-reactive material. (c) When the laser is focused within the cell, a photo-polymerization takes place only at the focus of the beam and a direct writing of the structures is possible. In these regions the LC orientation is locked-in. (d) When the cell is washed out and refilled with achiral dye-doped nematic, the LC assumes a ULH alignment in the regions where the polymerized network is present.

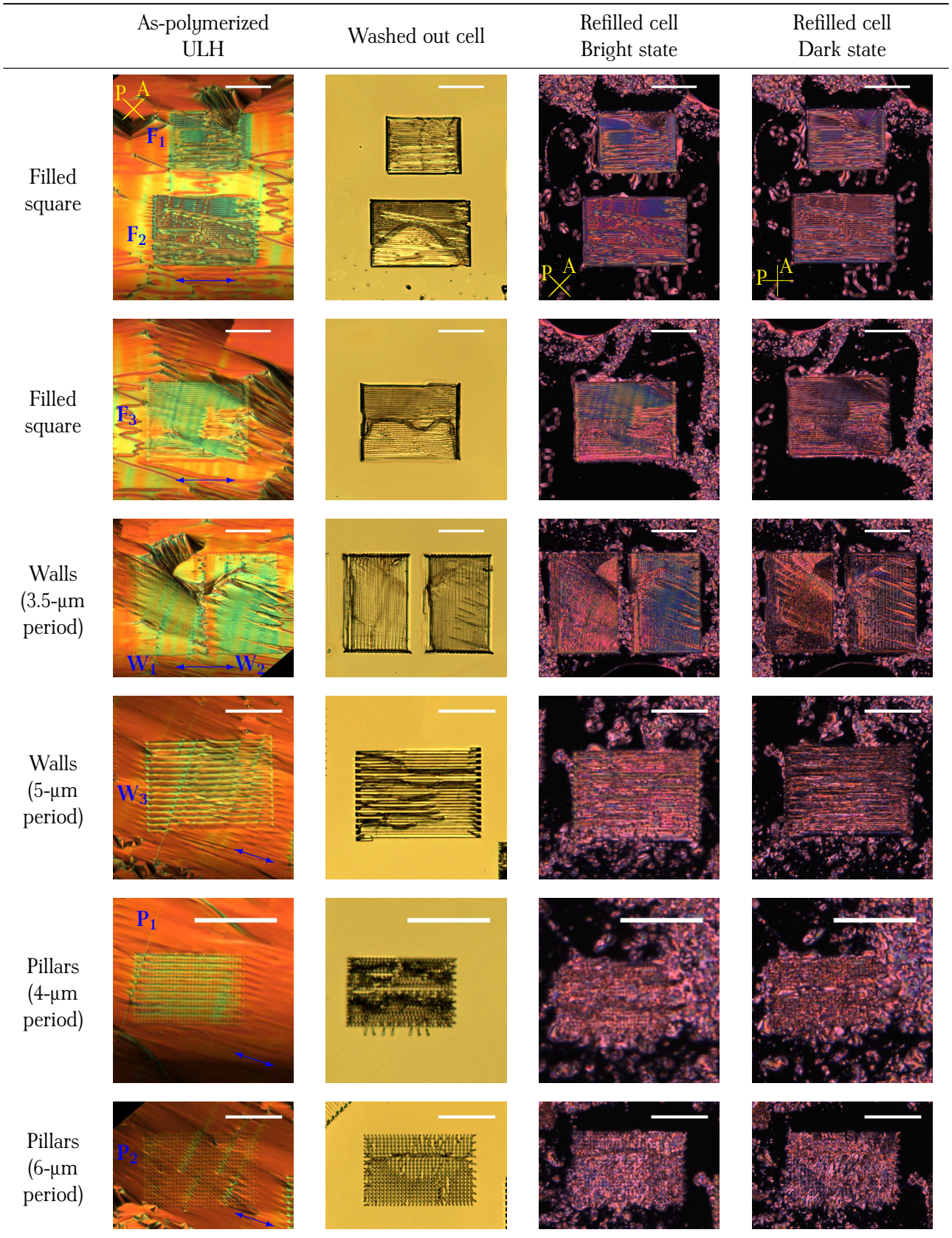

FIGURE 6.6: Microscope images of the fabrication steps via TPP for different geometries. The first two lines of the table report structures where the laser draws a filled square (F_1, F_2, F_3), the third and the fourth lines report walls written with different periodicity (W_1, W_2, W_3) and the last two lines report arrays of pillars (P_1, P_2). The writing parameters are F_1, F_2: 30 µm/s; F_3: 100 µm/s; W_1, W_3: 200 µm/s; W_2: 100 µm/s; P_1, P_2: 50 ms of exposure. The first column shows the structures right after the polymerization (crossed polarizers at 45°with respect to helix axis); the second column shows the washed out cell (uncrossed polarizers); the third and the fourth columns show the bright and the dark states of the cell refilled with the dye-doped mixture (crossed polarizers at 45°and parallel to the helix axis, respectively). The blue arrow indicates the helix axis orientation (scale bar: 100 µm).

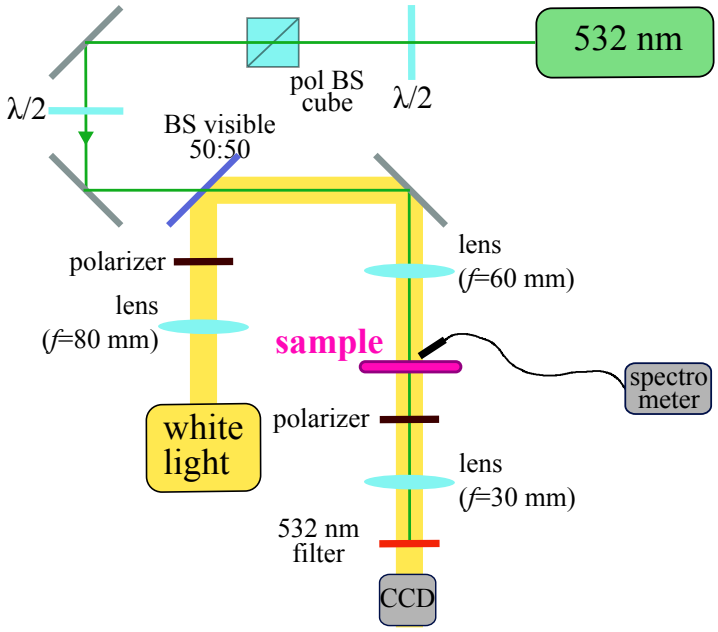

FIGURE 6.7: Scheme of the setup for the lasing emission from the dye-doped TPP structures. The green laser is focused orthogonal to the cell surface. The white light is sent onto the cell and then on to the CCD camera in order to have an image of the region illuminated by the pump. Two crossed polarizers are inserted in the white light path to increase the contrast between the structures and the non-polymerized surrounding.

polymerized structures. Also, the perturbation appears to decrease when the filling factor of the structures is decreased. From this point of view, the pillar arrays seem to give the better results.

When the cell is washed out (second column of Fig. 6.6), however, the pillar arrays appear to be more fragile while the filled squares are less deteriorated by the action of the solvent. In our case, since all the structures were written in the same cell, it was not possible to adapt the duration of the acetone bath for the different filling factors. Indeed, in future works, the acetone bath duration should be optimized as a compromise between a complete removal of the non-reacted mesogen (to avoid the deterioration of the sample under utilization in ambient light) and the smallest damage possible of the polymer network.

Finally, the cell is filled with a dye-doped LC (1 wt% PM597 in E7) and observed under cross-polarized microscope light. The bright and the dark states are reported in the third and the fourth columns, respectively, of Fig. 6.6. The sample W_3 and the pillar arrays show almost no birefringence, since the dark and the bright states are very similar. This indicates that in these structures the polymer network is not able to induce the ULH alignment when the cell is filled with the nematic LC. A small anisotropy is however visible for W_1, W_2 and the filled square structures. In particular F_3 and W_2 present quite large homogeneous regions, making them the better candidates for the observation of the lasing emission.

The black regions around the structures are due to the homeotropic alignment of the LC, while the scrambled regions indicate that the LC is not well aligned. This could be due to the fact that there is some polymer left in the cell, or that the homeotropic alignment layers on the glass plates have been damaged. An optimization of the washing procedure would notably decrease this problem. In the following Section we analyze the difference in the PL emission between the non-polymerized regions and from the polymerized ULH structures, where the emission is influenced by the CLC optical band-gap.

6.2.2 Investigation of laser emission

The setup for the spectral characterization of the lasing emission is reported in Fig. 6.7. A Q-switched Nd:YAG doubled in frequency (532 nm, 400 ps, 10 Hz) is focused in the sample with a diameter smaller than the structure sizes (some tens of micrometers). A white light source and a CCD are used to image the region of the cell illuminated by the laser, in order to distinguish the different structures. The two polarizers on the white light path are orthogonal, in order to have better contrast between the structures (birefringent) and the surrounding

(isotropic since in homeotropic configuration). A fiber spectrometer (Ocean Optics USB2000) is placed close to the illuminated area of the cell to collect the laser emission. The white light is switched off during the spectral measurements.

The collected spectra are reported in Fig. 6.8. When the pump beam is focused in to a region without polymerized structures, the emission spectra present a peak only at high pulse energies (>4.0 µJ/pulse). The

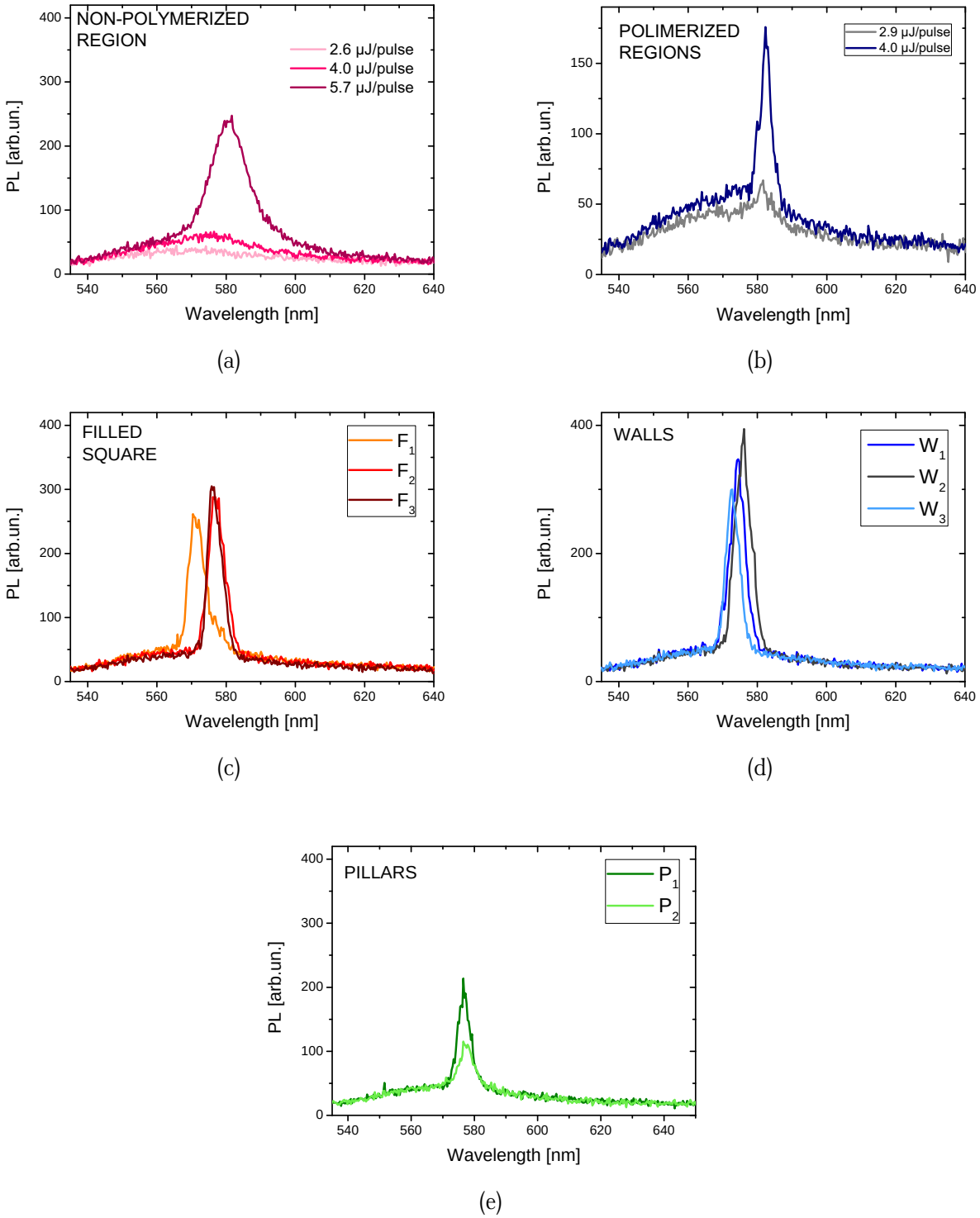

FIGURE 6.8: Example of emission from the non-polymerized regions (a) and structures (b) at different excitation powers. A peak arises from the florescence broad spectra by increasing the power. The presence of the polymerized structures considerably decreases the width of the peak. (b-d) Emission from the polymerized structures for the different geometries: filled square (b), walls (c) and pillars (d). For the polymerization structures the excitation pump is 4.0 µJ/pulse.

peak is quite broad (∼15 nm), even compared to the case of ASE studied in Sect. 4.3. The differences in both the threshold and the spectrum compared to the ASE case presented in Sect. 4.3 could be due both to the defects in the cell and to differences in the pumping geometry. Indeed, the quite small circular spot is not optimal for the wavelength selection that occurs in ASE [52–55].

When the laser is focused on the polymerized ULH structures, the peak is narrower (∼5 nm) and centered at different wavelengths, all compatible with the position of the left band-gap edge of the CLC. An example of the evolution of the spectra for a polymerized structure is showed in Fig. 6.8b. Indeed, the ULH alignment appears to generate a narrower emission than the case without the polymerized structure. Moreover, in these structures, the peak threshold appears to be lower: ∼2.9 µJ/pulse for the pillars, ∼2.1 µJ/pulse for the walls, and ∼2.4 µJ/pulse for the filled squares. The lowest threshold is observed for the more homogeneous structures. Further characterizations are needed to claim that what we observe is lasing emission, such as the input-output power relation, the coherence of the light and the beam intensity profile [280, 281]. Indeed, the threshold for the spectral narrowing is an encouraging result that indicates the interest in pursuing the study of light emission from these structures.

The next step would be the study of the flexoelectro-optic coupling of the lasing emission. Indeed, by applying a modulated electric field with peaks and dips and return to zero between them, it should be possible to see a difference in the wavelength emission between the peak/dip case (when the helix optic axis is tilted) and the zero voltage case. If the modulation frequency is high enough, it should be possible to exclude dielectric coupling and obtain flexoelectrically-driven sub-ms wavelength tuning.

6.3 Conclusion

We have demonstrated experimentally that the ASE collection from a LC device can be increased by one order of magnitude with the help of a nematicon that acts as a waveguide between the pump stripe where the ASE is generated and the fiber input face. The nematicon waveguiding property improves the spectral purity and the polarization degree of the collected light and it also introduces a small spectral shift, which does not come from the gain anisotropy. Once the polarized ASE light is collected into the fiber, it can easily be used for applications that require integrated and compact incoherent light sources, like lab-on-chip sources.

In the second part of the Chapter, we have looked for another kind of source that could be potentially tuned. We have shown how the polymerized structures in the solvent-induced ULH alignment give rise to in-plane narrowband emission in the presence of optical gain. Even if some of the fabrication parameters, such as the polymerization speed or the washing out procedure, need to be optimized, it is possible to observe an in-plane narrow spectral emission, not visible outside the structures. We hope to have set in this way the starting point for sub-ms tunable integrated light source, where the injection of a nematicon could improve the light collection and extraction.

Conclusions

Chapter 7

In this thesis, we have studied the nonlinear nematicon propagation in LCs, the optical gain and the electrical switching of chiral nematic LCs. In the beginning, these three aspects are analyzed separately.

The nematicon regime is firstly analyzed, with a particular attention to the spatial fluctuations observed at high powers. We propose a way to model the fluctuations based on the spatial correlation of the thermal noise in nematic LCs. This allows us to explain the power-dependent behavior of the fluctuation amplitudes and the scattering-induced losses in nematicon propagation. We believe that this will help the modeling of both linear phenomena involving speckle generation and more complex nonlinear behavior in LCs, such as modulation instabilities or filamentation.

Secondly, the optical gain is analyzed in the case of PM597 and PFO dispersed in LCs. The PM597 dye dispersed in LC provides an optical gain that is polarized along the LC director and that shows a blue-shift when the polarization passes from parallel to orthogonal with respect to the director. For this reason, the ASE wavelength can be tuned over a range of 10 nm changing the orientation of the pump stripe in the sample. When the PFO is dispersed at high concentrations in LCs, it presents a complex morphology, composed of homogeneous domains separated by polymer-rich boundaries. Within the boundaries, the isolation and orientation of the polymeric chains allows the observation of polarized optical gain from the oxidized units of the PFO, the keto defects. For the first time the keto defects are not associated with the degradation of the sample, but they provide optical gain. This kind of sample cannot be employed for the soliton propagation due to the high scattering provided by the domain boundaries and experienced by the light propagating in the plane of the cell. The PM597 dye is therefore used in this work to provide optical gain.

Thirdly, the solvent-induced self-assembly method is presented for chiral nematic LCs in order to obtain a ULH alignment, which presents sub-ms flexoelectro-optic switching. This solvent-evaporation method allows us to obtain high-quality textures associated with the same flexoelectro-optic response observed in samples obtained with traditional methods. We believe that this alignment method could be useful not only for the ULH alignment, but also for other geometries or phases that usually present a difficulty in the alignment.

These three aspects are combined in the last Chapter. A soliton and ASE are generated in the same dye-doped nematic LC device. The nematicon is used to collect the ASE and inject it into the fiber used to generate the soliton. The nematicon waveguiding improves the spectral purity, the polarization degree of the collected light, and the intensity of the signal extracted from the cell. The optical gain combined with the feedback provided by the ULH is also tested and in-plane emission is observed. The two-photon polymerization technique allows us to pin the ULH alignment only in a confined region of the cell, while the surroundings can assume a uniform nematic alignment. In such a sample it would eventually be possible to combine the in-plane narrowband emission from the ULH regions with the nematicon propagation in the nematic surrounding, opening opportunities for electrically-tuned integrated laser sources.

7.1 Outlook

During this thesis many different subjects have been analyzed. There is also indeed also space for some improvements and developments that, due to the limited time duration of this thesis, have not been pursued.

We propose a numerical modeling for thermal fluctuations in LCs and we apply it to linear and nonlinear

propagation, showing a good agreement with the experimental results. There are however improvements that could be implemented to the code, such as the modeling of the correlation in three dimensions or the introduction of the three elastic constants. The introduction of the temporal evolution of the director orientation would also help to model the temporal oscillations of the nematicon and improve the statistical analysis of the phenomenon. The model could be applied to other noise-induced phenomena in LCs, such as the spatial modulation instability and the subsequent filament formation [25, 114–116]. These phenomena spontaneously appear for beams with an elongated profile in the plane orthogonal to the propagation and high powers. The speckle formation reported in Ch. 3, should cause filament formation when occurring in high power beams. In this way, the modulation instability would not be artificially seeded by the initial condition of the launched beam, but it would arise from the physical propertied of the considered LC. The matlab program reported in Appendix B could be easily adapted for this kind of elongated profile, but the use of a supercomputer for the calculations would however be necessary, since a much larger simulation window (several hundreds of micrometers) and a finer grid (to resolve the filaments) would be required.

With the help of ultra-fast spectroscopy, it was showed how the LC anisotropy as a host can polarize the optical gain in both polymers and dyes in LC dispersed in it, and how, in particular situations, the charge generation can be inhibited and therefore the optical gain uncovered. Interestingly, not a lot of work has been done in this area, despite the interest that polarized and switchable light sources can have in display technology or biomedical applications. If, on one hand, the dyes are easy to dissolve in LCs, on the other hand, semiconducting polymers are of particular interest since they can exhibit electroluminescence. Indeed, with the careful engineering of the solubility of the dissolved polymer and the conducting properties of the LC host, it is possible to obtain an electroluminescent LC film [135]. The study of these materials *via* the pump-probe technique would help the optimization of the optical properties of these systems.

We developed a new method for the alignment of LCs. LCs are characterized, as we already explained in different points of this work, by a long-range interaction. This is particularly interesting when the boundary conditions provided by the cell match the distribution of minimal energy of the LC, as the LC naturally disposes itself in that configuration without the need of an external driving force. This is the case, for example, of CLCs in Grandjean configuration or nematic LCs in planar and homeotropic cells. However, in the case of particular geometries, the mismatch from the boundary conditions can generate defects that decrease the optical quality of the sample. In particular, the technique could be used to align highly viscous bi-mesogen LC, particularly interesting for display applications due to their large flexoelectro-optic response [65, 66, 282], or in templated and structured devices, where LC defects are difficult to avoid. In this work, the solvent-induced alignment was tested only for a few mixtures, one cell thickness and one LC geometry (the ULH alignment). A more systematic study of this technique on different samples and geometries would highlight the advantages as well as the limitations of this technique. Also, the high-quality solvent-induced ULH seems to show a new flexoelectrically-driven instability. A more complete theory would help to understand the origin and the director distribution of these instabilities. Also, their observation in cells of different thicknesses would help to evaluate the contribution of the surface interaction, in particular for the threshold in the evolution of the period as a function of the applied electric field.

Finally, only the prelude to the polymerized fast-switchable laser sources has been outlined here. Indeed, a spectral narrowing is observed in the polymerized regions by increasing the pump power. However, a more thorough characterization is needed in order to claim that we are observing lasing emission [280, 281]. Also, the fabrication parameters have to be tuned in order to obtain defect-free two-photon polymerized ULH structures and achieve efficient lasing. The following step should be the observation of flexoelectro-optically tuned in-plane lasing. The interest would be twofold. Firstly, the laser tuning would be faster compared to other reorientation mechanisms in LCs, such as those due to the dielectric coupling (typically, µs instead of ms). Secondly, it would be possible to study the evolution of the optical band-gap in ULH alignment during the flexoelectrically-driven tuning through the evolution of the lasing wavelength. To be able to study this phenomenon, the pumping, the electric field for the flexoelectric driving and the acquisition instruments have to be synchronized and their frequency has to be high enough to exclude slow dielectric coupling. After the laser characterization, the fabrication of a thicker cell, able to sustain the propagation of a nematicon, should be considered. The nematicon would then be injected in the nematic regions and its interaction with the emission from the polymerized structures would be studied, with the aim to obtain an integrated source that is possible to electrically switch/tune.

Notation for the permittivity

Appendix A

It is worth spending a few words on the notation used to express the relative permittivity, for example in Eq. (2.10). The response of the medium to a generic stimulus is described, in the temporal domain, through the convolution ($\otimes$) of the function describing the stimulus with the function that characterizes the local response of the material. Using, for example, the polarization, the electric field and the susceptibility, it is possible to write

$$\bar{P}(\bar{r},t) = \varepsilon_0 \bar{\bar{\chi}}(t) \otimes \bar{E}(\bar{r},t). \tag{A.1}$$

The quantities that describe the response of a medium to an external stimulus, such as the relative permittivity $\bar{\bar{\varepsilon}}_r$, the susceptibility tensor $\bar{\bar{\chi}}$ (of all order) and the refractive index n, are usually defined in the frequency domain. Taking the Fourier transform (in time) $\mathscr{F}$ of Eq. (A.1)

$$\tilde{\bar{P}}(\bar{r},\omega) = \varepsilon_0 \tilde{\bar{\bar{\chi}}}(\omega) \tilde{\bar{E}}(\bar{r},\omega), \tag{A.2}$$

where the tilde indicates the Fourier transform $\tilde{\bar{E}}(\bar{r},\omega) = \mathscr{F}[\bar{E}(\bar{r},t)]$.

From now on, the approximation of a monochromatic wave will be assumed. The (real) field $\bar{E}(\bar{r},t)$ can therefore be written as

$$\bar{E}(\bar{r},t) = \frac{1}{2}\left[\bar{\mathcal{E}}(\bar{r})e^{i\omega_0 t} + \text{c.c.}\right], \tag{A.3}$$

composed by the single carrier frequency ω_0. Replacing only the first term of this equation in Eq. (A.1), and not the complex conjugate in order to simplify the notation, we obtain

$$\begin{aligned}
\mathscr{P}(\bar{r},t) &= \varepsilon_0 \bar{\bar{\chi}}(t) \otimes \left(\bar{\mathcal{E}}(\bar{r})e^{i\omega_0 t}\right) && \text{(A.4)}\\
&= \varepsilon_0 \bar{\mathcal{E}}(\bar{r}) \mathscr{F}^{-1}\left[\mathscr{F}\left[\bar{\chi}(t) \otimes e^{i\omega_0 t}\right]\right] && \text{(A.5)}\\
&= \varepsilon_0 \bar{\mathcal{E}}(\bar{r}) \mathscr{F}^{-1}\left[\tilde{\bar{\bar{\chi}}}(\omega)\delta(\omega-\omega_0)\right] && \text{(A.6)}\\
&= \varepsilon_0 \bar{\mathcal{E}}(\bar{r}) \mathscr{F}^{-1}\left[\tilde{\bar{\bar{\chi}}}(\omega_0)\delta(\omega-\omega_0)\right] && \text{(A.7)}\\
&= \varepsilon_0 \tilde{\bar{\bar{\chi}}}(\omega_0) \bar{\mathcal{E}}(\bar{r}) e^{i\omega_0 t} && \text{(A.8)}
\end{aligned}$$

where $\delta(\omega-\omega_0)$ is the delta distribution centered in ω_0. The equivalence of Eq. (A.4) and Eq. (A.8) justifies the substitution of the temporal convolution of the function $\bar{\bar{\chi}}(t)$ with its Fourier transform evaluated at the carrier frequency ω_0. In this way we are able to work exclusively with the fields in the temporal domain and, at the same time, to express the quantities that describes the response of the medium as a function of the frequency, without the need for the temporal convolution.[1] From now on, in order to simplify the notation, we will drop for $\bar{\bar{\varepsilon}}_r$, $\bar{\bar{\chi}}$ and n the tildes that indicate the frequency dependence, as these variables will not be defined otherwise in our work. This explains the notation used in Eq. (2.9) and Eq. (2.10) and in the rest of this dissertation.

[1] This result is more general than the monochromatic case. Indeed, in the case of a non-continuum wave electromagnetic beam, if the response of the medium is fast compared to the duration of the pulse, it is possible to truncate the response to the first order, that corresponds to Eq. (A.8). [283]

Matlab code

Appendix B

B.1 Main section

The main matlab code used for soliton propagation in LC is reported in this section.

```
1
2
3  %% Propagation of the beam
4  % SCHEME: the position of the glasses is rotated
5  %
6  %
7  %           ^
8  %     x,    ę       ę ę glass                       ę ę glass
9  % M points ę       ę ę                               ę ę
10 %           ę       ę ę         <--j-->               ę ę
11 %           ę       ę ę                               ę ę
12 %           ę       ę ę                        ^      ę ę
13 %           ę       ę ę            /-\         ę      ę ę
14 %           ę       ę ę            \-/         k      ę ę
15 %           ę       ę ę                        ę      ę ę
16 %           ę       ę ę                        v      ę ę
17 %           ę       ę ę                               ę ę
18 %           ę    z  ę ę                               ę ę
19 %           ę  /    ę ę                               ę ę
20 %           ę /     ę ę                               ę ę
21 %           ę/-------------------------------------------->
22 %                                                  y, N points
23 %
24 %     !!!!!!!!!!!! SIZE(MATRIX) = (M,N) !!!!!!!!!!!!!!!!!
25 %%%%%%%%%%%%%%%%%%%%%%%%%%%%%%%%%%%%%%%%%%%%%%%%%%%%%%%%%%%%%%%%%%%%%%%%%%%%
26
27 % function [Output,Param] = nematicon(Param)
28 function [Output,Param] = nematicon(Param,num_sim) % [corr,delta_theta] = nematicon
     (Param)
29
30
31 %% INPUT PARAMETERS STRUCTURES
32 % if a structure does not exist, we create it
33 if nargin==0; Param = struct; end
34
35 if ~isfield(Param,'cell'); Param.cell = struct; end
36 if ~isfield(Param,'soliton'); Param.soliton = struct; end
37 if ~isfield(Param,'pump'); Param.pump = struct; end
38 if ~isfield(Param,'dye'); Param.dye = struct; end
39 if ~isfield(Param,'E7'); Param.E7 = struct; end
40
41 %% CELL PARAMETERS
42
43 if ~isfield(Param.cell,'M');
```

```
    Param.cell.M = 155; % raws %155;
end

if ~isfield(Param.cell,'x_size')
    Param.cell.x_size = 55e-6; % 55e-6  [m] "wideness" of the cell
end

if ~isfield(Param.cell,'N')
    Param.cell.N =  211; % columns %211;
end

if ~isfield(Param.cell,'y_size')
    Param.cell.y_size = 75e-6; % 75e-6  [m] thickness of the cell SQUARED PIXELS!!!
end

if ~isfield(Param.cell,'dz')
    Param.cell.dz = 0.9e-6; % 0.4e-6;    % [m] stepsize along z
end

if ~isfield(Param.cell,'z_step_number')
    Param.cell.z_step_number = 4000;
end

if ~isfield(Param.cell,'theta_boundary')
    Param.cell.theta_boundary = 45*pi/180; % [radiant] rubbing direction with the respect to the nematicon propagation
end

if ~isfield(Param.cell,'step_optim')
    Param.cell.step_optim = 1;           % nb of steps between two optimization of theta
end

if ~isfield(Param.cell,'step_noise')
    Param.cell.step_noise = 47;           % nb of steps between two generation of the noise 33 - 67 - 100
end

% if ~isfield(Param.cell,'dist_noise')
%     Param.cell.dist_noise = Inf;           % nb of steps until which I generate the noise
% end


%% SOLITON PARAMETERS

if ~isfield(Param.soliton,'P_inj')
    Param.soliton.P_inj = 3.7e-3; % [W] Power of the injected Nd/YAG
end

if ~isfield(Param.soliton,'w_0x')
    Param.soliton.w_0x = 3.7e-6; % 25e-6;   % [m] radius at 1/e^2 of the intensity
end

if ~isfield(Param.soliton,'w_0y')
    Param.soliton.w_0y = 3.7e-6; % 25e-6;   % [m] radius at 1/e^2 of the intensity
end

if ~isfield(Param.soliton,'lambda')
    Param.soliton.lambda = 1064e-9;     % [m]
end

if ~isfield(Param.soliton,'R_phase')
    Param.soliton.R_phase = Inf; %50e-6;     % [m], radius of the quadratic phase
```

```
      of the injected beam
end

%% E7 PARAMETERS

% refractive index: from  Li et al. 2005, IR refractive index of LC
% n_i = A_i + B_i/(lambda^2) + C_i/(lambda^2), and lambda is in ţm
% we take 25 řC [avant c'était eps_o=1.5212^2 et delta_eps=1.7137^2-Param.E7.eps_o
  =0.6227
if ~isfield(Param.E7,'eps_o')
    Param.E7.eps_o = (1.4998+0.0067/((Param.soliton.lambda*10^6)^2)+0.0004/((Param.
      soliton.lambda*10^6)^4))^2;            % ordinary dielectric constant
end

if ~isfield(Param.E7,'delta_eps')
    Param.E7.delta_eps = (1.6993+0.0085/((Param.soliton.lambda*10^6)^2)+0.0027/((
      Param.soliton.lambda*10^6)^4))^2-Param.E7.eps_o;
end

if ~isfield(Param.E7,'K')
    Param.E7.K = 12e-12;                   % [N] one constant approximation
end

if ~isfield(Param.E7,'alpha')
    Param.E7.alpha = 0; %-100;                % we modeled the scattering!!! % [m
      ^-1]; - -> losses due to the scattering of the LC (-830m-1 @ 633nm (Beeckman
      2009)); see also Wu and Lim on LC scattering
end

if ~isfield(Param.E7,'rho_E7')
    Param.E7.rho_E7 = 1.03e3 ;             % [g/dm^3]  density of E7 [Kim et al.,
      Nat. Comm., 3, 1133 (2012)]
end

if ~isfield(Param.E7,'corr_dR')
    Param.E7.corr_dR = 0*1.4*880*10^-9 ;        % 880*10^-9 [m] minimal distance
      over which the continuum theory is valid (for a 155x211 matrix), see notes of
       31/03/2016
end                                        % I put the max value to have definite
  positive corr (it changes changing dx and dy !!)

if ~isfield(Param.E7,'r_par')
    Param.E7.r_par = 0.605 ;               % order factor of the LC, see notes on
      17/10/2014
end

if ~isfield(Param.E7,'r_ort')
    Param.E7.r_ort = 0.198 ;               % order factor of the LC, see notes on
      17/10/2014
end

if ~isfield(Param.E7,'err_theta_opt')
    Param.E7.err_theta_opt = 0.5e-13;              % before 17/05/2016 it was
      ALWAYS 1e-13  !!!
end


%%
tic

%% Discretization geometry: NEW COORDINATES!
% axis: THE DELTAx AND y DO NOT CHANGE!
dx = Param.cell.x_size/(Param.cell.M-1); % [m]
dy = Param.cell.y_size/(Param.cell.N-1);  % [m]
```

```
155 z_size = Param.cell.z_step_number*Param.cell.dz; % [m] propagation length of the
      simulation
156
157
158 %% PREALLOCATION
159
160 E_x_vect = zeros(Param.cell.N*Param.cell.M,Param.cell.z_step_number+1); % Electric
      field (VECTOR!!), AT ALL Z!!!!
161 Poynt = zeros(Param.cell.z_step_number+1,1);  % Energy
162 % Sections INTENSITIES!!!
163 I2_plane_zy = zeros(Param.cell.z_step_number+1,Param.cell.N);
164 I2_plane_zx = zeros(Param.cell.z_step_number+1,Param.cell.M);
165
166
167 %% INITIAL VALUES
168
169 % Definition of the injected field (polarized along x)
170 amplitudeE = sqrt((2*4*pi*10^-7*3*10^8*Param.soliton.P_inj)/(pi*Param.soliton.w_0x*
      Param.soliton.w_0y)); % P = Area I = Area (E)^2/(2 c mu_0), we take w0 to
      calculate the area, mu_0=4*pi*10^-7
171
172 n_0 = sqrt(Param.E7.eps_o+Param.E7.delta_eps*sin(Param.cell.theta_boundary).^2); %
      Fissato, è quello iniziale
173 E_x_0 = create_Ex(Param.soliton,n_0,amplitudeE, Param.cell.M,Param.cell.N,Param.
      cell.x_size,Param.cell.y_size);  % matrix
174
175 E_x_vect_0 = matrix2vect(E_x_0,Param.cell.M,Param.cell.N);  % we put the E_x matrix
       into a vector
176
177 % HOMOGENEOUS DISTRIBUTION OF THETA
178 theta_0 = zeros(size(E_x_0))+Param.cell.theta_boundary; % matrix
179 theta_0_vect = matrix2vect(theta_0,Param.cell.M,Param.cell.N);
180 n_0 = sqrt(Param.E7.eps_o+Param.E7.delta_eps*sin(theta_0).^2); % Fissato, è quello
      iniziale
181
182 %% NOISE CORRELATION IN ONE PLANE xy
183
184 % I leave mu and sigma for the comprehension
185 mu = 0;  % variation around the equilibrium
186 sigma = 1;  % variance is already in the corr matrix
187
188 [corr] = correlation_plane_xy(Param,0); % (M*N, M*N)
189
190 U = chol(corr);
191
192 random_mtrx = randn(Param.cell.M,Param.cell.N); % matrix
193 random_mtrx(:,1)=0;
194 random_mtrx(:,Param.cell.N)=0;
195 random = matrix2vect(random_mtrx,Param.cell.M,Param.cell.N); % vector
196
197 err_n_x = mu + sigma*U*random; % error on the variable n_x (fluctuations of the
      director), also (mu + sigma*prova'*U)', but U is symmetric! :D
198 % clear random
199 delta_theta = atan(err_n_x); %%% % I leave the angle in radians
200
201 delta_theta_mtrx = vect2matrix(delta_theta,Param.cell.M,Param.cell.N); % radians [M
      , z_step_number]
202
203
204 %% INITIAL (OPTIMIZED) value of the angle theta
205 eps12vect = matrix2vect(Param.E7.delta_eps*sin(theta_0).*cos(theta_0), Param.cell.M
      , Param.cell.N);
206 eps22vect = matrix2vect(Param.E7.eps_o + Param.E7.delta_eps*cos(theta_0).^2, Param.
      cell.M, Param.cell.N);
```

```
207 theta_0_vect = theta_opt(E_x_vect_0, theta_0_vect, eps12vect, eps22vect, Param); %
      theta_0 in matrix form!
208 theta_0 = vect2matrix(theta_0_vect,Param.cell.M,Param.cell.N);
209
210 % storage of theta
211 theta_storage(:,1) = theta_0_vect;
212
213 % new dielectric constants
214 eps11 = Param.E7.eps_o + Param.E7.delta_eps*sin(theta_0).^2;  % NB theta_0 already
      optimized for the field, theta_0 is a matrix!
215 eps12 = Param.E7.delta_eps*sin(theta_0).*cos(theta_0); % NB theta_0 already
      optimized for the field, theta_0 is a matrix!
216 eps22 = Param.E7.eps_o + Param.E7.delta_eps*cos(theta_0).^2;     % NB theta_0
      already optimized for the field, theta_0 is a matrix!
217 % versione precedente
218 % eps12 = vect2matrix(eps12vect,Param.cell.M,Param.cell.N); % eps12vect obtained
      from theta_opt
219 % eps22 = vect2matrix(eps22vect,Param.cell.M,Param.cell.N); % eps22vect obtained
      from theta_opt
220
221 % H_y_0 = (1/(4e-7*pi*3e8))*sqrt(eps11-(eps12.^2)./eps22).*E_x_0; % Magnetic field
      % matrix % I use the E_x inside the materials: we take into account the part that
       is reflected
222 H_y_0 = (1/(4e-7*pi*3e8)).*E_x_0;
223
224 % fields/intensities at the step zero
225 E_x_vect(:,1) = E_x_vect_0;
226 I2_plane_zy(1,:) = sum(abs(E_x_0).^2,1); % NB SUM!!
227 I2_plane_zx(1,:) = sum(abs(E_x_0).^2,2);  % NB SUM!
228
229 Poynt(1,1) =  sum(sum(abs(E_x_0.*H_y_0*dx*dy)))+...  % Poynt vector : [W/m^2]; this
      is an integral! -> [W]
230       -0.5*sum(abs(E_x_0(1:Param.cell.M,1).*H_y_0(1:Param.cell.M,1))*dx*dy)-...
231       0.5*sum(abs(E_x_0(1:Param.cell.M,Param.cell.N).*H_y_0(1:Param.cell.M,Param.
        cell.N))*dx*dy); %%% FATTO con gli n-1 punti! % [W/m^2]
232
233
234 %% ***** PROPAGATION ***** %%
235 %%
236 % [Poynt,I2_plane_zx,I2_plane_zy,theta_storage,E_x_vect,Pump_profile_storage] =
    Propagation_Crank_Nich(delta_theta_mtrx,U,theta_storage,n_0,E_x_vect,Flux,Poynt,
    I2_plane_zx,I2_plane_zy,P_pump,conc_mol,Param);
237 [Poynt,I2_plane_zx,I2_plane_zy,theta_storage,E_x_vect] = Propagation_Crank_Nich(
    random,delta_theta_mtrx,U,theta_storage,n_0,E_x_vect,Poynt,I2_plane_zx,
    I2_plane_zy,Param);
238 %%
239 %% ********************** %%
240
241 %%
242 delta = 100*(Poynt(max(size(Poynt)),1)-Poynt(1,1))/Poynt(1,1); % losses in %
243
244 toc
245
246 %% OUTPUT PARAMETERS STRUCTURE
247 Output = struct;
248 Output.delta = delta;
249 Output.z_size = z_size;
250 Output.fwhm = fwhm((0:Param.cell.M-1)'*dx,I2_plane_zx(Param.cell.z_step_number+1,:)
    ');  % [m]
251 Output.max_E = max(abs(E_x_vect(:,Param.cell.z_step_number+1)));
252 Output.theta = theta_storage; % theta_storage(:,1:40:Param.cell.z_step_number+1); %
     every 40 steps
253 Output.Poynt = Poynt;
254 Output.I2_plane_zx = I2_plane_zx;
```

```
255 Output.I2_plane_zy = I2_plane_zy;
256 Output.E_x_vect = E_x_vect(:,1:1:Param.cell.z_step_number+1); % every 40 steps
257
258
259 %% Images
260 % walk-off parameter
261 eps12 = Param.E7.delta_eps*sin(Param.cell.theta_boundary).*cos(Param.cell.
      theta_boundary);
262 eps22 = Param.E7.eps_o + Param.E7.delta_eps*cos(Param.cell.theta_boundary).^2;
263 tan_delta_0 = eps12/eps22;
264
265 % Energy evolution
266 h1=figure();
267 plot((0:Param.cell.z_step_number)*Param.cell.dz*10^6, Poynt, 'g*'); % transversal
      section of the beam, for cycle
268 xlabel('z [\mum]')
269 ylabel('Power [W]')
270
271 % Side view
272 [Y_sect,Z] = meshgrid((0:Param.cell.N-1)*dy*10^6,(0:Param.cell.z_step_number)*Param
      .cell.dz*10^6);  % in microns!!!
273 h2=figure();
274 surf(Y_sect,Z,I2_plane_zy); colorbar
275 shading flat
276 view(0,90); %axis equal
277 title('Intensity zy')
278 xlabel('y [\mum ]')
279 ylabel('z [\mum]')
280
281 % Top view
282 [X_sect,Z] = meshgrid((0:Param.cell.M-1)*dx*10^6,(0:Param.cell.z_step_number)*Param
      .cell.dz*10^6);  % in microns!!!
283 h3=figure();
284 surf(X_sect-tan_delta_0.*Z,Z,I2_plane_zx); colorbar
285 shading flat;
286 view(0,90);
287 caxis([min(min(I2_plane_zx)) max(max(I2_plane_zx))]);
288 title('Intensity zx')
289 xlabel('x [\mum ]')
290 ylabel('z [\mum]')
291
292 % Entry profile: no need to change the coordinates
293 [Y_sect,X_sect] = meshgrid((0:Param.cell.N-1)*dy*10^6,(0:Param.cell.M-1)*dx*10^6);
      % in microns!!!
294 h4=figure();
295 surf(Y_sect,X_sect,abs(E_x_0)); colorbar
296 shading flat
297 view(0,90); axis equal
298 title('Input abs(field)')
299 xlabel('y thickness [\mum ]')
300 ylabel('x glass [\mum]')
301
302 % Exit profile: no need to change the coordinates
303 % [Y_sect,X_sect] = meshgrid((0:Param.cell.N-1)*dy*10^6,(0:Param.cell.M-1)*dx*10^6)
      ;  % in microns!!!
304 h5=figure();
305 surf(Y_sect,X_sect,abs(vect2matrix(E_x_vect(:,Param.cell.z_step_number+1),Param.
      cell.M,Param.cell.N))); colorbar
306 shading flat
307 view(0,90); axis equal
308 title('Output abs(field)')
309 xlabel('y thickness [\mum ]')
310 ylabel('x glass [\mum]')
311
```

```
312 % % correlation
313 % h6=figure();
314 % surf(Y_sect,X_sect,vect2matrix(corr(:,1),Param.cell.M,Param.cell.N));  colorbar
315 % shading flat
316 % view(0,90);
317 % title('Correlation')
318 % xlabel('y thickness [\mum ]'); ylabel('x glass [\mum]')
319
320 % % Initial random variable
321 % h7=figure();
322 % surf(Y_sect,X_sect,random_mtrx)
323 % shading flat
324 % view(0,90); axis equal
325 % title('Initial random variable')
326 % xlabel('y thickness [\mum ]'); ylabel('x glass [\mum]'); colorbar
327
328 % Error on theta
329 % [Y_sect,X_sect] = meshgrid((0:Param.cell.N-1)*dy*10^6,(0:Param.cell.M-1)*dx*10^6)
      ;  % in microns!!
330 h8=figure();
331 surf(Y_sect,X_sect,delta_theta_mtrx*180/pi); colorbar
332 shading flat
333 view(0,90); axis equal
334 %caxis([-0.05 0.05]);
335 title('Noise on \theta [ř]')
336 xlabel('y thickness [\mum ]'); ylabel('x glass [\mum]');
337
338
339
340 %% SAVING
341
342 directory =  strcat(pwd,'\Simulations');
343 name = strcat('P_inj_',num2str(Param.soliton.P_inj*10^3),'mW_',num2str(Param.cell.M
      ),'x',num2str(Param.cell.N),'_',...
344                   num2str(Param.cell.z_step_number),'x',num2str(Param.cell.dz*10^6),
                        '_um_steps_aver_1_8618e-4_noise_every_',num2str(Param.cell.
                        step_noise),'_steps_',num2str(num_sim));
345
346
347 mkdir(directory,name)
348
349
350 % IMAGES
351 print(h1,'-dpng',strcat(directory,'\',name,'\Energy.png'),'-r300'); close (h1)
352 print(h2,'-dpng',strcat(directory,'\',name,'\Intensity_Profile_zy.png'),'-r300');
      close (h2)
353 print(h3,'-dpng',strcat(directory,'\',name,'\Intensity_Profile_zx.png'),'-r300');
      close (h3)
354 print(h4,'-dpng',strcat(directory,'\',name,'\Field_section_Input.png'),'-r300');
      close (h4)
355 print(h5,'-dpng',strcat(directory,'\',name,'\Field_section_Output.png'),'-r300');
      close (h5)
356 print(h8,'-dpng',strcat(directory,'\',name,'\Noise_on_theta.png'),'-r300'); close (
      h8)
357 save(strcat(directory,'\',name,'\Output.mat'),'-struct','Output','-v7.3')
358 save(strcat(directory,'\',name,'\Param.mat'),'-struct','Param','-v7.3')
359
360
361 end
```

B.2 Propagation equation

In this section we report the code of the function that describes the propagation of the beam.

```
function [Poynt,I2_plane_zx,I2_plane_zy,theta_storage,E_x_vect] =
  Propagation_Crank_Nich(random_1,delta_theta_mtrx,U,theta_storage_mtrx,n_0,
  E_x_vect_0,Poynt,I2_plane_zx,I2_plane_zy,Param)

%% discretization
dx = Param.cell.x_size/(Param.cell.M-1);
dy = Param.cell.y_size/(Param.cell.N-1);

%% INITIAL values of the dielectric constant
theta_0 = vect2matrix(theta_storage_mtrx(:,1),Param.cell.M,Param.cell.N);
delta_theta = matrix2vect(delta_theta_mtrx,Param.cell.M,Param.cell.N);

% we add the noise ()
theta_0 = theta_0 + delta_theta_mtrx;   %%% !!! add delta_theta !!!!!!!!!!! %%%

eps11 = Param.E7.eps_o + Param.E7.delta_eps*sin(theta_0).^2;  % NB theta_0 already
  optimized for the field, theta_0 is a matrix!
eps12 = Param.E7.delta_eps*sin(theta_0).*cos(theta_0);
eps22 = Param.E7.eps_o + Param.E7.delta_eps*cos(theta_0).^2;

%% INITIAL propagation parameters
k_0 =    2*pi/Param.soliton.lambda;
tan_delta_0 = eps12(1,1)./eps22(1,1); % initial value of the walk-off, calculated
  with the rubbing angle
etha =   2*1i*k_0*n_0;
gamma =  k_0^2*(eps11-n_0.^2)+1i*k_0*n_0*Param.E7.alpha;
zeta =   2*1i*k_0.*n_0.*(eps12./eps22-tan_delta_0);

a = etha/Param.cell.dz-gamma/2+1/dy^2+1/dx^2;   % it depends on theta
b = ( zeta/(4*dx)+1/(2*dx^2));         % it depends on theta
c = (-zeta/(4*dx)+1/(2*dx^2));        % it depends on theta
d = ones(size(a))*(1/(2*dy^2));
f = (etha/Param.cell.dz+gamma/2-1/dy^2-1/dx^2); % it depends on theta

[A,B] = discret(Param.cell.M,Param.cell.N,a,b,c,d,f);

theta_n_vect = matrix2vect(theta_0,Param.cell.M,Param.cell.N);
E_x_vect =     E_x_vect_0;

%% New noise generation
random_mtrx_2 = randn(Param.cell.M,Param.cell.N); % matrix
random_mtrx_2(:,1)=0;
random_mtrx_2(:,Param.cell.N)=0;
random_2 = matrix2vect(random_mtrx_2,Param.cell.M,Param.cell.N); % vector

ang_coeff = (random_2-random_1)/(Param.cell.step_noise-1); % I calculate the
  angular coefficient between each correspondent pixel of 2planes, the distance
  along z is in PIXELS!!!


%% propagation loop
% preallocation: già fatta!
theta_storage = zeros(Param.cell.N*Param.cell.M,Param.cell.z_step_number+1);
theta_storage(:,1) = theta_n_vect;

for z_step = 1 : Param.cell.z_step_number
    E_x_vect(:,z_step+1) = A\(B*E_x_vect(:,z_step));
    E_x = vect2matrix(E_x_vect(:,z_step+1),Param.cell.M,Param.cell.N);

    % Theta optimization for this new field
```

```
55      if (mod(z_step,Param.cell.step_optim)==0 || z_step==1)  % not at every step
56          eps12vect = matrix2vect(eps12, Param.cell.M, Param.cell.N);
57          eps22vect = matrix2vect(eps22, Param.cell.M, Param.cell.N);
58          theta_n1_vect = theta_opt(E_x_vect(:,z_step+1), theta_n_vect, eps12vect,
              eps22vect,Param);
59      end
60
61      % New noise generation for the interpolation, , the first one is already
          calculated!
62      if  (z_step==1)
63          random = random_1; % for the first step :)
64
65      elseif (mod(z_step,Param.cell.step_noise)==0)  % not at every step
66          random_1 = random_2;
67
68          random_mtrx_2 = randn(Param.cell.M,Param.cell.N); % matrix
69          random_mtrx_2(:,1)=0;
70          random_mtrx_2(:,Param.cell.N)=0;
71          random_2 = matrix2vect(random_mtrx_2,Param.cell.M,Param.cell.N); % vector
72
73          ang_coeff = (random_2-random_1)/(Param.cell.step_noise-1); % I calculate
              the angular coefficient between each correspondent pixel of 2planes, the
              distance along z is in PIXELS!!!
74
75          random = random_1;
76      else
77          random = ang_coeff*mod(z_step,Param.cell.step_noise) + random_1; % NB mod(
              z_step,Param.cell.step_noise)=dz in the formula y_2 = ang_coeff*dz + y_1,
               only because z is in pixel!!
78
79      end
80
81
82      err_n_x = U*random; % error on the variable n_x (fluctuations of the director),
           also (mu + sigma*prova'*U)', but U is symmetric! :D; mu=0; sigma=1
83      delta_theta = atan(err_n_x); %%%%  I leave the angle in radians ; it is a
          vector
84
85      theta_n1_vect = theta_n1_vect + delta_theta; %%% !!! add delta_theta
          !!!!!!!!!!! %%%
86
87      % new dielectric constants
88      eps11 = vect2matrix(Param.E7.eps_o + Param.E7.delta_eps*sin(theta_n1_vect).^2,
          Param.cell.M,Param.cell.N);  % NB theta_n1 already optimized for the field
89      eps12 = vect2matrix(Param.E7.delta_eps*sin(theta_n1_vect).*cos(theta_n1_vect),
          Param.cell.M,Param.cell.N); % NB theta_n1 already optimized for the field
90      eps22 = vect2matrix(Param.E7.eps_o + Param.E7.delta_eps*cos(theta_n1_vect).^2,
          Param.cell.M,Param.cell.N);     % NB theta_n1 already optimized for the field
91
92      % Magnetic field and Energy
93      H_y = (1/(4*10^-7*pi*3*10^8)).*E_x;
94      Poynt(z_step+1,1) =  sum(sum(abs(E_x.*H_y*dx*dy)))+...
95          -0.5*sum(abs(E_x(1:Param.cell.M,1).*H_y(1:Param.cell.M,1))*dx*dy)-0.5*sum(
              abs(E_x(1:Param.cell.M,Param.cell.N).*H_y(1:Param.cell.M,Param.cell.N))*
              dx*dy);  %%% FATTO con gli n-1 punti!
96
97      % Section of the field
98      I2_plane_zy(z_step+1,:) = sum(abs(E_x).^2,1);
99      I2_plane_zx(z_step+1,:) = sum(abs(E_x).^2,2)';
100
101     % theta storage
102     theta_storage(:,z_step+1) = theta_n1_vect;
103
104     % new A and B matrix
```

```
    etha = 2*1i*k_0*n_0;
    gamma = k_0^2*(eps11-n_0.^2)+1i*k_0*n_0*Param.E7.alpha;
    zeta = 2*1i*k_0.*n_0.*(eps12./eps22-tan_delta_0);
    a = etha/Param.cell.dz-gamma/2+1/dy^2+1/dx^2;   % it depends on theta
    b = (zeta/(4*dx)+1/(2*dx^2));         % it depends on theta
    c = (-zeta/(4*dx)+1/(2*dx^2));        % it depends on theta
    d = ones(size(a))*(1/(2*dy^2));
    f = (etha/Param.cell.dz+gamma/2-1/dy^2-1/dx^2); % it depends on theta
    [A,B] = discret(Param.cell.M,Param.cell.N,a,b,c,d,f);

    theta_n_vect = theta_n1_vect;

end

end
```

B.3 Optimization of the moleculer orientation

```
function [theta_final_vect] = theta_opt(E_x_vect_0, theta_0_vect, eps12vect,
  eps22vect, Param)


%% Discretization geometry
%axis
dx = Param.cell.x_size/(Param.cell.M-1);
dy = Param.cell.y_size/(Param.cell.N-1);
% coordinates of the glasses (for the VECTORIZED matrix!!)
glass_left = (1:Param.cell.N:((Param.cell.M-1)*Param.cell.N+1));
glass_right = (Param.cell.N:Param.cell.N:Param.cell.M*Param.cell.N);

eps_zero = 8.854e-12;         % F/m    % vacuum dielectric constant

%% Definition of the matrix
a = -2*Param.E7.K/dx^2-2*Param.E7.K/dy^2;
b = (Param.E7.K/(dy^2));
d = (Param.E7.K/(dx^2));
A = discret_NR(Param.cell.M,Param.cell.N,a,b,d); % A is fixed! A is a sparse matrix
   M*NxM*N

noto = zeros(size(theta_0_vect));
noto((glass_left),1) = Param.cell.theta_boundary;
noto((glass_right),1) = Param.cell.theta_boundary;

% equation
F_n1 = F_bound(A,theta_0_vect,noto,E_x_vect_0, eps12vect, eps22vect,Param.E7.
  delta_eps); % F is a funtion!

theta_n1 = theta_0_vect;

while (norm(F_n1)/(Param.cell.N^2*Param.cell.M^2)) > Param.E7.err_theta_opt

    % re-indexing
    F_n = F_n1;
    theta_n = theta_n1;

    % Jacobian calculus:
    coeff = 0.5*eps_zero*Param.E7.delta_eps*abs(E_x_vect_0).^2.*cos(2*(theta_n-atan
      (eps12vect./eps22vect))).*...
        (2-(2*Param.E7.delta_eps*((Param.E7.delta_eps+2*Param.E7.eps_o)*cos(2*
          theta_n)+Param.E7.delta_eps)./...  % numeratore deriv delta
        (Param.E7.delta_eps^2+Param.E7.delta_eps*(Param.E7.delta_eps+2*Param.E7.
          eps_o)*cos(2*theta_n)+2*Param.E7.delta_eps*Param.E7.eps_o+2*Param.E7.
```

```
          eps_o^2)));     % denomin deriv delta
    coeff((glass_left),1) = 0; % coordinates of the glass in the VECTORIZED matrix
    coeff((glass_right),1) = 0;
    NL = discret_NR_diag(Param.cell.M,Param.cell.N,coeff); % on the glasses the
      element is zero
    NL((glass_left),1) = 0;
    NL((glass_right),1) = 0;

    J = A + NL; %(=0 on the glasses)

    d_theta = -J\(F_n); % correction the theta (no correction on the glasses)

    theta_n1 = theta_n + d_theta; % new theta, vector

    % we have to "update the values of eps also!!
    eps12vect = Param.E7.delta_eps*sin(theta_n1).*cos(theta_n1); % vector
    eps22vect = Param.E7.eps_o + Param.E7.delta_eps*cos(theta_n1).^2;     % vector

    F_n1 = F_bound(A,theta_n1,noto,E_x_vect_0, eps12vect, eps22vect, Param.E7.
      delta_eps);

end

theta_final_vect = theta_n1;

% figure();
% [X,Y] = meshgrid((0:N-1)*dy*10^6,(0:M-1)*dx*10^6);
% surf(X,Y,theta_final*180/pi);
% % surf(theta_final*180/pi);
% axis equal
% shading flat
% view(0,90); colorbar
% title('Theta (final)')
% xlabel('y [\mum ]')
% ylabel('x [\mum]')

end
```

B.4 Correlation matrix

Function that calculates the correlation matrix in the plane $\hat{x}\hat{y}$ (Eq.(3.58) and (3.63))

```
%% definition of the matrix  (De Gennes, pp. 141-143)
% corr = (M*N, M*N) = corr(s,p)
% p,s are the indexes!! p,s = j + N*(k-1)

function [corr] = correlation_plane_xy(Param, E_external)

M = Param.cell.M;    % number of raws
N = Param.cell.N;    % number of columns
dx = Param.cell.x_size/(Param.cell.M-1);   % [m]
dy = Param.cell.y_size/(Param.cell.N-1);   % [m]
K = Param.E7.K;   % [N]

% physical constant
k_B = 1.38064852*10^(-23);  % [J/K] Boltzmann constant
T = 300;                    % [K]
eps_zero = 8.854187817*10^(-12);  % [F/m]

% applied electric field
% E_external = 0; %10^-12;

% Field coherence lenght (De Gennes p.142)
```

```
Xi = (Param.E7.K)/(eps_zero*Param.E7.delta_eps*E_external);

% empty matrix
corr = zeros(M*N,M*N);

% dR = Param.E7.corr_dR; %sqrt(dx^2+dy^2);
aver = 1.8618e-4; % average(Param,Xi,dx); %  aver=1.8618e-4 for 155x211 (55x75um^2)


%% versione pedissequa: i cicli for sono luuuunghissimi!!!

for s = 1:M*N  % we go along the COLUMN

    raw_s = floor(s/N)+1;
    col_s = mod(s,N);

    for p = s:M*N  % we go along the ROW

        raw_p = floor(p/N)+1;
        col_p = mod(p,N);

        if (s==p) % the diagonal is "by hand"
            corr(s,p) = 0.5*aver; %0.5*(k_B*T)/(pi*K*dR); % After I make corr +
              corr': we have 2 times the diagonal
        elseif (abs(raw_p-raw_s)<(M/2))  % the smaller vertical distance between
          the two points is "the usual"
            R = sqrt((abs(raw_s-raw_p)*dx)^2+(abs(col_s-col_p)*dy)^2);
            corr(s,p) = ((k_B*T)/(4*pi*K*R))*exp(-R/Xi);
        else  % the smaller vertical distance between the two points is "across the
           boundary"
            R = sqrt(((abs(raw_s-raw_p)-M)*dx)^2+(abs(col_s-col_p)*dy)^2);
            corr(s,p) = ((k_B*T)/(4*pi*K*R))*exp(-R/Xi);
        end

     end
end;

corr = corr + corr';
```

B.5 Auxiliary functions

Algorithm B.1 Function that builds the matrices A and B, as described in paragraphs Sect. 3.1.1.

```
% Generates discretization of equation
% etha*u_z = u_xx + u_yy + gamma*u + zeta*u_x
% using Crank Nicholson discretisation
%
%
%           ^
%    x,     ę       ę ę glass                        ę ę glass
% M points ę       ę ę                              ę ę
%          ę       ę ę         <--j-->              ę ę
%          ę       ę ę                              ę ę
%          ę       ę ę                        ^     ę ę
%          ę       ę ę            /-\         ę     ę ę
%          ę       ę ę            \-/         k     ę ę
%          ę       ę ę                        ę     ę ę
%          ę       ę ę                        v     ę ę
%          ę       ę ę                              ę ę
%          ę    z  ę ę                              ę ę
%          ę  /    ę ę                              ę ę
%          ę /     ę ę                              ę ę
```

```
%           ę/------------------------------------------->
%                                                   y, N points
%
%     !!!!!!!!!!!! SIZE(MATRIX) = (M,N) !!!!!!!!!!!!!!!!!!
%
% with M grid pts in x, N grid pts in y
% The ordering (y first, then x) is used. (RIGA x COLONNA)
% dx,dy : stepsize of the discretization along x and y
% function A = ellprob(M,N,dx,dy)

%% all the variables are in the SI!!!!!!!!!!

function [A,B] = discret(M,N,a,b,c,d,f) %#codegen


%% definition of the matrix

tot = 2*N*(M-1)+M*(N+2*(N-1)); % total number of elements different from zero
K = complex(zeros(tot, 1), zeros(tot,1));
J = K;
S_A = K;
S_B = K;

counter = 0;

for k = 1:M  % we go along the COLUMN
    for j = 1:N  % we go along the ROW
        ind = j + N*(k-1);
        counter = counter +1; K(counter,1) = ind; J(counter,1) = ind; S_A(counter
          ,1) = a(k,j); S_B(counter,1) = f(k,j);
        if (j > 1),
            counter = counter +1;  K(counter,1) = ind; J(counter,1) = ind-1; S_A(
              counter,1) = -d(k,j); S_B(counter,1) = d(k,j); end;
        if (j < N),
            counter = counter +1;  K(counter,1) = ind; J(counter,1) = ind+1; S_A(
              counter,1) = -d(k,j); S_B(counter,1) = d(k,j); end;
        if (k == 1), % cyclic boundary conditions
            counter = counter +1;  K(counter,1) = ind; J(counter,1) = ind+N*(M-1);
              S_A(counter,1) = -c(k,j); S_B(counter,1) = c(k,j);
            counter = counter +1;  K(counter,1) = ind; J(counter,1) = ind+N; S_A(
              counter,1) = -b(k,j); S_B(counter,1) = b(k,j);
        elseif (k == M), % cyclic boundary conditions
            counter = counter +1;  K(counter,1) = ind; J(counter,1) = ind-N*(M-1);
              S_A(counter,1) = -b(k,j); S_B(counter,1) = b(k,j);
            counter = counter +1;  K(counter,1) = ind; J(counter,1) = ind-N; S_A(
              counter,1) = -c(k,j); S_B(counter,1) = c(k,j);
        else
            counter = counter +1;  K(counter,1) = ind; J(counter,1) = ind-N; S_A(
              counter,1) = -c(k,j); S_B(counter,1) = c(k,j);
            counter = counter +1;  K(counter,1) = ind; J(counter,1) = ind+N; S_A(
              counter,1) = -b(k,j); S_B(counter,1) = b(k,j);
        end
     end
end;

A = sparse(K,J,S_A);
B = sparse(K,J,S_B);

% [outmax_file,outmax_path] = uigetfile('*.txt','Select Data to Open','C:\Program
  Files\Geo-information\Reliability\input_copied\');
% outmax_user_input_data = fullfile(outmax_path,outmax_file);
```

Algorithm B.2 Function that creates the initial field E_x.

```
% creation of the field E_x

function [E_x] = create_Ex(Param_soliton,n_0,amplitudeE,M,N,x_size,y_size) %#
  codegen

x = linspace(-0.5*x_size, 0.5*x_size, M);  % better, due to numerical approximation
y = linspace(-0.5*y_size, 0.5*y_size, N);

% attenzione meshgrid inverte linee e colonne!!!
[X,Y] = meshgrid(y,x);

beta_0 = 2*pi*n_0/Param_soliton.lambda;

E_x = amplitudeE*exp((1i*beta_0/(2*Param_soliton.R_phase)-1/Param_soliton.w_0x^2)*X
  .^2+ ...
        (1i*beta_0/(2*Param_soliton.R_phase)-1/Param_soliton.w_0y^2)*Y.^2);
```

Algorithm B.3 Function vect2matrix for the re-indexing of a vector and transform it in a matrix.

```
%% re-indexing of the vector, in order to have a matrix A
% we read the matrix "line by line"
% [1 2 3; 4 5 6]  ->  [1 2 3 4 5 6]

function [A] = vect2matrix(u,M,N)

A = complex(zeros(M,N),zeros(M,N));

for k = 1:M
    for j = 1:N
        ind = j + N*(k-1) ;
        A(k,j) = u(ind,1);
     end
end;
```

Algorithm B.4 Function matrix2vect for the re-indexing of a matrix and transform it in a vector.

```
%% re-indexing of the matrix A, in order to have a vector
% we read the matrix "line by line"
% [1 2 3; 4 5 6]  ->  [1 2 3 4 5 6]

function [u] = matrix2vect(A,M,N)

u = zeros(N*M,1);

for k = 1:M
    for j = 1:N
        ind = j + N*(k-1) ;
        u(ind,1) = A(k,j);
     end
end;
```

Algorithm B.5 Function that discretizes the Eq. (3.25).

```
% Generates discretization of equation
% etha*u_z = u_xx + u_yy + gamma*u + zeta*u_x
% using Crank Nicholson discretisation

%% Propagation of the beam
% SCHEME: the position of the glasses is rotated
%
%
%          ^
```

```
%     x,     ę       ę ę glass                         ę ę glass
% M points ę       ę ę                                 ę ę
%          ę       ę ę         <--j-->                 ę ę
%          ę       ę ę                                 ę ę
%          ę       ę ę                        ^        ę ę
%          ę       ę ę            /-\         ę        ę ę
%          ę       ę ę            \-/         k        ę ę
%          ę       ę ę                        ę        ę ę
%          ę       ę ę                        v        ę ę
%          ę       ę ę                                 ę ę
%          ę    z  ę ę                                 ę ę
%          ę  /    ę ę                                 ę ę
%          ę /     ę ę                                 ę ę
%          ę/-------------------------------------------->
%                                                 y, N points
%
%     !!!!!!!!!!!! SIZE(MATRIX) = (M,N) !!!!!!!!!!!!!!!!!
%
% with N grid pts in x, M grid pts in y
% The ordering (y first, then x) is used. (RIGA x COLONNA)
% dx,dy : stepsize of the discretization along x and y
% function A = ellprob(M,N,dx,dy)

%% all the variables are in the SI!!!!!!!!!!

function [A] = discret_NR(M,N,a,b,d) %#codegen


%% definition of the matrix

% tot = 2*N*(M-1)+M*(N+2*(N-1)); % total number of elements different from zero,
  the "-2*N" is because we do not have the equation on the glasses

K = complex(zeros(100, 1), zeros(100,1));
J = K;
S_A = K;

counter = 0; % solo per incrementare la posizione nei vettori che diamo in pasto a
  sparse

for k = 1:M
    for j = 1:N
        ind = j + N*(k-1);

        if (j==1 || j==N), counter = counter +1; K(counter,1) = ind; J(counter,1) =
           ind; S_A(counter,1) = 1; % glass boundary conditions
        else
            counter = counter +1; K(counter,1) = ind; J(counter,1) = ind; S_A(
              counter,1) = a;
            counter = counter +1;  K(counter,1) = ind; J(counter,1) = ind-1; S_A(
              counter,1) = b;
            counter = counter +1;  K(counter,1) = ind; J(counter,1) = ind+1; S_A(
              counter,1) = b;

            if (k == 1),  % cyclic boundary conditions
                counter = counter +1;  K(counter,1) = ind; J(counter,1) = ind+N;
                  S_A(counter,1) = d;
                counter = counter +1;  K(counter,1) = ind; J(counter,1) = ind+N*(M
                  -1); S_A(counter,1) = d;
            elseif (k == M), % cyclic boundary conditions
                counter = counter +1;  K(counter,1) = ind; J(counter,1) = ind-N;
                  S_A(counter,1) = d;
                counter = counter +1;  K(counter,1) = ind; J(counter,1) = ind-N*(M
                  -1); S_A(counter,1) = d;
```

```
            else
                counter = counter +1;  K(counter,1) = ind; J(counter,1) = ind-N;
                  S_A(counter,1) = d;
                counter = counter +1;  K(counter,1) = ind; J(counter,1) = ind+N;
                  S_A(counter,1) = d;

            end
        end
    end
end;

A = sparse(K,J,S_A);
```

Algorithm B.6 Function that imposes $\delta\bar{\vartheta} = 0$ on the boundary.

```
% Generates discretization of equation
% etha*u_z = u_xx + u_yy + gamma*u + zeta*u_x
% using Crank Nicholson discretisation
%
%
%           ^
%     x,    ę     ------------------------------ glass
% M points ę     ------------------------------
%           ę            <--j-->
%           ę
%           ę                          ^
%           ę               /-\        ę
%           ę               \-/        k
%           ę                          ę
%           ę                          v
%           ę
%           ę   z
%           ę  /   ------------------------------
%           ę /    ------------------------------ glass
%           ę/-------------------------------------------->
%                                                  y, N points
%
%     !!!!!!!!!!!! SIZE(MATRIX) = (M,N) !!!!!!!!!!!!!!!!!!
%
% with N grid pts in x, M grid pts in y
% The ordering (y first, then x) is used. (RIGA x COLONNA)
% dx,dy : stepsize of the discretization along x and y
% function A = ellprob(M,N,dx,dy)

%% all the variables are in the SI!!!!!!!!!!

function [A] = discret_NR_diag(M,N,a)

% NB a is a vector!! it depends on theta!!

%% definition of the matrix

tot = M*N; % total number of elements different from zero
K = (1:1:tot);
J = (1:1:tot);

A = sparse(K,J,a);
```

Algorithm B.7 Function that calculates $\bar{F}$ Eq. (3.34).

```
%% it calculates the function
%% F = K(d^2theta/dx^2 + d^2theta/dy^2) + 0.5*eps_zero*delta_eps*|E|^2*sin(2*theta)

```

```
4
5  function [F] = F_bound (A_norm,theta,b,E,eps12vect,eps22vect, delta_eps)
6
7  eps_zero = 8.854e-12;          % F/m    % vacuum dielectric constant
8
9  F = A_norm*theta + (0.5*eps_zero*delta_eps*abs(E).^2.*sin(2*(theta-atan(eps12vect./
     eps22vect)))-b);
10 end
```

Algorithm B.8 Function that calculates the average of the correlation function over one cell Eq. (3.63).

```
1  function [aver] = average(Param,T,Xi,dx)
2
3  K = Param.E7.K;    % [N] one constant approximation
4
5  % physial constant
6  k_B = 1.38064852*10^(-23);  % [J/K] Boltzmann constant                    % [K]
7
8  a =  dx; %3*10^-9;  % [m]
9
10 %% integral
11 fun = @(q) ((k_B*T)/(a*2*K*pi^2))*((q.*sinint(q*a))./(q.^2+Xi^-2));
12 aver = integral(fun,0,2*pi/a);
13
14 end
```

Bibliography

1. B. Bahadur, "Liquid crystal displays", *Molecular Crystals and Liquid Crystals* **109**, 3–93 (1984).
2. M. Schadt, "Liquid crystal materials and liquid crystal displays", *Annual Review of Materials Science* **27**, 305–379 (1997).
3. C. Weder, C. Sarwa, A. Montali, C. Bastiaansen, and P. Smith, "Incorporation of photoluminescent polarizers into liquid crystal displays", *Science* **279**, 835–837 (1998).
4. H.-W. Chen, R.-D. Zhu, J. He, W. Duan, W. Hu, Y.-Q. Lu, M.-C. Li, S.-L. Lee, Y.-J. Dong, and S.-T. Wu, "Going beyond the limit of an lcd's color gamut", *Light: Science & Applications* **6**, e17043 (2017).
5. C. Lampert, "Large-area smart glass and integrated photovoltaics", *Solar Energy Materials and Solar Cells* **76**, 489–499 (2003).
6. D. Coates, "Polymer-dispersed liquid crystals", *Journal of Materials Chemistry* **5**, 2063–2072 (1995).
7. K. Sun, Z. Xiao, S. Lu, W. Zajaczkowski, W. Pisula, E. Hanssen, J. M. White, R. M. Williamson, J. Subbiah, J. Ouyang, et al., "A molecular nematic liquid crystalline material for high-performance organic photovoltaics", *Nature Communications* **6**, 6013 (2015).
8. V. I. Kopp, B. Fan, H. K. M. Vithana, and A. Z. Genack, "Low-threshold lasing at the edge of a photonic stop band in cholesteric liquid crystal", *Optics Letters* **23**, 1707–1709 (1998).
9. B. Taheri, A. Munoz, P. Palffy-Muhoray, and R. Twieg, "Low threshold lasing in cholesteric liquid crystals", *Molecular Crystals and Liquid Crystals* **358**, 73–82 (2001).
10. H. J. Coles and S. M. Morris, "Liquid-crystal lasers", *Nature Photonics* **4**, 676–685 (2010).
11. A. Ford, S. Morris, and H. Coles, "Photonics and lasing in liquid crystals", *Materials Today* **9**, 36 (2006).
12. C. Maurer, A. Jesacher, S. Bernet, and M. Ritsch-Marte, "What spatial light modulators can do for optical microscopy", *Laser & Photonics Reviews* **5**, 81–101 (2011).
13. E. Braun, L. P. Faucheux, and A. Libchaber, "Strong self-focusing in nematic liquid crystals", *Physical Review A* **48**, 611–622 (1993).
14. M. A. Karpierz, M. Sierakowski, M. Świłło, and T. Woliński, "Self focusing in liquid crystalline waveguides", *Molecular Crystals and Liquid Crystals* **320**, 157–163 (1998).
15. M. Warenghem, J. Henninot, and G. Abbate, "Non linearly induced self waveguiding structure in dye doped nematic liquid crystals confined in capillaries", *Optics Express* **2**, 483–490 (1998).
16. M. Peccianti, A. D. Rossi, G. Assanto, A. D. Luca, C. Umeton, and I. Khoo, "Electrically assisted self-confinement and waveguiding in planar nematic liquid crystal cells", *Applied Physics Letters* **77**, 7–9 (2000).
17. M. Peccianti and G. Assanto, "Nematicons", *Physics Reports* **516**, 147–208 (2012).
18. G. Assanto, *Nematicons: spatial optical solitons in nematic liquid crystals*, Vol. 74 (John Wiley & Sons, 2012).
19. A. Piccardi, A. Alberucci, and G. Assanto, "Soliton self-deflection via power-dependent walk-off", *Applied Physics Letters* **96**, 061105 (2010).
20. A. Alberucci, A. Piccardi, M. Peccianti, M. Kaczmarek, and G. Assanto, "Propagation of spatial optical solitons in a dielectric with adjustable nonlinearity", *Physical Review A* **82**, 023806 (2010).
21. M. Kwasny, A. Piccardi, A. Alberucci, M. Peccianti, M. Kaczmarek, M. A. Karpierz, and G. Assanto, "Nematicon–nematicon interactions in a medium with tunable nonlinearity and fixed nonlocality", *Optics Letters* **36**, 2566–2568 (2011).

22. A. Piccardi, M. Trotta, M. Kwasny, A. Alberucci, R. Asquini, M. Karpierz, A. d'Alessandro, and G. Assanto, "Trends and trade-offs in nematicon propagation", *Applied Physics B* **104**, 805–811 (2011).
23. G. Assanto, M. Peccianti, and C. Conti, "Nematicons: optical spatial solitons in nematic liquid crystals", *Optics and Photonics News* **14**, 44–48 (2003).
24. A. Piccardi, A. Alberucci, and G. Assanto, "Self-turning self-confined light beams in guest-host media", *Physical Review Letters* **104**, 213904 (2010).
25. M. Peccianti, C. Conti, G. Assanto, A. De Luca, and C. Umeton, "Routing of anisotropic spatial solitons and modulational instability in liquid crystals", *Nature* **432**, 733–737 (2004).
26. M. Peccianti and G. Assanto, "Incoherent spatial solitary waves in nematic liquid crystals", *Optics Letters* **26**, 1791–1793 (2001).
27. M. Peccianti and G. Assanto, "Nematic liquid crystals: a suitable medium for self-confinement of coherent and incoherent light", *Physical Review E* **65**, 035603 (2002).
28. P. de Gennes and J. Prost, *The physics of liquid crystals*, 2nd (Oxford University Press, 1995).
29. J. Beeckman, K. Neyts, X. Hutsebaut, C. Cambournac, and M. Haelterman, "Simulations and experiments on self-focusing conditions in nematic liquid-crystal planar cells", *Optics Express* **12**, 1011–1018 (2004).
30. X. Hutsebaut, C. Cambournac, M. Haelterman, J. Beeckman, and K. Neyts, "Measurement of the self-induced waveguide of a solitonlike optical beam in a nematic liquid crystal", *JOSA B* **22**, 1424–1431 (2005).
31. M. Peccianti, K. A. Brzdąkiewicz, and G. Assanto, "Nonlocal spatial soliton interactions in nematic liquid crystals", *Optics Letters* **27**, 1460–1462 (2002).
32. Y. Izdebskaya, V. Shvedov, A. Desyatnikov, W. Krolikowski, M. Belic, G. Assanto, and Y. Kivshar, "Counterpropagating nematicons in bias-free liquid crystals", *Optics Express* **18**, 3258–3263 (2010).
33. Y. Izdebskaya, V. Shvedov, A. Desyatnikov, W. Krolikowski, G. Assanto, and Y. Kivshar, "Incoherent interaction of nematicons in bias-free liquid-crystal cells", *Journal of the European Optical Society - Rapid publications* **5**, 10008 (2010).
34. Y. V. Izdebskaya, A. S. Desyatnikov, G. Assanto, and Y. S. Kivshar, "Multimode nematicon waveguides", *Optics letters* **36**, 184–186 (2011).
35. M. Peccianti and G. Assanto, "Signal readdressing by steering of spatial solitons in bulk nematic liquid crystals", *Optics Letters* **26**, 1690–1692 (2001).
36. S. Perumbilavil, A. Piccardi, O. Buchnev, M. Kauranen, G. Strangi, and G. Assanto, "Soliton-assisted random lasing in optically-pumped liquid crystals", *Applied Physics Letters* **109**, 161105 (2016).
37. S. Perumbilavil, A. Piccardi, O. Buchnev, M. Kauranen, G. Strangi, and G. Assanto, "All-optical guided-wave random laser in nematic liquid crystals", *Optics Express* **25**, 4672–4679 (2017).
38. M. Peccianti, C. Conti, G. Assanto, A. De Luca, and C. Umeton, "All-optical switching and logic gating with spatial solitons in liquid crystals", *Applied Physics Letters* **81**, 3335 (2002).
39. Y. V. Izdebskaya, J Rebling, A. Desyatnikov, G Assanto, and Y. S. Kivshar, "All-optical switching of a signal by a pair of interacting nematicons", *Optics Express* **20**, 24701–24707 (2012).
40. A. Piccardi, A. Alberucci, U. Bortolozzo, S. Residori, and G. Assanto, "Soliton gating and switching in liquid crystal light valve", *Applied Physics Letters* **96**, 071104 (2010).
41. A. Piccardi, A. Alberucci, U. Bortolozzo, S. Residori, and G. Assanto, "Readdressable interconnects with spatial soliton waveguides in liquid crystal light valves", *IEEE Photonics Technology Letters* **22**, 694–696 (2010).
42. S.-T. Wu and K.-C. Lim, "Absorption and scattering measurements of nematic liquid crystals", *Applied Optics* **26**, 1722–1727 (1987).
43. A. I. Strinić, D. V. Timotijević, D. Arsenović, M. S. Petrović, and M. R. Belić, "Spatiotemporal optical instabilities in nematic solitons", *Optics Express* **13**, 493–504 (2005).

44. J. Beeckman, H. Azarinia, and M. Haelterman, "Countering spatial soliton breakdown in nematic liquid crystals", *Optics Letters* **34**, 1900–1902 (2009).

45. A. Alberucci and G. Assanto, "Dissipative self-confined optical beams in doped nematic liquid crystals", *Journal of Nonlinear Optical Physics & Materials* **16**, 295–305 (2007).

46. B. Redding, M. Choma, and H. Cao, "Speckle-free laser imaging using random laser illumination", *Nature Photonics* **6**, 355–359 (2012).

47. B. Redding, P. Ahmadi, V. Mokan, M. Seifert, M. A. Choma, and H. Cao, "Low-spatial-coherence high-radiance broadband fiber source for speckle free imaging", *Optics Letters* **40**, 4607–4610 (2015).

48. A. F. Fercher, W. Drexler, C. K. Hitzenberger, and T. Lasser, "Optical coherence tomography-principles and applications", *Reports on Progress in Physics* **66**, 239–303 (2003).

49. C. M. Eigenwillig, T. Klein, W. Wieser, B. R. Biedermann, and R. Huber, "Wavelength swept amplified spontaneous emission source for high speed retinal optical coherence tomography at 1060 nm", *Journal of Biophotonics* **4**, 552–558 (2011).

50. C. M. Eigenwillig, B. R. Biedermann, W. Wieser, and R. Huber, "Wavelength swept amplified spontaneous emission source", *Optics Express* **17**, 18794–18807 (2009).

51. A Piccardi, A Alberucci, and G Assanto, "Sub-milliwatt dissipative nematicons and spontaneous light emission in dye-doped nematic liquid crystals", *Electronics Letters* **46**, 790–791 (2010).

52. O. Svelto, S. Taccheo, and C. Svelto, "Analysis of amplified spontaneous emission: some corrections to the linford formula", *Optics Communications* **149**, 277–282 (1998).

53. S. Stagira, M. Nisoli, G. Cerullo, M. Zavelani-Rossi, S. D. Silvestri, G. Lanzani, W. Graupner, and G. Leising, "The role of amplified spontaneous emission in the ultrafast relaxation dynamics of polymer films", *Chemical Physics Letters* **289**, 205–210 (1998).

54. J. Ribierre, G. Tsiminis, S. Richardson, G. Turnbull, I. Samuel, H. Barcena, and P. Burn, "Amplified spontaneous emission and lasing properties of bisfluorene-cored dendrimers", *Applied Physics Letters* **91**, 081108 (2007).

55. G. Tsiminis, N. Montgomery, A. Kanibolotsky, A. Ruseckas, I. Perepichka, P. Skabara, G. Turnbull, and I. Samuel, "Laser characteristics of a family of benzene-cored star-shaped oligofluorenes", *Semiconductor Science and Technology* **27**, 094005 (2012).

56. S. J. Woltman, G. D. Jay, and G. P. Crawford, "Liquid-crystal materials find a new order in biomedical applications", *Nature Materials* **6**, 929–938 (2007).

57. L. Blinov, G Cipparrone, P Pagliusi, V. Lazarev, and S. Palto, "Mirrorless lasing from nematic liquid crystals in the plane waveguide geometry without refractive index or gain modulation", *Applied Physics Letters* **89**, 031114 (2006).

58. T. Matsui, M. Ozaki, and K. Yoshino, "Electro-tunable laser action in a dye-doped nematic liquid crystal waveguide under holographic excitation", *Applied Physics Letters* **83**, 422–424 (2003).

59. T. Matsui, M. Ozaki, and K. Yoshino, "Tunable laser action in a dye-doped nematic liquid-crystal waveguide under holographic excitation based on electric-field-induced tm guided-mode modulation", *JOSA B* **21**, 1651–1658 (2004).

60. Y. Inoue, H. Yoshida, K. Inoue, A. Fujii, and M. Ozaki, "Improved lasing threshold of cholesteric liquid crystal lasers with in-plane helix alignment", *Applied Physics Express* **3**, 102702 (2010).

61. H. Yoshida, Y. Inoue, T. Isomura, Y. Matsuhisa, A. Fujii, and M. Ozaki, "Position sensitive, continuous wavelength tunable laser based on photopolymerizable cholesteric liquid crystals with an in-plane helix alignment", *Applied Physics Letters* **94**, 093306 (2009).

62. Y. Inoue, Y. Matsuhisa, H. Yoshida, R. Ozaki, H. Moritake, A. Fujii, and M. Ozaki, "Electric field dependence of lasing wavelength in cholesteric liquid crystal with an in-plane helix alignment", *Molecular Crystals and Liquid Crystals* **516**, 182–189 (2010).

63. J. Patel and R. Meyer, "Flexoelectric electro-optics of a cholesteric liquid crystal", *Physical Review Letters* **58**, 1538–1540 (1987).

64. P. Rudquist, L. Komitov, and S. Lagerwall, "Linear electro-optic effect in a cholesteric liquid crystal", *Physical Review E* **50**, 4735–4743 (1994).

65. A. Varanytsia and L.-C. Chien, "Giant flexoelectro-optic effect with liquid crystal dimer CB7CB", *Scientific Reports* **7**, 41333 (2017).

66. H. Coles, M. Clarke, S. Morris, B. Broughton, and A. Blatch, "Strong flexoelectric behavior in bimesogenic liquid crystals.", *Journal of Applied Physics* **99**, 034104 (2006).

67. D. R. Corbett and S. J. Elston, "Modeling the helical flexoelectro-optic effect", *Physical Review E* **84**, 041706 (2011).

68. H. J. Coles and S. M. Morris, *Flexoelectro-optic liquid crystal displays (in handbook of visual display technology)* (Springer, 2012), pp. 1681–1694.

69. J. Chen, S. M. Morris, T. D. Wilkinson, J. P. Freeman, and H. J. Coles, "High speed liquid crystal over silicon display based on the flexoelectro-optic effect", *Optics Express* **17**, 7130–7137 (2009).

70. A. Yariv and P. Yeh, *Optical waves in crystals*, Vol. 10 (Wiley, New York, 1984).

71. R. B. Meyer, "Piezoelectric effects in liquid crystals", *Physical Review Letters* **22**, 918 (1969).

72. L. Parry-Jones, R. Meyer, and S. Elston, "Mechanisms of flexoelectric switching in a zenithally bistable nematic device", *Journal of Applied Physics* **106**, 014510 (2009).

73. V. A. Belyakov, V. E. Dmitrienko, and V. P. Orlov, "Optics of cholesteric liquid crystals", *Soviet Physics Uspekhi* **22**, 63 (1979).

74. W. D. S. John, W. J. Fritz, Z. J. Lu, and D.-K. Yang, "Bragg reflection from cholesteric liquid crystals", *Physical Review E* **51**, 1191–1198 (1995).

75. R. B. Meyer, "Distortion of a cholesteric structure by a magnetic field", *Applied Physics Letters* **14**, 208–209 (1969).

76. Y. Inoue and H. Moritake, "Discovery of a transiently separable high-speed response component in cholesteric liquid crystals with a uniform lying helix", *Applied Physics Express* **8**, 061701 (2015).

77. F. J. Kahn, "Electric-field-induced color changes and pitch dilation in cholesteric liquid crystals", *Physical Review Letters* **24**, 209–212 (1970).

78. S.-D. Lee, J. Patel, and R. B. Meyer, "Effect of flexoelectric coupling on helix distortions in cholesteric liquid crystals", *Journal of Applied Physics* **67**, 1293–1297 (1990).

79. P. Rudquist, T. Carlsson, L. Komitov, and S. Lagerwall, "The flexoelectro-optic effect in cholesterics", *Liquid Crystals* **22**, 445–449 (1997).

80. G. Li, V. Shrotriya, J. Huang, Y. Yao, T. Moriarty, K. Emery, and Y. Yang, "High-efficiency solution processable polymer photovoltaic cells by self-organization of polymer blends", *Nature Materials* **4**, 864 (2005).

81. D. B. Mitzi, M. Yuan, W. Liu, A. J. Kellock, S. J. Chey, V. Deline, and A. G. Schrott, "A high-efficiency solution-deposited thin-film photovoltaic device", *Advanced Materials* **20**, 3657–3662 (2008).

82. L. Ruan, J. Sambles, and J Seaver, "Director configuration of a ferroelectric liquid crystal in a cell with antiparallel surface tilt", *Liquid Crystals* **21**, 909–914 (1996).

83. P. Salter, C Kischka, S. Elston, and E. Raynes, "The influence of chirality on the difference in flexoelectric coefficients investigated in uniform lying helix, grandjean and twisted nematic structures", *Liquid Crystals* **36**, 1355–1364 (2009).

84. S. Tatarkova, D. Burnham, A. Kirby, G. Love, and E. Terentjev, "Colloidal interactions and transport in nematic liquid crystals", *Physical Review Letters* **98**, 157801 (2007).

85. J. Li, S.-T. Wu, S. Brugioni, R. Meucci, and S. Faetti, "Infrared refractive indices of liquid crystals", *Journal of Applied Physics* **97**, 073501 (2005).

86. G. Gray and S. Kelly, "Mesomorphic transition temperatures and viscosities for some cyano-biphenyls and-p-terphenyls with branched terminal alkyl groups", *Molecular Crystals and Liquid Crystals* **104**, 335–345 (1984).
87. A. J. S. Russell, *Report on waves, report of the 14th meeting of the British Association for the Advancement of Science, 311-390*, 1844.
88. R. Y. Chiao, E Garmire, and C. H. Townes, "Self-trapping of optical beams", *Physical Review Letters* **13**, 479–482 (1964).
89. V. I. Talanov, "Self-focusing of electromagnetic waves in non-linear media", *Izv. Vysshikh Uchebn. Zavedenii, Radiofiz.* **7**, 564 (1964).
90. R. W. Boyd, *Nonlinear optics*, Third Edition (Academic Press, 2008).
91. Y. S. Kivshar and G. Agrawal, *Optical solitons: from fibers to photonic crystals* (Academic Press, 2003).
92. V. Semak and M. Shneider, "Electromagnetic beam propagation in nonlinear media", *High Power Laser Science and Engineering* **3**, e11 (2015).
93. H. Kogelnik and T. Li, "Laser beams and resonators", *Proceedings of the IEEE* **54**, 1312–1329 (1966).
94. S. Gorza, "Étude expérimentale de la propagation non linéaire dans les guides optiques plans: instabilité serpentine et soliton de Bragg", PhD thesis (Université libre de Bruxelles, 2004-2005).
95. G. Agrawal, *Nonlinear fiber optics*, 4th (Academic press, 2007).
96. J. J. Rasmussen and K. Rypdal, "Blow-up in nonlinear Schrödinger equations-I a general review", *Physica Scripta* **33**, 481–497 (1986).
97. O. Bang, W. Krolikowski, J. Wyller, and J. J. Rasmussen, "Collapse arrest and soliton stabilization in nonlocal nonlinear media", *Physical Review E* **66**, 046619 (2002).
98. S. K. Turitsyn, "Spatial dispersion of nonlinearity and stability of multidimensional solitons", *Theoretical and Mathematical Physics* **64**, 797–801 (1985).
99. N. Vakhitov and A. A. Kolokolov, "Stationary solutions of the wave equation in a medium with nonlinearity saturation", *Radiophysics and Quantum Electronics* **16**, 783–789 (1973).
100. M. Feit and J. Fleck, "Beam nonparaxiality, filament formation, and beam breakup in the self-focusing of optical beams", *JOSA B* **5**, 633–640 (1988).
101. A. Sheppard and M. Haelterman, "Nonparaxiality stabilizes three-dimensional soliton beams in kerr media", *Optics Letters* **23**, 1820–1822 (1998).
102. I.-C. Khoo, *Liquid crystals: physical properties and nonlinear optical phenomena*, Vol. 64 (John Wiley & Sons, 2007).
103. I. Khoo, "A review of nonlinear optical properties of nematic liquid crystals", *Journal of Nonlinear Optical Physics & Materials* **8**, 305–317 (1999).
104. G. Assanto and M. Peccianti, "Spatial solitons in nematic liquid crystals", *IEEE Journal of Quantum Electronics* **39**, 13–21 (2003).
105. M. Peccianti, A. Fratalocchi, and G. Assanto, "Transverse dynamics of nematicons", *Optics Express* **12**, 6524–6529 (2004).
106. P. M. Morse and H. Feshbach, *Methods of theoretical physics, Vol. I* (McGraw-Hill, 1953).
107. A. Alberucci, A. Piccardi, N. Kravets, O. Buchnev, and G. Assanto, "Soliton enhancement of spontaneous symmetry breaking", *Optica* **2**, 783–789 (2015).
108. M. S. Petrović, N. B. Aleksić, A. I. Strinić, and M. R. Belić, "Reduction of power-dependent walk-off in bias-free nematic liquid crystals", *Optical and Quantum Electronics* **48**, 157 (2016).
109. N. Karimi, A. Alberucci, O. Buchnev, M. Virkki, M. Kauranen, and G. Assanto, "Phase-front curvature effects on nematicon generation", *JOSA B* **33**, 903–909 (2016).

110. S. Bolis, S.-P. Gorza, S. J. Elston, K. Neyts, P. Kockaert, and J. Beeckman, "Spatial fluctuations of optical solitons due to long-range correlated dielectric perturbations in liquid crystals", *Physical Review A* **96**, 031803(R) (2017).

111. P. de Gennes, "Fluctuations d'orientation et diffusion rayleigh dans un cristal nématique", *Comptes Rendus de l'Académie des Sciences, Paris* **266**, 15–17 (1968).

112. B. Halle, P. Quist, and I. Furó, "Director fluctuations and nuclear-spin relaxation in lyotropic nematic liquid crystals", *Physical Review A* **45**, 3763–3777 (1992).

113. S. Brooks, G. Luckhurst, and G. Pedulli, "Thermal fluctuations in the nematic mesophase", *Chemical Physics Letters* **11**, 159–162 (1971).

114. M. Peccianti, C. Conti, and G. Assanto, "Optical modulational instability in a nonlocal medium", *Physical Review E* **68**, 025602 (2003).

115. J. Beeckman, X. Hutsebaut, M. Haelterman, and K. Neyts, "Induced modulation instability and recurrence in nematic liquid crystals", *Optics Express* **15**, 11185–11195 (2007).

116. M. Peccianti, C. Conti, and G. Assanto, "Optical multisoliton generation in nematic liquid crystals", *Optics Letters* **28**, 2231–2233 (2003).

117. G. Agez, P. Glorieux, C. Szwaj, and E. Louvergneaux, "Using noise speckle pattern for the measurements of director reorientational relaxation time and diffusion length of aligned liquid crystals", *Optics Communications* **245**, 243–247 (2005).

118. H. Orihara, N. Sakurai, Y. Sasaki, and T. Nagaya, "Direct observation of coupling between orientation and flow fluctuations in a nematic liquid crystal at equilibrium", *Physical Review E* **95**, 042705 (2017).

119. J. Henninot, J. Blach, and M Warenghem, "The investigation of an electrically stabilized optical spatial soliton induced in a nematic liquid crystal", *Journal of Optics A: Pure and Applied Optics* **10**, 085104 (2008).

120. N. Karimi, A. Alberucci, M. Virkki, A. Priimagi, M. Kauranen, and G. Assanto, "Quenching nematicon fluctuations via photo-stabilization", *Photonics Letters of Poland* **8**, 2–4 (2016).

121. W. Press, B. Flannery, S. Teukolsky, and W. Vetterling, *Numerical recipes in C: the art of scientific computing*, Second (Cambridge University Press, 1992).

122. G. Hadley, "Wide-angle beam propagation using padé approximant operators", *Optics Letters* **17**, 1426–1428 (1992).

123. A. Briggs, M. Sculpher, and K. Claxton, *Decision modelling for health economic evaluation* (OUP Oxford, 2006).

124. I. Lelidis, M. Nobili, and G. Durand, "Electric-field-induced change of the order parameter in a nematic liquid crystal", *Physical Review E* **48**, 3818–3821 (1993).

125. J. Beeckman, "Lateral light propagation and spatial optical solitons in liquid crystal devices", PhD thesis (Universiteit Gent, 2005-2006).

126. C. Conti, M. Peccianti, and G. Assanto, "Observation of optical spatial solitons in a highly nonlocal medium", *Physical Review Letters* **92**, 113902 (2004).

127. A. Alberucci, G. Assanto, A. A. Minzoni, and N. F. Smyth, "Scattering of reorientational optical solitary waves at dielectric perturbations", *Physical Review A* **85**, 013804 (2012).

128. S. Bolis, "Optical gain and photophysics of organic materials for photonic applications", MA thesis (Politecnico di Milano (Milano, Italy), 2013).

129. S. Bolis, M. Celebrano, L. Ghirardini, M. Finazzi, C. Botta, J. Beeckman, P. Kockaert, and T. Virgili, "Optical gain from polyfluorene keto defects in a liquid crystal mixture", *Chemical Communications* **51**, 9686 (2015).

130. L. Ghirardini, T. Virgili, S. Bolis, J. Beeckman, P. Kockaert, M. Finazzi, and M. Celebrano, "The role of segregation in the polarized emission from polyfluorene embedded in a liquid crystal", *Journal of Polymer Science Part B: Polymer Physics* **54**, 1558–1563 (2016).

131. S. Bolis, T. Virgili, S. K. Rajendran, J. Beeckman, and P. Kockaert, "Nematicon-driven injection of amplified spontaneous emission into an optical fiber", *Optics Letters* **41**, 2245–2248 (2016).

132. M. Grell, D. Bradley, G. Ungar, J. Hill, and K. S. Whitehead, "Interplay of physical structure and photophysics for a liquid crystalline polyfluorene", *Macromolecules* **32**, 5810–5817 (1999).

133. C. Bauer, G. Urbasch, H. Giessen, A. Meisel, H.-G. Nothofer, D. Neher, U. Scherf, and R. F. Mahrt, "Polarized photoluminescence and spectral narrowing in an oriented polyfluorene thin film", *ChemPhysChem* **1**, 142–146 (2000).

134. T. Virgili, D. Lidzey, M. Grell, D. Bradley, S. Stagira, M. Zavelani-Rossi, and S. De Silvestri, "Influence of the orientation of liquid crystalline poly (9, 9-dioctylfluorene) on its lasing properties in a planar microcavity", *Applied Physics Letters* **80**, 4088–4090 (2002).

135. M. O'Neill and S. M. Kelly, "Ordered materials for organic electronics and photonics", *Advanced Materials* **23**, 566–584 (2011).

136. T. Martyński, E. Mykowska, and D. Bauman, "Spectral properties of fluorescent dyes in nematic liquid crystals", *Journal of Molecular Structure* **325**, 161–167 (1994).

137. S. Morris, A. Ford, M. Pivnenko, and H. Coles, "Enhanced emission from liquid-crystal lasers", *Journal of Applied Physics* **97**, 023103 (2005).

138. C. Mowatt, S. M. Morris, M. H. Song, T. D. Wilkinson, R. H. Friend, and H. J. Coles, "Comparison of the performance of photonic band-edge liquid crystal lasers using different dyes as the gain medium", *Journal of Applied Physics* **107**, 043101 (2010).

139. S. M. Morris, M. M. Qasim, D. J. Gardiner, P. J. W. Hands, F. Castles, G. Tu, W. T. S. Huck, R. H. Friend, and H. J. Coles, "Liquid crystalline chromophores for photonic band-edge laser devices", *Optical Materials* **35**, 837–842 (2013).

140. X. Tong and Y. Zhao, "Liquid-crystal gel-dispersed quantum dots: reversible modulation of photoluminescence intensity using an electric field", *Journal of the American Chemical Society* **129**, 6372–6373 (2007).

141. J. Mirzaei, M. Reznikov, and T. Hegmann, "Quantum dots as liquid crystal dopants", *Journal of Materials Chemistry* **22**, 22350–22365 (2012).

142. G. Petriashvili, G. Chilaya, M. Matranga, M. D. Santo, G. Cozza, R. Barberi, J. del Barrio, L. Chinelatto, L. Oriol, and M. Piñol, "Chiral luminescent compounds as a perspective for cholesteric liquid crystal lasers", *Optical Materials* **31**, 1693–1696 (2009).

143. L. Blinov, G Cipparrone, A Mazzulla, P Pagliusi, V. Lazarev, and S. Palto, "Simple voltage tunable liquid crystal laser", *Applied Physics Letters* **90**, 131103 (2007).

144. S. Morris, A. Ford, M. Pivnenko, and H. Coles, "The effects of reorientation on the emission properties of a photonic band edge liquid crystal laser", *Journal of Optics A: Pure and Applied Optics* **7**, 215–223 (2005).

145. H. Yoshida, Y. Shiozaki, Y. Inoue, M. Takahashi, Y. Ogawa, A. Fujii, and M. Ozaki, "Threshold improvement in uniformly lying helix cholesteric liquid crystal laser using auxiliary π-conjugated polymer active layer", *Journal of Applied Physics* **113**, 203105 (2013).

146. M. H. Song, B. Park, K.-C. Shin, T. Ohta, Y. Tsunoda, H. Hoshi, Y. Takanishi, K. Ishikawa, J. Watanabe, S. Nishimura, et al., "Effect of phase retardation on defect-mode lasing in polymeric cholesteric liquid crystals", *Advanced Materials* **16**, 779–783 (2004).

147. M. H. Song, B. Park, Y. Takanishi, K. Ishikawa, S. Nishimura, T. Toyooka, and H. Takezoe, "Lasing from thick anisotropic layer sandwiched between polymeric cholesteric liquid crystal films", *Japanese journal of applied physics* **44**, 8165–8167 (2005).

148. L. Onsager, "The effects of shape on the interaction of colloidal particles", *Annals of the New York Academy of Sciences* **51**, 627–659 (1949).

149. T. Adachi, J. Brazard, P. Chokshi, J. Bolinger, V. Ganesan, and P. Barbara, "Highly ordered single conjugated polymer chain rod morphologies", *Journal of Physical Chemistry C* **114**, 20896 (2010).

150. K. P. Fritz and G. D. Scholes, "Alignment of conjugated polymers in a nematic liquid-crystal host", *The Journal of Physical Chemistry B* **107**, 10141–10147 (2003).

151. G. H. Heilmeier, J. A. Castellano, and L. A. Zanoni, "Guest-host interactions in nematic liquid crystals", *Molecular Crystals and Liquid Crystals* **8**, 293–304 (1969).

152. Z. Zhu and T. M. Swager, "Conjugated polymer liquid crystal solutions: control of conformation and alignment", *Journal of the American Chemical Society* **124**, 9670–9671 (2002).

153. F. Araoka, K. Shin, Y. Takanishi, K. Ishikawa, H. Takezoe, Z. Zhu, and T. Swager, "How doping a cholesteric liquid crystal with polymeric dye improves an order parameter and makes possible low threshold lasing", *Journal of Applied Physics* **94**, 279–283 (2003).

154. M. Grell, D. D. Bradley, M. Inbasekaran, and E. P. Woo, "A glass-forming conjugated main-chain liquid crystal polymer for polarized electroluminescence applications", *Advanced Materials* **9**, 798–802 (1997).

155. T. Endo, T. Kobayashi, T. Nagase, and H. Naito, "Anisotropic optical properties of aligned β phase polyfluorene thin films", *Thin Solid Films* **517**, 1324–1326 (2008).

156. K. Whitehead, M Grell, D. Bradley, M Inbasekaran, and E. Woo, "Polarized emission from liquid crystal polymers", *Synthetic Metals* **111**, 181–185 (2000).

157. G. Strangi, S. Ferjani, V. Barna, A. De Luca, C. Versace, N. Scaramuzza, and R. Bartolino, "Random lasing and weak localization of light in dye-doped nematic liquid crystals", *Optics Express* **14**, 7737–7744 (2006).

158. B. Valeur, *Molecular fluorescence: principles and applications* (2001Wiley-VCH, 2001).

159. N. M. Shtykov, M. I. Barnik, L. M. Blinov, B. A. Umanskii, and S. P. Palto, "Amplification of the emission of a liquid-crystal microlaser by means of a uniform liquid-crystal layer", *JETP Letters* **85**, 602–604 (2007).

160. N. Shtykov, M. Barnik, V. Lazarev, S. Palto, B. Umanskii, L. Blinov, and G Cipparrone, "Amplification of laser emission from cholesteric liquid crystals by planar cells with laser dye nematic and isotropic solutions", *Molecular Crystals and Liquid Crystals* **494**, 258–271 (2008).

161. L. Blinov, G. Cipparrone, V. Lazarev, P. Pagliusi, and T. Rugiero, "Liquid crystal as laser medium with tunable gain spectra", *Optics Express* **16**, 6625–6630 (2008).

162. R. Fan, Y. Jiang, Y. Xia, and D. Chen, "Widely tunable amplified spontaneous emission of pyrromethene-650-doped nematic liquid crystal", *Journal of Russian Laser Research* **32**, 139–143 (2011).

163. P. Chandrasekhar, *Conducting polymers, fundamentals and applications: a practical approach* (Kluwer Academic Publishers, 1999).

164. M. Pope and C. E., *Electronic processes in organic crystals and polymers*, 2nd (Oxford University Press, 1999).

165. J. C. Kotz, P. M. Treichel, and G. C. Weaver, *Chemistry and chemical reactivity*, 6th (Thomson Learning Inc., 2006).

166. H. Hart and J. Conia, *Introduction à la chimie organique* (InterEdition, 1987).

167. J. March, *Advanced organic chemistry: reactions, mechanisms, and structure* (John Wiley & Sons, 1992).

168. N. Ashcroft and N. Mermin, *Solid state physics*, edited by R. New York : Holt and Winston (Saunders College Publishing, 1976).

169. O. Svelto, *Principles of laser*, 5th (Springer, New York, 2010).

170. D. Griffiths, *Introduction to quantum mechanics* (Pearson Prentice Hal, 2005).

171. A. Weiner, *Ultrafast optics* (John Wiley & Sons, Inc, 2009).

172. J. B. Prieto, F. L. Arbeloa, V. M. Martínez, T. A. López, and I. L. Arbeloa, "Photophysical properties of the pyrromethene 597 dye: solvent effect", *The Journal of Physical Chemistry A* **108**, 5503–5508 (2004).

173. C. Reichardt, "Solvatochromic dyes as solvent polarity indicators", *Chemical Reviews* **94**, 2319–2358 (1994).

174. L.-O. Pålsson, M. Szablewski, A. Roberts, A. Masutani, G. D. Love, G. H. Cross, D. Bloor, A. J. Kay, A. D. Woolhouse, A. Masutani, et al., "Orientation and solvatochromism of dyes in liquid crystals", *Mol. Cryst. Liq. Cryst.* **402**, 43–53 (2003).

175. S. Gottardo, S. Cavalieri, O. Yaroshchuk, and D. S. Wiersma, "Quasi-two-dimensional diffusive random laser action", *Physical Review Letters* **93**, 263901 (2004).

176. M. D. McGehee, R. Gupta, S. Veenstra, E. K. Miller, M. A Díaz-García, and A. Heeger, "Amplified spontaneous emission from photopumped films of a conjugated polymer", *Physical Review B* **58**, 7035 (1998).

177. G. Heliotis, D. Bradley, G. Turnbull, and I. Samuel, "Light amplification and gain in polyfluorene waveguides", *Applied Physics Letters* **81**, 415 –417 (2002).

178. F. Lahoz, C. J. Oton, N. Capuj, M. Ferrer-González, S. Cheylan, and D. Navarro-Urrios, "Reduction of the amplified spontaneous emission threshold in semiconducting polymer waveguides on porous silica.", *Optics Express* **17**, 16766 (2009).

179. E. Calzado, M. Ramírez, P. Boj, and M. Díaz-García, "Thickness dependence of amplified spontaneous emission in low-absorbing organic waveguides", *Applied Optics* **51**, 3287–3293 (2012).

180. S. Bolis, M. Pasini, and T. Virgili, "A core copolymer approach to improve the gain properties of a red-emitting molecule", *Chemical Communications* **49**, 11761–11761 (2013).

181. K. Vishnubhatla, J. Clark, G. Lanzani, R. Ramponi, R. Osellame, and T. Virgili, "Ultrafast optofluidic gain switch based on conjugated polymer in femtosecond laser fabricated microchannels", *Applied Physics Letters* **94**, 041123 (2009).

182. R. M. Gerosa, A. Sudirman, L. d. S. Menezes, W. Margulis, and C. J. de Matos, "All-fiber high repetition rate microfluidic dye laser", *Optica* **2**, 186–193 (2015).

183. A. Sheridan, G. Turnbull, A. Safonov, and I. Samuel, "Tuneability of amplified spontaneous emission through control of the waveguide-mode structure in conjugated polymer films", *Physical Review B* **62**, 11929(R) (2000).

184. E. Calzado, J. Villalvilla, P. Boj, J. Quintana, and M. Díaz-García, "Tuneability of amplified spontaneous emission through control of the thickness in organic-based waveguides", *Journal of Applied Physics* **97**, 093103 (2005).

185. P. Barbara, W. Chang, S. Link, G. Scholes, and A. Yethiraj, "Structure and dynamics of conjugated polymers in liquid crystalline solvents", *Annual Review of Physical Chemistry* **58**, 565 (2007).

186. A. Tcherniak, D. Solis, S. Khatua, A. Tangonan, T. Lee, and S. Link, "Chain-length dependent nematic ordering of conjugated polymers in a liquid crystal solvent", *Journal of the American Chemical Society* **130**, 12262 (2008).

187. A. Ohira and T. Swager, "Ordering of poly(p-phenylene ethynylene)s in liquid crystals", *Macromolecules* **40**, 19 (2007).

188. M. Grell and D. D. Bradley, "Polarized luminescence from oriented molecular materials", *Advanced Materials* **11**, 895–905 (1999).

189. C. Silva, A. S. Dhoot, D. M. Russell, M. A. Stevens, A. C. Arias, J. D. MacKenzie, N. C. Greenham, R. H. Friend, S. Setayesh, and K. Müllen, "Efficient exciton dissociation via two-step photoexcitation in polymeric semiconductors", *Physical Review B* **64**, 125211 (2001).

190. H Neugebauer, C. Brabec, J. Hummelen, R. Janssen, and N. Sariciftci, "Stability studies and degradation analysis of plastic solar cell materials by ftir spectroscopy", *Synthetic metals* **102**, 1002–1003 (1999).

191. T. Virgili, D. Marinotto, G. Lanzani, and D. Bradley, "Ultrafast resonant optical switching in isolated polyfluorenes chains", *Applied Physics Letters* **86**, 091113 (2005).

192. M. M. Mróz, S. Perissinotto, T. Virgili, G. Gigli, M. Salerno, M. J. Frampton, G. Sforazzini, H. L. Anderson, and G. Lanzani, "Laser action from a sugar-threaded polyrotaxane", *Applied Physics Letters* **95**, 031108 (2009).

193. D. Polli, G. Grancini, J. Clark, M. Celebrano, T. Virgili, G. Cerullo, and G. Lanzani, "Nanoscale imaging of the interface dynamics in polymer blends by femtosecond pump-probe confocal microscopy", *Advanced Materials* **22**, 3048–3051 (2010).

194. T. Virgili, D. Marinotto, C. Manzoni, G. Cerullo, and G. Lanzani, "Ultrafast intrachain photoexcitation of polymeric semiconductors", *Physical Review Letters* **94**, 117402 (2005).

195. T. Virgili, G. Grancini, E. Molotokaite, I. Suarez-Lopez, S. K. Rajendran, A. Liscio, V. Palermo, G. Lanzani, D. Polli, and G. Cerullo, "Confocal ultrafast pump–probe spectroscopy: a new technique to explore nanoscale composites", *Nanoscale* **4**, 2219–2226 (2012).

196. S. Gamerith, C. Gadermaier, U. Scherf, and E. J. List, "Emission properties of pristine and oxidatively degraded polyfluorene type polymers", *Physica Status Solidi (a)* **201**, 1132–1151 (2004).

197. E. J. List, R. Guentner, P. Scanducci de Freitas, and U. Scherf, "The effect of keto defect sites on the emission properties of polyfluorene-type materials", *Advanced Materials* **14**, 374–378 (2002).

198. P Biagioni, M Celebrano, M Zavelani-Rossi, D Polli, M Labardi, G Lanzani, G Cerullo, M Finazzi, and L Duò, "High-resolution imaging of local oxidation in polyfluorene thin films by nonlinear near-field microscopy", *Applied Physics Letters* **91**, 191118 (2007).

199. B. He, J. Li, Z. Bo, and Y. Huang, "Studies of green emission in polyfluorenes using a model polymer", *Polymer Journal* **39**, 1345–1350 (2007).

200. X. Gong, D Moses, A. J. Heeger, and S. Xiao, "White light electrophosphorescence from polyfluorene-based light-emitting diodes: utilization of fluorenone defects", *The Journal of Physical Chemistry B* **108**, 8601–8605 (2004).

201. Y.-Y. Noh, D.-Y. Kim, Y. Yoshida, K. Yase, B.-J. Jung, E. Lim, H.-K. Shim, and R. Azumi, "Keto defect sites in fluorene-based organic field-effect transistors: the origin of rapid degradation on the performance of the device", *Journal of Applied Physics* **97**, 104504 (2005).

202. L. Rozanski, C. Cone, D. Ostrowski, and D. V. Bout, "Effect of film morphology on the energy transfer to emissive green defects in dialkyl polyfluorenes", *Macromolecules* **40**, 4524–4529 (2007).

203. A. P. Kulkarni, X. Kong, and S. A. Jenekhe, "Fluorenone-containing polyfluorenes and oligofluorenes: photophysics, origin of the green emission and efficient green electroluminescence", *The Journal of Physical Chemistry B* **108**, 8689–8701 (2004).

204. M. Sims, D. D. Bradley, M. Ariu, M. Koeberg, A. Asimakis, M. Grell, and D. G. Lidzey, "Understanding the origin of the 535 nm emission band in oxidized poly (9, 9-dioctylfluorene): the essential role of inter-chain/inter-segment interactions", *Advanced Functional Materials* **14**, 765–781 (2004).

205. K. Becker, J. M. Lupton, J. Feldmann, B. S. Nehls, F. Galbrecht, D. Gao, and U. Scherf, "On-chain fluorenone defect emission from single polyfluorene molecules in the absence of intermolecular interactions", *Advanced Functional Materials* **16**, 364–370 (2006).

206. F. Montilla and R. Mallavia, "On the origin of green emission bands in fluorene-based conjugated polymers", *Advanced Functional Materials* **17**, 71–78 (2007).

207. R Dabrowski, J Dziaduszek, and T Szczuciński, "Mesomorphic characteristics of some new homologous series with the isothiocyanato terminal group", *Molecular Crystals and Liquid Crystals* **124**, 241–257 (1985).

208. L. Chinelatto, J. del Barrio, M. Piñol, L. Oriol, M. Matranga, M. D. Santo, and R. Barberi, "Oligofluorene blue emitters for cholesteric liquid crystal lasers", *Journal of Photochemistry and Photobiology A* **210**, 130–139 (2010).

209. C.-H. Wen, S. Gauza, and S.-T. Wu, "Ultraviolet stability of liquid crystals containing cyano and isothiocyanato terminal groups", *Liquid Crystals* **31**, 1479–1485 (2004).

210. A. J. Cadby, P. A. Lane, H. Mellor, S. J. Martin, M. Grell, C. Giebeler, D. D. C. Bradley, M. Wohlgenannt, C. An, and Z. V. Vardeny, "Film morphology and photophysics of polyfluorene", *Physical Review B* **62**, 15604 (2000).

211. A. L. T. Khan, L. M. Sreearunothai P. Herz, M. J. Banach, and A. Köhler, "Morphology-dependent energy transfer within polyfluorene thin films", *Physical Review B* **69**, 085201 (2004).

212. M. Grell, D. Bradley, X. long, T. Chamberlain, M. Inbasekaran, E. P. Woo, and M. Soliman, "Chain geometry, solution aggregation and enhanced dichroism in the liquid-crystalline conjugated polymer poly(9,9-dioctylfluorene)", *Acta Polymerica* **49**, 439–444 (1998).

213. F. B. Dias, J. Morgado, A. L. Macanita, F. P. da Costa, H. D. Burrows, and A. P. Monkman, "Kinetics and thermodynamics of poly (9, 9-dioctylfluorene) β -phase formation in dilute solution", *Macromolecules* **39**, 5854–5864 (2006).

214. M. Misaki, M. Chikamatsu, Y. Yoshida, R. Azumi, N. Tanigaki, K. Yase, S. Nagamatsu, and Y. Ueda, "Highly efficient polarized polymer light-emitting diodes utilizing oriented films of β-phase poly (9, 9-dioctylfluorene)", *Applied Physics Letters* **93**, 023304 (2008).

215. T. Kawamura, M. Misaki, Y. Koshiba, S. Horie, K. Kinashi, K. Ishida, and Y. Ueda, "Crystalline thin films of β-phase poly(9,9-dioctylfluorene)", *Thin Solid Films* **519**, 2247–2250 (2011).

216. M. Ariu, D. Lidzey, M. Sims, A. Cadby, P. Lane, and D. Bradley, "The effect of morphology on the temperature-dependent photoluminescence quantum efficiency of the conjugated polymer poly (9, 9-dioctylfluorene)", *Journal of Physics: Condensed Matter* **14**, 9975–9986 (2002).

217. X. Gong, D. Moses, A. J. Heeger, and S. Xiao, "Excitation energy transfer from polyfluorene to fluorenone defects", *Synthetic Metals* **141**, 17–20 (2004).

218. X. Yang, D Neher, C Spitz, E. Zojer, J.-L. Brédas, R Güntner, and U Scherf, "On the polarization of the green emission of polyfluorenes", *The Journal of Chemical Physics* **119**, 6832–6839 (2003).

219. T. Sugiyama, O. Sato, S. Kang, M. Tokita, and J. Watanabe, *Soft Matter* **7**, 6998–7002 (2011).

220. O. Sato, Y. Inagaki, S. Kang, M. Tokita, and J. Watanabe, "Regular network pattern evolution observed in phase separation in low-molecular-weight LC and LC block copolymer mixture", *Macromolecules* **42**, 5442–5445 (2009).

221. O. Korovyanko and Z. Vardeny, "Film morphology and ultrafast photoexcitation dynamics in polyfluorene", *Chemical Physics Letters* **356**, 361–367 (2002).

222. C. Gadermaier, L. Romaner, T. Piok, E. List, B. Souharce, U. Scherf, G. Cerullo, and G. Lanzani, "Comprehensive photophysical studies of polyfluorenes containing on-chain emissive defects", *Physical Review B* **72**, 045208 (2005).

223. S Xu, V. Klimov, B Kraabel, H Wang, and D. McBranch, "Femtosecond transient absorption study of oriented poly (9, 9-dioctylfluorene) film: hot carriers, excitons, and charged polarons", *Physical Review B* **64**, 193201 (2001).

224. S. Bolis, C. C. Tartan, J. Beeckman, P. Kockaert, S. J. Elston, and S. M. Morris, "Solvent-induced self-assembly of uniform lying helix alignment of the cholesteric liquid crystal phase for the flexoelectro-optic effect", *Liquid Crystals* (2018) DOI:10.1080/02678292.2018.1425492.

225. J. Patel and S.-D. Lee, "Fast linear electro-optic effect based on cholesteric liquid crystals", *Journal of Applied Physics* **66**, 1879–1881 (1989).

226. B. Broughton, M. Clarke, A. Blatch, and H. Coles, "Optimized flexoelectric response in a chiral liquid-crystal phase device", *Journal of Applied Physics* **98**, 034109 (2005).

227. F. Castles, S. Morris, and H. Coles, "Flexoelectro-optic properties of chiral nematic liquid crystals in the uniform standing helix configuration", *Physical Review E* **80**, 031709 (2009).

228. M. S. Kim, P. J. Bos, D.-W. Kim, D.-K. Yang, J. H. Lee, and S. H. Lee, "Flexoelectric effect in an in-plane switching (IPS) liquid crystal cell for low-power consumption display devices", *Scientific Reports* **6**, 35254 (2016).

229. P. S. Salter, S. J. Elston, P. Raynes, and L. A. Parry-Jones, "Alignment of the uniform lying helix structure in cholesteric liquid crystals", *Japanese Journal of Applied Physics* **48**, 101302 (2009).

230. P. S. Salter, G. Carbone, S. A. Jewell, S. J. Elston, and P. Raynes, "Unwinding of the uniform lying helix structure in cholesteric liquid crystals next to a spatially uniform aligning surface", *Physical Review E* **80**, 041707 (2009).

231. Y. Inoue and H. Moritake, "Formation of a defect-free uniform lying helix in a thick cholesteric liquid crystal cell", *Applied Physics Express* **8**, 071701 (2015).

232. D. J. Gardiner, S. M. Morris, P. J. Hands, F. Castles, M. M. Qasim, W.-S. Kim, S. S. Choi, T. D. Wilkinson, and H. J. Coles, "Spontaneous induction of the uniform lying helix alignment in bimesogenic liquid crystals for the flexoelectro-optic effect", *Applied Physics Letters* **100**, 063501 (2012).

233. B. Outram and S. Elston, "Spontaneous and stable uniform lying helix liquid-crystal alignment", *Journal of Applied Physics* **113**, 043103 (2013).

234. G. Carbone, D. Corbett, S. J. Elston, P. Raynes, A. Jesacher, R. Simmonds, and M. Booth, "Uniform lying helix alignment on periodic surface relief structure generated via laser scanning lithography", *Molecular Crystals and Liquid Crystals* **544**, 37–49 (2011).

235. G. Carbone, P. Salter, S. J. Elston, P. Raynes, L. De Sio, S. Ferjani, G. Strangi, C. Umeton, and R. Bartolino, "Short pitch cholesteric electro-optical device based on periodic polymer structures", *Applied Physics Letters* **95**, 011102 (2009).

236. R. Caputo, A. De Luca, L. De Sio, L. Pezzi, G. Strangi, C. Umeton, A. Veltri, R. Asquini, A. d'Alessandro, and D. Donisi, "POLICRYPS: a liquid crystal composed nano/microstructure with a wide range of optical and electro-optical applications", *Journal of Optics A: Pure and Applied Optics* **11**, 024017 (2009).

237. C. C. Tartan, P. S. Salter, M. J. Booth, S. M. Morris, and S. J. Elston, "Localised polymer networks in chiral nematic liquid crystals for high speed photonic switching", *Journal of Applied Physics* **119**, 183106 (2016).

238. T. P. Bigioni, X.-M. Lin, T. T. Nguyen, E. I. Corwin, T. A. Witten, and H. M. Jaeger, "Kinetically driven self assembly of highly ordered nanoparticle monolayers", *Nature Materials* **5**, 265–270 (2006).

239. T. K. Sau and C. J. Murphy, "Self-assembly patterns formed upon solvent evaporation of aqueous cetyltrimethylammonium bromide-coated gold nanoparticles of various shapes", *Langmuir* **21**, 2923–2929 (2005).

240. P. C. Ohara, D. V. Leff, J. R. Heath, and W. M. Gelbart, "Crystallization of opals from polydisperse nanoparticles", *Physical Review Letters* **75**, 3466–3469 (1995).

241. J. Tang, G. Ge, and L. E. Brus, "Gas- liquid- solid phase transition model for two-dimensional nanocrystal self-assembly on graphite", *The Journal of Physical Chemistry B* **106**, 5653–5658 (2002).

242. H. Zhang, E. W. Edwards, D. Wang, and H. Möhwald, "Directing the self-assembly of nanocrystals beyond colloidal crystallization", *Physical Chemistry Chemical Physics* **8**, 3288–3299 (2006).

243. M. Maillard, L. Motte, A. Ngo, and M. Pileni, "Rings and hexagons made of nanocrystals: a marangoni effect", *The Journal of Physical Chemistry B* **104**, 11871–11877 (2000).

244. E. Rabani, D. R. Reichman, P. L. Geissler, and L. E. Brus, "Drying-mediated self-assembly of nanoparticles", *Nature* **426**, 271–274 (2003).

245. F. X. Redl, K.-S. Cho, C. B. Murray, and S. O'Brien, "Three-dimensional binary superlattices of magnetic nanocrystals and semiconductor quantum dots", *Nature* **423**, 968–971 (2003).

246. Z. Nie, A. Petukhova, and E. Kumacheva, "Properties and emerging applications of self-assembled structures made from inorganic nanoparticles", *Nature Nanotechnology* **5**, 15–25 (2010).

247. E. V. Shevchenko, D. V. Talapin, N. A. Kotov, S. O'brien, and C. B. Murray, "Structural diversity in binary nanoparticle superlattices", *Nature* **439**, 55–59 (2006).

248. Y. Min, M. Akbulut, K. Kristiansen, Y. Golan, and J. Israelachvili, "The role of interparticle and external forces in nanoparticle assembly", *Nature Materials* **7**, 527–538 (2008).

249. N. V. Dziomkina and G. J. Vancso, "Colloidal crystal assembly on topologically patterned templates", *Soft Matter* **1**, 265–279 (2005).

250. X. Lin, H. Jaeger, C. Sorensen, and K. Klabunde, "Formation of long-range-ordered nanocrystal superlattices on silicon nitride substrates", *The Journal of Physical Chemistry B* **105**, 3353–3357 (2001).

251. Z. Zhang and M. Lin, "High-yield preparation of vertically aligned gold nanorod arrays via a controlled evaporation-induced self-assembly method", *Journal of Materials Chemistry C* **2**, 4545–4551 (2014).

252. N. Goubet, J. Richardi, P.-A. Albouy, and M.-P. Pileni, "How to predict the growth mechanism of supracrystals from gold nanocrystals", *The Journal of Physical Chemistry Letters* **2**, 417–422 (2011).

253. M. B. Sigman, A. E. Saunders, and B. A. Korgel, "Metal nanocrystal superlattice nucleation and growth", *Langmuir* **20**, 978–983 (2004).

254. W. Guo, M. Wang, W. Xia, and L. Dai, "Evaporation-induced self-assembly of capillary cylindrical colloidal crystal in a face-centered cubic structure with controllable thickness", *Journal of Materials Research* **27**, 1663–1671 (2012).

255. P. Rudquist, L. Komitov, and S. Lagerwall, "Volume-stabilized ulh structure for the flexoelectro-optic effect and the phase-shift effect in cholesterics", *Liquid crystals* **24**, 329–334 (1998).

256. L. V. Natarajan, J. M. Wofford, V. P. Tondiglia, R. L. Sutherland, H. Koerner, R. A. Vaia, and T. J. Bunning, "Electro-thermal tuning in a negative dielectric cholesteric liquid crystal material", *Journal of Applied Physics* **103**, 093107 (2008).

257. A. Sengupta, S. Herminghaus, and C. Bahr, "Liquid crystal microfluidics: surface, elastic and viscous interactions at microscales", *Liquid Crystals Reviews* **2**, 73–110 (2014).

258. R. J. Carlton, C. D. Ma, J. K. Gupta, and N. L. Abbott, "Influence of specific anions on the orientational ordering of thermotropic liquid crystals at aqueous interfaces", *Langmuir* **28**, 12796–12805 (2012).

259. P. De Gennes, "Calcul de la distorsion d'une structure cholesterique par un champ magnetique", *Solid State Communications* **6**, 163–165 (1968).

260. E. Parry, S. Bolis, S. J. Elston, A. A. Castrejón-Pita, and S. M. Morris, "Drop-on-demand inkjet printing of thermally tunable liquid crystal microlenses", *Advanced Engineering Materials*, 1700774 (2017).

261. G. Strangi, V. Barna, R. Caputo, A. De Luca, C. Versace, N. Scaramuzza, C. Umeton, R. Bartolino, and G. N. Price, "Color-tunable organic microcavity laser array using distributed feedback", *Physical Review Letters* **94**, 063903 (2005).

262. J. Henninot, J. Blach, and M. Warenghem, "Enhancement of dye fluorescence recovery in nematic liquid crystals using a spatial optical soliton", *Journal of Applied Physics* **107**, 113111 (2010).

263. J. Arrue, J. Zubia, G. Durana, and J. Mateo, "Parameters affecting bending losses in graded-index polymer optical fibers", *IEEE Journal of Selected Topics in Quantum Electronics* **7**, 836–844 (2001).

264. R. Sapienza, S. Mujumdar, C. Cheung, A. Yodh, and D. Wiersma, "Anisotropic weak localization of light", *Physical Review Letters* **92**, 033903 (2004).

265. L. W. Casperson, "Threshold characteristics of mirrorless lasers", *Journal of Applied Physics* **48**, 256–262 (1977).

266. M. Tocci, M. Scalora, M. Bloemer, J. Dowling, and C. Bowden, "Measurement of spontaneous-emission enhancement near the one-dimensional photonic band edge of semiconductor heterostructures", *Physical Review A* **53**, 2799–2803 (1996).

267. J. Schmidtke and W. Stille, "Fluorescence of a dye-doped cholesteric liquid crystal film in the region of the stop band: theory and experiment", *The European Physical Journal B* **31**, 179–194 (2003).

268. H. Finkelmann, S. T. Kim, A Munoz, P. Palffy-Muhoray, B. Taheri, et al., "Tunable mirrorless lasing in cholesteric liquid crystalline elastomers", *Advanced Materials* **13**, 1069–1072 (2001).

269. L. Natarajan, T. White, J. Wofford, V. Tondiglia, R. Sutherland, S. Siwecki, and T. Bunning, "Laser initiated thermal tuning of a cholesteric liquid crystal", *Applied Physics Letters* **97**, 011107 (2010).

270. T.-H. Lin, H.-C. Jau, C.-H. Chen, Y.-J. Chen, T.-H. Wei, C.-W. Chen, and A. Y.-G. Fuh, "Electrically controllable laser based on cholesteric liquid crystal with negative dielectric anisotropy", *Applied Physics Letters* **88**, 061122 (2006).

271. A. Chanishvili, G. Chilaya, G. Petriashvili, R. Barberi, R. Bartolino, G. Cipparrone, A. Mazzulla, and L. Oriol, "Lasing in dye-doped cholesteric liquid crystals: two new tuning strategies", *Advanced Materials* **16**, 791–795 (2004).

272. T. Matsui, M. Ozaki, and K. Yoshino, "Tunable photonic defect modes in a cholesteric liquid crystal induced by optical deformation of helix", *Physical Review E* **69**, 061715 (2004).

273. T.-H. Lin, Y.-J. Chen, C.-H. Wu, A. Y.-G. Fuh, J.-H. Liu, and P.-C. Yang, "Cholesteric liquid crystal laser with wide tuning capability", *Applied Physics Letters* **86**, 161120 (2005).

274. B. H. Cumpston, S. P. Ananthavel, S. Barlow, D. L. Dyer, J. E. Ehrlich, L. L. Erskine, A. A. Heikal, S. M. Kuebler, I.-Y. S. Lee, D. McCord-Maughon, et al., "Two-photon polymerization initiators for three-dimensional optical data storage and microfabrication", *Nature* **398**, 51–54 (1999).

275. H. Zeng, D. Martella, P. Wasylczyk, G. Cerretti, J.-C. G. Lavocat, C.-H. Ho, C. Parmeggiani, and D. S. Wiersma, "High-resolution 3d direct laser writing for liquid-crystalline elastomer microstructures", *Advanced materials* **26**, 2319–2322 (2014).

276. C. C. Tartan, P. S. Salter, T. D. Wilkinson, M. J. Booth, S. M. Morris, and S. J. Elston, "Generation of 3-dimensional polymer structures in liquid crystalline devices using direct laser writing", *RSC Advances* **7**, 507–511 (2017).

277. S. M. Wood, J. A. J. Fells, S. J. Elston, and S. M. Morris, "Wavelength tuning of the photonic band gap of an achiral nematic liquid crystal filled into a chiral polymer scaffold", *Macromolecules* **49**, 8643–8652 (2016).

278. Y. Li, D. Luo, and Z. H. Peng, "Full-color reflective display based on narrow bandwidth templated cholesteric liquid crystal film", *Optical Materials Express* **7**, 16–24 (2017).

279. P. S. Salter and M. J. Booth, "Focussing over the edge: adaptive subsurface laser fabrication up to the sample face", *Optics Express* **20**, 19978–19989 (2012).

280. Editorial, "Scrutinizing lasers", *Nature Photonics* **11** (2017) doi:10.1038/nphoton.2017.28.

281. I. D. Samuel, E. B. Namdas, and G. A. Turnbull, "How to recognize lasing", *Nature Photonics* **3**, 546 (2009).

282. S. Morris, M. Clarke, A. Blatch, and H. Coles, "Structure-flexoelastic properties of bimesogenic liquid crystals", *Physical Review E* **75**, 041701 (2007).

283. P. Kockaert, P. Tassin, I. Veretennicoff, G. Van der Sande, and M. Tlidi, "Beyond the zero-diffraction regime in optical cavities with a left-handed material", *JOSA B* **26**, B148–B155 (2009).